Spin Liquids on the Centred Pyrochlore Lattice

Rajah Pascal Nutakki

München, 2023

Spin Liquids on the Centred Pyrochlore Lattice

Rajah Pascal Nutakki

Dissertation
der Fakultät für Physik
der Ludwig-Maximilians-Universität
München

vorgelegt von
Rajah Pascal Nutakki
aus Calgary

München, den 6 November 2023

Erstgutachter: Prof. Dr. Lode Pollet
Zweitgutachter: Prof. Dr. Johannes Knolle
Tag der mündlichen Prüfung: 19 Dezember 2023

Abstract

The study of both classical and quantum spin models on geometrically frustrated lattices has proven fertile ground for the theoretical discovery of states of matter beyond Landau's symmetry-breaking paradigm. In three dimensions, the most well-studied of these is the pyrochlore lattice, which hosts quantum and classical spin liquids, giving rise to remarkable emergent phenomena such as magnetic monopoles or an effective quantum electrodynamics. In this thesis, we study classical and quantum models on the *centred* pyrochlore lattice, where there is an additional site at the centre of every tetrahedron. Using a combination of Monte Carlo simulations and analytical mean-field calculations, we show that the minimal classical $J_1 - J_2$ Heisenberg model hosts a rich variety of phases, with competition between ferrimagnetic order on the one hand, and the disorder of a Coulomb spin liquid on the other. A large region of the parameter space hosts a classical spin liquid which realizes an emergent electrostatics with mobile charges in the ground state, an emergent charge fluid. This can also be understood as the thin-film realization of a higher-dimensional Coulomb spin liquid. We find that the addition of dipolar interactions induces ordering at low temperatures, but the spin liquid survives at finite temperature. Comparing to experiments on the metal-organic framework [Mn(ta)$_2$], we find that this spin liquid regime well-approximates bulk specific heat, magnetization and susceptibility measurements. Therefore we propose that [Mn(ta)$_2$] realizes a classical spin liquid in the regime $1\ \mathrm{K} \lesssim T \lesssim 6\ \mathrm{K}$. Turning to the quantum $S = 1/2$ XXZ model, we propose, using degenerate perturbation theory, that the effective low-energy description in the small $J^{\perp}$ limit is a $\mathrm{U}(1)$ lattice gauge theory coupled to fermionic matter. Exact diagonalization on small clusters and gauge mean-field calculations suggest a $\mathrm{U}(1)$ quantum spin liquid ground state, corresponding to the deconfined phase of the gauge theory. As the first study of spin models on the centred pyrochlore lattice, this thesis provides the framework for understanding both classical and quantum models with this geometry. Since the lattice is experimentally realizable in metal-organic frameworks, which are highly modular, this provides a route to probing the exotic physics of emergent electrostatics and quantum electrodynamics in the lab.

Zusammenfassung

Die Untersuchung von klassischen und Quantenspinmodellen auf geometrisch frustrierten Gittern hat sich als fruchtbarer Boden für die theoretische Entdeckung von Materiezuständen erwiesen, die über das Paradigma der Landau Symmetriebrechung hinausgehen. Das am meisten untersuchte dreidimensionale Gitter ist das Pyrochlor-Gitter, das sowohl klassische als auch Quantenspinflüssigkeiten beherbergt und zu bemerkenswerten emergenten Phänomenen wie magnetischen Monopolen und einer effektiver Quantenelektrodynamik führt. In dieser Dissertation untersuchen wir klassische und Quantenmodelle auf dem *zentrierten* Pyrochlor-Gitter, bei dem sich im Zentrum jedes Tetraeders eine zusätzliche Gitterstelle befindet. Mithilfe einer Kombination aus Monte-Carlo-Simulationen und analytischen Mittelfeldberechnungen zeigen wir, dass das minimale klassische $J_1 - J_2$ Heisenberg-Modell eine Vielzahl von Phasen besitzt, in denen die ferrimagnetische Ordnung und die Unordnung einer Coulomb-Spinflüssigkeit konkurrieren. Ein groSSer Bereich des Parameterraums beherbergt eine klassische Spinflüssigkeit, die eine emergente Elektrostatik mit beweglichen Ladungen im Grundzustand realisiert, eine emergente Ladungsflüssigkeit. Dies kann auch als die Dünnschicht-Realisierung einer höherdimensionalen Coulomb-Spinflüssigkeit verstanden werden. Wir stellen fest, dass das Hinzufügen von dipolaren Wechselwirkungen bei niedrigen Temperaturen eine Ordnung verursacht, welche die Spinflüssigkeit jedoch bei Temperaturen über dem Nullpunkt übersteht. Im Vergleich zu Experimenten mit dem metallorganischen Gerüst [Mn(ta)$_2$] stellen wir fest, dass die Spinflüssigkeitsphase die Messungen der spezifischen Wärme, der Magnetisierung und der Suszeptibilität gut approximiert. Daher schlagen wir vor, dass [Mn(ta)$_2$] eine klassische Spinflüssigkeit im Bereich $1\,\mathrm{K} \lesssim T \lesssim 6\,\mathrm{K}$ realisiert. Wir widmen uns dem $S = 1/2$ XXZ-Quantenmodell und schlagen unter Verwendung einer entarteten Störungstheorie vor, dass es effektiv und bei niedriger Energie durch eine an fermionische Materie gekoppelte $\mathrm{U}(1)$ -Gittereichtheorie beschrieben wird. Des Weiteren, legen exakte Diagonalisierung auf kleinen Clustern und Eich-Mittelfeldtheorie nahe, dass der Grundzustand eine $\mathrm{U}(1)$ Quantenspinflüssigkeit ist. Dies hat zur Folge, dass die emergente Eichtheorie ungebunden ist. Bei der vorliegenden Arbeit handelt es sich um die erste Untersuchung von Spinmodellen auf dem zentrierten Pyrochlor-Gitter und bildet somit den Rahmen für das Verständnis von klassischen und Quantenmodellen auf diesem Gitter. Da das Gitter durch hochgradig modulare metallorganische Gerüste experimentell realisierbar ist, bietet es sich zur Erforschung der exotischen Physik von emergenter Elektrostatik und Quantenelektrodynamik im Labor an.

Related Publications

The following publications resulted from work included in this thesis:

[1] **R.P. Nutakki**, L.D.C. Jaubert and L. Pollet. “The classical Heisenberg model on the centred pyrochlore lattice", *SciPost Phys.* **15**, 040 (2023).

[2] **R.P. Nutakki**, R. Röß-Ohlenroth, D. Volkmer, A. Jesche, H-A K. von Nidda, A.A. Tsirlin, P. Gegenwart, L. Pollet, L.D.C. Jaubert. “Frustration on a centered pyrochlore lattice in metal-organic frameworks", *Phys. Rev. Research* **5**, L022018 (2023).

Chapter 2 is largely a reproduction of [1] with some additional explanations and clarifications. Similarly, chapter 3 contains many of the same results and figures as [2], but is presented from the theoretical perspective and contains many details which are not included in the publication. A publication based on chapter 4 is in preparation.

Contents

Introduction

One of the fundamental concepts of contemporary physics is Landau's theory of phase transitions [3], where phases of matter are classified by their symmetries, or lack thereof. This leads to a framework, where, given a system with a set of symmetries, phase transitions occur via their spontaneous breaking, captured by a local order parameter that transforms non-trivially under the broken symmetry. These effects can be captured by a phenomenological Landau-Ginzburg theory [4, 5].

A simple (mean-field) example is provided by considering the free energy

$$F(m) = -\frac{a}{2}m^2 + \frac{b}{4}m^4, \tag{1}$$

where m is a continuous variable and a, b are non-negative parameters. $F(m)$ possesses a global $\mathbb{Z}_2$ symmetry, as it is invariant under the transformation $m \to -m$. For $a = 0$, the free energy is minimized by the unique value $m = 0$, which is invariant under the inversion of m. On the other hand, as shown in fig. 1, for a finite, the free energy has degenerate minima at

$$m_\pm = \pm\sqrt{\frac{a}{b}}. \tag{2}$$

Therefore the system must "choose" one of these minima, which breaks the $\mathbb{Z}_2$ symmetry, as under inversion $m_+ \to m_-$.

This quantity m could be, for example, the average magnetization,

$$m = \frac{1}{N}\sum_{i=1}^{N}\sigma_i, \quad \sigma_i = \pm 1, \tag{3}$$

of an Ising model [6], a toy model for magnetism. The states with $m = 0$ and $m_\pm$ correspond to distinct phases of matter. Those with $m = 0$ are in a symmetric, disordered phase, whereas those with $m = m_\pm$ are in an ordered, symmetry-broken phase, with the inversion operation mapping between the two degenerate possibilities. Furthermore, entropic considerations tell us to expect the symmetric phase at high temperature and a symmetry-broken one at low temperature.

The Landau-Ginzburg paradigm describes a huge variety of phases of matter, from liquids and crystalline solids, normal and superfluid states (of liquid He for example [7]), to fer-

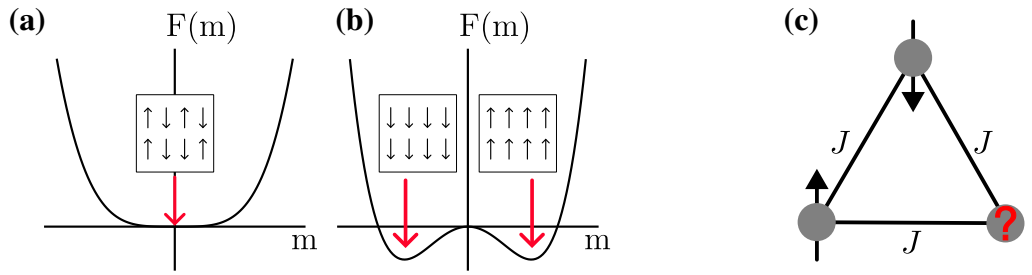

Figure 1: **(a,b)** The free energy in eq. (1), with $a = 0$ **(a)** and finite $a > 0$ **(b)**. Corresponding Ising model states for the minima are shown, where an up (down) arrow corresponds to $\sigma_i = +(-)1$. The appearance of degenerate minima at $m \neq 0$ signals the symmetry-breaking phase transition. **(c)** Geometric frustration in an Ising model (eq. (4)) where the spins are coupled antiferromagnetically. It is not possible to simultaneously minimize the energy of all bonds so a spin of either value on the lattice site marked by the red question mark will give the same energy.

romagnets, antiferromagnets and the many more complex (sometimes hidden [8]) forms of order in magnetic systems.

However, despite the success of this idea, it is not the end of the story when it comes to classifying states of matter. In the 1950s, it was found that antiferromagnetic ($J > 0$) nearest-neighbour Ising models,

$$E = J \sum_{\langle ij \rangle} \sigma_i \sigma_j, \tag{4}$$

on the triangular [9], kagome [10] and pyrochlore [11] lattices, host disordered ground states, so that there is no symmetry-breaking transition at any temperature. These ground states can be thought of as examples of classical spin liquids. The common feature of these lattices is that they are geometrically frustrated [12, 13], the interactions cannot simultaneously be satisfied, as illustrated in fig. 1(c). The pertinent question is, if the low temperature states do not break any symmetries, to what extent, and, in what way, can they be considered distinct from the high temperature paramagnet?

Ising models are, in general, rather crude models of the quantum magnetic moments in real materials, so it is natural to ask whether this evasion of symmetry-breaking can survive the inclusion of quantum effects. In 1973, Anderson [14] proposed that the ground state of the antiferromagnetic Heisenberg Hamiltonian on the triangular lattice would be a so-called resonating valence bond (RVB) state, a quantum superposition of nearest-neighbour spin singlets which does not break any symmetries. It was not until the 1990s that a consensus began to emerge that the ground state was actually 120° ordered [15–20], yet the idea lives on as a fundamental example of a quantum spin liquid (QSL) [12, 21–24].

The discovery of the fractional quantum Hall (FQH) effect in 1982 [25] (see also [26–30]), characterized by plateaus in the Hall resistivity at fractional filling factors (in units of the

flux quantum), began to provide experimental evidence for states of matter beyond the symmetry-breaking paradigm. In these systems, where a strong magnetic field is applied to a two-dimensional electron gas, the states at different filling factors are in some way distinct, yet they do not break any symmetries [31, 32]. Wen and Niu [33] (see also [34, 35]) found that the distinction between FQH states could be understood through the lens of *topological* order, a property of a many-body ground state wavefunction which arises as a consequence of long-range quantum entanglement [36]. Topologically ordered states are gapped and exhibit a topological ground state degeneracy alongside fractional excitations which may possess anyonic statistics [37–39]. In fact, these phenomena can be understood through the emergence of effective gauge theories [28, 29].

The notion of topological order is not restricted to the fractional quantum Hall effect, the RVB state and a (bosonic) FQH state were shown to be equivalent [40], so must also possess topological order [41]. In the late 1980s and 1990s, the RVB state had begun to attract considerable attention as a possible part of the mechanism leading to high-temperature superconductivity in cuprates [42, 43]. Wen later generalized the concept of topological order to include gapless states of matter, defining the notion of *quantum* order and proposing a huge array of spin liquid ground states [44] distinguished by their quantum order rather than symmetry.

Parallel to this, the experimental discovery in 1997 of dipolar spin ice in rare-earth pyrochlore oxides [45] whose properties can be understood by mapping to Anderson's Ising model on the pyrochlore lattice [11, 46, 47], provides an example of a low temperature state of matter, which does not break symmetries, yet can be understood in terms of a *classical* model. Indeed, dipolar spin ice demonstrates many of the features usually associated with quantum order [48], such as fractionalization (in the form of magnetic monopoles) [49], emergent gauge fields [50], and a classical analogue of topological ground state degeneracy [51, 52].

In 2003, the theoretical notion of QSLs and the potential for utilizing their fractional excitations in topological quantum computing [39, 53], was clarified by Kitaev's toric code [54], an exactly solvable model with a QSL ground state. He later introduced another exactly solvable model on the honeycomb lattice [55] with a QSL ground state, for which a route to experimental realization in strong spin-orbit coupled d^5 materials was proposed [56], spawning the field of Kitaev materials [57]. In the spin liquid, the fractional excitations are Majorana fermions, whose detection would be a smoking gun for the spin liquid state. Probably the most famous of the Kitaev materials is α-$RuCl_3$, which despite hosting a magnetically ordered ground state, appears to show signatures of fractionalized fermionic excitations at temperatures above the ordering transition (summarized in [57]). In an external field it is claimed that α-$RuCl_3$ exhibits a half-integer thermal quantum Hall effect, which could be explained by the presence of a Majorana edge mode [58], however, this remains controversial, as the results have so far not been reproduced elsewhere.

There has also been significant progress in the last few decades on the study of geomet-

rically frustrated systems in the solid-state. For example, Herbertsmithite [59], which is thought to realize a spin 1/2 Heisenberg antiferromagnet on the kagome lattice, shows a tantalizing broad continuum in its dynamical structure factor [60], which can be interpreted as a result of fractionalization. Returning to the rare-earth pyrochlores, recent neutron scattering experiments [61], show signatures of the expected fractional excitations in the quantum version of spin ice. The inherent complexity of solid-state systems means that one must rely on the detection of fractional excitations to diagnose the realization of quantum ordered states of matter. However, it is challenging to definitively exclude other effects which could give rise to similar signals.

This leaves fractional quantum Hall systems as the only ones to unambiguously realize quantum ordered ground states, with recent experiments showing the fractional *statistics* of the excitations in collisions [62] and using electron interferometry [63]. Furthermore, the observation of fractional quantum Hall signatures in the absence of an external magnetic field has been recently reported in twisted bilayers of the transition metal dichalcogenide $MoTe_2$ [64, 65].

The growing capabilities of quantum simulation platforms [66] in recent years also suggests an alternative route to the realization of exotic states of matter. Here, one can, in principle, artificially engineer Hamiltonians, rather than synthesizing materials with specific properties. Despite issues with scalability and heating, there have been some notable results. For example, experiments using Rydberg atoms showed signatures of a topological spin liquid [67], although it was later clarified that this is a non-equilibrium phenomenon, as a result of the state preparation procedure [68]. Nevertheless, this experiment highlights the advantages of these platforms, where measurements are performed by taking "snapshots" of the wavefunction, allowing access to non-local string and loop expectation values, which can give clear signals of quantum order. Another notable experiment, in a quantum gas with an optical lattice, claims the formation of a FQH state governed by an interacting Harper-Hofstadter model [69], albeit with only two particles.

Another approach in digital quantum computers or simulators is to directly prepare desired states [70–75], rather than realizing a low-energy state of a particular Hamiltonian. For example, in [72], the authors prepare the ground state of the toric code by operating on superconducting qubits with a specific sequence of gates, then apply another series of gates to simulate the braiding of fractional excitations.

The huge diversity of experimental systems available, from solid-state to quantum gases, opens up the possibility to discover, and experimentally realize, a whole zoo of states of matter beyond Landau's symmetry-breaking paradigm. This is a central part of the quest to understand the types of collective phenomena possible, given the laws of nature that govern our universe.

In this thesis, we present results on a specific set of models, classical and quantum spins on the centred pyrochlore lattice, which can host examples of these exotic states of mat-

ter. We find that these lead, rather naturally, to effective low-energy theories of emergent charges and gauge fields, describing spin liquid states. Since the centred pyrochlore lattice is experimentally realizable in metal-organic frameworks [2], this introduces a new experimental system for probing physics beyond the symmetry-breaking paradigm.

Chapter 1

Background

This chapter introduces the relevant background information for understanding the results presented in this thesis. These results are for classical and quantum spin models defined on the *centred* pyrochlore lattice, closely related to the pyrochlore lattice, which is the focus of this chapter. First we introduce the lattice, then discuss the classical Coulomb spin liquid which is the ground state of nearest neighbour classical spin models. We explain how its low energy properties are described by an emergent electrostatics, giving rise to distinct "pinch point" features in the spin structure factor. The signatures of a classical spin liquid which can be measured in experiments are then discussed. Subsequently, we introduce the notion of a quantum spin liquid, using the examples of a quantum dimer liquid, the toric code and quantum spin ice, a $\mathrm{U}(1)$ quantum spin liquid on the pyrochlore lattice, which is described by an emergent quantum electrodynamics.

1.1 The Pyrochlore Lattice

The pyrochlore lattice is probably the most well-studied 3D lattice in the context of frustrated magnetism, due to its inherent geometric frustration [12, 13]. It can be thought of as being derived from a parent, pre-medial, diamond lattice [76], which is defined by the positions

$$\mathbf{R}_t = \mathbf{B}_I + \boldsymbol{\delta}_x, \tag{1.1}$$

where $\mathbf{B}_I$ are sites of the face-centred cubic (FCC) Bravais lattice, $\mathbf{B}_I = \sum_i n_i \mathbf{a}_i$, with lattice vectors

$$\mathbf{a}_1 = \frac{1}{2}(1,1,0), \qquad \mathbf{a}_2 = \frac{1}{2}(1,0,1), \qquad \mathbf{a}_3 = \frac{1}{2}(0,1,1), \tag{1.2}$$

and the two-site basis

$$\boldsymbol{\delta}_a = (0,0,0), \qquad \boldsymbol{\delta}_b = \frac{1}{4}(1,1,1), \tag{1.3}$$

in units where the side length of the conventional cubic unit cell, $a = 1$.

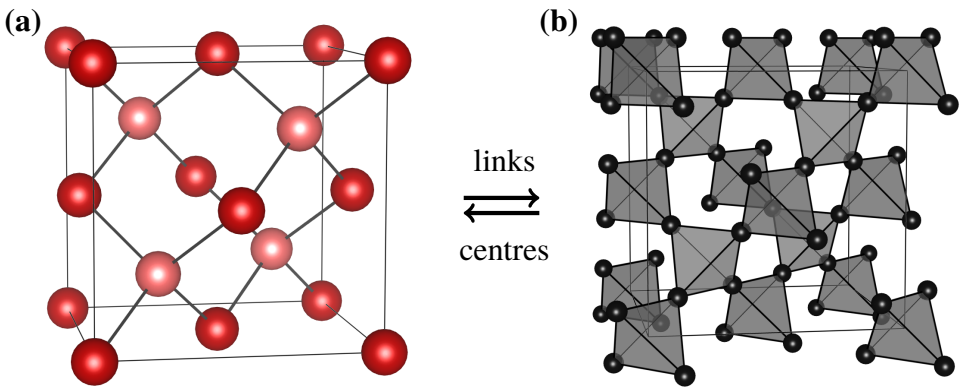

Figure 1.1: **(a)** The cubic unit cell of the diamond lattice, the two sublattices are differentiated by dark and light colours. **(b)** The cubic unit cell of the pyrochlore lattice. It can be generated by putting sites at the midpoints of all links on the diamond lattice. Correspondingly, the diamond lattice is made up of the positions on which the tetrahedra of the pyrochlore lattice are centred.

Defining new lattice sites at the midpoints of the links connecting diamond sites results in the pyrochlore lattice of corner-sharing tetrahedra, as shown in fig. 1.1. As a result, the tetrahedra of the pyrochlore lattice are centred on diamond sites. Tetrahedra centred on $a(b)$ diamond lattice sites are denoted as $a(b)$ tetrahedra respectively. Specifically, the pyrochlore lattice is defined by

$$\mathbf{r}_i = \mathbf{B}_I + \boldsymbol{\delta}_m, \tag{1.4}$$

with $\mathbf{B}_I$ the sites of the FCC lattice (see eq. (1.2)) and the four-site basis

$$\boldsymbol{\delta}_1 = \frac{1}{8}(1,1,1), \qquad \boldsymbol{\delta}_2 = \frac{1}{8}(1,-1,-1), \qquad \boldsymbol{\delta}_3 = \frac{1}{8}(-1,1,-1), \qquad \boldsymbol{\delta}_4 = \frac{1}{8}(-1,-1,1). \tag{1.5}$$

We generally consider cubic systems of size $L \times L \times L$, i.e L specifies the number of cubic unit cells along each Cartesian axis.

1.2 A Classical Spin Liquid on the Pyrochlore Lattice

The low temperature states of antiferromagnetic nearest neighbour spin models on the pyrochlore lattice are prototypical examples of classical spin liquids (CSLs). They exhibit the characteristic properties of such a state of matter: an extensive ground state degeneracy, conservation of global symmetries, and an effective low-energy description in terms of emergent gauge fields. Explicitly, consider n component classical spins (vectors), $\mathbf{S}_i$, which are normalized such that $|\mathbf{S}_i| = 1$, occupying the sites i, j, of the pyrochlore lattice, with Hamiltonian

$$H_{\text{pyro}} = J \sum_{\langle ij \rangle} \mathbf{S}_i \cdot \mathbf{S}_j, \tag{1.6}$$

where the sum is over all nearest neighbour pairs of sites and the exchange interaction is antiferromagnetic, $J > 0$. We will focus on the cases of Ising ($n = 1$) and Heisenberg

($n = 3$) spins. Since the lattice is made up of corner-sharing tetrahedra, the Hamiltonian can be rewritten as the sum

$$H_{\text{pyro}} = \frac{J}{2}\left(\sum_t L_t^2 - 2N_t\right), \tag{1.7}$$

where t labels the tetrahedra, $N_t = 8L^3$ is the total number of tetrahedra and,

$$L_t = |\mathbf{L}_t| = \left|\sum_{i\in t} \mathbf{S}_i\right|, \tag{1.8}$$

with $\mathbf{L}_t$ the sum of all spins belonging to the tetrahedron t. Equation (1.7) is minimized by any state which satisfies the local constraint [77],

$$L_t = 0, \tag{1.9}$$

for all tetrahedra. Since adjacent tetrahedra share one spin this constraint leads to a non-trivial correlation structure in the ground state, as will be discussed in the next section. A local constraint of this form is a necessary but not sufficient condition to realize a classical spin liquid, the constraint must also be compatible with an extensive ground state degeneracy. Even then, order by disorder [13, 78] may ultimately select an ordered state.

For Ising spins, $S_i = \pm 1$, eq. (1.9) tells us that each tetrahedron must have two $+1$ and two -1 spins in the ground state, which we call the 2:2 state. There are six different spin configurations which achieve this on a single tetrahedron. The 2:2 state is often referred to in the literature as spin ice [47, 48, 79] due to the analogy with water ice, where each oxygen atom is bonded to two nearby and two further away hydrogen atoms. The ground state can equivalently be thought of as an emergent 6-vertex model [47, 80, 81] on the diamond lattice, due to the six different spin configurations allowed on a single tetrahedron. Spin ice materials such as $Ho_2Ti_2O_7$ are properly described by long-range dipolar interactions between Ising spins constrained to point along the axes connecting diamond sites, but upon truncating to nearest neighbours the model can be mapped to eq. (1.6) with Ising spins [45, 46]. Anderson [11] applied Pauling's argument [82] for the residual entropy of water ice to the pyrochlore lattice, estimating the number of ground state configurations as $W = (\frac{3}{2})^{N_t}$ and therefore a ground state entropy of $S = k_B N_t \ln \frac{3}{2}$. Pauling's argument can be summarized as follows:

- A spin is shared between two tetrahedra, t_1 and t_2.
- There are 3 configurations on t_1 where the spin is up and 3 where it is down.
- The probability the configuration on t_2 is compatible with the spin being up or down is $\frac{1}{2}$ in both cases.
- The total number of viable configurations for two tetrahedra is therefore $\frac{3}{2} + \frac{3}{2} = 3$. For a single tetrahedron the number of viable configurations is $\frac{3}{2}$.

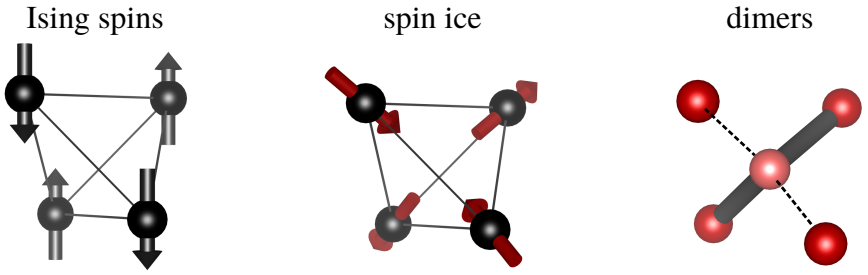

Figure 1.2: (Left) A spin configuration on a single tetrahedron which fulfills the ground state constraint for the nearest neighbour Ising model, eq. (1.6). (Centre) The same spin configuration mapped to the spin ice representation, as described in eq. (1.11). The two-up, two-down configuration of the model spins is mapped to a two-in, two-out configuration in the spin ice representation. The field, $\mathbf{E}^\alpha$, is the sum of the spin ice vectors. (Right) The dimer representation of the same state which has two dimers touching every diamond lattice site.

Similarly, for $n \geq 2$ one can also estimate the ground state degeneracy using a mode-counting argument [83–85]. For each tetrahedron there are $F = \frac{4(n-1)}{2}$ degrees of freedom (the factor of $1/2$ comes from the fact that spins are shared between two tetrahedra) and $C = n$ constraints from eq. (1.9), one for each component of $\mathbf{L}_t$. Therefore for Heisenberg spins, this leaves $D = F - C = 1$ unconstrained degrees of freedom per tetrahedron yielding an N_t-dimensional ground state manifold. Both Ising and Heisenberg spins therefore admit a ground state whose degeneracy scales with system size, which prevents symmetry-breaking order at any temperature (order by disorder does not apply in these cases [84]).

1.3 Coulomb Phase

In addition to the highly degenerate, disordered nature of the ground state, the local constraint suggests that the ground state will have some kind of structure. However, L_t is symmetric under both $\mathbb{Z}_2$ and $\mathrm{O}(3)$ transformations (which are global symmetries of the Hamiltonian for Ising and Heisenberg spins respectively) so is not a local order parameter associated with a symmetry-broken phase [3, 86]. Rather, the structure imparted by the local constraint lies beyond this framework. It turns out that the low-energy physics has an elegant description in terms of an emergent classical electrostatics [50, 76, 87] and therefore the spin liquid is known as a *Coulomb phase*. This is an example of an emergent gauge field in a classical many-body system, where the emergent description is a field theory with a $\mathrm{U}(1)$ gauge invariance.

The mapping, initially proposed in [50], is as follows. On each tetrahedron, at position $\mathbf{R}_t$, define the three-component (since the lattice is three-dimensional) vector field,

$$\mathbf{E}^\alpha(\mathbf{R}_t) = \sum_{m=1}^{4} \mathbf{u}_m S^\alpha(\mathbf{R}_t \pm \boldsymbol{\delta}_m), \tag{1.10}$$

where there are n copies of this field, one for each spin component α, and $\mathbf{u}_m = \frac{\boldsymbol{\delta}_m}{|\boldsymbol{\delta}_m|}$. $\pm = +(-)$ for $\mathbf{R}_t$ specifying an $a(b)$ tetrahedron. This is equivalent to mapping each S^α

to a spin in the spin ice representation (see fig. 1.2(a)),

$$\mathbf{T}^{\alpha}(\mathbf{R}_t \pm \boldsymbol{\delta}_m) = \mathbf{u}_m S^{\alpha}(\mathbf{R}_t \pm \boldsymbol{\delta}_m), \tag{1.11}$$

then taking the vector sum on each tetrahedron. For example, in the Ising case, an up spin is mapped to a spin pointing from an a to b tetrahedron (out) and a down spin to point from b to a (in).

In the ground state, $\mathbf{E}^{\alpha}$ is always finite for Ising spins and only zero for specific configurations in the Heisenberg case. On the other hand, defining the lattice divergence of a generic field, $\mathbf{F}$,

$$\nabla_{\mathrm{l}} \cdot \mathbf{F}(\mathbf{R_t}) = \sum_m \mathbf{u}_m \cdot \mathbf{F}(\mathbf{R}_t), \tag{1.12}$$

which is proportional to the flux exiting/entering a given tetrahedron, we see that

$$\nabla_l \cdot \mathbf{E}^{\alpha}(\mathbf{R}_t) \propto |\mathbf{L}_t^{\alpha}| = 0, \tag{1.13}$$

where the equality applies when we are in the ground state, so the local constraint is enforced. This tells us that the flux of $\mathbf{E}^{\alpha}$ is conserved and hence after coarse-graining and taking the continuum limit we obtain the ground state condition

$$\nabla \cdot \mathbf{E}^{\alpha}(\mathbf{r}) = 0. \tag{1.14}$$

What does the ground state manifold look like? For Ising spins, moves between different states in the ground state manifold consist of flipping closed loops of alternating $+, -$ spins, as shown in fig. 1.4. Averaging $\mathbf{E}^{\alpha}$ over such a flippable loop will yield zero, which is easiest to see when considering the flippable loop in the spin ice representation, where it is a directed closed loop. If a state has a large number of flippable loops this implies that there are a large number of related ground states which can be reached by flipping them. Therefore the ground state manifold is dominated by states with large numbers of flippable loops, so choosing a random ground state and coarse-graining is highly likely to lead to a state with small $\mathbf{E}^{\alpha}$. This entropic effect can be captured by assuming an effective Gaussian partition function of the form

$$Z_{\mathrm{G}} = \int D\mathbf{E}^{\alpha}(\mathbf{r}) \exp\left(-\frac{K}{2} \int d^3\mathbf{r} |\mathbf{E}^{\alpha}(\mathbf{r})|^2 \right), \tag{1.15}$$

where K is a phenomenological stiffness constant [50]. The effective free energy (the exponent) is equivalent to the energy of a classical electric field [88]. Combined with the divergence-free constraint, eq. (1.14), the effective description of the ground state is classical electrostatics in the absence of charges. For $n > 1$ spins, one assumes that the effective partition function should take the form of eq. (1.15), which is justified a posteriori as predictions from the resulting effective theory match results from the microscopic theory [50].

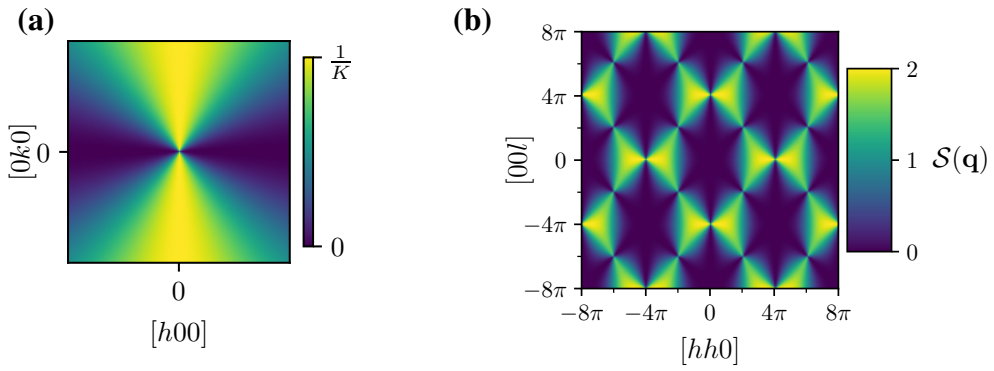

Figure 1.3: **(a)** The field structure factor, $E_{xx}(\mathbf{q})$, as predicted by eq. (1.20) in the $\mathbf{q} = (h, k, 0)$ plane, showing the characteristic point point structure centred at $\mathbf{q} = (0, 0, 0)$. **(b)** The spin structure factor, $\mathcal{S}^{\alpha\alpha}(\mathbf{q})$, of the Coulomb phase on the pyrochlore lattice, computed using the mean-field projection matrix method of [87]. Some of the pinch points at the Brillouin zone centres are absent as a result of the relation between the field structure factor and the spin structure factor.

As for the magnetic field in classical electromagnetism [88], due to the divergence-free constraint, we can write $\mathbf{E}^\alpha$ in terms of a vector potential, $\mathbf{E}^\alpha(\mathbf{r}) = \nabla \times \mathbf{A}^\alpha(\mathbf{r})$ where the theory is invariant under $\mathrm{U}(1)$ gauge transformations of the form $\mathbf{A}^\alpha(\mathbf{r}) \to \mathbf{A}^\alpha(\mathbf{r}) + \nabla\Psi(\mathbf{r})$, where $\Psi(\mathbf{r})$ is an arbitrary scalar function. Therefore we see that the structure imparted by the local constraint is a gauge theory with local $\mathrm{U}(1)$ invariance.

1.3.1 Pinch Points and Algebraic Decay in Spin Correlations

The effective theory of the ground state has important consequences for the form that spin correlations in the Coulomb phase take [50, 76, 87], providing an important diagnostic tool for identifying a Coulomb spin liquid. Defining the Fourier transform

$$\mathbf{E}^\alpha(\mathbf{r}) = \int \frac{d^3\mathbf{q}}{(2\pi)^3}\, \mathbf{E}^\alpha(\mathbf{q}) e^{i\mathbf{q}\cdot\mathbf{r}}, \tag{1.16}$$

then substituting into eq. (1.14), we obtain

$$\mathbf{q} \cdot \mathbf{E}^\alpha(\mathbf{q}) = 0, \tag{1.17}$$

which tells us that the component of $\mathbf{E}^\alpha$ parallel to $\mathbf{q}$ vanishes and thus we should project it out,

$$E_\mu(\mathbf{q}) \to E_\mu^\perp(\mathbf{q}) = E_\mu(\mathbf{q}) - \frac{\mathbf{q}\cdot\mathbf{E}}{q^2} q_\mu, \tag{1.18}$$

where $\mu \in \{x, y, z\}$ labels the vector components, and we have dropped the α label for clarity. Since the effective partition function, eq. (1.15), is Gaussian, the unprojected expectation value for the $\mathbf{E}$ structure factor is

$$\langle E_\mu(\mathbf{q}) E_\nu(-\mathbf{q}')\rangle = \frac{\delta(\mathbf{q}-\mathbf{q}')\delta_{\mu\nu}}{K}. \tag{1.19}$$

For the projected case, we should calculate $\langle E^{\perp}_{\mu}(\mathbf{q})E^{\perp}_{\nu}(-\mathbf{q})\rangle$. Substituting in eq. (1.18) gives

$$E_{\mu\nu}(\mathbf{q}) = \langle E_{\mu}(\mathbf{q})^{\perp}E^{\perp}_{\nu}(-\mathbf{q})\rangle = \frac{1}{K}(\delta_{\mu\nu} - \frac{q_{\mu}q_{\nu}}{q^2}). \tag{1.20}$$

This is a non-analytic function in momentum space with a singularity at $\mathbf{q} = 0$. It has a characteristic shape called a pinch point as shown in fig. 1.3(a). In the example shown, $\lim_{q_x\to 0} E_{xx}(q_x, 0, 0) = 0$ and $\lim_{q_y\to 0} E_{xx}(0, q_y, 0) = \frac{1}{K}$. Taking the inverse Fourier transform of eq. (1.20) and assuming the distance r is large, one obtains the real space correlations [50]

$$\langle E_{\mu}(0)E_{\nu}(\mathbf{r})\rangle \propto \frac{\delta_{\mu\nu}}{r^3} - \frac{3r_{\mu}r_{\nu}}{r^5}, \tag{1.21}$$

which have a characteristic dipolar form, where r_{μ} is a vector component of position $\mathbf{r} = (r_x, r_y, r_z)$. Along a particular direction the correlations decay algebraically as $\frac{1}{r^3}$. This is a key distinguishing feature of the Coulomb spin liquid from a high temperature paramagnet where the spin correlations decay exponentially [89].

The $\mathbf{E}^{\alpha}$ field is not straightforwardly related to a physical degree of freedom, except for in dipolar spin ice, so cannot in general be directly accessed in experiment. Instead, the spin structure factor

$$\mathcal{S}^{\alpha\beta}(\mathbf{q}) = \langle S^{\alpha}(\mathbf{q})S^{\beta}(-\mathbf{q})\rangle = \frac{1}{N}\sum_{i,j} e^{i\mathbf{q}\cdot(\mathbf{r}_i-\mathbf{r}_j)}\langle S^{\alpha}(\mathbf{r}_i)S^{\beta}(\mathbf{r}_j)\rangle, \tag{1.22}$$

is measurable (see for example eq. (1.41)). The definition of $\mathbf{E}^{\alpha}$ in terms of spin variables is invertible [87], as long as a generalized local constraint of the form

$$\sum_{m} S^{\alpha}(\mathbf{R}_t \pm \boldsymbol{\delta}_m) = f(\mathbf{R}_t), \tag{1.23}$$

is satisfied. The inverse mapping from field to spins is

$$S^{\alpha}(\mathbf{R}_t \pm \boldsymbol{\delta}_m) = \frac{1}{4}(3\mathbf{u}_m \cdot \mathbf{E}^{\alpha}(\mathbf{R}_t) + f(\mathbf{R}_t)), \tag{1.24}$$

so $\mathcal{S}^{\alpha\beta}(\mathbf{q})$ is related to $E_{\mu\nu}(\mathbf{q})$ in some non-trivial way where the pinch points are repeated at some, but not all, Brillouin zone centres. The nodes where there are no pinch points arise as a consequence of the symmetry of the lattice [87]. The spin structure factor for the Coulomb phase on the pyrochlore lattice is shown in fig. 1.3(b).

1.3.2 Topological Sectors

In the case of Ising spins, the ground state manifold has a topological nature, where distinct topological sectors can be labelled by a $\mathrm{U}(1)$ winding number [52]. By mapping the Ising spins to dimers occupying the links of the diamond lattice, such that $S_i = +1(-1) \to n_i = 1(0)$ [90], we see that this is related to the topological order in quantum dimer models [29, 91], albeit fluctuations are thermal (assuming $T = 0^+$) rather than quantum

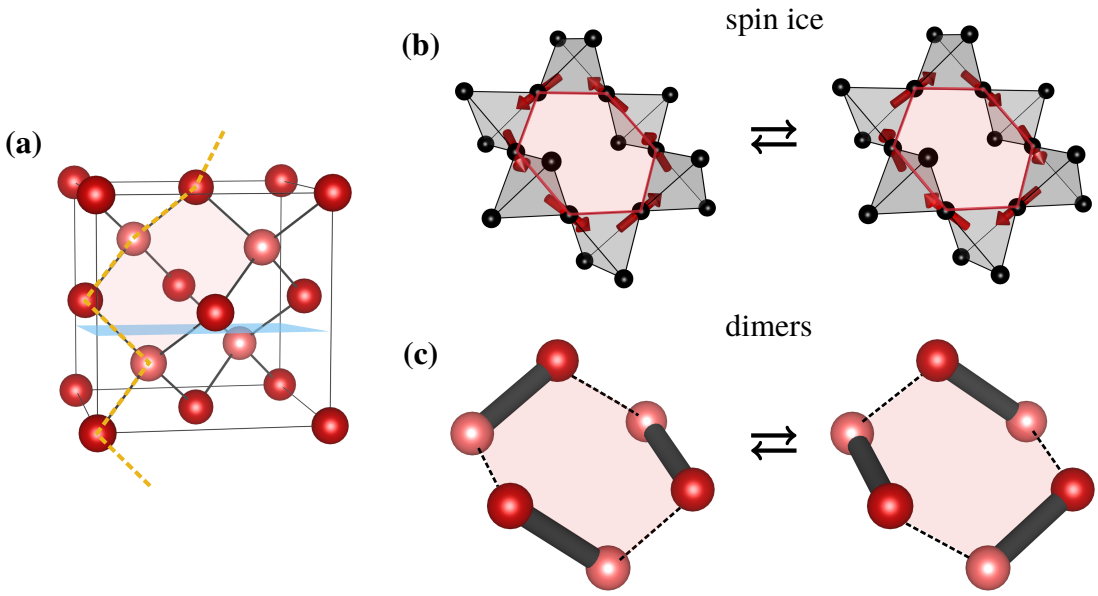

Figure 1.4: **(a)** A plane oriented perpendicular to $\hat{\mathbf{z}}$ intersecting the links of the diamond lattice on which the winding number can be measured. A non-winding loop which intersects an even number of times is shaded in red whereas a winding loop which intersects an odd number of times is shown by the yellow dotted line. **(b)** The shortest possible loop move which maintains the ground state constraint for the Ising spin liquid on the pyrochlore lattice in the spin ice representation. A flippable loop is a directed closed loop, corresponding to an alternating string of Ising spins e.g $+1, -1, +1, \ldots$. **(c)** The corresponding move in the dimer picture, with spheres representing the sites of the diamond lattice and dimers shown on the links. The number of dimers intersecting a plane perpendicular to, for example, $\hat{\mathbf{z}}$ is unchanged by the move, which is the w_z component of the winding number. This plaquette move is the third order ring-exchange process in the quantum spin $1/2$ XXZ model discussed in section 1.6.3.

effects. As mentioned when deriving the effective free energy of the ground state, one can move between ground states by flipping closed loops of alternating $+1, -1$ spins as this amounts to swapping $+1$ and -1 spins on each tetrahedron, preserving the local constraint. In the spin ice representation, this flippable loop is a directed closed string which begins and ends on the same tetrahedron, as shown in fig. 1.4(b).

The ground state can be split into distinct sectors which are connected by only non-winding moves. A winding move is on a loop which spans the entire lattice through a periodic boundary, whereas a non-winding loop closes within the confines of a single periodic image. The ground state is thus topological in the sense that the ability to move between distinct sectors depends on the topology of the lattice; with open boundary conditions the ground state is restricted to a single sector, whereas with periodic boundary conditions winding moves connect the different sectors.

We can assign each microstate a topological sector by measuring the winding numbers,

$\mathbf{w} = (w_x, w_y, w_z)$. Each component,

$$w_k = \sum_{i \in \text{plane}_k} n_i, \tag{1.25}$$

measures the number of dimers intersecting a plane oriented perpendicular to $\hat{\mathbf{k}}$ which spans the system, as illustrated for a single unit cell in fig. 1.4(a). This is invariant under non-winding moves because the closed loop will cross the plane an even number of times with an equal number of dimers and non-dimers intersecting the plane. On the other hand, a winding move which goes around the periodic boundaries does not need to cross the plane an even number of times; it can cross an odd number of times and then wind around the periodic boundary to close the loop. The number of links intersected by the plane is $4L^2$ so the w_k take integer values from 0 to $4L^2$, with a non-local winding loop changing w_k by $\pm n$, where n is the number of times the loop winds around a periodic boundary.

These topological sectors have consequences for the spin fluctuations in thermal equilibrium [52], whereas in a related quantum model, each hosts a degenerate ground state in the thermodynamic limit [90] (see also section 1.6.3).

1.3.3 Low-energy Excited States

Besides the properties of the ground state, the effective theory also describes the nature of low-energy excitations. In the Ising case, an excitation is created by flipping a single spin, which results in the pair of tetrahedra, t, t', which share this spin obtaining a finite magnetization, $L_t = L_t' = \pm 2$. The defects can be propagated at zero energy cost by flipping a string of alternating spins (in an analogous way to fig. 1.9(b)), resulting in two well-separated defects. In the coarse-grained language this yields

$$\nabla \cdot \mathbf{E}^{\alpha}(\mathbf{r}) = Q_1 \delta^3(\mathbf{r} - \mathbf{r}_1) + Q_2 \delta^3(\mathbf{r} - \mathbf{r}_2), \tag{1.26}$$

where the defects are located at positions $\mathbf{r}_1, \mathbf{r}_2$ and the breaking of the ground state constraint is parametrized by $Q_1 = -Q_2$. The defects will have opposite charge as the defect, anti-defect pair initially reside on neighbouring tetrahedra which belong to different sublattices.

An effective interaction energy, $U(\mathbf{r}_1, \mathbf{r}_2))$ can be defined between the defects

$$\exp(-\beta^* U(\mathbf{r}_1, \mathbf{r}_2)) \propto \frac{Z|_{Q_1,Q_2}}{Z} \tag{1.27}$$

where β^* is an effective temperature and the partition function in the numerator is integrated subject to the constraint in eq. (1.26). This gives

$$U(\mathbf{r}_1, \mathbf{r}_2) \propto \frac{Q_1 Q_2}{|\mathbf{r}_1 - \mathbf{r}_2|}, \tag{1.28}$$

that is, the charges interact via a Coulomb potential. This can be generalized to a system of N_c charges at positions $\{\mathbf{r}_i\}$, with an effective interaction energy of

$$U(\{\mathbf{r}_i\}) \propto \sum_{i<j} \frac{Q_i Q_j}{|\mathbf{r}_i - \mathbf{r}_j|} \tag{1.29}$$

and an effective partition function

$$Z_{\text{charge}} = \int d^3\mathbf{r}_1 \cdots \int d^3\mathbf{r}_{N_c}\, e^{-\beta^* U(\{\mathbf{r}_i\})}. \tag{1.30}$$

This is the partition function of a fluid of mobile electric charges [92], which is the effective picture which emerges to describe the low-energy states. Hence there is a useful connection between the low-energy physics of the pyrochlore spin liquid and classical Coulomb fluids, the study of which has a long and rich history [93]. Results from the electrostatic context can be directly applied to understand phenomena in the spin system, with often remarkable agreement, see for example [94].

Consider a system with a dilute concentration, n_Q, of charge-anticharge pairs of strength Q, so that the system can be described as a charge neutral Coulomb fluid, analogous to ions in a solvent. Provided the effective temperature is high enough, Debye-Hueckel theory [92, 93, 95, 96] applies [76]. This predicts that electric fields emanating from a charge will be exponentially screened,

$$\mathbf{E}(\mathbf{r}) \to \mathbf{E}(\mathbf{r}) e^{-\kappa r}, \tag{1.31}$$

where $\mathbf{r}$ measures the position relative to the reference charge and $1/\kappa$ is the screening length with

$$\kappa \propto \sqrt{n_Q Q^2}. \tag{1.32}$$

In momentum space, the screening causes broadening of the pinch points into bow tie structures with the form

$$E_{\mu\nu}(\mathbf{q}) = \frac{1}{K}(\delta_{\mu\nu} - \frac{q_\mu q_\nu}{q^2 + \kappa^2}), \tag{1.33}$$

where κ parametrizes the width of the bow ties.

Debye-Hueckel theory is derived for a charge neutral, low concentration and high effective temperature setting, yet this screening is a robust phenomenon in charged fluids [96]. In the spin system at finite temperature, where there will be some finite concentration of charges, the sharp pinch points of the Coulomb phase become broadened bow ties with κ increasing as the number of charges increases with temperature.

1.4 Experimental Signatures of a Classical Spin Liquid

The theoretical study of spin liquids has been constantly informed by results from experiments on solid state materials, whether in identifying interesting lattice structures and

models, or areas where new concepts are required to make sense of experimental results. But what sort of signatures should one look out for to actually identify a CSL? In this section we discuss some of these characteristic features.

First of all, at what sort of temperatures would a CSL exist? Consider the following effective spin Hamiltonian to describe an experimental solid state system, with the generic form

$$\begin{aligned} H_{\text{spin}} &= \sum_{\langle ij \rangle} \sum_{\alpha,\beta} J_{1ij}^{\alpha\beta} S_i^\alpha S_j^\beta + \sum_{\langle\langle ij \rangle\rangle} \sum_{\alpha,\beta} J_{2ij}^{\alpha\beta} S_i^\alpha S_j^\beta + \dots \\ &= H_{\text{SL}} + H_{\text{order}} + \dots \end{aligned} \tag{1.34}$$

where H_{SL} has a CSL ground state and H_{order} may include effects which favour long-range (symmetry-breaking) order such as quantum fluctuations, disorder, longer-range interactions and anisotropies, to name but a handful of possibilities. Assuming the energy scale of H_{order} is significantly less than that of H_{SL}, one can treat it as a perturbation to the low energy classical spin liquid, which causes the ground state to possess some kind of long-range order.

Therefore, one would not generally expect a solid state system as $T \to 0$ to be a CSL, rather there will be some finite temperature window $T_c < T < T^*$, where T_c and T^* are of the order of the energy scales of H_{order} and H_{SL} respectively, that will host a CSL, provided it has large enough entropy to wash out the effect of H_{order}. Systems where $f = \frac{T^*}{T_c}$ [97] is large have a broad regime where we might expect to find spin liquid physics and even the finite temperature behaviour in this regime may be very well approximated by the ground state of H_{SL}. In synthetic systems such as artificial spin ice [98], or quantum simulators [66] with a high effective spin, where one has greater control over the system Hamiltonian, one could in principle also engineer a system with very large f in order to probe the low energy behaviour of H_{SL}.

1.4.1 Magnetic Susceptibility

An important bulk probe of the magnetic properties of a material is the molar magnetic susceptibility [99, 100]

$$\chi = V_m \left(\frac{\partial \mathbf{M}}{\partial \mathbf{H}} \right)_{\mathbf{H}} \text{m}^3\text{mol}^{-1} \tag{1.35}$$

which measures the response of the magnetization per unit volume of a material, $\mathbf{M}$, in an external magnetic field, $\mathbf{H}$. In SI units both are measured in Am^{-1} and we assume that the response is isotropic. Here, V_m is the molar volume of the material. At high temperatures, in a paramagnet, the susceptibility follows a Curie-Weiss law [99]

$$\chi = \frac{C}{T - \theta_{\text{CW}}}, \tag{1.36}$$

where C is the material dependent Curie constant and θ_{CW} is the Curie-Weiss constant whose sign indicates whether magnetic interactions in the material are predominantly

ferro(+) or antiferromagnetic(−) and its magnitude the strength of these interactions [13]. In an unfrustrated system, $T_c \approx |\theta_{\mathrm{CW}}|$, so the frustration factor [97]

$$f = \frac{|\theta_{\mathrm{CW}}|}{T_c} \tag{1.37}$$

gives a measure of the amount of magnetic frustration in a material and, since $|\theta_{\mathrm{CW}}|$ measures the energy scale of interactions, the region to look for spin liquid physics is $T_c < T < |\theta_{\mathrm{CW}}|$.

Equation (1.36) describes the behaviour of a paramagnet at high temperature, which can be derived from a mean-field argument, so deviations from eq. (1.36) indicate the onset of correlations in the material. In a conventional magnetic transition, where $|\mathbf{M}|$ or a closely related quantity is the order parameter, χ would generically have a peak (or a cusp if plotting χ^{-1}) at T_c, so can be used to locate this ordering transition. Furthermore, θ_{CW} can be extracted from a linear fit of eq. (1.36) to χ^{-1} at high temperature, so an estimate of f can be obtained.

Upon entering a spin liquid, there will not be an obvious signal such as a peak or cusp, as there is no symmetry breaking, yet correlations are distinct from the paramagnet. In [101] the authors argue that a CSL will show a characteristic crossover from a high-temperature paramagnetic Curie law to a low-temperature spin liquid Curie law with a different Curie constant. This can be understood from the fact that in the ground state, the spins are allowed to fluctuate, but in a characteristic constrained way, giving rise to a characteristic correlation structure and related susceptibility. Therefore, plotting χT from experimental measurements of a material with a spin liquid regime, one would expect to see a pair of plateaus, one at high temperature in the paramagnetic regime, and one at low temperature in the spin liquid regime, before a peak if there is ordering at lower temperature. An example of the susceptibility measured for various frustrated Ising models is shown in fig. 1.5(a).

1.4.2 Entropy and Specific Heat

A lattice spin system can typically be treated as a canonical ensemble with free energy $F = U - TS$, where U is the internal energy and S the entropy of the system [89]. The specific heat

$$C = \frac{\partial U}{\partial T} = -T\frac{\partial^2 F}{\partial T^2}, \tag{1.38}$$

will generally pick up non-analyticities in the free energy associated with a phase transition. Since it does not depend on identifying an order parameter, measurement of the specific heat in experiment provides an unbiased way to detect phase transitions. However, in a solid state system it may not always be possible to subtract the non-magnetic contribution to the specific heat from the magnetic one, so, for example, a structural transition in the lattice cannot necessarily be distinguished from a magnetic ordering transition by

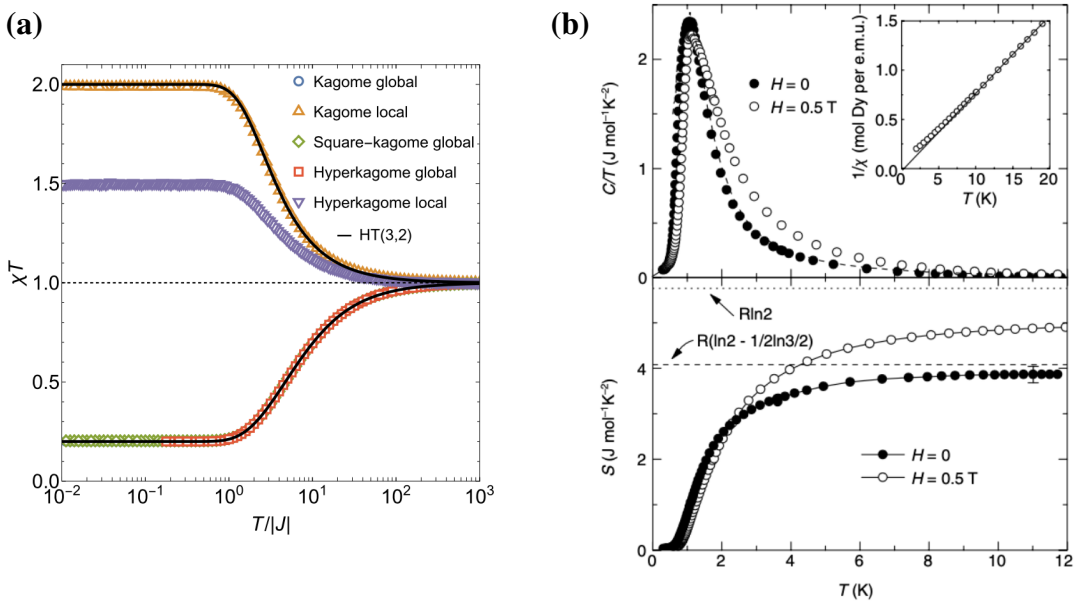

Figure 1.5: **(a)** χT for various frustrated Ising models with spin liquid ground states as a function of temperature. At high temperature $\chi T \to 1$, the paramagnetic Curie law in these units, whereas at low temperature the spin liquids have a characteristic Curie constant. Adapted from [101]. **(b)** Specific heat measurements (upper) and resulting entropy (lower) obtained by integrating the data from the upper panel for the dipolar spin ice material $Dy_2Ti_2O_7$. The mismatch at high temperature with the entropy of a paramagnet ($R \ln 2$, see dotted line) is indicative of the residual entropy of the spin liquid, which in zero field ($H = 0$) is well-approximated by the Pauling estimate for the nearest neighbour Ising model ($R/2 \ln 3/2$ in these units, see section 1.2 and [11]). Adapted from [102].

looking at the specific heat alone. However, combined with other measurements it can be possible to ascertain the origin of any transitions. Therefore, the specific heat can be a useful tool for measuring T_c of a magnetic ordering transition in a material, giving a first indication of whether there is significant magnetic frustration in the system.

Since CSLs are characterized by a highly degenerate ground state manifold, this manifests itself as a large residual entropy at low temperatures. The entropy change as a function of temperature can be computed by integrating the experimentally measured specific heat using the relation

$$\Delta S = \int_{T_1}^{T_2} \frac{C(T)}{T} dT. \tag{1.39}$$

Integrating from an appropriate minimum temperature gives an estimate of the absolute entropy which can be compared to the known entropy of a high temperature paramagnet (modelled as free magnetic moments), where, provided care is taken to exclude the influence of other effects, the discrepancy between the two entropies gives the residual ground state entropy, as shown in fig. 1.5(b). The figure shows how the Pauling estimate, $S = k_B N_t \ln \frac{3}{2}$ [11], for the residual ground state entropy in nearest neighbour spin ice was measured experimentally in a dipolar spin ice compound [102] (see also [103]). Models

of classical spins with number of components $n \geq 2$ are unable to correctly describe the entropy of a physical system at low temperature, so we cannot obtain an estimate for the residual ground state entropy as in the Ising case. This is due to the fact that the spins are continuous variables so $C(T \to 0)$ is finite and hence $\Delta S \to \infty$ as $T \to 0$. Nevertheless one still expects to find a large entropy at low temperature in a CSL.

Returning to the specific heat itself, for $n \geq 2$ systems with a global $O(n)$ symmetry, in the standard symmetry-broken phase, there will be $n-1$ transverse Goldstone modes (magnons) about the ordered state with quadratic dispersion [104]. Therefore by equipartition of energy, $U = \langle E \rangle = (n-1)\frac{k_B}{2}T$, and consequently the specific heat per spin, $c_O = (n-1)\frac{k_B}{2}$. On the other hand, a CSL may host zero modes, fluctuations that remain within the ground state manifold, as well as quartic (x^4) modes [84, 85]. This will reduce the specific heat per spin to some characteristic fraction of c_0, for example in the Heisenberg model on the pyrochlore lattice $c_{\mathrm{SL}} = \frac{3}{4}k_B$ [85]. However, this characteristic plateau in the specific heat is often difficult to observe in experiment due to the true quantum nature of the magnetic moments in a material, resulting instead in a broad bump as quantum effects begin to take hold.

1.4.3 Spin Structure Factor

The thermodynamic quantities discussed above offer important diagnostic tools for identifying spin liquids, but are somewhat blunt, in that they do not give access to the microscopic properties of the material. Alternatively, the spin structure factor offers direct access to the spin correlations in a material, and, is experimentally measurable, so is often the method of choice for studying exotic magnetic phenomena.

The general form of the dynamical spin structure factor at momentum $\mathbf{q}$ and frequency ω is defined as [105, 106]

$$\mathcal{S}^{\alpha\beta}(\mathbf{q},\omega) = \frac{1}{N}\sum_{i,j}\int dt\, e^{i\omega t}e^{i\mathbf{q}\cdot(\mathbf{r}_i-\mathbf{r}_j)}\langle S^{\alpha}(\mathbf{r_i},t)S^{\beta}(\mathbf{r_j},0)\rangle, \tag{1.40}$$

where i,j label the N lattice sites at corresponding positions $\mathbf{r}_i$ and $\langle \dots \rangle$ denotes the thermal expectation value. The dynamical spin structure factor measures the excitations of the material as a function of momentum and frequency, so can be used to measure the dispersion relation $\omega(\mathbf{q})$ of, for example, magnons, as well as more exotic excitations which may occur in classical or quantum spin liquids (see section 1.6). The spectrum of excitations depends on the precise nature of a spin liquid and may be gapped or gapless, with characteristic dispersions. Therefore it is difficult to speak of generic features of a spin liquid in the dynamical structure factor. Instead, a good theoretical understanding of the spin liquid is required to be able to make specific predictions to look out for in experiments.

The static spin structure factor, eq. (1.22), is obtained by integrating eq. (1.40) over all frequencies, $\mathcal{S}^{\alpha\beta}(\mathbf{q}) = \int \frac{d\omega}{2\pi}\mathcal{S}^{\alpha\beta}(\mathbf{q},\omega)$. This gives probes equilibrium spin correlations in

a material so can be used to understand any magnetic ordering in the system, offering more information than bulk magnetization measurements. Magnetic order is characterized by the appearance of Bragg peaks at characteristic momenta. On the other hand, a spin liquid is generically characterized by broad liquid-like features. Characteristic features of a spin liquid may appear in the static structure factor, such as the pinch points of the Coulomb phase, providing a clear signature by which to identify it.

Both dynamical and static structure factors can be measured experimentally using neutron scattering. Neglecting the scattering off nuclei via the strong force, such that only the contribution from scattering off the magnetic moments of atoms/ions in the material remains, the differential cross section for unpolarized neutrons is [106]

$$\frac{d^2\sigma}{d\Omega dE} = r_0^2 \frac{k_f}{k_i} f(\mathbf{q})^2 \sum_{\alpha\beta} (\delta_{\alpha\beta} - \hat{q}_\alpha \hat{q}_\beta) \mathcal{S}^{\alpha\beta}(\mathbf{q}, \omega), \tag{1.41}$$

where r_0 is a magnetic scattering length, k_f and k_i the magnitudes of the wavevectors of the outgoing and incoming neutrons respectively and $f(\mathbf{q})$ an atom/ion dependent form factor. Different components, α, β, of the structure factor can be accessed through the use of polarization analysis [107]. By accessing the spin structure factor, neutron scattering experiments can provide a detailed comparison to the theoretically predicted correlations and excitations of a particular spin liquid. As a prominent example, fig. 1.6 shows a comparison of the structure factor measured in the dipolar spin ice material $Ho_2Ti_2O_7$ and results from Monte Carlo simulations [108].

Whilst neutron scattering experiments offer unparalleled access to spin correlations, they can be challenging to perform. First of all, the typically weak interactions of neutrons with matter [105] means that large samples must be used. Furthermore, if one wants spatial $\mathbf{q}$ resolution, the sample must be a single crystal. The growth of large single crystals is a subtle art and procedures to do so are the subject of a great deal of research at the intersection of the chemistry, physics and materials science communities [109]. Moreover, the large flux of incident neutrons required and the difficulty of creating free neutrons typically requires the use of large-scale specialized facilities such as nuclear reactors or spallation sources [110]. These drawbacks, amongst others, mean that from the identification of a new material of interest to an experimentally measured and well-understood spin structure factor can take many years of work.

1.4.4 Pyrochlore Classical Spin Liquids

Research on materials realizing a magnetic pyrochlore lattice has focussed predominantly on the $A_2B_2O_7$ pyrochlore family (it is this class of minerals from which the lattice takes its name) and cubic spinels, AB_2O_4 [111]. Of the pyrochlores, it is rare-earth pyrochlores of the form, $R_2M_2O_7$, where R is a $3+$ rare-earth metal ion and M is a $4+$ transition metal ion [112], which are the most well-studied. Specifically the dipolar spin ice materials [45, 47, 79] $Ho_2Ti_2O_7$ and $Dy_2Ti_2O_7$ offer probably the clearest examples of classical Coulomb

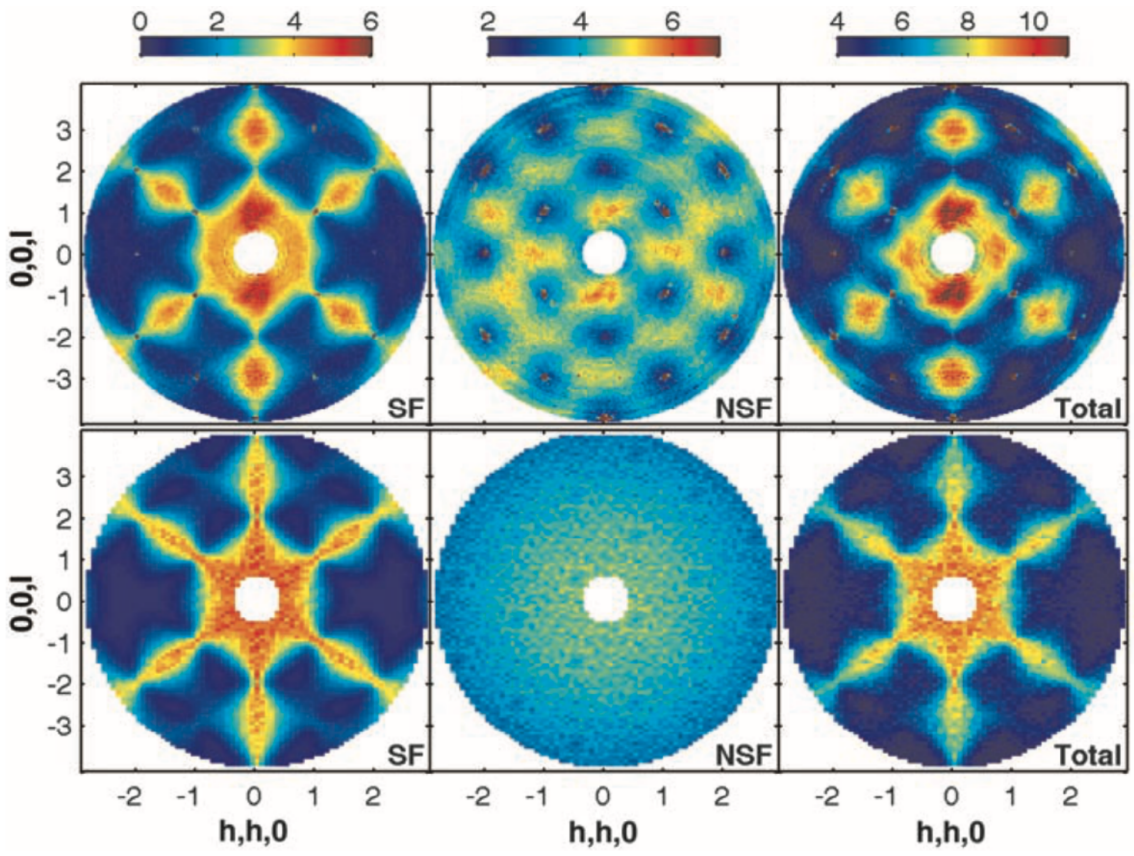

Figure 1.6: Static spin structure factors $\mathcal{S}^{yy}(\mathbf{q})$ (SF) and $\mathcal{S}^{zz}(\mathbf{q})$ (NSF) of $Ho_2Ti_2O_7$, measured by neutron scattering (top) and Monte Carlo simulations (bottom). z is the axis along which the neutrons are polarized and y is perpendicular to the scattering vector. Pinch points, characteristic of a Coulomb phase are clearly seen in the SF structure factor. Adapted from [108].

spin liquid behaviour, exhibiting the expected zero point entropy [102, 103] (fig. 1.5(b)) and pinch points in the structure factor measured by neutron scattering [108] (fig. 1.6). The behaviour of these materials are remarkably well captured by the simple nearest neighbour Ising model on the pyrochlore lattice [49, 113, 114].

Materials which are well approximated by the classical *Heisenberg* model on the pyrochlore lattice include $Y_2Mo_2O_7$ and $ZnCr_2O_4$, however in these materials disorder and spin-orbital effects [115, 116] or further neighbour interactions [117, 118] ultimately destroy the Coulomb spin liquid. Nevertheless, efforts continue to find Heisenberg pyrochlore materials, such as $NaCaNi_2F_7$ which is thought to be well described by an $S = 1$ Heisenberg antiferromagnet [119].

1.5 Metal-Organic Frameworks

The compounds named above which realize magnetic pyrochlore lattices are inorganic, but what about using organic constituents to form such a structure? In the chemistry com-

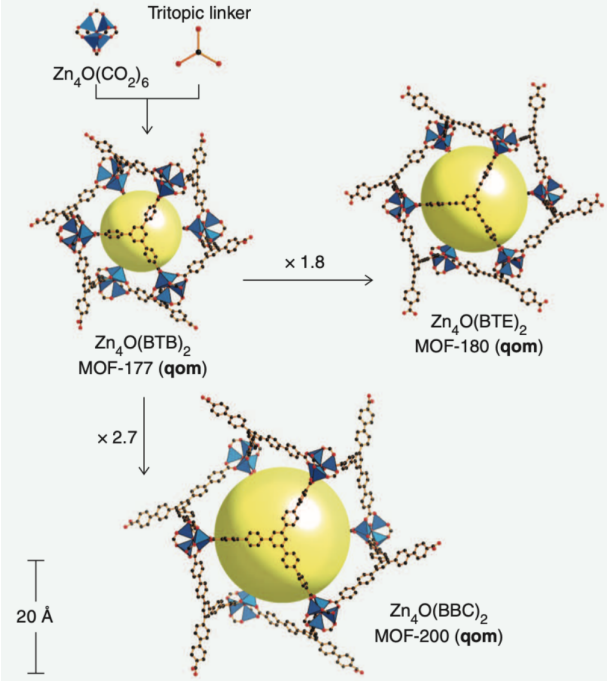

Figure 1.7: An example of a metal-organic framework. An inorganic node and organic linker combine to form a desired structure. Here, using different species for the linker, but the same inorganic node, one can synthesize materials with a varying pore size. Adapted from [120].

munity, a class of materials called metal-organic frameworks (MOFs) [120] have been the subject of intense research over the last few decades. These are made up of inorganic nodes and organic linker units, where the linkers are generally chosen to create a desired structure and the inorganic nodes to affect the functionality of the material. This approach leads to a great deal of flexibility, nodes and linkers can in principle be substituted for other compounds to engineer desired properties, as illustrated in fig. 1.7.

These materials tend to have very high porosity which leads to diverse applications from gas adsorption and separation [121], carbon capture [122] , catalysis [123] to biomedicine [124]. They have also been studied in the context of magnetism [125], in some cases realizing magnetically frustrated structures. Yet, there has been little study of the physical states of matter realized at low temperatures in frustrated metal-organic frameworks, where one might expect to find spin liquid physics. Recently, in [126], the authors studied the MOF $Na[Mn(HCOO)_3]$ which realizes a trillium lattice. Despite ordering at low temperatures, this displays a classical spin liquid regime at finite temperature. Thus, metal-organic frameworks offer a flexible platform for realizing spin liquids in the solid state, which have to date been little explored, due to challenges in synthesizing materials with sufficiently large exchange interactions [127].

1.6 Quantum Spin Liquids

In section 1.4 we discussed how a CSL will typically transition to a long-range ordered phase at some low temperature. However, what happens when this is not the case? Then, at low enough temperatures, quantum effects will become significant, which can lead to a *quantum* spin liquid (QSL). These are highly entangled states of matter which host fractionalized excitations and emergent gauge fields [22–24]. They can be thought of as quantum analogues of CSLs, where the degenerate ground state manifold is replaced with a quantum superposition. They possess quantum order [44], as opposed to symmetry-breaking long-range order, although only gapped spin liquids can properly be called topologically ordered [24]. QSLs can be classified by the local symmetry of their low-energy emergent gauge theory. In this section we will discuss a prominent example of a $\mathbb{Z}_2$ and a $\mathrm{U}(1)$ QSL, the toric code and quantum spin ice respectively, explaining some of the key properties which are typical of QSLs more generally. In both cases, we make clear the connection to "parent" CSLs, from which the QSLs can be thought to emerge as a result of the addition of quantum fluctuations of the correct form.

1.6.1 Quantum Dimer Models and the Rokhsar-Kivelson Point

Before discussing quantum spin liquids, we make a short detour to discuss closely related quantum *dimer* liquids. In some spin models, the relevant low temperature properties are described by a quantum dimer model, whose liquid phase corresponds to a QSL state.

In a quantum dimer model [29, 91], the variables, $n_{ii'} \in \{0, 1\}$ occupy the links of a lattice with sites i, i', where $n_{ii'} = 0(1)$ corresponds to the absence(presence) of a dimer on that link. Typically what is referred to as a dimer model in the literature refers to a model of non-overlapping dimers, where the Hilbert space is constrained such that there is one dimer touching every site of the lattice. Related models, with a constraint of two dimers touching every site, are called quantum loop models [128] as the configurations of dimers form closed loops on the lattice, since every site has a dimer coming "in" towards it and back "out" again. In this section, we do not make such a distinction, our only requirement being that the Hilbert space is constrained so that there are a constant number, n, of dimers touching every site, where $0 < n < z$ and z is the connectivity of the lattice. We will see that there is a point in the parameter space of particular forms of these models which host an exact quantum liquid ground state [129].

Consider a quantum dimer model on the square lattice with Hamiltonian

$$
\begin{aligned}
H &= -g \sum_{\square} \Big(|\square\rangle\langle\square| + |\square\rangle\langle\square| \Big) + \mu \sum_{\square} \Big(|\square\rangle\langle\square| + |\square\rangle\langle\square| \Big) \\
&= -g \sum_{\square} \Big(A_{\square} + A_{\square}^{\dagger} \Big) + \mu \sum_{\square} \Big(A_{\square}^{\dagger} A_{\square} + A_{\square} A_{\square}^{\dagger} \Big),
\end{aligned}
\tag{1.42}
$$

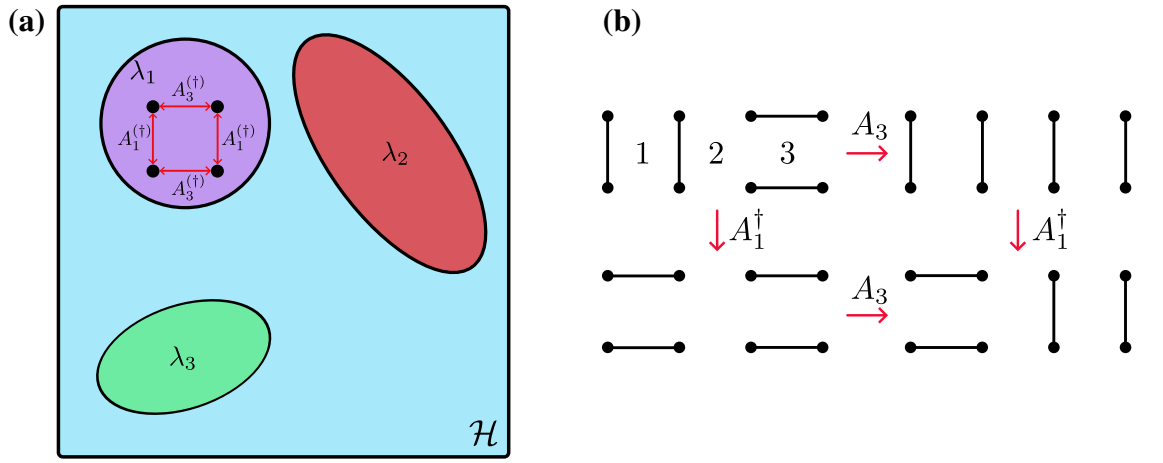

Figure 1.8: **(a)** The structure of the Hilbert space, $\mathcal{H}$, of a dimer model of the form eq. (1.42). λ labels distinct topological sectors. Inside each topological sector, states are connected by operators $A_\square^{(\dagger)}$ in a pair-wise fashion such that there is a state with each flippable plaquette flipped and not flipped. **(b)** An example of the internal structure of a topological sector for $n = 1$. The operators which move between the states are shown with the numbering of plaquettes indicated. Due to the pair-wise structure there are an equal number of states with a flippable plaquette in either of its possible configurations.

where the terms act on square plaquettes. The g term "flips" the plaquettes, whilst the μ term counts the number of flippable plaquettes. The Hamiltonian acts on a Hilbert space spanned by the orthonormal states, $\{c\}$, where c is a specific configuration of dimers on the lattice. For example, if the links are occupied by spin $1/2$ variables, the many-body states in the S^z basis provide a valid orthonormal dimer basis, and there is a simple mapping from spins to dimers. On the other hand, if the dimers are used to represent a valence bond, i.e a spin singlet, then care must be taken to orthonormalize the valence bond basis in order to map between the two.

Now, let us consider the structure of the Hilbert space. Starting from a particular reference configuration, we can generate all other configurations by exhaustively applying $A_\square^{(\dagger)}$. Generically, there will be several disconnected sectors with no non-zero matrix elements in the Hamiltonian connecting them, as illustrated in fig. 1.8. We label the sectors with λ. For $\mu, g > 0$, H is positive semidefinite [129] and therefore its minimum eigenvalue is 0. Furthermore, all off-diagonal elements are non-negative, so H is stoquastic [130], and its ground state (in each sector) can be written as

$$|\Psi_0\rangle_\lambda = \sum_{c\in\lambda} p_c |c\rangle , \quad p_c > 0, \ \forall c \in \lambda. \tag{1.43}$$

For $\mu = g$, H can be written in terms of the projector [131]

$$P_\square = \Big(|\, \vdots\, \vdots \,\rangle - |\, \vdots\!\cdot\!\vdots \,\rangle \Big)\Big(\langle\, \vdots\, \vdots \,| - \langle\, \vdots\!\cdot\!\vdots \,| \Big), \tag{1.44}$$

such that $H = \sum_{\square} P_{\square}$. Since the eigenvalues of $P_{\square} = 0, 1$, a state with $P_{\square} = 0$ on every plaquette must be a ground state. Within each sector, there will be exactly the same number of configurations with ⁞ ⁞ as ⁘ on each plaquette, so an equal superposition of all configurations,

$$|\mathrm{RK}\rangle_{\lambda} \propto \sum_{c \in \lambda} |c\rangle \,, \tag{1.45}$$

will have $P_{\square} = 0$ on every plaquette and is therefore a ground state. This special point in the phase diagram is called the Rokhsar-Kivelson (RK) point and the ground state is a quantum dimer liquid, with no broken symmetries, analogous to the paradigmatic resonating valence bond state proposed by Anderson [14].

Whether the RK point is a critical point or forms a liquid phase with finite extent in parameter space depends on the details of the model, such as the lattice geometry, as does the local symmetry of its related gauge theory. Note that the existence of the RK ground state is quite general, the validity of the argument only requires a Hamiltonian of the form eq. (1.42), an orthonormal dimer configuration basis and a Hilbert space where $A_{\square}^{(\dagger)}$ generates the configurations within a sector. We return to this point later when studying the quantum XXZ Hamiltonian on the centred pyrochlore lattice.

1.6.2 The Toric Code: A $\mathbb{Z}_2$ Quantum Spin Liquid

Now moving to a system with spins as explicit variables, the toric code [54] is a 2D exactly solvable model which hosts a $\mathbb{Z}_2$ QSL ground state, which, due to its relative simplicity, is often used as the fruit fly model for studying topologically ordered states. It was introduced as a stabilizer quantum code for (topological) fault-tolerant quantum computing. This section was inspired by [132].

To begin with, consider the classical Ising model

$$H = -\Delta_s \sum_{s} A_s \tag{1.46}$$

where

$$A_s = \prod_{i \in s} S_i, \tag{1.47}$$

on a square lattice with periodic boundary conditions labelled by sites s, with spins $S_i = \pm 1$, occupying the links. A_s measures the product of all spins in the "star" connected to site s, as illustrated in fig. 1.9(a). For $\Delta_s > 0$, the ground state is where $A_s = 1$ on all sites, i.e the ground state is defined by a local constraint, which gives rise to an emergent eight-vertex model [81]. There are eight configurations which satisfy this constraint on a star, all four spins up or down and the six different ways of having two spins up and two down, which make up the analogous six-vertex model in spin ice (see section 1.2). As we will see, there are many similarities between the model described by eq. (1.46) and spin ice on the pyrochlore lattice.

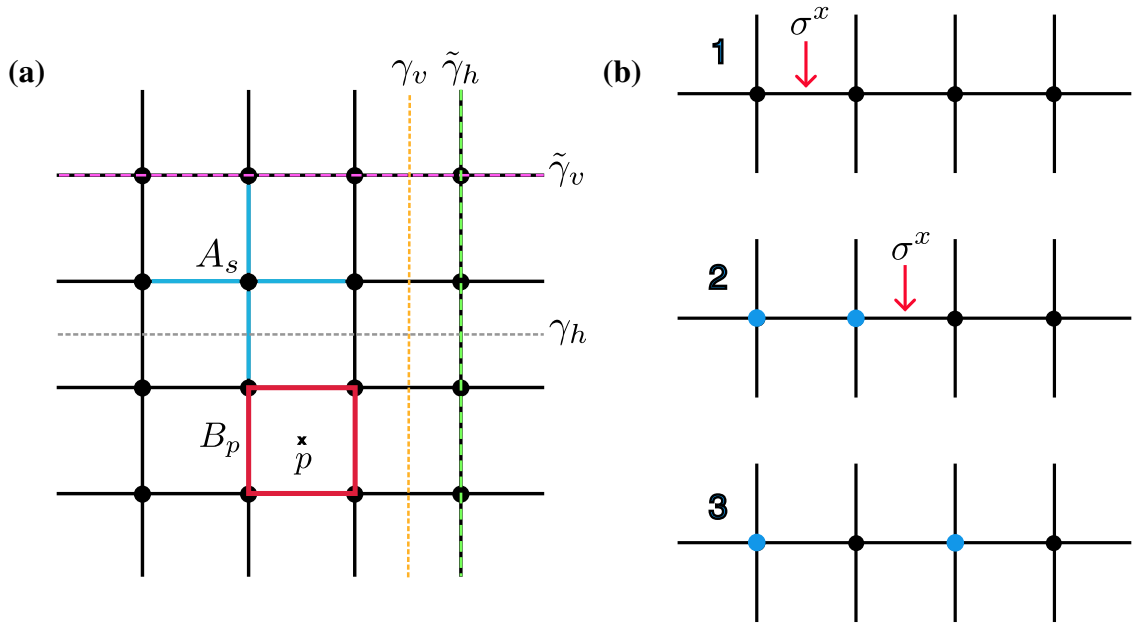

Figure 1.9: **(a)** The toric code. The links on which star, A_s, and plaquette, B_p operators act are shown as well as the winding loops along which the operators that label ($\gamma_{v,h}$) and move between ($\tilde{\gamma}_{v,h}$) topological sectors are defined. A site, p, of the dual lattice which has sites at the centres of square plaquettes is indicated. **(b)** Creating and separating a pair of spinons in the toric code. Acting with a σ^x operator creates two defect stars with $A_s = -1$ (blue circles). The spinons can be propagated by applying a string of σ^x operators. In the U(1) QSL on the pyrochlore lattice, acting with S^x creates a spinon-antispinon pair on neighbouring diamond sites which can be propagated in a similar fashion.

For a lattice, with N sites, we can estimate the ground state degeneracy, D, by applying Pauling's argument [82], which gives $D = 2^N$; the model has an extensively degenerate ground state manifold. However, this does not take into account the boundary conditions of the lattice. Let us define the dual lattice, with sites labelled by p, occupying the centre of each square plaquette. If we start with a ground state configuration and flip all the spins on a plaquette then we obtain another ground state. Therefore, starting from some reference ground state, we can create another ground state by flipping or not flipping on all N plaquettes of the lattice. This gives 2^{N-1} ground states, since with periodic boundaries one plaquette flip can be constructed from a combination of flips on adjacent plaquettes, so is not independent. Furthermore, one can flip a string of spins which winds around the periodic boundaries in either the horizontal or vertical direction and remain in the ground state. These moves cannot be constituted of plaquette flips. This gives a total of 2^{N+1} ground states.

The winding spin flips around the periodic boundaries take the system between different topological sectors, whereas any combination of plaquette flips will remain within the same topological sector. The sectors are labelled by a pair of $\mathbb{Z}_2$ topological invariants,

which together creates a $\mathbb{Z}_2 \otimes \mathbb{Z}_2$ object. These invariants are

$$\Gamma_v = \prod_{i \in \gamma_v} S_i = \pm 1, \qquad \Gamma_h = \prod_{i \in \gamma_h} S_i = \pm 1, \tag{1.48}$$

where $\gamma_{v,h}$ are paths intersecting the links which span the system in either the vertical or horizontal directions respectively, as shown in fig. 1.9(a). For periodic boundary conditions there are 4 topological sectors since the lattice is defined on a torus, but in general there are 2^g sectors where g is the genus of the manifold on which the lattice is defined.

An excitation is created by flipping a spin on a single link, which creates a pair of defect stars with $A_{s,s'} = -1$ on the neighbouring sites s, s'. Creating this excitation comes at a finite energy cost of $\Delta E = 4\Delta_s$. By flipping a long string of spins these defects can be separated to arbitrary distance at zero energy, so the defects are deconfined excitations. Deconfined objects are defined as those which can be separated to infinite distance at finite energy cost [29]. We will call these excitations spinons, as they are the fractionalization of a spin-flip operation. The original $\Delta S_i = 2$ spin-flip *fractionalizes* into a pair of independent $\Delta S_i = 1$ excitations. This gives an alternative view of the moves which take us between topological sectors as creating a pair of spinons, transporting one around the periodic boundaries, then annihilating with the other.

Separation of a pair of spinons implies there should be some kind of local structure which ensures that the local constraint is satisfied on the path in between the spinons. Here, we can introduce a compact, binary electric field, $e_{ss'} \in \{0, 1\}$ which lives on the links through the mapping [22]

$$S_i \to e^{i\pi e_{ss'}}. \tag{1.49}$$

Defining the lattice divergence, $\mathrm{div}(e)_s = \sum_{s' \to s} e_{ss'}$, where the sum is over all sites s' connected to s, then we can rewrite

$$A_s = e^{i\pi \mathrm{div}(e)_s}. \tag{1.50}$$

Defining an electric charge through the analogue of Gauss's law,

$$q_s = \mathrm{div}(e)_s, \tag{1.51}$$

we can now reinterpret the low energy physics in terms of the emergent field and charge. The ground state, $A_s = 1$ for all s, corresponds to the vacuum, $q_s = 0$ on all sites. Spinons can be identified as electric charges which act as sources and sinks of the emergent field. One can make a similar argument for the existence of deconfined spinons in the Ising model on the pyrochlore lattice.

Therefore, since the ground state of this classical model is governed by a local constraint and exhibits an extensive ground state degeneracy and emergent gauge field, it is a classical spin liquid.

Now to construct a quantum spin liquid, we must add quantum fluctuations to the model. The toric code is obtained from eq. (1.46) by replacing the Ising variables with Pauli z

operators, σ_i^z, and adding a plaquette flip term, $B_p = \prod_{i\in p} \sigma_i^x$, such that the Hamiltonian reads

$$H = -\Delta_s \sum_s A_s - \Delta_p \sum_p B_p. \tag{1.52}$$

Since $[A_s, B_p] = 0$ for all s and p, $[H, A_s] = [H, B_p] = 0$, so the ground state is defined as where $A_s |\Psi_0\rangle = |\Psi_0\rangle$ and $B_p |\Psi_0\rangle = |\Psi_0\rangle$ for all s and p. One possible ground state is

$$|\Psi_0\rangle \propto \prod_p \frac{1 + B_p}{2} \otimes_i |\sigma_i^z = +1\rangle , \tag{1.53}$$

where $\otimes_i |\sigma_i^z = +1\rangle$ is a ferromagnetic product state which satisfies $A_s = 1$ and the operator $(1 + B_p)$ is a projector ensuring $B_p = 1$. This state is an equal superposition of all states which satisfy $A_s = 1$, or, equivalently, an equal superposition of all loop coverings, which are connected to $\otimes_i |\sigma_i^z = +1\rangle$ by B_p [29].

How do the topological sectors of the classical model carry over to the quantum case? Promoting the topological invariants in eq. (1.48) to quantum operators, we see that $[H, \Gamma_{v,h}] = 0$, so can now used to label distinct topological sectors of the Hilbert space. The operators which change the eigenvalues obtained by acting with $\Gamma_{v,h}$ are

$$\tilde{\Gamma}_v = \prod_{i\in\tilde{\gamma}_v} \sigma_i^x, \qquad \tilde{\Gamma}_h = \prod_{i\in\tilde{\gamma}_h} \sigma_i^x, \tag{1.54}$$

where $\tilde{\gamma}_{v,h}$ are strings of operators along the links which go around the periodic boundaries, such that they intersect $\gamma_{v,h}$ an odd number of times respectively, see fig. 1.9(a). Since $[H, \tilde{\Gamma}_{v,h}] = 0$, with periodic boundary conditions the four distinct ground states $|\Psi_0\rangle , \tilde{\Gamma}_v |\Psi_0\rangle , \tilde{\Gamma}_h |\Psi_0\rangle , \tilde{\Gamma}_v\tilde{\Gamma}_h |\Psi_0\rangle$ are degenerate. The degeneracy of ground states is 2^g, where g is the genus of the manifold the lattice is defined on. We see that the topological sectors of the classical theory become topological order in the ground state, with the degenerate ground states distinguished by the eigenvalues of $\Gamma_{v,h}$.

Analogous to the classical case, a pair of separated spinons at sites s, s' are created by operating with the string operator $O_{ss'} = \prod_{i\in\tilde{\gamma}_{ss'}} \prod_i \sigma_i^x$ on a series of links, creating a pair of $A_{ss'} = -1$ defects with a finite energy cost of $\Delta E = 4\Delta_s$, independent of s, s'. This is illustrated in fig. 1.9(b). An excited state with spinons at s, s', $O_{ss'} |\Psi_0\rangle$, is an equal superposition of all possible ways of creating this pair at s, s', so they should be thought of as independent, deconfined particles. In the quantum model, it is also possible to have excitations where $B_p = -1$, which are typically called visons. Their properties are analogous to that of the spinons, with the operator $O_{pp'} = \prod_{i\in\gamma_{pp'}} \prod_i \sigma_i^z$ creating a pair of visons at dual lattice sites p, p' with an energy cost of $\Delta E = 4\Delta_p$. The spinons and visons are anyons due to their mutual statistics; exchanging the position of a spinon and vison gives the wavefunction a fractional phase factor $e^{i\frac{\pi}{2}}$ [22].

We can map the Hamiltonian to a type of electromagnetic gauge theory, which allows us to identify the spinons and visons with electric and magnetic excitations respectively. We

let

$$\sigma_i^z \to e^{i\pi e_{ss'}}, \qquad \sigma_i^x \to e^{ia_{ss'}}, \tag{1.55}$$

where the mapping for σ_i^z variables is analogous to the classical case, eq. (1.50), and we define the compact vector potential $a_{ss'} \in \{0, \pi\}$ [22]. Defining the lattice curl, $\mathrm{curl}(a)_p = \sum_{ss' \in \square_p} a_{ss'}$, which is the magnetic flux through the plaquette centred on p, then

$$B_p = \cos(\mathrm{curl}(a)_p), \tag{1.56}$$

and we identify the visons as magnetic excitations, with the spinons as electric excitations, as in the classical model. The Hamiltonian of the gauge theory is

$$H_{\mathrm{EM}} = -\Delta_s \sum_s e^{i\pi \mathrm{div}(e)_s} - \Delta_p \sum_p \cos(\mathrm{curl}(a)_p). \tag{1.57}$$

It is easiest to see that the toric code is a $\mathbb{Z}_2$ gauge theory in the spin language. Since $[H, A_s] = 0$, A_s is a local conserved quantity, so we treat it as a Gauss law, $G_s = A_s = \prod_{i \in s} \sigma_i^z$. G_s generates the local gauge transformation

$$G_s \sigma_{i'}^x G_s = -\sigma_{i'}^x, \tag{1.58}$$

where i' is a link attached to the site s, which leaves H invariant. Since $G_s^2 = 1$, the transformation has a local $\mathbb{Z}_2$ structure [133]. The local values of G_s label distinct sectors of the theory, where the ground state is in the sector with $G_s = 0$, corresponding to zero electric charge, $q_s = 0$, on all sites.

The topological order of the toric code ground state is readily diagnosed by extracting the topological entanglement entropy [134, 135]. For the ground state of a topologically ordered 2D system, partitioned into regions A and B, the von Neumann entropy [136] is given by

$$S(\rho_A) = \alpha L - \gamma \tag{1.59}$$

in the $L \to \infty$ limit, where $S(\rho_A) = -\mathrm{Tr}_A \rho_A \log(\rho_A)$, the reduced density matrix $\rho_A = \mathrm{Tr}_B |\Psi_0\rangle \langle\Psi_0|$ and L is the length of the boundary between A and B. For a 2D model with Abelian anyons, the topological entanglement entropy,

$$\gamma = \ln\left(\sqrt{N_{\mathrm{sectors}}}\right), \tag{1.60}$$

where N_{sectors} is the number of topological sectors [135], so for the toric code $\gamma = \ln 2$ [137]. Thus the measurement of a constant contribution to the entanglement entropy is often used as a diagnostic for topological order in numerical simulations, see for instance [138–141], and has even been measured on a quantum processor [72].

The toric code can be generalized to three dimensions (on a cubic lattice) [142] with an analogous ground state, topological degeneracy of $2^3 = 8$ and finite topological entanglement entropy [143]. However, in 3D there is also a topologically trivial, constant contribution to the entanglement entropy [144], so the topological contribution is not readily extracted from numerics as in the 2D case.

1.6.3 Quantum Spin Ice: A U(1) Quantum Spin Liquid

We have seen how adding quantum fluctuations to a classical 8-vertex model on the square lattice can lead to a quantum spin liquid, so, similarly, what happens when we add quantum fluctuations to nearest neighbour spin ice on the pyrochlore lattice, whose ground state is an emergent 6-vertex model? Hermele, Fisher and Balents (HFB) [90] proposed, using degenerate perturbation theory, that the ground state of the spin $1/2$ XXZ model on the pyrochlore lattice,

$$H_{\mathrm{XXZ}} = J^z \sum_{\langle ij \rangle} S_i^z S_j^z + J^\perp \sum_{\langle ij \rangle} \Big(S_i^+ S_j^- + \mathrm{h.c} \Big), \tag{1.61}$$

in the $\left|J^\perp\right| \ll J^z$ limit, could be a $\mathrm{U}(1)$ quantum spin liquid described by an effective theory of frustrated compact quantum electrodynamics. This was later confirmed numerically [145] and the spin liquid has come to be known as quantum spin ice.

Both the perturbative effective model and XXZ Hamiltonian have been extensively studied over the past years both numerically and with various flavours of mean-field theory [145–153], such that the existence of a π-flux QSL is well-established for $J^\perp > 0$, 0-flux for $J^\perp < 0$. Recently, there has been a particular focus on the properties of the emergent quantum electrodynamics (eQED) [154, 155], contrasting to the quantum electrodynamics which describes our universe. On the experimental side, dipolar-octupolar pyrochlores are thought to realize the XYZ variant of eq. (1.61) [156], with the candidate materials $Ce_2Zr_2O_7$ and $Ce_2Sn_2O_7$ recently showing tantalizing glimpses of the characteristic eQED [61, 157], as well as signatures in other rare-earth pyrochlores such as $Pr_2Hf_2O_7$ [158].

Here, we reiterate the perturbative argument of HFB for the existence of a $\mathrm{U}(1)$ QSL as the ground state of eq. (1.61), deriving an effective dimer model and lattice gauge theory. This same approach is applied to the XXZ model on the centred pyrochlore lattice in chapter 4. HFB use the Schrieffer-Wolff formalism [159–161] of degenerate perturbation theory. Given a Hamiltonian $H = H_0 + \lambda H_1$, where H_0 has a degenerate ground state with energy E_0, the aim is to find an effective Hamiltonian, H_{eff}, which describes the effect of the perturbation H_1 on the ground state manifold. In constructing the effective Hamiltonian, the projector onto the ground state manifold, $\hat{P}$, and operator

$$\hat{D} = -\frac{1-\hat{P}}{\hat{H}_0 - E_0}, \tag{1.62}$$

which projects onto the subspace orthogonal to the ground state manifold are useful.

For this model, eq. (1.61) is rewritten (up to a constant) as

$$\begin{aligned} H_{\mathrm{XXZ}} &= H_0 + H_1, \qquad H_0 = \frac{J^z}{2} \sum_t L_t^2, \\ H_1 &= J^\perp \sum_{\langle ij \rangle} \Big(S_i^+ S_j^- + \mathrm{h.c} \Big), \end{aligned} \tag{1.63}$$

where $L_t = \sum_{i \in t} S_i^z$ is the tetrahedron magnetization for which the ground state constraint of the Ising model (H_0) is $L_t = 0$ on all tetrahedra. In the degenerate perturbation theory, one considers the effect of H_1 acting on the degenerate manifold specified by this local constraint.

The lowest order non-constant contribution to H_{eff} occurs at third order, where the contribution to the effective Hamiltonian,

$$H_{\text{eff}}^{(3)} = PH_1DH_1DH_1P, \tag{1.64}$$

results in the non-constant term

$$H_{\text{eff}}^{(3)} = J_{\text{ring}} \sum_{\hexagon} \left(S_0^+ S_1^- S_2^+ S_3^- S_4^+ S_5^- + \text{h.c} \right), \tag{1.65}$$

where $J_{\text{ring}} = \frac{12(J^\perp)^3}{(J^z)^2}$, the sum is over all hexagonal plaquettes of the pyrochlore lattice (see fig. 1.4) and sites are numbered in a clockwise fashion around the hexagonal plaquette. The correct prefactor is obtained by considering the number of different ways to construct a valid hexagonal loop and the fact that in the virtual excited states there are always two defect tetrahedra with $L_t = 1$, meaning that each D gives a factor of $-\frac{1}{J^z}$ per hexagon. The sign of J_{ring} can be changed by a unitary transformation which rotates a subset of the spins [90], so that eq. (1.65) is applicable for $J^\perp$ of either sign.

Equation (1.65) can be reinterpreted as a quantum dimer model (sees section 1.6.1) on the diamond lattice. This is done by mapping $S_i^z = \frac{1}{2}(-\frac{1}{2}) \to n_i = 1(0)$, where n_i measures the presence (or absence) of a dimer on the link of the diamond lattice corresponding to site i of the pyrochlore lattice. The ground state constraint, $L_t = 0$, maps to the constraint that there must be two dimers touching every site, and ring exchange to flipping a hexagon, as shown in fig. 1.4. Thus, as a dimer model, the effective Hamiltonian is

$$H_{\text{eff}}^{(3)} = J_{\text{ring}} \sum_{\hexagon} \left| \hexagon \right\rangle \left\langle \hexagon \right| + \left| \hexagon \right\rangle \left\langle \hexagon \right|, \tag{1.66}$$

where the Hilbert space is constrained to have two dimers touching each site, i.e it is actually a quantum loop model.

As discussed in section 1.6.1, a Hamiltonian of the form

$$H_{\text{RK}} = -|J_{\text{ring}}| \sum_{\hexagon} \left| \hexagon \right\rangle \left\langle \hexagon \right| + \left| \hexagon \right\rangle \left\langle \hexagon \right| + \mu \sum_{\hexagon} \left| \hexagon \right\rangle \left\langle \hexagon \right| + \left| \hexagon \right\rangle \left\langle \hexagon \right| \tag{1.67}$$

will have an exact quantum liquid ground state at the RK point, $\mu = |J_{\text{ring}}|$. HFB speculated that this liquid state survives as the ground state until $\mu = 0$ in the dimer model and therefore the ground state of the XXZ Hamiltonian in the perturbative limit is a QSL. Quantum Monte Carlo simulations of eq. (1.67) [145] showed that this was indeed the case, with the quantum liquid occupying the $-0.5 \leq \mu \leq 1$ region of the ground state phase diagram.

To further understand the low energy properties of the effective Hamiltonian, HFB derived an effective $\mathrm{U}(1)$ gauge theory, which then leads to the interpretation of the spin liquid as the deconfined phase of an emergent quantum electrodynamics. First, rather than mapping the spins to dimers with a local 2-dimensional Hilbert space, one can instead map the spins to (infinite-dimensional) quantum rotors (see chapter A) with angular momentum $m_i \in \mathbb{Z}$ and orientation $\theta_i \in [0, 2\pi)$. An exact mapping from $S = 1/2$ spins to quantum rotors is

$$S_i^z \to m_i - \frac{1}{2}, \qquad S_i^{\pm} = e^{\pm i\theta_i}, \tag{1.68}$$

provided that the constraint $m_i = 0, 1$ is imposed, such that the dimension of the local Hilbert space matches that of the spins. Thus in terms of rotors, eq. (1.65) can be written as

$$H_{\mathrm{rotor}} = \frac{U}{2}\sum_i (m_i - \frac{1}{2})^2 - K\sum_{\hexagon} \cos(\theta_0 - \theta_1 + \theta_2 - \theta_3 + \theta_4 - \theta_5), \tag{1.69}$$

where $K = 2|J_{\mathrm{ring}}|$ and the first term enforces the constraint on the Hilbert space exactly when taking the $\frac{U}{K} \to \infty$ limit.

To proceed, the rotors can be rewritten in terms of directed link variables which are the lattice analogue of vector fields. Labelling sites of the diamond lattice r, so the pyrochlore site i is the link between two diamond sites rr', a half-integer electric field can be defined,

$$e_{rr'} = \sigma_r(m_{rr'} - \frac{1}{2}), \tag{1.70}$$

where $\sigma_r = +(-)1$ on the $a(b)$ diamond sublattice. This is analogous to the writing of the z component of $S = 1/2$ classical spins in the spin-ice representation in eq. (1.11), so this link variable is related to the classical field defined in eq. (1.10). Similarly, we also define a vector potential

$$a_{rr'} = \eta_r \theta_{rr'}. \tag{1.71}$$

This new pair of variables are canonically conjugate, $[a_{rr'}, e_{rr'}] = i$, as expected for an electric field and vector potential [22]. In these variables eq. (1.69) becomes

$$H_{\mathrm{rotor}} = \frac{U}{2}\sum_{\langle rr'\rangle} e_{rr'}^2 - K\sum_{\hexagon} \cos(\mathrm{curl}a)_{\hexagon}, \tag{1.72}$$

where we have defined the lattice analog of the curl

$$(\mathrm{curl}a)_{\hexagon} = \sum_{rr'\in\hexagon} a_{rr'} = a_{r_0r_1} + a_{r_1r_2} + a_{r_2r_3} + a_{r_3r_4} + a_{r_4r_5} + + a_{r_5r_0} \tag{1.73}$$

which is a directed sum around the hexagonal plaquette. H_{rotor} is invariant under the $\mathrm{U}(1)$ gauge transformation

$$a_{rr'} \to a_{rr'} + \chi_r' - \chi_r, \tag{1.74}$$

where $\chi_r \in [0, 2\pi)$, since the χ_r enter the curl twice with opposite sign. The associated conserved quantity (Gauss law) is

$$G_r = \mathrm{div}(e)_r = \sum_{r' \to r} e_{rr'} = \sigma_r L_r \tag{1.75}$$

which can be interpreted as an electric charge, where the sum is over all sites neighbouring the site r. The ground state manifold of the spin model corresponds to the gauge sector with no charges.

A magnetic field is defined on the links, ss' of the dual lattice, which pierce the centres of hexagonal loops on the diamond lattice,

$$b_{ss'} = \frac{(\mathrm{curl}a)_{\hexagon_{ss'}}}{\pi}, \tag{1.76}$$

so that the effective Hamiltonian

$$H_{\mathrm{rotor}} = \frac{U}{2} \sum_{\langle rr' \rangle} e_{rr'}^2 - K \sum_{\langle ss' \rangle} \cos(\pi b_{ss'}), \tag{1.77}$$

where we have the theory in terms of electric and magnetic fields.

Let us first consider the phases of a related compact $\mathrm{U}(1)$ lattice gauge theory on the cubic lattice [162], with Hamiltonian of the form

$$H_{\mathrm{LGT}} = \frac{\tilde{U}}{2} \sum_{\langle \mathrm{rr'} \rangle} \tilde{e}_{\mathrm{rr'}}^2 - \tilde{K} \sum_{\square} \cos(\mathrm{curl}\tilde{a})_{\square}, \tag{1.78}$$

where

$$\tilde{e}_{rr'} \in \{0, \pm 1, \pm 2, \dots\}, \tag{1.79}$$

rather than the half integer values of $e_{rr'}$. In the $\frac{U}{K} \to \infty$ limit, the ground state has $\tilde{e}_{\mathrm{rr'}} = 0$ on all links, excitations are gapped and electric charges experience a linear confining potential. This phase is expected to persist over some finite region away from the $\frac{U}{K} \to \infty$ limit. On the other hand, for small $\frac{U}{K}$, one obtains a deconfined Coulomb phase, where the electric charges interact via a $1/r$ potential and there is a gapless, linearly dispersing photon excitation. The effective low energy description is that of Gaussian QED, with effective Hamiltonian of the form

$$H_{\mathrm{QED}} = \frac{1}{2} \int d^3\mathbf{r} (|\mathbf{E}(\mathbf{r})|^2 + |\mathbf{B}(\mathbf{r})|^2), \tag{1.80}$$

where $\mathbf{E}$ and $\mathbf{B}$ are coarse-grained electric and magnetic fields.

There will be some transition between the two regimes at $\frac{U}{K} \approx 1$ [90, 162]. Now for the theory described by H_{rotor}, the phase in the physically relevant $\frac{U}{K} \to \infty$ limit is not obvious; the ground state has the constraint that $e_{rr'} = \pm\frac{1}{2}$, which can be satisfied by a macroscopic number of configurations. HFB dub this a *frustrated* gauge theory. The

question of whether the ground state of $H_{\text{eff}}^{(3)}$ is a quantum spin liquid is the same as asking whether the deconfined phase of this theory stretches all the way to $\frac{U}{K} \to \infty$. Since numerical simulations [145] have shown that the ground state of the dimer form of $H_{\text{eff}}^{(3)}$ is a quantum liquid, the theory is deconfined in the $\frac{U}{K} \to \infty$ limit and physical gauge sector, and therefore the effective theory is Gaussian QED, with the properties outlined above. In particular, there is a gapless photon excitation which is associated with the ring-exchange term acting within the $L_t = 0$ manifold.

What are the properties of the deconfined excitations? Consider acting with the physical spin operator $S_{\tilde{r}\tilde{r}'+}$, which is equivalent to acting with the electric field raising operator, $e^{ia_{\tilde{r}\tilde{r}'}}$, where $\tilde{r}$ belongs to the a sublattice. The effect is to flip the direction of $e_{\tilde{r}\tilde{r}'}$ which was originally pointing from $\tilde{r}$ to $\tilde{r}'$. Therefore according to eq. (1.75) we have created a charge-anticharge pair on the sites $\tilde{r}$ and $\tilde{r}'$. By applying a succesion of $e^{ia_{rr'}}$ operators, or equivalently alternating $S^+_{rr'}$ and $S^-_{rr'}$, the pair can be separated to infinite distance with finite energy cost. This is similar to separating spinons in the toric code, which is depicted in fig. 1.9(b). These isolated charges are spinons, where the initial $\Delta S^z = 1$ excitation has fractionalized into independent $S^z = \frac{1}{2}$ excitations.

Similar to a $\mathbb{Z}_2$ quantum spin liquid, the ground state of the U(1) quantum spin liquid also has a form of topological degeneracy [90, 131, 163]. In the gauge theory picture, consider the electric flux through a plane oriented perpendicular to the cubic axis $k \in \{x, y, z\}$,

$$\Phi_k^E = \sum_{rr' \in \text{plane}_k} e_{rr'}, \tag{1.81}$$

where the sum is over all links intersecting the plane. This is analogous to the winding number discussed in the context of spin ice (see section 1.3.2).

Consider a particular ground state in the deconfined phase, so that it's effective, coarse-grained Hamiltonian is eq. (1.80). If a quantum Φ_0^E of flux is added, the lowest energy cost is if the flux is spread evenly across the plane which has area proportional to L^2, so that $E_k(\mathbf{r}) \to E_k(\mathbf{r}) + c\frac{\Phi_0^E}{L^2}$, where c is a constant. Since the system has volume proportional to L^3, the total energy cost is $\Delta E = \frac{(c\Phi_0^E)^2}{L}$, which vanishes in the thermodynamic limit, so each electric flux sector contains a degenerate ground state of the system. Microscopically, creating one flux quantum piercing a plane perpendicular to the $\hat{\mathbf{k}}$ direction is equivalent to creating a spinon-antispinon pair and winding one around the periodic boundary before annihilating with its partner. The lowest energy configuration as they are separated is a superposition of all possible field lines between them, resulting in a uniformly distributed flux. Therefore we can label topological sectors in the ground state by the number of electric flux quanta through planes oriented perpendicular to each of the cubic axes, which are analogous to the topological sectors discussed for the ground state of classical spin ice.

In fact, in the quantum model, there are similar arguments for the magnetic flux, so a topological sector is characterized by six integers in total [90]. This also gives a characteristic

finite size scaling of the energy which can be used to identify the $\mathrm{U}(1)$ quantum spin liquid, as was done in [131, 145].

1.7 Summary

In this section we have discussed the properties of classical and quantum spin liquids, with a focus on those realized on the pyrochlore lattice. Classical Ising and Heisenberg models on the pyrochlore have a Coulomb spin liquid ground state, described by an emergent electrostatics where excitations interact via an effective Coulomb interaction. This is a paradigmatic example of a classical spin liquid, exhibiting:

- A ground state governed by a local constraint.
- An extensive ground state degeneracy.
- A lack of symmetry-breaking order.
- An emergent gauge field.

We presented an argument that classical spin liquids in solid-state materials are generically expected to be destroyed by effects such as small symmetry-breaking interactions or quantum fluctuations at a low enough temperature, so will be found at slightly elevated temperatures. We also outlined some of their experimental signatures in the magnetic susceptibility, specific heat and spin structure factor.

We then moved on to discuss quantum spin liquids, using a quantum dimer liquid, the toric code, and finally quantum spin ice on the pyrochlore lattice, as examples. We made clear how classical spin liquids can be thought of as parent states for quantum spin liquids, which are characterized by:

- A lack of symmetry-breaking order.
- Fractionalized excitations.
- Emergent gauge fields.
- Quantum order.

We explained in depth how the emergent compact quantum electrodynamics of quantum spin ice is derived in perturbation theory from the XXZ model on the pyrochlore lattice, as well as its topological properties and excitations.

The rest of this thesis is devoted to the study of classical and quantum spin models on the closely related *centred* pyrochlore lattice. In chapter 2 we study the properties of a classical Heisenberg model, drawing on many of the ideas presented in this section about the classical spin liquid on the pyrochlore. Chapter 3 compares the properties of this model (with added dipolar interactions) to experimental magnetization, susceptibility and specific heat measurements of the metal-organic framework $[\mathrm{Mn(ta)_2}]$, where we observe glimpses of the experimental signatures discussed here. Finally, in chapter 4 we study the quantum XXZ model, finding an analogous low-energy $\mathrm{U}(1)$ lattice gauge theory to the

pyrochlore case, but coupled to fermionic matter. Gauge mean-field calculations and exact diagonalization on a small cluster suggest the ground state could be a $\mathrm{U}(1)$ quantum spin liquid.

Chapter 2

Classical Minimal Models

In this chapter we present results on minimal classical spin models on the centred pyrochlore lattice, focusing on the antiferromagnetic $J_1 - J_2$ Heisenberg model. This chapter is closely based on [1], with many of the figures and portions of the text directly reproduced. We find that the low energy physics is governed by a modified local constraint where the coupling ratio $\eta = \frac{J_2}{J_1}$ determines the nature of correlations. The phase diagram demonstrates the interplay between strong ferrimagnetic correlation at small η and the complete decoupling of corner and vertex spins as $\eta \to \infty$. In the Ising model, this opens up a region where the ground state configuration has an effective charge on every tetrahedron, modifying the $\mathrm{U}(1)$ topological invariant in spin ice to a $\mathbb{Z}_2$ quantity. Similarly, in the Heisenberg model, for $\gamma = \frac{1}{\eta} \lesssim 1.25$, the low temperature correlations can be understood in terms of screening in an emergent charge fluid, where the central spins act as mobile charges with a strength parametrized by γ. We also discuss how the centred pyrochlore lattice can be viewed as a thin film of a four-dimensional lattice, making clear the connection to spin ice thin films [164, 165]. We elaborate on this by showing how an appropriate model on the the two-dimensional centred kagome lattice exhibits the same phenomenon, due to its equivalence with a thin film of the pyrochlore lattice. Furthermore, the large ground state degeneracy of the $J_1 - J_2$ model allows one to stabilize exotic ground states, by the addition of perturbations. We demonstrate this by stabilizing a three-dimensional Coulomb phase through the addition of a J_3 term. We leave the relevance of the $J_1 - J_2$ Heisenberg model for the metal-organic framework $[\mathrm{Mn(ta)_2}]$ to chapter 3.

This chapter is structured as follows. We first introduce the lattice and model, then discuss the ground state properties with Ising and Heisenberg spins using analytical arguments and mean-field calculations. Next, we present Monte Carlo results for the Heisenberg model at finite temperature. We then discuss the effective description of the spin liquid, before moving on to the properties of the analogous model on the centred kagome lattice and the effect of adding a J_3 term.

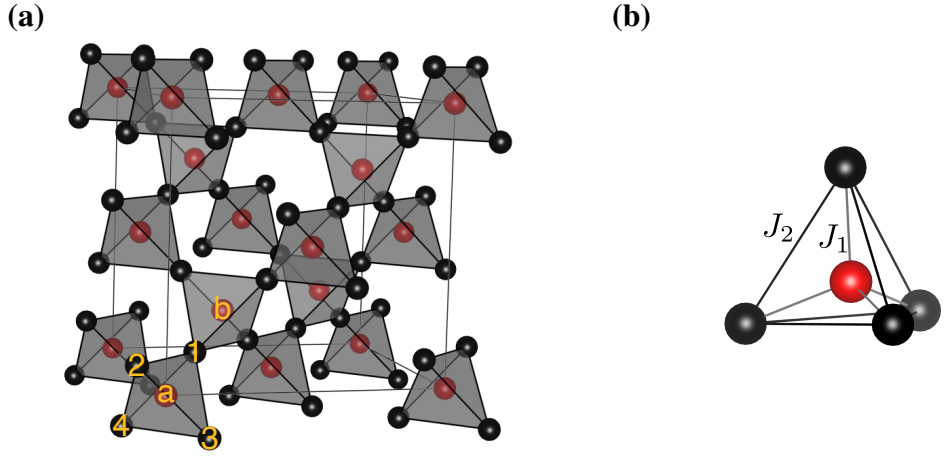

Figure 2.1: **(a)** The conventional 24 site cubic unit cell of the centred pyrochlore lattice with the six sublattices labelled. **(b)** A single tetrahedron with J_1 (nearest neighbour) and J_2 (next nearest neighbour) couplings labelled.

2.1 Lattice and Model

The centred pyrochlore lattice, shown in fig. 2.1, is obtained from the pyrochlore lattice by the addition of a lattice site at the centre of each tetrahedron, so that sites on both the pre-medial diamond and medial pyrochlore lattice are occupied. Explicitly, it is defined by sites at positions

$$\mathbf{r}_i = \mathbf{R}_I + \boldsymbol{\delta}_\mu, \tag{2.1}$$

where $\mathbf{R}_I$ are the sites of the fcc lattice (see eq. (1.2)), and μ labels the six sublattices with basis vectors

$$\begin{gathered}\boldsymbol{\delta}_a = (0,0,0),\ \boldsymbol{\delta}_b = \frac{1}{4}(1,1,1),\\ \boldsymbol{\delta}_1 = \frac{1}{8}(1,1,1),\ \boldsymbol{\delta}_2 = \frac{1}{8}(1,-1,-1),\ \boldsymbol{\delta}_3 = \frac{1}{8}(-1,1,-1),\ \boldsymbol{\delta}_4 = \frac{1}{8}(-1,-1,1),\end{gathered} \tag{2.2}$$

in units where the cubic unit cell side length $a = 1$. We will typically consider cubic systems of integer side length L with periodic boundary conditions. In what follows, sites at the centre of a tetrahedron, $\mu = a, b$, are referred to as central sites and those at the vertices of the tetrahedron, $\mu = 1, 2, 3, 4$, as vertex sites.

The minimal classical spin model we consider is the isotropic $J_1 - J_2$ model,

$$H = J_1 \sum_{\langle ij \rangle} \mathbf{S}_i \cdot \mathbf{S}_j + J_2 \sum_{\langle\langle ij \rangle\rangle} \mathbf{S}_i \cdot \mathbf{S}_j, \tag{2.3}$$

where the $\mathbf{S}_i$ are n-component classical spins. The J_1 terms couple the centre and vertex spins on a tetrahedron, whilst the J_2 term is the nearest neighbour interaction on the pyrochlore lattice, coupling vertex spins as shown in fig. 2.1(b). In this chapter, without loss of generality, we set the spin length $S = |\mathbf{S}| = 1$, $J_1 = 1$, and typically parametrize the model with the coupling ratio $\eta = J_2/J_1$, using $\gamma = 1/\eta$ instead when we would like to work close to the pyrochlore limit ($\eta \to \infty$, where centre and vertex spins are decoupled).

Given the classical spin liquid ground state on the pyrochlore lattice (see chapter 1), in this chapter we investigate whether the centred pyrochlore also hosts a spin liquid in models with Ising ($n = 1$) and Heisenberg ($n = 3$) spins, as well as the nature of any such spin liquids.

2.2 Ground State Properties

2.2.1 Local Constraint

For $J_2 < 0$ the model is unfrustrated and the ground state is a simple ferro- or ferri-magnet, depending on the sign of J_1. In the ferrimagnet all central spins are anti-parallel to vertex spins. We focus on the frustrated and experimentally relevant (see chapter 3) quadrant of parameter space where $J_1 > 0, J_2 > 0$. We can map from J_1 to $-J_1$ by a global inversion of all central spins, so the results presented here can be straightforwardly generalized to the $J_1 < 0$ region of the parameter space.

As on the pyrochlore, the Hamiltonian can be rewritten in terms of the tetrahedral units, t, of the lattice,

$$H = \frac{J_2}{2} \sum_t |\mathbf{L}_t|^2 - \frac{N}{3}\left(\frac{J_1^2}{2J_2} + 2J_2\right), \tag{2.4}$$

however, due to the presence of the centre site, we require that $\mathbf{L}_t$ be given by

$$\mathbf{L}_t = \gamma \mathbf{S}_{t,c} + \sum_{v=1}^{4} \mathbf{S}_{t,v}, \tag{2.5}$$

where γ rescales the contribution of the central spin. Centre sites are labelled by the index c, and the sum over v runs over the vertices of the tetrahedron. The ground state is that which minimizes $L_t = |\mathbf{L}_t|$ on all tetrahedra.

2.2.2 Ising Spins

To understand how the form of the Hamiltonian in equation (2.4) affects the possible ground states, it is instructive to first consider the Ising model, with spin variables $\sigma_i = \pm 1$. The ground state is obtained by minimizing

$$L_t^I = \left| \gamma \sigma_{t,c} + \sum_{v=1}^{4} \sigma_{t,v} \right| \tag{2.6}$$

on all tetrahedra, which results in the ground state phase diagram displayed in figure fig. 2.2(d). For $\eta < 1/3$, ground state is a long-range ordered ferrimagnet with centre spins antiparallel to vertex spins, which we dub the 4:0 state as the vertices are either all-up or all-down on every tetrahedron. There are also a pair of extensively degenerate disordered ground states. For $\eta > 1$ the ground state is the familiar spin ice state of the

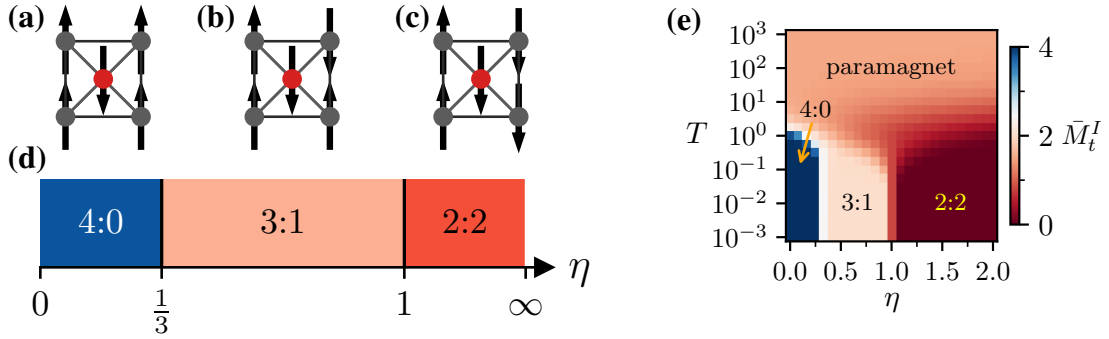

Figure 2.2: Ground states of the Ising model on the centred pyrochlore lattice. **(a)-(c)** Examples of the allowed single tetrahedron spin configurations in each of the ground states and **(d)** the ground state phase diagram. For $\eta < 1/3$ (**(a)**), the ground state is a long range ordered ferrimagnet. In the region $1/3 < \eta < 1$ (**(b)**) the ground state manifold is made up of 3-up/1-down and 3-down/1-up vertex spin configurations with central spins correspondingly pointing opposite to the net polarization on each tetrahedron. For $\eta > 1$ (**(c)**) the ground state is the spin ice state of the pyrochlore lattice, with paramagnetic central spins which are decoupled from those at the vertices. **(e)** Finite temperature Ising phase diagram obtained from Monte Carlo simulations. $\bar{M}_t^I$, which distinguishes the various states, is defined in eq. (2.7). The data is taken from [166].

antiferromagnetic Ising model on the pyrochlore lattice (see section 1.2). The vertex spins of each tetrahedron must satisfy the 2-up/2-down (2:2) rule, but there is now an additional free spin variable occupying the central sites. This doubles the number of spin configurations allowed on a tetrahedron in the ground state to 12 and therefore, by Pauling's argument [11, 82], gives a residual entropy of $\ln(3)$ per tetrahedron.

In between the ferrimagnet and 2:2 state, from $1/3 < \eta < 1$, the ground state is where the vertex spins have either 3-up/1-down or 3-down/1-up single-tetrahedron configurations (3:1), with the corresponding central spins constrained to point antiparallel to the net moment of the vertex spins. There are 8 possible spin configurations satisfying this constraint, with a residual entropy of $\ln(2)$ per tetrahedron. Such 3:1 single tetrahedra configurations are the same as those discussed in section 1.3.3, where defects act as charges of the emergent field. In the presence of dipolar interactions in spin ice, these charges become monopoles of the magnetic field [49]. On the centred pyrochlore, the "monopoles" (they are *not* sources of a physical magnetic field) are stabilized in the ground state of a large region of the parameter space. They are disordered and have maximal density, with a monopole (either positive or negative) on each tetrahedron.

At, $\eta = 1$, the boundary of the 2:2 and 3:1 states, the ground state manifold contains all compatible combinations of 2:2 and 3:1 single-tetrahedron states, with a large residual entropy of $\ln(5)$ per tetrahedron. Here, the ground state manifold contains densities of monopoles from 0 to N_t, where N_t is the number of tetrahedra, albeit at a fine-tuned point in the parameter space.

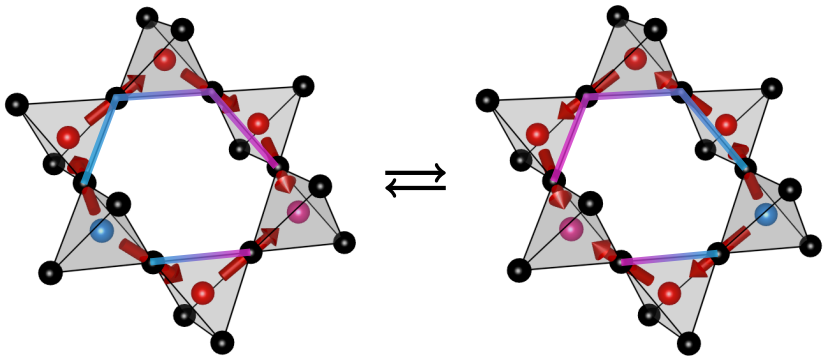

Figure 2.3: Example of a move which changes the parity of the winding number in the 3:1 ground state of the Ising model, c.f fig. 1.4. Cyan (pink) spheres represent a centre site with spin $-1(+1)$ and we use the spin ice convention for the spins at the vertices which are flipped during the move. All other spins remain unchanged. The move can be viewed as switching the direction of a pair of directed strings (highlighted) which begin and end on the same tetrahedra.

The 2:2 and 3:1 ground states can be distinguished by the topological nature of the respective ground state manifolds, characterized by a winding number or its parity respectively. For the 2:2 states, the central spins are entirely decoupled from the vertex spins so the $\mathrm{U}(1)$ topological nature of the spin ice ground state is preserved and topological ground state sectors are labelled by the winding numbers, $\mathbf{w} = (w_x, w_y, w_z)$, as discussed in section 1.3.2. However, in the 3:1 ground state, only their parity is conserved by non-winding operations, so one can instead define analogous $\mathbb{Z}_2$ topological invariants. An example of a non-winding operation which changes the winding number, yet remains in the 3:1 ground state, is shown in fig. 2.3. In general, any pair of strings of alternating vertex spins which begin and end on the same tetrahedra are now flippable, by flipping both of the centre spins at the beginning and end tetrahedra and all vertex spins in between. This is easiest to see in the spin ice representation, where the strings of alternating vertex spins become vectors pointing from and to the same tetrahedra.

As a result, the 2:2 and 3:1 ground states of the Ising model can be viewed as distinct classical topological spin liquids. Spin ice thin films also feature $\mathrm{U}(1)$ and $\mathbb{Z}_2$ spin liquids [165], as we discuss in section 2.4.2 there is a more explicit connection to such thin films as a consequence of the geometry of the centred pyrochlore lattice. In the case of spin ice thin films, the transition between topological spin liquids requires a change in sign of the orphan bonds, whereas here this transition can occur by tuning the ratio of exchange couplings. The different ground state manifolds of the Ising model as a function of γ also has important consequences for the quantum XXZ model, which we investigate in chapter 4.

Monte Carlo simulations of the Ising model [166], including a novel loop update based on moves of the form illustrated in fig. 2.3, find the finite temperature phase diagram in fig. 2.2(e), where the distinct states are distinguished by the average magnetization of the vertex spins on each tetrahedron,

$$\bar{M}_t^I = \frac{1}{N_t} \sum_t \left| \sum_v \sigma_{t,v} \right|. \tag{2.7}$$

These results are in agreement with the ground state phase diagram presented here, with no ordering detected in the putative spin liquid regimes. The specific heat and magnetization in the various states are very well reproduced by analytical Husimi tree calculations [167], which neglect the effect of closed loops on the lattice. It has been shown [101] that the thermodynamic properties of many frustrated Ising models are very well-approximated by Husimi calculations.

2.2.3 Degeneracy and Flat Bands

For the remainder of this chapter we focus on the case of Heisenberg spins, which we call the centred pyrochlore Heisenberg antiferromagnet (CPHAF). First of all, minimizing L_t on every tetrahedron immediately tells us that for $\eta \leq 1/4$, the ground state is the long-range ordered ferrimagnet, whereas for $\eta > 1/4$ the ground state is defined by the local constraint

$$L_t = 0 \tag{2.8}$$

for all tetrahedra. Let us consider how the form of this constraint restricts the possible ground states of the model. For a single tetrahedron, the degree of ferrimagnetic correlation decreases continuously as η is increased, from a saturated ferrimagnet at $\eta \leq 1/4$ to decoupled centre and vertex spins as $\eta \to \infty$. The corresponding Ising ground states, 4:0, 3:1, 2:2, form part of the Heisenberg ground state manifold at $\eta \leq 1/4$, $\eta = 1/2$ and $\eta \to \infty$ respectively. The degeneracy, D, of the ground state manifold may be estimated for $\eta \approx 1$ using the counting argument [83–85] discussed in section 1.2, yielding $D = 3N_t$. This is a higher degeneracy than the pyrochlore Heisenberg antiferromagnet (PHAF) ground state, where $D = N_t$, with the additional degeneracy arising from the degrees of freedom carried by the (fixed length) central spin.

Furthermore, the ground state degeneracy of a spin liquid can manifest itself in momentum space as degenerate flat bands, for example in the kagome [168] and pyrochlore [169] antiferromagnets, with 1 out of 3 and 2 out of 4 flat bands respectively. In the next section we show how both the generalized Luttinger-Tisza method and the rewriting of the Hamiltonian in terms of a connectivity matrix reveal the disordered state of the CPHAF is characterized by a ground state with 4 out of 6 flat bands. As a result, the ground state provides a high-dimensional manifold to which perturbations can be added to stabilize desired states, suggesting the centred pyrochlore lattice as an ideal platform for engineering exotic states of matter. Furthermore, this large degeneracy means that, at finite temperature, entropy can wash out the effect of perturbations, maintaining the behaviour of the

unperturbed $J_1 - J_2$ model, as is discussed for the addition of dipolar interactions in chapter 3.

Luttinger-Tisza method

The generalized Luttinger-Tisza (LT) method [170, 171] is a mean-field method to obtain the energy spectrum of a classical spin Hamiltonian in momentum space. To apply the LT, we first rewrite the Hamiltonian in Fourier space by introducing the momentum space spin variables

$$\mathbf{S}^{\mu}_{\mathbf{q}} = \frac{1}{\sqrt{N_{\mathrm{u.c}}}} \sum_{I} e^{-i\mathbf{q}\cdot(\mathbf{R}_I + \boldsymbol{\delta}_\mu)} \mathbf{S}^{\mu}_{I}, \tag{2.9}$$

where I labels the primitive unit cell, μ the sublattice of the spin and $N_{\mathrm{u.c}} = N/6$ is the number of primitive unit cells. This yields the Hamiltonian

$$\frac{H}{J_1} = \sum_{\mathbf{q}} \sum_{\mu,\nu} \mathrm{K}^{\mu\nu}_{\mathbf{q}} \mathbf{S}^{\mu}_{\mathbf{q}} \cdot \mathbf{S}^{\nu}_{-\mathbf{q}}, \tag{2.10}$$

with (Hermitian) coupling matrix

$$\mathrm{K}^{\mu\nu}_{\mathbf{q}}(\eta) = \begin{pmatrix} 0 & 0 & a_1 & a_2 & a_3 & a_4 \\ 0 & 0 & a_1^* & a_2^* & a_3^* & a_4^* \\ a_1^* & a_1 & 0 & c_{12} & c_{13} & c_{14} \\ a_2^* & a_2 & c_{12} & 0 & c_{23} & c_{24} \\ a_3^* & a_3 & c_{13} & c_{23} & 0 & c_{34} \\ a_4^* & a_4 & c_{14} & c_{24} & c_{34} & 0 \end{pmatrix} \tag{2.11}$$

and components

$$a_\mu = \frac{1}{2} e^{-i\mathbf{q}\cdot\boldsymbol{\delta}_\mu}, \qquad c_{\mu\nu} = \eta \cos(\mathbf{q} \cdot (\boldsymbol{\delta}_\mu - \boldsymbol{\delta}_\nu)) \tag{2.12}$$

In the standard LT method [170], the strong constraint, that the spin on each lattice site is normalized,

$$|\mathbf{S}_i|^2 = 1, \qquad \forall i, \tag{2.13}$$

is replaced by the weak constraint,

$$\sum_i |\mathbf{S}_i|^2 = \sum_{\mathbf{q}} \sum_{\mu} \mathbf{S}^{\mu}_{\mathbf{q}} \cdot \mathbf{S}^{\mu}_{-\mathbf{q}} = N, \tag{2.14}$$

where the normalization is only enforced on average. Diagonalizing $\mathrm{K}^{\mu\nu}_{\mathbf{q}}$, one can propose a ground state of the system by putting all of the weight from eq. (2.14) into the mode at momentum $\mathbf{q}$ which corresponds to the minimum eigenvalue. However, this state will only be a valid physical ground state of the system if it also respects equation (2.13). In models with inequivalent spins, as is the case here, this standard method often fails to find physical states.

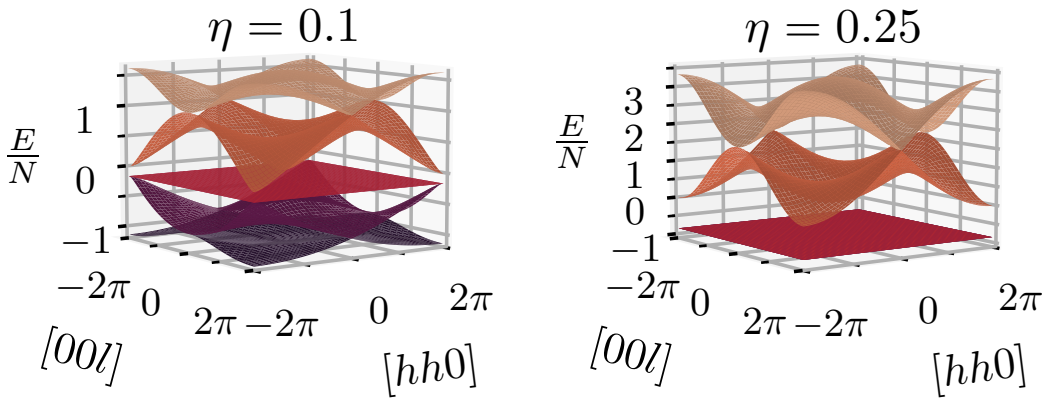

Figure 2.4: Energy spectrum obtained from the generalized LT method. For $\eta < 0.25$ (left), there is a unique ferrimagnetic ground state, corresponding to the band minimum at $\mathbf{q} = 0$. For $\eta \geq 0.25$ (right), the ground state is defined by a four-fold degenerate flat band with a gap to excitations.

Lyons and Kaplan realized [171] that this can be remedied by modifying eq. (2.14) to the form

$$\sum_I \sum_\mu \frac{|\mathbf{S}_I^\mu|^2}{\beta_\mu^2} = \sum_{\mathbf{q}} \sum_\mu \mathbf{t}_{\mathbf{q}}^\mu \cdot \mathbf{t}_{-\mathbf{q}}^\mu = N_{\text{u.c}} \sum_\mu \frac{1}{\beta_\mu^2}, \tag{2.15}$$

where we introduced the rescaled momentum space spin variables, $\mathbf{t}_{\mathbf{q}}^\mu = \mathbf{S}_{\mathbf{q}}^\mu / \beta_\mu$ and $\{\beta_\mu\}$ are sublattice dependent parameters.

Using Lagrange multipliers to incorporate the constraint in eq. (2.15) gives the condition that the state which minimizes the energy must satisfy the eigenvalue equation

$$\sum_\nu \mathrm{L}_{\mathbf{q}}^{\mu\nu} \mathbf{t}_{\mathbf{q}}^\nu = \lambda \mathbf{t}_{\mathbf{q}}^\mu, \tag{2.16}$$

with energy per unit cell

$$\epsilon = \lambda \sum_\mu \frac{1}{\beta_\mu^2}, \tag{2.17}$$

where the matrix $\mathrm{L}_{\mathbf{q}}^{\mu\nu} = \beta_\mu \beta_\nu \mathrm{K}_{\mathbf{q}}^{\mu\nu}$. As before, a candidate ground state can be found by placing all of the weight into the mode corresponding to the minimum eigenvalue (over all $\mathbf{q}$) of $\mathrm{L}_{\mathbf{q}}^{\mu\nu}$. But now the eigenvalues and eigenvectors of $\mathrm{L}_{\mathbf{q}}^{\mu\nu}$ depend on the $\{\beta_\mu\}$ so these can be tuned to ensure that the proposed ground state also satisfies eq. (2.13).

For our model, we make the ansatz

$$\beta_\mu = \begin{cases} 1, & \mu = a, b \\ \beta, & \mu = 1, ..., 4, \end{cases} \tag{2.18}$$

which means the matrices in the standard and generalized variants of the LT method are related by

$$\mathrm{L}^{\mu\nu}_{\mathbf{q}}(\beta,\eta) = \beta \mathrm{K}^{\mu\nu}_{\mathbf{q}}(\eta_{\text{eff}} = \beta\eta), \tag{2.19}$$

where $\mathrm{K}^{\mu\nu}_{\mathbf{q}}$ is evaluated for a rescaled effective η, dependent on the β we choose. For $0 < \eta < 1/4$, we recover the known ferrimagnetic ground state by setting $\beta = \sqrt{2/(1-3\eta)}$. On the other hand, for $\eta \geq 1/4$, an important observation is that at $\eta_{\text{eff}} = 1/\sqrt{2}$ the spectrum of $\mathrm{K}^{\mu\nu}_{\mathbf{q}}$ consists of a lower four-fold degenerate flat band and two higher dispersive bands. This degeneracy can be preserved in the spectrum of $\mathrm{L}^{\mu\nu}_{\mathbf{q}}$ for arbitrary η by choosing $\beta = 1/(\sqrt{2}\eta)$, ensuring

$$\mathrm{L}^{\mu\nu}_{\mathbf{q}}(\beta,\eta) \propto \mathrm{K}^{\mu\nu}_{\mathbf{q}}\left(\eta_{\text{eff}} = \frac{1}{\sqrt{2}}\right). \tag{2.20}$$

From eq. (2.17) one obtains the energy corresponding to the minimum eigenvalues

$$\frac{E}{J_1 N} = -\frac{1}{6\eta} - \frac{2\eta}{3}. \tag{2.21}$$

Comparing to eq. (2.4), we know that this is the ground state energy of the system for $\eta \geq \frac{1}{4}$. Therefore, assuming that eq. (2.13) can be satisfied by forming superpositions of the flat band modes, we have found physical ground states of the system. Note that in this construction β is continuous across the boundary at $\eta = 1/4$.

To summarize, for $\eta \geq 1/4$, the CPH ground state may be described in terms of a four-fold degenerate flat band. The full energy spectrum obtained using the generalized LT method is displayed in fig. 2.4. Besides the increased number of flat bands, there is a gap in the mean-field spectrum, whereas for the kagome [168] and pyrochlore [169] the spectrum is gapless.

Connectivity matrix

Here, we apply the method from [172, 173] to the centred pyrochlore lattice, which provides complementary evidence the ground state corresponds to a four-fold degenerate flat band for $\eta \geq 1/4$. The Hamiltonian in the form of eq. (2.4), can be rewritten in terms of an $N/3 \times N$ connectivity matrix, $\mathrm{A}_{t,n}$,

$$H = \frac{J_2}{2} \sum_{t=1}^{N/3} \sum_{n,m=1}^{N} \mathrm{A}_{t,n}\mathrm{A}_{t,m}\mathbf{S}_n \cdot \mathbf{S}_m, \tag{2.22}$$

where the constant term has been dropped. The elements of A are given by

$$\mathrm{A}_{t,n} = \begin{cases} 1, & \text{if } n \in \text{vertices of } t \\ \gamma, & \text{if } n \in \text{centre of } t \\ 0, & \text{otherwise.} \end{cases} \tag{2.23}$$

The labels n, m enumerate all sites of the lattice, whereas t enumerates the tetrahedra. The dimension of the null space of A imposes a limit on the number of zero modes of H and

thus on the number of flat bands. For $\eta \geq 1/4$ the minimum energy of H as written in eq. (2.22) is zero, so these zero modes make up the ground state. Since

$$\mathrm{rank(A)} \leq \frac{N}{3}, \tag{2.24}$$

the dimension of the null space,

$$\mathrm{Nullity(A)} \geq N - \frac{N}{3} = \frac{2N}{3}, \tag{2.25}$$

by the rank-nullity theorem [174, 175]. The dimension of a band in momentum space is $N/6$, so 4 out of 6 bands of the mean-field energy spectrum of the CPHAF must belong to the ground state.

2.3 Monte Carlo Simulations

Moving beyond mean-field methods, we use classical Monte Carlo (MC) simulations to obtain the phase diagram of the CPHAF, as well as to understand the properties of the different phases that we find. Our MC simulations are based off of the implementation in [176]. They were performed for cubic systems of $N = 24L^3$ spins, where L is the number of conventional unit cells along each Cartesian axis. We used a minimum of 10^5 thermalization and measurement sweeps, up to a maximum of 10^7 where necessary to compensate for longer autocorrelation times at low temperatures. Each MC sweep consisted of a sweep of single-spin overrelaxation [8, 177–179] and heatbath [8, 180, 181] updates through the entire lattice.

The implementation of these updates requires the computation of the effective local field experienced by each spin,

$$\mathbf{H}_i^H = J_1 \sum_{j \in \mathrm{nn(i)}} \mathbf{S}_j + J_2 \sum_{j \in \mathrm{nnn(i)}} \mathbf{S}_j, \tag{2.26}$$

so that $\mathbf{S}_i \cdot \mathbf{H}_i^H$ is the total energy of all terms involving the spin at site i according to eq. (2.3).

Equilibrium quantities computed during MC simulations include: magnetizations,

$$\mathbf{m}_k = \frac{1}{N_k} \langle \sum_{i \in k} \mathbf{S}_i \rangle, \tag{2.27}$$

where k may include all or a subset of spins on the lattice, a ferrimagnetic order parameter,

$$f = \langle \mathbf{m}_{\mathrm{centres}} \cdot \mathbf{m}_{\mathrm{vertices}} \rangle \tag{2.28}$$

which is -1 in the saturated ferrimagnet and 0 in a paramagnet, the nematic order parameter, $Q^{(2)}$, defined in [182], which measures quadrupolar moments, the magnetic susceptibility (per site)

$$\chi = \frac{N}{T} \left(\langle m_{\mathrm{all}}^2 \rangle - \langle m_{\mathrm{all}} \rangle^2 \right), \tag{2.29}$$

and specific heat (per site)

$$c = \frac{1}{NT^2}\Big(\langle E^2\rangle - \langle E\rangle^2\Big), \tag{2.30}$$

where E is the energy calculated according to eq. (2.3).

To probe spin correlations we also compute the structure factor

$$S(\mathbf{q})_k = \frac{1}{N_k}\sum_{i,j\in k} e^{i\mathbf{q}\cdot(\mathbf{r}_j-\mathbf{r}_i)}\langle \mathbf{S}(\mathbf{r}_i)\cdot\mathbf{S}(\mathbf{r}_j)\rangle, \tag{2.31}$$

where i, j are indices for the sites in the set k and N_k is the number of sites in k, as well as the structure factor of the effective field (eq. (1.10)),

$$E^{\alpha}_{\mu\nu}(\mathbf{q}) = \frac{1}{N_t}\sum_{I,J} e^{i\mathbf{q}\cdot(\mathbf{R}_J-\mathbf{R}_I)}\langle E^{\alpha}_{\mu}(\mathbf{R}_I)E^{\alpha}_{\nu}(\mathbf{R}_J)\rangle, \tag{2.32}$$

where I, J label the centres of the tetrahedra and $\alpha \in \{x, y, z\}$ the spin components.

2.3.1 Phase Diagram

The finite temperature phase diagram obtained from MC simulations is presented in fig. 2.5. In addition to the predicted disordered and ferrimagnetic regimes, simulations reveal a partially ferrimagnetically ordered state. Furthermore, the low temperature disordered regime of the model is characterized by two distinct correlation regimes. Some important thermodynamic quantities which distinguish the various low temperature states, as well as the spin structure factors in the disordered regimes are displayed in fig. 2.6.

The low temperature states we find are:

- **Ferrimagnet**, $0 < \eta \leq 1/4$:
  The state identified analytically in section 2.2.1, with saturated ferrimagnetic order as $T \to 0$, magnetization $m_{\text{all}} = \frac{1}{3}$ and $f = -1$. Low energy excitations about the ground state are transverse spin waves so the specific heat $c \to 1$ as $T \to 0$.

- **Partial Ferrimagnet (PF)**, $1/4 < \eta \lesssim 0.343(3)$:
  This phase is characterized by unsaturated ferrimagnetic order, $m_{all} < 1/3$ and $f > -1$, with both continuously approaching zero as η is increased. Fluctuations which preserve the local constraint are allowed, giving rise to zero modes which lower the heat capacity below 1 at the boundary ($\eta = 1/4$) and to $c = 1/2$ for $\eta > 1/4$. We also observe a low temperature Curie law, $\chi T = \text{const}$, a signature of a spin liquid [101], below the ordering transition. In the structure factor we do not observe any additional features beyond those associated with peaks at momenta corresponding to ferrimagnetic ordering. The coexistence of long-range order and fluctuations in the PF is superficially reminiscent of magnetic fragmentation in Coulomb spin liquids [183], however as we discuss in section 2.4 we do not expect an effective field description to capture this behaviour.

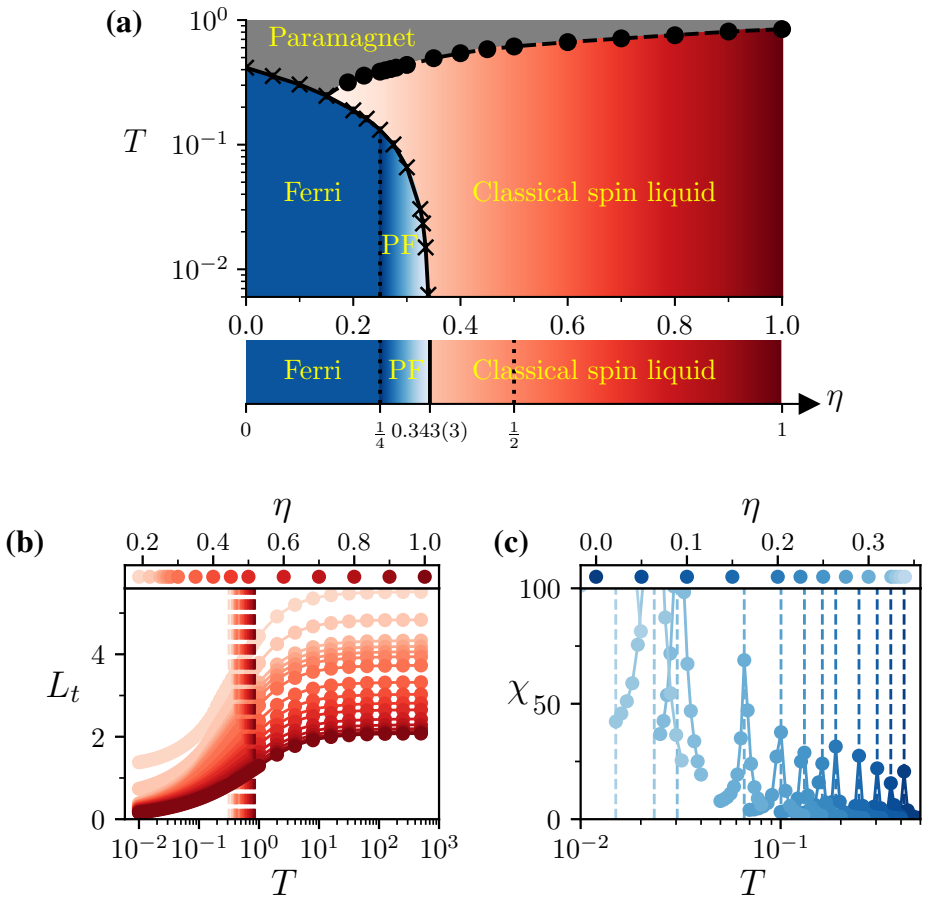

Figure 2.5: **(a)** (Upper) Finite temperature phase diagram of the antiferromagnetic $J_1 - J_2$ Heisenberg model obtained from MC simulations for $L = 14$. Circles are where $\partial L_t/\partial T$ is a maximum, see **(b)**, crosses where there is a peak in the susceptibility, see **(c)**. At $T = 0$, the ferrimagnetic (ferri) phase is characterized by saturated ferrimagnetic order, whereas the partial ferrimagnet (PF) remains unsaturated. In the spin liquid regime no ordering is observed for the temperatures simulated and the spin structure factor evolves continuously with η. (Lower) Approximate ground state phase diagram constructed using MC results at $T = 5 \times 10^{-3}$. **(b)** The local constraint, eq. (2.5), from MC simulations for $L = 14$ and various η, with interpolating curves and the position of the maximum of $\partial L_t/\partial T$ shown with dashed lines. **(c)** The susceptibility from MC simulations for $L = 14$ and various η. The locations of the maxima are shown by dashed lines.

- **Spin Liquid (SL)**, $\eta \gtrsim 0.343(3)$:
  We do not identify long range order in the magnetization or nematic order parameter, $Q^{(2)}$, nor do we find peaks in the specific heat or susceptibility. The susceptibility displays a Curie law crossover, where the low temperature Curie constant decreases continuously as η increases, reaching zero at $\eta = 0.5$, before again increasing continuously with η. As in the partial ferrimagnet, $c = 1/2$, indicative of the zero modes allowed by the local constraint. We can further distinguish two different regimes of the spin liquid by the spin structure factor. Firstly, for $0.343 \lesssim \eta \lesssim 0.5$,

the structure factor is characterized by broad maxima at momenta associated with ferrimagnetic ordering (fig. 2.6(d)), indicative of short range ferrimagnetic correlations in the ground state. Secondly, for $\eta \gtrsim 0.5$, diffuse broadened pinch points (bow ties) are the key features of the structure factor (fig. 2.6(e,f)). The width of these pinch points decreases as the pyrochlore limit, $\eta \to \infty$, is approached. These regimes of the structure factor evolve continuously into one another as η crosses 0.5.

We can qualitatively rationalize the location of the different correlation regimes in parameter space by inspecting the single tetrahedron configurations allowed by the local constraint in more detail. For $1/4 \leq \eta \leq 1/(2\sqrt{2})$ all vertex spins must have a component antiparallel to the central spin, as illustrated in fig. 2.7. Enforcing this on closed loops in the lattice would restrict the degree to which the central spins may deviate from pointing along a global direction, giving rise to long-range partial ferrimagnetic order. For $\eta > 1/(2\sqrt{2})$, a vertex spin may have a component parallel to the central spin. This would weaken the correlations between neighbouring central spins and could destroy any long-range order in the system. In MC simulations, extrapolating to the $L \to \infty$ limit at $T = 0.005$, the transition between the PF and SL occurs at $\eta = 0.343(3)$ (fig. 2.7(a)), not too far away from the predicted value of $\eta = 1/(2\sqrt{2}) \approx 0.354$. A similar effect could be responsible for the change in correlations across $\eta = 0.5$, with 1 or 2 vertex spins allowed components parallel to the central spin for $\eta < 0.5$ and $\eta > 0.5$ respectively.

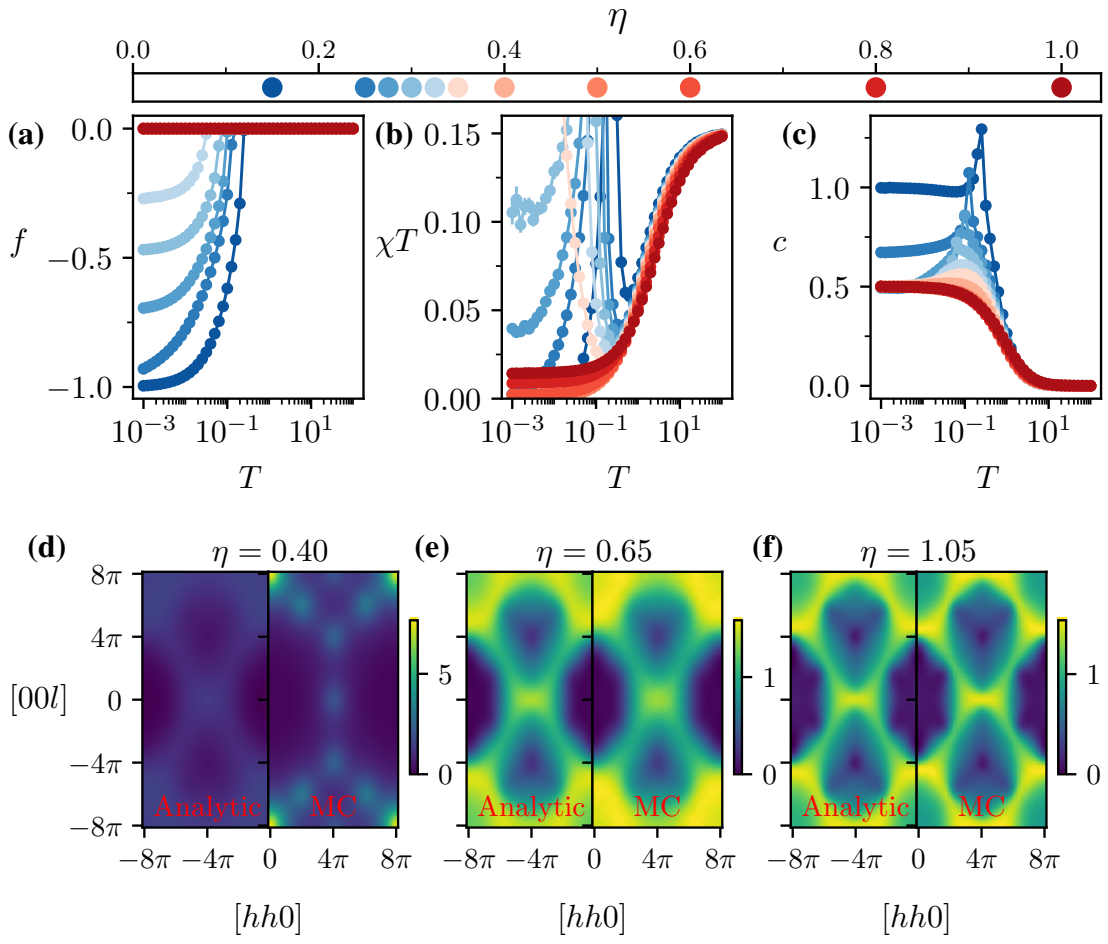

Figure 2.6: **(a-c)** MC results of bulk thermodynamic quantities for various η. **(a)** The ferrimagnetic order parameter (eq. (2.28)). In the range $0.25 \leq \eta \leq 0.325$ its (finite) $T \to 0$ value decreases continuously, until vanishing in the SL phase. **(b)** The susceptibility exhibits a low temperature Curie law, $\chi T = \text{const}$ for $\eta > 1/4$. The low T Curie constant decreases to zero at $\eta = 0.5$ before increasing again. **(c)** The specific heat, $c(T \to 0) \to 0.5$ for all $\eta > 1/4$, indicative of soft fluctuation modes about the ground state manifold. **(d-f)** Structure factors calculated from mean-field (eq. (2.39), left panels) and MC at $T = 0.005$ (right panels). For $\eta < 0.4$ (**(d)**), the mean-field calculation does not capture the broad maxima observed in MC. For $\eta > 0.5$ (**(e,f)**), the structure factor is characterized by broadened pinch points whose width decreases as η is increased.

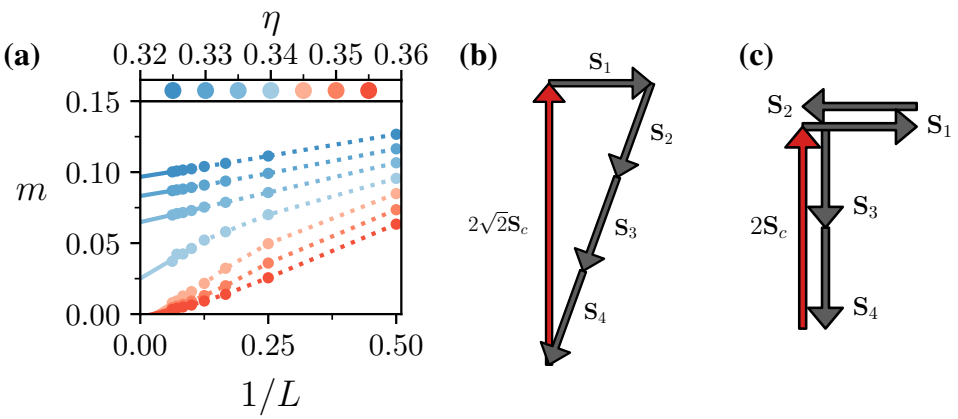

Figure 2.7: **(a)** Finite size scaling of magnetization at $T = 0.005$ for various η. The markers are MC results for system sizes $L = 2$ to 16, the solid lines a linear fit to the four largest system sizes. We see that $m \to 0$ in the infinite system size limit between $\eta = 0.34$ and 0.345. Therefore we take the phase boundary to be at $\eta = 0.343(3)$. **(b,c)** Diagrams representing the single tetrahedron spin configurations which satisfy eq. (2.8) for $\eta = 1/(2\sqrt{2})$, **(b)**, and $\eta = 1/2$, **(c)**, whilst allowing for one or two spins respectively to be perpendicular to the central spin. Increasing η decreases the effective central spin length, $\frac{1}{\eta}\mathbf{S}_c$, meaning that the perpendicular spins can acquire a finite component parallel to the direction of the centre spin, whereas decreasing η leads to a finite anti-parallel component for at least one of these spins. We propose this as a qualitative explanation for the different correlation regimes we observe in our MC simulations.

2.4 Spin Liquid

Having identified a large region of the phase diagram which hosts a disordered low temperature state, we now characterize its properties. MC calculations of the spin structure factor in the $\eta \gtrsim 0.5$ regime are characterized by broadened bow ties (fig. 2.8), related to the pinch points of the pyrochlore lattice. In this section we discuss how these correlations can be understood as the consequence of an emergent charge fluid in the Coulomb phase framework, or equivalently, as a higher-dimensional spin liquid restricted to a thin-film.

2.4.1 Mean-field Structure Factor

To calculate the ground state structure factor in the regime governed by the local constraint, we employ Henley's (mean-field) projection-based approach [87]. This method is equivalent to the lowest order of a large-N expansion (see for example [50] on the pyrochlore lattice) and was recently employed to distinguish classical spin liquids from a topological perspective [184].

We are interested in the regime where the ground state is defined by eq. (2.8), so restrict our attention to $\eta > 1/4$. On the centred pyrochlore lattice, taking the Fourier transform of eq. (2.5) yields

$$\mathbf{L}_x(\mathbf{q}) = \gamma \mathbf{S}_{c_x}(\mathbf{q}) + \sum_{m=1}^{4} e^{\pm i\mathbf{q}\cdot\boldsymbol{\delta}_m} \mathbf{S}_m(\mathbf{q}) = 0, \tag{2.33}$$

where $x = a, b$ labels the tetrahedra centred on the corresponding sublattice, with spin $\mathbf{S}_{c_x}$ occupying the centre site. The exponent takes positive (negative) sign for $x = a(b)$ and the second equality is the ground state constraint. This may be rewritten in vector form as

$$\mathbf{L}_x(\mathbf{q}) = \vec{L}_x(\mathbf{q}) \cdot \vec{S}(\mathbf{q}) = 0, \tag{2.34}$$

where

$$\begin{aligned} \vec{L}_a(\mathbf{q}) &= (\gamma, 0, e^{i\mathbf{q}\cdot\boldsymbol{\delta}_1}, e^{i\mathbf{q}\cdot\boldsymbol{\delta}_2}, e^{i\mathbf{q}\cdot\boldsymbol{\delta}_3}, e^{i\mathbf{q}\cdot\boldsymbol{\delta}_4})^T, \\ \vec{L}_b(\mathbf{q}) &= (0, \gamma, e^{-i\mathbf{q}\cdot\boldsymbol{\delta}_1}, e^{-i\mathbf{q}\cdot\boldsymbol{\delta}_2}, e^{-i\mathbf{q}\cdot\boldsymbol{\delta}_3}, e^{-i\mathbf{q}\cdot\boldsymbol{\delta}_4})^T, \\ \vec{S}(\mathbf{q}) &= (\mathbf{S}_{c_a}(\mathbf{q}), \mathbf{S}_{c_b}(\mathbf{q}), \mathbf{S}_1(\mathbf{q}), \mathbf{S}_2(\mathbf{q}), \mathbf{S}_3(\mathbf{q}), \mathbf{S}_4(\mathbf{q}))^T. \end{aligned} \tag{2.35}$$

The key object is the 6×2 matrix

$$\mathrm{E} = \begin{pmatrix} \vec{L}_a^* & \vec{L}_b^* \end{pmatrix}, \tag{2.36}$$

whose columns are the $\vec{L}_x^*$. Assuming weakly interacting spins, such that the probability distribution of spin configurations is Gaussian in the spin variables and enforcing equation eq. (2.34) by projecting onto the subspace orthogonal to the L_x^*, the structure factor is given by

$$\langle \mathbf{S}_\mu(-\mathbf{q}) \cdot \mathbf{S}_\nu(\mathbf{q}) \rangle = s_0^2 \mathrm{P}_{\mu\nu}(\mathbf{q}), \tag{2.37}$$

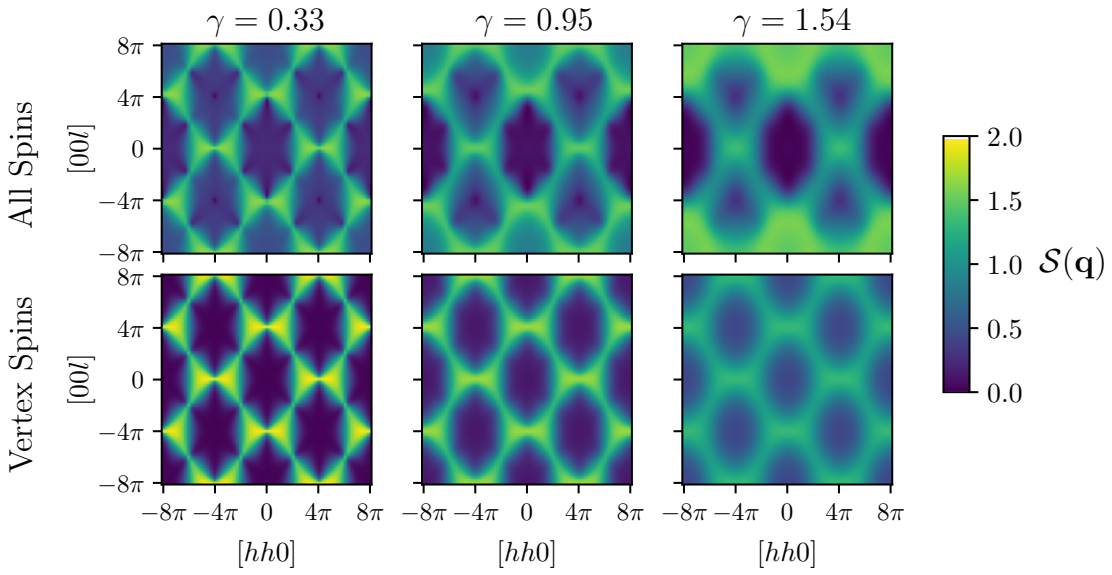

Figure 2.8: Spin structure factors computed from MC simulations for $L = 8$ at $T = 0.005$ for all spins (top) and only vertex spins (bottom). The structure factor of vertex spins shows a broadening of the bow tie features as γ is increased, as well as an increase in diffuse background intensity, with the structure factor for all spins additionally showing the emergence of new features. Adapted from [2].

where μ, ν label the sublattices, s_0^2 is a normalization constant and

$$\mathrm{P}_{\mu\nu}(\mathbf{q}) = \delta_{\mu\nu} - [\mathrm{E}(\mathrm{E}^\dagger\mathrm{E})^{-1}\mathrm{E}^\dagger]_{\mu\nu}. \tag{2.38}$$

Enforcing spin normalization on average, the structure factor over all sublattices (see eq. (2.31)) is

$$S(\mathbf{q}) = \frac{N_{\mathrm{u.c}}}{N}\sum_{\mu,\nu}\langle \mathbf{S}_\mu(-\mathbf{q})\cdot\mathbf{S}_\nu(\mathbf{q})\rangle = \frac{1}{\mathrm{Tr(P)}}M^T\mathrm{P}M, \tag{2.39}$$

where $M = (1,1,1,1,1,1)^T$.

Pinch point singularities may arise in the structure factor at the $\mathbf{q}$ where $\mathrm{E}^\dagger\mathrm{E}$ is singular. Since

$$\det(\mathrm{E}^\dagger\mathrm{E}) = (\gamma^2+4)^2 - \left|\sum_{m=1}^{4} e^{2i\mathbf{q}\cdot\boldsymbol{\delta}_m}\right|^2, \tag{2.40}$$

for any finite γ, $\det(\mathrm{E}^\dagger\mathrm{E}) \neq 0$ and thus we do not expect to find pinch point singularities in the structure factor on the centred pyrochlore lattice. This is confirmed by our MC simulations.

Since these mean-field structure factors correspond to $T = 0$, they are displayed alongside those from low T MC simulations in figs. 2.6(d-f). We find good agreement for $\eta > 0.5$, so expect that a long wavelength effective description is appropriate in this regime. Although

the structure factor here does not have sharp pinch points for any finite η, the finite width bow ties suggest a close connection to the 3D Coulomb phase on the pyrochlore lattice, which we explore in more detail in the next section. On the other hand, for $0.25 < \eta < 0.5$, we find mean-field deviates from MC; it cannot properly capture the short-range ferrimagnetic correlations which result from microscopically satisfying the local constraint. Nevertheless at intermediate temperature, $T \approx 0.5$, mean-field and MC are in good agreement for all relevant η, even in the $0.25 < \eta < 0.5$ regime, likely due to the large entropy of the long wavelength spin liquid. This crossover from long wavelength spin liquid to short-range ferrimagnetic correlations could also explain the bump in specific heat seen for these values of η around $T \approx 0.1$ in fig. 2.6(c) which indicates a loss in entropy.

2.4.2 Coulomb Physics

Charge Fluid Description

As discussed in section 1.3, spins on the pyrochlore lattice can be mapped to an effective field, with the local constraint

$$\mathbf{L}_t^{\mathrm{p}} = \sum_{v=1}^{4} \mathbf{S}_{t,v} = 0 \tag{2.41}$$

mapping to the coarse-grained divergence-free constraint

$$\nabla \cdot \mathbf{E}^{\alpha} = 0. \tag{2.42}$$

Now in the case of the centred pyrochlore lattice the ground state constraint, $\mathbf{L}_t = 0$, can be written as

$$\mathbf{L}_t^{\mathrm{p}} = -\gamma \mathbf{S}_{t,c}, \tag{2.43}$$

see eq. (2.5). What consequences would this have for the effective field picture?

Consider switching on a small, but finite, γ in the local constraint on only n "defect" tetrahedra, whilst maintaining $\gamma = 0$ on all others. Provided these defects are well separated, after coarse graining the central spins on the defects can be viewed as n charges

$$\nabla \cdot \mathbf{E}^{\alpha}(\mathbf{R}_t) = Q^{\alpha}(\mathbf{R}_t) \propto \pm\gamma S^{\alpha}(\mathbf{R}_t) \tag{2.44}$$

in each of the α channels with $-(+)$ on $a(b)$ tetrahedra. $Q^{\alpha} \in [-\gamma, \gamma]$ and therefore γ parametrizes the maximum charge strength. Now the low-energy picture is that of three copies of an emergent field coupled to scalar charges on diamond lattice sites. Following the same arguments for the pyrochlore, outlined in section 1.3.3, these charges will experience an entropic effective Coulomb interaction. Then arguments from Debye-Hueckel theory [92, 95, 96] tell us that the field correlations must be screened as $e^{-\kappa r}$ with $\kappa \propto \gamma$, as any charge in the system carries a factor of γ. In momentum space, this results in the pinch points acquiring a finite width parameterized by κ

$$E^{\alpha}_{\mu\nu}(\mathbf{q}) \propto \delta_{\mu\nu} - \frac{q_\mu q_\nu}{q^2 + \kappa^2}. \tag{2.45}$$

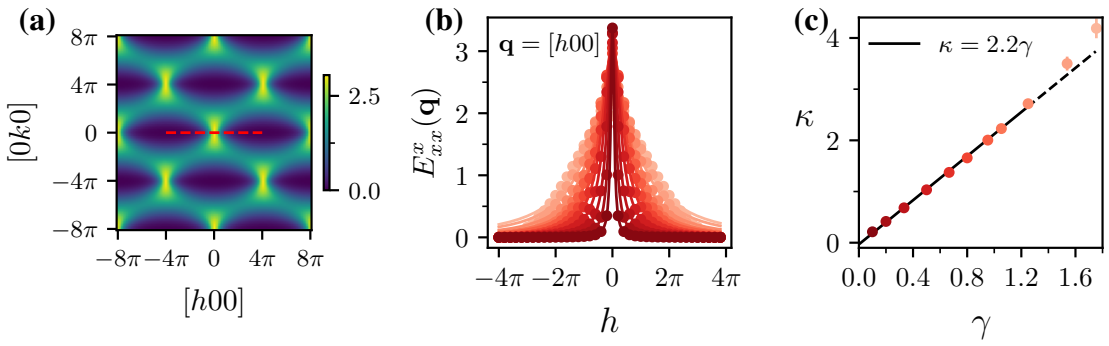

Figure 2.9: Computing the width of pinch points in $E^x_{xx}(\mathbf{q})$ from MC simulations. **(a)** The $E^x_{xx}(\mathbf{q})$ structure factor, eq. (2.32), as computed from MC for $\gamma = 0.67, T = 0.005$ in the $[hk0]$ plane. A cut is taken along the red line shown. **(b)** Fitting the Lorentzian in eq. (2.46) to the MC data for various γ (the same colour scheme is used in **(b)** and **(c)**). **(c)** κ which parametrizes the width of the pinch point against γ, with linear fit up to $\gamma = 1.25$. The linear relation is characteristic of a dilute charge fluid with charge strength parameterized by γ. Adapted from [2].

Remarkably when we compute the structure factor of the CPHAF in MC simulations and fit to the form

$$E^x_{xx}(q_x, q_y = 0, q_z = 0) = \frac{A}{q_x^2 + \kappa^2}, \tag{2.46}$$

wth A and κ fitting parameters, we find that $\kappa \propto \gamma$ over a large region of the parameter space, $0 < \gamma \lesssim 1.25$. These results are summarized in fig. 2.9. This is despite the fact that the centred pyrochlore lattice corresponds to taking the limit $n \to N_t$ and Debye-Hueckel theory is used to describe systems of *dilute* charges at high temperature. Here, there are charges, albeit with strength parametrized by γ, in at least one α channel on every tetrahedron (the effective temperature is a priori not known). The ground state can thus be viewed as the Heisenberg model variant of a monopole fluid in spin ice, studied in [185, 186]. This description does not impose any energetic constraints on the distribution of central spins, only accounting for how the central spins entropically rearrange themselves according to the effective electrostatic interactions between them. For small γ, we expect that all possible configurations of central spins will be allowed in the ground state. However for larger γ, certain configurations may no longer be energetically feasible and thus this view of the central spins as mobile charges will break down.

Analogy with pyrochlore thin films

Finite width pinch points have also been observed in the study of spin-ice thin-films [165], where they are attributed to a $\mathbb{Z}_2$ classical spin liquid, analogous to what we found for the Ising model on the centred pyrochlore. The connection between pyrochlore thin-films and the centred pyrochlore lattice can be clarified by mapping the centred pyrochlore to a slab of a 4D lattice of corner-sharing pentachora, which we term the pentachore lattice.

The slab geometry is obtained by shifting central sites of the $a(b)$ tetrahedra alternately

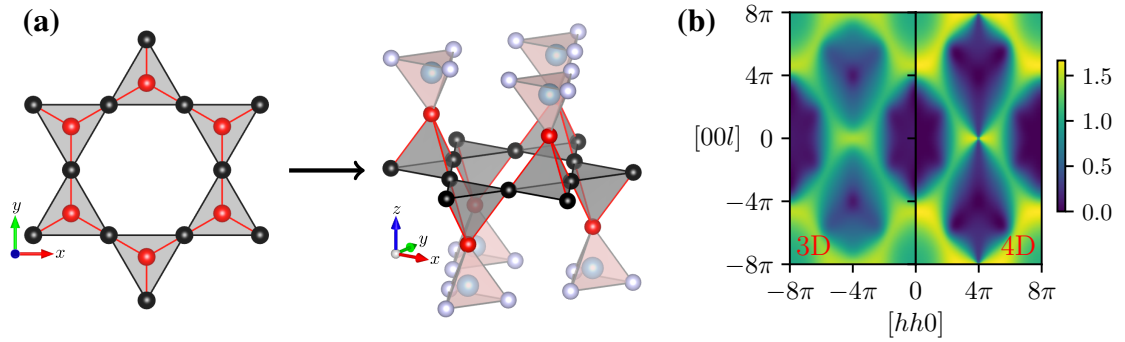

Figure 2.10: **(a)** Mapping of the 2D centred kagome lattice to a slab of the pyrochlore lattice in 3D, analogous to the mapping of the 3D centred pyrochlore lattice to a slab of the 4D pentachore lattice. Left: The centred kagome lattice made up of corner-sharing centred triangles. Right: The corresponding slab of the pyrochlore lattice. Bulk tetrahedra are grey, whereas the pink virtual tetrahedra above and below the slab host unordered surface charges (blue) in the spin liquid ground state. **(b)** Structure factor, $S(\mathbf{q})$, in the $[hhl0]$ plane calculated using the analytical mean-field calculation with $\eta = 1$ for the 3D centred pyrochlore lattice (left) and 4D pentachore lattice (right). The sharp pinch points on the 4D lattice along $[4\pi, 4\pi, l, 0]$ become broadened in the 3D case as pinch point singularities are not allowed by the symmetry of the 3D lattice.

by $\delta_t = +(-)\sqrt{5}/8$, whilst the vertex spins remain in the $t = 0$ hyperplane, where t is the additional Cartesian coordinate needed to describe the 4D space. Thus the slab has open boundaries at the $t = \pm\sqrt{5}/8$ edges. To illustrate the idea, the analogous 2D to 3D mapping from a centred kagome lattice to a slab of the pyrochlore lattice is shown in fig. 2.10(a). We study the connection between spin liquids on the centred kagome and pyrochlore lattices in more detail in the next section.

Returning to 4D, the slab can be generalized to a fully periodic pentachore lattice, specified by the positions

$$\mathbf{r}^{(4)}_{I,\mu} = \mathbf{R}^{(4)}_I + \boldsymbol{\delta}^{(4)}_\mu, \tag{2.47}$$

with lattice vectors

$$\mathbf{R}^{(4)}_I = n_1\mathbf{a}_1 + n_2\mathbf{a}_2 + n_3\mathbf{a}_3 + n_4\mathbf{a}_4, \tag{2.48}$$

where,

$$\mathbf{a}_1 = \frac{1}{2}\begin{pmatrix}1\\1\\0\\0\end{pmatrix},\ \mathbf{a}_2 = \frac{1}{2}\begin{pmatrix}1\\0\\1\\0\end{pmatrix},\ \mathbf{a}_3 = \frac{1}{2}\begin{pmatrix}0\\1\\1\\0\end{pmatrix},\ \mathbf{a}_4 = \frac{1}{4}\begin{pmatrix}-1\\-1\\-1\\\sqrt{5}\end{pmatrix}, \tag{2.49}$$

and basis vectors

$$\begin{gathered}\boldsymbol{\delta}_1^{(4)} = \frac{1}{8}\begin{pmatrix}1\\1\\1\\-\frac{1}{\sqrt{5}}\end{pmatrix},\ \boldsymbol{\delta}_2^{(4)} = \frac{1}{8}\begin{pmatrix}-1\\-1\\1\\-\frac{1}{\sqrt{5}}\end{pmatrix},\\ \boldsymbol{\delta}_3^{(4)} = \frac{1}{8}\begin{pmatrix}1\\-1\\-1\\-\frac{1}{\sqrt{5}}\end{pmatrix},\ \boldsymbol{\delta}_4^{(4)} = \frac{1}{8}\begin{pmatrix}-1\\1\\-1\\-\frac{1}{\sqrt{5}}\end{pmatrix},\ \boldsymbol{\delta}_c^{(4)} = \frac{1}{8}\begin{pmatrix}0\\0\\0\\\frac{4}{\sqrt{5}}\end{pmatrix}.\end{gathered} \tag{2.50}$$

Note that the pentachore lattice has a 5-site basis, as the sites which in the slab geometry can be identified with central sites of the centred pyrochlore lattice become equivalent in the translational sense and are shared between neighbouring pentachora.

What can we say about the ground state on the periodic pentachore lattice? The generalization of our model will have a ground state (for $\eta > \frac{1}{4}$) defined by an analogous local constraint to eqs. (2.5) and (2.8), on each pentachoron. Crucially, now *all* spins are shared between clusters centred on a bipartite lattice. We can modify the mean-field structure factor calculation to account for the pentachore lattice geometry by letting

$$\begin{gathered}\vec{L}_a(\mathbf{q}) = (\gamma e^{i\mathbf{q}\cdot\boldsymbol{\delta}_c^{(4)}}, e^{i\mathbf{q}\cdot\boldsymbol{\delta}_1^{(4)}}, e^{i\mathbf{q}\cdot\boldsymbol{\delta}_2^{(4)}}, e^{i\mathbf{q}\cdot\boldsymbol{\delta}_3^{(4)}}, e^{i\mathbf{q}\cdot\boldsymbol{\delta}_4^{(4)}})^T,\\ \vec{L}_b(\mathbf{q}) = (\vec{L}_a(\mathbf{q}))^*,\\ \vec{\mathbf{S}}(\mathbf{q}) = (\mathbf{S}_c(\mathbf{q}), \mathbf{S}_1(\mathbf{q}), \mathbf{S}_2(\mathbf{q}), \mathbf{S}_3(\mathbf{q}), \mathbf{S}_4(\mathbf{q}))^T,\end{gathered} \tag{2.51}$$

where $(\dots)^*$ is the element-wise complex conjugate and redefining the E matrix accordingly. Now

$$\det(\mathrm{E}^\dagger\mathrm{E}) = (\gamma^2+4)^2 - \left|\gamma^2 e^{2i\mathbf{q}\cdot\boldsymbol{\delta}_c^{(4)}} \sum_{m=1}^{4} e^{2i\mathbf{q}\cdot\boldsymbol{\delta}_m^{(4)}}\right|^2, \tag{2.52}$$

which vanishes at certain $\mathbf{q}$, where the structure factor may exhibit singularities. Therefore we see that the symmetry of the centred pyrochlore lattice (equivalent to a pentachore slab) does not allow for sharp pinch points in the structure factor, whilst they are present for the fully periodic 4D pentachore lattice. A comparison of the structure factor in both cases is displayed in fig. 2.10(b).

The sharp pinch points on the pentachore lattice suggest that there is a description of the ground state in terms of a 4D Coulomb phase. Indeed, one can define such a Coulomb phase in terms of a four-component vector field which is the higher dimensional version of $\mathbf{E}^\alpha$ (eq. (1.10)). We introduce an orientation for the field with the unit vectors

$$\hat{\mathbf{u}}_\mu^{(4)} = 2\sqrt{5}\,\boldsymbol{\delta}_\mu^{(4)}, \qquad \mu = 1,2,3,4,c, \tag{2.53}$$

and then define the four-component vector field

$$\mathbf{E}^\alpha(\mathbf{R}_p^{(4)}) = \gamma\hat{\mathbf{u}}_c^{(4)} S^\alpha(\mathbf{R}_p^{(4)} \pm \boldsymbol{\delta}_c^{(4)}) + \sum_{m=1}^{4} \hat{\mathbf{u}}_m^{(4)} S^\alpha(\mathbf{R}_p^{(4)} \pm \boldsymbol{\delta}_m^{(4)}), \tag{2.54}$$

at the centre of each pentachoron, $\mathbf{R}_p^{(4)}$, for each spin component, $\alpha \in \{x, y, z\}$, with $\pm = +(-)$ for $a(b)$ pentachora. Note that the $E_x^\alpha, E_y^\alpha, E_z^\alpha$ vector components of the $\mathbf{E}^\alpha = (E_x^\alpha, E_y^\alpha, E_z^\alpha, E_t^\alpha)$ field are proportional to the corresponding components of the 3D field. After coarse-graining, the ground state constraint, eq. (2.8), becomes

$$\mathrm{div}(\mathbf{E}^\alpha(\mathbf{r}^{(4)})) = 0. \tag{2.55}$$

Following the same arguments as for the pyrochlore we expect sharp pinch points in the structure factor and a $1/r^4$ decay of correlations in real space. Defects would interact via a $1/r^2$ effective Coulomb potential; the effective theory for dilute defects is 4D electrostatics.

Returning to the pentachore slab, this can be viewed as the thinnest possible thin film which keeps both a and b pentachora of the lattice intact. Therefore, we can understand the properties of the ground state of the Heisenberg model on the centred pyrochlore lattice in a similar way to the spin ice thin films studied by Lantagne-Hurtubise, Rau and Gingras (L-HRG) in [165]. There, the authors considered various geometries of thin films of nearest neighbour spin ice, also including so-called orphan bonds; bonds at the surface which do not belong to a bulk tetrahedron, but instead can be thought of as belonging to a fictitious virtual tetrahedron. In our case, the central spins lie on the surface in the slab geometry, they not only belong to a bulk pentachoron but are also the single spin of a virtual pentachoron, see fig. 2.10(a). As a result, the closest analogue to the pentachore slab (albeit in 3D rather than 4D) studied in [165] is the $[001]$ thin-film with orphan bonds set to zero. For such systems, L-HRG showed that at low T the structure factor will also be characterized by finite width pinch points, which they argue is the result of fluctuating surface charges on the virtual tetrahedra. In our model, the flux entering/exiting a virtual pentachoron is γS_c^α, so is a continuous variable in $[-\gamma, \gamma]$. Note that due to the spin length constraint on a Heisenberg spin, there must be non-zero flux entering each bulk pentachoron in at least one of the α channels. Therefore we would also expect these fluctuating surface charges to destroy the Coulomb phase, with a screening length proportional to γ, as seen in our MC simulations.

The descriptions in terms of surface charges in higher dimensions or bulk charges as presented in the previous section describe the same effect. On the microsopic level, a spin at a surface or centre belongs only to a single (bulk) unit and therefore is less constrained than a spin shared between two corner-sharing units, modifying the allowed spin correlations in the ground state manifold in such a way as to destroy the Coulomb phase. The analogy between thin films and centred lattices can be useful in considering how to induce a desired effect in either system through the addition of perturbations as well as giving insight into the physics described by the bare Hamiltonian.

2.5 Centred Kagome Lattice

The mechanisms discussed on the centred pyrochlore lattice, whereby the central spins act as mobile sources of flux, should also apply to other lattices made up of suitable corner-

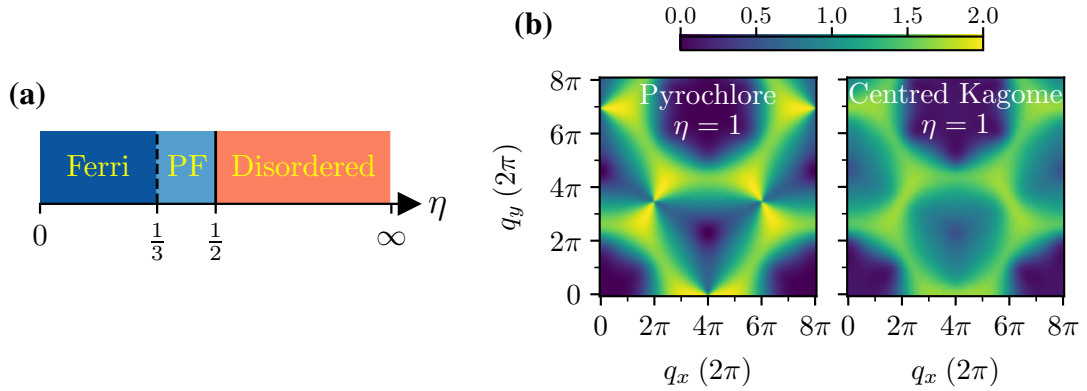

Figure 2.11: **(a)** Approximate zero temperature phase diagram for the $J_1 - J_2$ model on the centred kagome lattice, obtained from low temperature MC simulations and rewriting the Hamiltonian in terms of the local constraint. MC simulations find an analogous partial ferrimagnetic (PF) state to that on the centred pyrochlore in addition to the expected ferrimagnetic and disordered regimes. **(b)** Comparison of the structure factor of the nearest neighbour Heisenberg model on the pyrochlore lattice (left, computed using the mean-field calculation in [87]) and the centred kagome lattice (right, computed from MC at $T = 0.02$ for a system size of $L = 48$). The sharp pinch points on the pyrochlore become broadened upon reducing the dimension to the centred kagome lattice.

sharing centred clusters, regardless of dimensionality or number of spins making up the cluster. Therefore, we also investigate the Hamiltonian, eq. (2.3), on the 2D analogue of the centred pyrochlore lattice, the centred kagome lattice (fig. 2.10(a)). Here, an additional site at the centre of each triangular unit of the kagome lattice is coupled to the vertex spins by J_1 and the vertex spins are mutually coupled by J_2.

The centred kagome lattice is defined by the position vectors

$$\mathbf{r}^{(2)}_{i,\mu} = \mathbf{R}^{(2)}_i + \boldsymbol{\delta}^{(2)}_\mu, \tag{2.56}$$

where $\mathbf{R}^{(2)}_i = n_1\mathbf{a}^{(2)}_1 + n_2\mathbf{a}^{(2)}_2$, with the triangular lattice vectors $\mathbf{a}^{(2)}_1 = \frac{1}{2}(1, -\sqrt{3})$, $\mathbf{a}^{(2)}_2 = \frac{1}{2}(-1, -\sqrt{3})$ and integer n_1, n_2. We choose units of $\left|\mathbf{a}^{(2)}_1\right| = \left|\mathbf{a}^{(2)}_2\right| = 1$. The lattice has a 5-site basis of

$$\boldsymbol{\delta}^{(2)}_a = \begin{pmatrix} 0 \\ 0 \end{pmatrix}, \qquad \boldsymbol{\delta}^{(2)}_b = \begin{pmatrix} 0 \\ \frac{1}{\sqrt{3}} \end{pmatrix}, \tag{2.57}$$

$$\boldsymbol{\delta}^{(2)}_1 = \begin{pmatrix} 0 \\ \frac{1}{2\sqrt{3}} \end{pmatrix}, \qquad \boldsymbol{\delta}^{(2)}_2 = \begin{pmatrix} \frac{1}{4} \\ \frac{-1}{4\sqrt{3}} \end{pmatrix}, \qquad \boldsymbol{\delta}^{(2)}_3 = \begin{pmatrix} \frac{-1}{4} \\ \frac{-1}{4\sqrt{3}} \end{pmatrix}.$$

Sites labelled by $a(b)$ occupy the centre of up (down) triangles. As for the centred pyrochlore, the Hamiltonian may be rewritten in the form of eq. (2.4), which gives rise to the ground state constraint

$$L^{\mathrm{CK}}_t = 0, \qquad \forall t \tag{2.58}$$

for $\eta \geq 1/3$, where

$$\mathbf{L}_t^{\mathrm{CK}} = \gamma \mathbf{S}_{t,c} + \sum_{v=1}^{3} \mathbf{S}_{t,v}, \tag{2.59}$$

with t now labelling centred triangular units. For $\eta \leq 1/3$, the energy is minimized by the ferrimagnetic state. Furthermore, finite size MC simulations find a partial ferrimagnetic state, analogous to that seen on the centred pyrochlore, at low temperatures. Like the mapping from the 3D centred pyrochlore lattice to the 4D pentachore slab, one can map the 2D centred kagome lattice to a slab of the 3D pyrochlore lattice, as shown in fig. 2.10(a). This is done by considering the centred kagome lattice as occupying the $z = 0$ plane of a 3D space, then shifting the central sites alternately up (down) to $z = +(-)1/\sqrt{6}$. Thus the centred triangles become tetrahedra and we have a pyrochlore slab with open boundaries at the $z = \pm 1/\sqrt{6}$ edges, which is the thinnest possible thin-film geometry keeping both a and b tetrahedra intact. Adapting the mean-field calculations of section 2.4.1 to the centred kagome,

$$\begin{aligned} \vec{L}_a(\mathbf{q}) &= (\gamma, 0, e^{i\mathbf{q}\cdot\boldsymbol{\delta}_1^{(2)}}, e^{i\mathbf{q}\cdot\boldsymbol{\delta}_2^{(2)}}, e^{i\mathbf{q}\cdot\boldsymbol{\delta}_3^{(2)}}), \\ \vec{L}_b(\mathbf{q}) &= (0, \gamma, e^{-i\mathbf{q}\cdot\boldsymbol{\delta}_1^{(2)}}, e^{-i\mathbf{q}\cdot\boldsymbol{\delta}_2^{(2)}}, e^{-i\mathbf{q}\cdot\boldsymbol{\delta}_3^{(2)}}), \end{aligned} \tag{2.60}$$

and therefore

$$\det(\mathrm{E}^\dagger \mathrm{E}) = (\gamma^2 + 3)^2 - \left| \sum_{m=1}^{3} e^{2i\mathbf{q}\cdot\boldsymbol{\delta}_m^{(2)}} \right|^2, \tag{2.61}$$

which is non-zero for any finite γ. Therefore the disordered state will not have any singularities in the structure factor, as we would expect from the arguments of previous sections. This is confirmed by our MC simulations on the centred kagome lattice where we find broadened pinch points in the structure factor, as shown in fig. 2.11(b). Thus, we see that the picture of central spins acting as mobile sources of flux in the effective low energy field theory is not unique to the centred pyrochlore lattice.

2.6 $\mathsf{J}_1 - \mathsf{J}_2 - \mathsf{J}_3$ Model

Returning to the centred pyrochlore lattice, we now investigate the possibility to realize different states of matter by applying perturbations to the bare $J_1 - J_2$ Hamiltonian, targeting specific regions of the degenerate ground state manifold. In particular, we consider the effect of a J_3 term coupling third nearest neighbours, i.e centre spins on adjacent tetrahedra.

2.6.1 Ferromagnetic J_3

After the addition of a ferromagnetic J_3 the ground state manifold is made up of states with ferromagnetic centre spins and vertex spins correspondingly satisfying the local constraint.

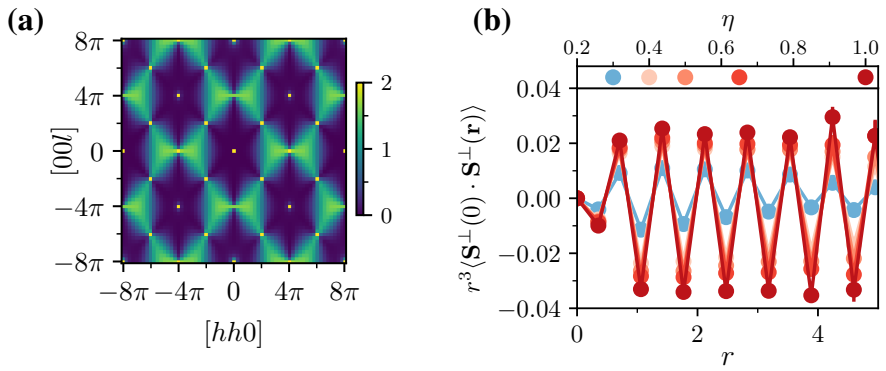

Figure 2.12: **(a)** Structure factor for $\eta = 0.4$, $J_3 = -0.1$ at $T = 0.001$ computed from MC. The colour scale is restricted to a maximum of 2 to show the coexistence of Bragg peaks from long-range ordering of the centre spins and pinch points from the vertex spins. The width of the pinch points continues to decrease with temperature up to the resolution allowed by the finite system size. **(b)** Real space spin correlations (for perpendicular spin components to the ordering axis) computed from MC in the $[110]$ direction at $T = 0.001$. They decay as $1/r^3$ for all η shown, except at $\eta = 0.3$, where we are not able to access low enough temperatures in our simulations.

Selecting the $\hat{\mathbf{z}}$ direction as that along which the centres are aligned, the local constraint can be rewritten as

$$\sum_{v=1}^{4} \begin{pmatrix} S_v^x \\ S_v^y \\ S_v^z + \frac{\gamma}{4} \end{pmatrix} = \sum_{v=1}^{4} \tilde{\mathbf{S}}_v = 0, \tag{2.62}$$

such that the rescaled vertex spins, $\tilde{\mathbf{S}}_v$ can be mapped to the usual divergence-less field of the 3D Coulomb phase (eq. (1.10)). The structure factor of $\tilde{\mathbf{S}}_v$ should then yield sharp pinch points as well as a $1/r^3$ algebraic decay in real space. This is verified in MC simulations, by calculating the structure factor

$$S^\perp(\mathbf{q}) = \frac{1}{N} \sum_{i,j} \mathbf{S}_i^\perp \cdot \mathbf{S}_j^\perp e^{i\mathbf{q}\cdot(\mathbf{r}_i - \mathbf{r}_j)}, \tag{2.63}$$

where $\mathbf{S}_i^\perp = (S_i^x, S_i^y)^T$ and the orientation of the axes is chosen such that $\hat{\mathbf{z}} = \hat{\mathbf{m}}_{\text{centres}}$ for each spin configuration sampled. We find sharp pinch points for all $\eta > 0.3$ simulated. The full structure factor, eq. (2.31), for $\eta = 0.4$ is presented in fig. 2.12(a), showing the coexistence of Bragg peaks and pinch points. Considering the local constraint, we would expect sharp pinch points to persist all the way down to $\eta = 1/4$, but the lower temperature required to enter the Coulomb phase at low η and the reduced weight in the perpendicular spin components, makes their observation challenging as this limit is approached. Furthermore, we also calculate the real space spin correlations for perpendicular spin components and find the characteristic $1/r^3$ decay expected for a 3D Coulomb phase, as shown in fig. 2.12(b).

This recovery of the Coulomb phase can be easily understood in the effective field theory picture. When the central spins order ferromagnetically they form a perfect zinc blende

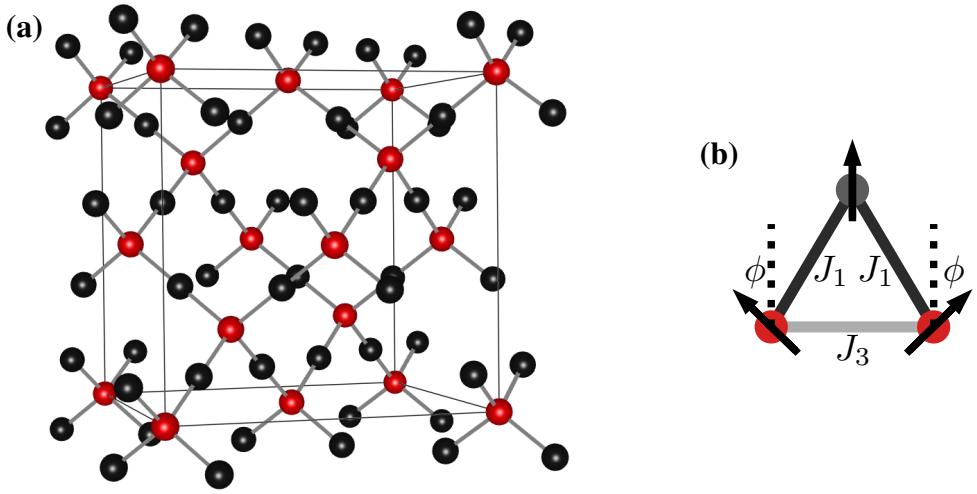

Figure 2.13: **(a)** The centred pyrochlore lattice with only J_1 bonds shown, J_3 bonds couple nearest neighbour centres (red) sites. **(b)** The basic frustrated unit of the antiferromagnetic $J_1 - J_3$ model on the centred pyrochlore lattice. For $\frac{J_3}{J_1} > \frac{1}{2}$ the ground state is that shown with the angle between centre spins (red) and their shared vertex spin (grey) given by $\cos\phi = -\frac{J_1}{2J_3}$.

charge crystal in the z channel with charges $Q^z = \pm\gamma$ on alternating diamond sublattices. This leaves the x and y channels of the effective field with no charges, therefore restoring the divergence-free condition of the 3D Coulomb phase. This is analogous to the situation in spin ice thin films where one can stabilize the 2D Coulomb phase by inducing ordering in the surface charges [164, 165].

2.6.2 Antiferromagnetic J_3

Taking antiferromagnetic J_3 introduces additional frustration into the model as J_1 and J_3 bonds cannot be simultaneously satisfied, J_1 bonds connecting a pair of centre sites through an intermediate vertex spin favours ferromagnetic order of the centres, whereas J_3 favours Néel order. For $J_2 = 0$ one can think of the lattice as a singly decorated diamond lattice, where the basic frustrated unit can be represented as a triangle, see fig. 2.13. Minimizing the energy on a single triangle, the ground state is the same ferrimagnetic state as in the $J_1 - J_2$ model for $\frac{J_3}{J_1} \leq 1/2$, whereas for $J_3/J_1 > 1/2$ the ground state is the canted state shown (fig. 2.13(b)), with the angle between the centres and their shared vertex spin given by $\cos\phi = -J_1/(2J_3)$. In the limit $J_3/J_1 \to \infty$ this becomes a state with Néel ordered centre sites which are decoupled from the vertex sites.

On the full lattice, the ferrimagnetic state remains the ground state, however for the canted state the spiral order of the centre spins must be commensurate with closed loops on the lattice to guarantee it remains a ground state. This requires that $N_{loop}\phi = \pi n$ where N_{loop} is the number of centre sites in a given loop. For example, considering only the shortest hexagonal loops, a commensurate spiral order of the centre sites is obtained at $\phi = 2\pi/3$ and $5\pi/6$, corresponding to $J_3/J_1 = 1$ and $J_3/J_1 = 1/\sqrt{3}$ respectively. The

difference in energy between the Nèel $J_3/J_1 \to \infty$ ground state and the canted state is $E_N - E_c = J_1^2/J_3$. Therefore for large but finite J_3 the energy difference is small. Combined with the fact that commensurate spiral orders will not be possible on hexagonal loops for large J_3/J_1, this leaves the state with Nèel ordered centres as the likely ground state.

Returning to the $J_1 - J_2 - J_3$ model and assuming Nèel ordered centre sites, the effective field felt by a vertex spin from its two neighbouring centre spins exactly cancels, and therefore vertices become decoupled from centres. As a consequence, the lowest energy configuration is achieved when the vertices satisfy the usual pyrochlore local constraint, eq. (2.41). Therefore the vertex spins should realize the usual 3D Coulomb phase, which unlike in the ferro J_3 case does not require any rescaling of the spins. In MC simulations, we find a state with Neel ordered centres and vertex spins satisfying the pyrochlore local constraint as $T \to 0$ (down to $T = 10^{-3}$) for a system size of $L = 4$ and $J_3 = 10$. However, upon increasing the system size, it becomes challenging to thermalize the MC simulations at low temperature. More experimentally relevant would be a *small* antiferromagnetic J_3, however MC simulations also struggle to thermalize in this case, so we were unable to identify which ground states such a perturbation would favour in the thermodynamic limit.

2.7 Summary and Outlook

Using a combination of analytical arguments, mean-field calculations and MC simulations we have outlined many of the key features of the antiferromagnetic $J_1 - J_2$ Heisenberg model. The model exhibits a competition between ferrimagnetism on the one hand and the Coulomb physics of the pyrochlore on the other, tuned by the coupling ratio $\eta = J_2/J_1$. This gives rise to ordered, partially ordered and disordered low temperature states. The disordered spin liquid can be understood up to $\gamma \approx 1.25$ as a dilute emergent charge fluid, where the central spins act as mobile sources of flux which are screened by the effective field of the corner spins. Alternatively, one can view the centred pyrochlore lattice as a thin film of a four-dimensional pentachore lattice with flux entering from the boundaries, resulting in the same effect. Combined with the knowledge of the Ising model which we have discussed, this provides the starting point for understanding magnetic materials on the centred pyrochlore lattice. The highly degenerate nature of the ground state manifold, combined with the emergent charge picture, suggests it is an ideal platform for engineering exotic states of matter, particularly those with an interplay between order and low-temperature fluctuations, as we showed with the addition of a J_3 term.

Going forwards, there remain some open questions to fully characterize the low temperature states of the CPHAF. First of all, we do not have a precise understanding of how the local constraint gives rise to the partial ferrimagnetic state out of the spin liquid manifold, as well as the ferrimagnetic correlations for $\eta < 0.5$. A microscopic understanding, for

example through an effective model on the diamond lattice which models how to satisfy the local constraint on closed loops in the lattice, is likely the key. For $\eta < 0.8$ the effective description in terms of a dilute fluid of charges begins to break down; a correct description would probably have to incorporate the energetic constraints on central spin configurations, as well as corrections to the Debye-Hueckel theory arising from the fact that the charge density becomes large. In the regime characterized by broadened pinch points and in light of the $\mathbb{Z}_2$ nature of the Ising ground state over a broad range of η, future work could investigate whether the CPHAF realizes a $\mathbb{Z}_2$ classical Heisenberg spin liquid as introduced in [187].

Chapter 3

Dipolar Interactions and [Mn(ta)$_2$]

We now turn to understanding the low temperature magnetic properties of the metal-organic framework material [Mn(ta)$_2$]. First, we describe the basic properties of [Mn(ta)$_2$], before justifying that an appropriate model to investigate is the antiferromagnetic $J_1 - J_2$ classical Heisenberg model with the addition of dipolar interactions. We then compare the results of magnetization measurements at temperatures above its ordering transition ($T_c = 0.43\,\mathrm{K}$) to Monte Carlo simulations, revealing that measurements at T above $1\,\mathrm{K}$ are consistent with the emergent charge fluid identified in the previous chapter. The specific heat, which must be modelled using quantum spins, is also consistent with these parameters. At these temperatures, the dipolar interactions have very little effect, however, at lower temperatures ($T_d = 0.25\ \mathrm{K}$), they induce ordering in our model. We characterize this order and show that the inclusion of dipolar interactions qualitatively reproduces specific heat and magnetization measurements in the regime $0.4\,\mathrm{K} < T < 1\,\mathrm{K}$. Furthermore, using mean-field calculations we show that the ordering in the model is robust when increasing the cut-off radius of dipolar interactions. This chapter closely follows [2] with some figures directly reproduced. It includes additional information on how theoretical and experimental results were compared, as well as more details on the effects of dipolar interactions in the model.

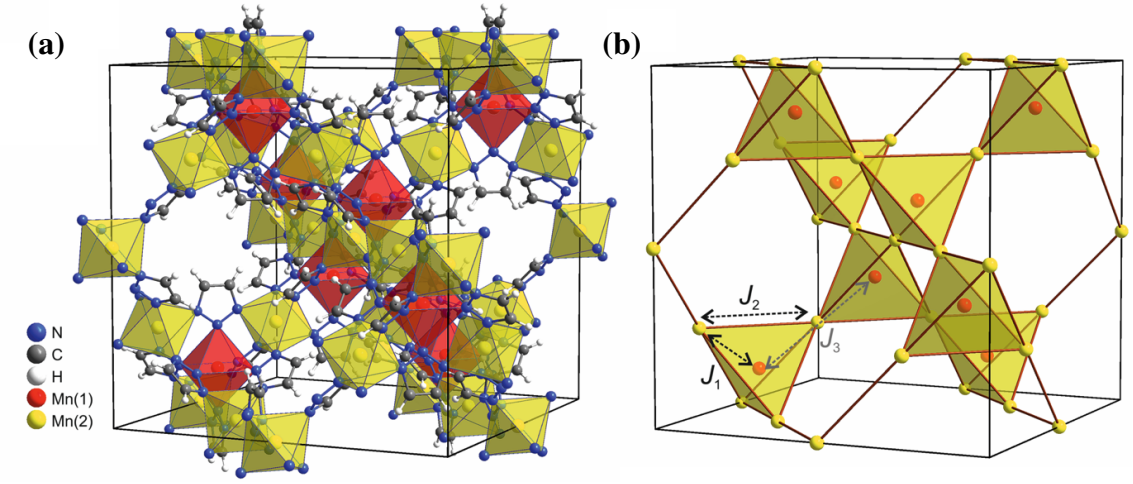

Figure 3.1: Structure of [Mn(ta)$_2$]. **(a)** The full chemical structure. All Mn ions are octahedrally coordinated by the ligands. The three N atoms of the triazolate ligand bind to three separate Mn ions, creating the centred pyrochlore structure. **(b)** The same portion of the lattice but with only Mn ions displayed, which form a centred pyrochlore lattice. The first three nearest neighbours are indicated. Adapted from [2].

3.1 [Mn(ta)$_2$] and the Heisenberg + dipolar model

The material in question belongs to a family of metal-azolate frameworks [M(II)(ta)$_2$], where M(II)=M^{2+} is a charge $+2$ transition metal ion and H-ta = 1H-1,2,3-triazole, which deprotonates to form a charge -1 triazolate ion [188]. The triazolate ligand in these materials is tridentate, each of the three N atoms bond to distinct M ions, which generally results in the formation of M-centred tetrahedra of M ions, as shown in fig. 3.1(a). On the larger scale, this leads to a structure where the M ions have the same network topology as the centred pyrochlore lattice, however there may be structural distortions (as seen in [Cu(ta)$_2$] [189]. Despite the possibility to study magnetic frustration in lattices closely related to the pyrochlore, the study of their magnetic properties remains limited [188–192], largely due to the difficulty in engineering strong magnetic interactions in these materials [127].

We choose to focus on M(II)=Mn(II) which has the electronic structure [Ar]3d^5. Since the Mn ions are octahedrally coordinated, they experience a cubic crystal field. Assuming a high spin configuration, each of the valence d orbitals (split into t_{2g} and e_g sets) are filled with a single unpaired electron, resulting in an effective $S = 5/2$ magnetic moment. X-ray diffraction measurements down to $T = 5$ K show that the Mn ions adopt the undistorted centred pyrochlore lattice [2], displayed in fig. 3.1. The distances between Mn ions are found to be $r_{\mathrm{nn}} = 3.929$ for nearest neighbours and $r_{\mathrm{nnn}} = 6.416$ for next nearest neighbours. Previous conductivity measurements and density functional theory (DFT) band-structure calculations [193] found a large band-gap of $3.1\ \mathrm{eV} = 36\,000$ K.

We would like to construct a simplified model of [Mn(ta)$_2$] in order to understand its low-

temperature magnetic properties. First of all, given the large bandgap and that we are interested in its properties for $T \lesssim 200$ K, the material can be assumed to be insulating and thus a model of localized magnetic moments is appropriate. Its high spin electronic configuration has equal filling of the d^5 orbitals, and thus orbital anisotropic effects will be minimized, so we assume isotropic (Heisenberg) spin exchange interactions mediated by the triazolate ligands. The large $S = 5/2$ value justifies treating the spin as a classical variable, in this case, a length $5/2$ three-dimensional vector, $\mathbf{S}$. In the $S \to \infty$ limit the partition function of the quantum spin system and its classical counterpart are equivalent [194, 195], and approximations as classical spins have been successful in describing many phenomena in pyrochlore materials with spins of similar magnitude, see for example [196–200].

DFT calculations assuming isotropic exchange interactions find they are antiferromagnetic and negligible beyond second nearest neighbours, with $J_1^{\mathrm{DFT}} \sim 2 - 4$ K, $J_1^{\mathrm{DFT}}/J_2^{\mathrm{DFT}} \approx 1.3 - 1.65$ and $|J_3| < 0.01$ K [2]. Both J_1 and J_2 have similar exchange pathways, through two and three N atoms of the ligand respectively, whereas J_3 exchange can only occur as a high order process through J_1 pathways. Dipolar interactions, which exist between any magnetic moments, have a strength of

$$\frac{DS^2}{r_{\mathrm{nn}}^3} = \frac{D_{\mathrm{exp}}S^2}{r_{\mathrm{nn}}^3} = \frac{g^2\mu_B^2\mu_0 S^2}{4\pi k_B r_{\mathrm{nn}}^3} \approx 0.27\ \mathrm{K} \tag{3.1}$$

between nearest neighbours, where g is the Landé g-factor. For $[Mn(ta)_2]$ g was experimentally determined from a Curie-Weiss fit to be 2.05 [2]. Therefore at temperatures below 1 K dipolar interactions will be significant, and should be included in any model. Bringing all of this together, our model for the magnetic interactions in $[Mn(ta)_2]$ is

$$\begin{aligned} H &= J_1 \sum_{\langle ij \rangle} \mathbf{S}_i \cdot \mathbf{S}_j + J_2 \sum_{\langle\langle ij \rangle\rangle} \mathbf{S}_i \cdot \mathbf{S}_j + \frac{D}{2} \sum_{i \neq j} \left(\frac{\mathbf{S}_i \cdot \mathbf{S}_j}{r_{ij}^3} - 3\frac{(\mathbf{S}_i \cdot \mathbf{r}_{ij})(\mathbf{S}_j \cdot \mathbf{r}_{ij})}{r_{ij}^5} \right) - \mathbf{h} \cdot \sum_i \mathbf{S}_i, \\ &= H_H + H_D - \mathbf{h} \cdot \sum_i \mathbf{S}_i \end{aligned} \tag{3.2}$$

on the centred pyrochlore lattice with classical three-component $S = 5/2$ spins, where $\vec{r}_{ij} = \vec{r}_j - \vec{r}_i$ is the displacement between sites i and j, and we have also included the possibility of applying an external magnetic field, h, in the last term. This is the classical Heisenberg model described in the previous chapter with the addition of dipolar interactions, which we call the Heisenberg + dipolar model.

3.2 Monte Carlo Simulations with Dipolar Interactions

Simulations are performed for the $S = 1$ system, with quantities appropriately rescaled after. We set the dipolar interaction strength to the experimentally relevant value, for $S = 1$

eq. (3.1) gives $D_{\rm exp}/r_{\rm nn}^3 = 0.043\,\mathrm{K}$.

As was the case for the Heisenberg model, we use heatbath [8, 180, 181] and overrelaxation [8, 177–179] single-spin updates. This requires computing the local (effective) field felt by each spin

$$\mathbf{H}_i = \mathbf{H}_i^H + D \sum_{j;r_{ij}<R} \left(\frac{\mathbf{S}_j}{r_{ij}^3} - 3\frac{\mathbf{S}_j \cdot \mathbf{r}_{ij}}{r_{ij}^5}\mathbf{r}_{ij} \right) - \mathbf{h}, \tag{3.3}$$

such that $\mathbf{S}_i \cdot \mathbf{H}_i$ gives the total contribution of all terms involving the spin at site i to eq. (3.2). $\mathbf{H}_i^H$ is the contribution from the Heisenberg terms and in the dipolar term we introduce a cut-off radius R, such that we only consider interactions with sites j within distance R of site i. In order to implement the computation of the dipolar contribution, for each site i we generate a vector containing the indices of all lattice sites j which are within the cutoff as well as the corresponding displacement $\mathbf{r}_{ij} = \mathbf{r}_j - \mathbf{r}_i$, which is stored in memory

To identify possible symmetry-broken states we measure the single-tetrahedron magnetizations defined in [197]. They transform under the non-trivial irreducible representations [133] of the symmetry group of a tetrahedron, thus capturing the different ways this symmetry can be broken. Since the Hamiltonian respects the symmetries of the lattice, order which breaks these symmetries will necessarily be symmetry-broken states of eq. (3.2). For our case, it turns out that the magnetization

$$\mathbf{m}_{\mathrm{T_{1,B}},t} = \frac{-1}{2\sqrt{2}} \begin{pmatrix} S_1^y + S_1^z - S_2^y - S_2^z - S_3^y + S_3^z + S_4^y - S_4^z \\ S_1^x + S_1^z - S_2^x + S_2^z - S_3^x - S_3^z + S_4^x - S_4^z \\ S_1^x + S_1^y - S_2^x + S_2^y + S_3^x - S_3^y - S_4^x - S_4^y \end{pmatrix} \tag{3.4}$$

is of particular importance, where the indices label the four sub-lattices of the vertex spins, according to the convention in eq. (2.2). In simulations we compute the magnetizations, averaged over all a (or equivalently b) tetrahedra

$$\bar{\mathbf{m}}_\lambda = \frac{1}{N_t} \sum_{t \in a} \mathbf{m}_\lambda, \tag{3.5}$$

where N_t is the total number of a and b tetrahedra, such that the saturated value $|\bar{\mathbf{m}}_\lambda| = 1$ corresponds to an ordered state which repeats the same maximal $|\mathbf{m}_\lambda|$ configuration on every a tetrahedron of the lattice.

3.3 Converting to Experimental Units

Here we outline how to convert the relevant quantities obtained from MC simulations to experimental units. First of all, since in our simulations we set $k_B = 1$, all energies are in units of K. We work with $J_1 = 1$ and $S = 1$ in simulations, so to convert temperatures and energies we should multiply by a factor of $J_1 S^2$ where J_1 is the energy scale of the

J_1 exchange interaction in K. Explicitly, $T_{\rm exp} = J_1 S^2 T_{\rm sim}$. We determine J_1 by fitting the magnetic susceptibility measured in simulations to experiments. This procedure is discussed in detail in the next section. For the specific heat (per site), we measure

$$c_{\rm sim} = \frac{1}{N}\frac{\partial E}{\partial T} = \frac{1}{NT^2}\Big(\langle E^2\rangle - \langle E\rangle^2\Big), \tag{3.6}$$

so to convert to experimental units of $\mathrm{Jmol^{-1}K^{-1}}$, we should multiply by the molar gas constant, $R = k_B N_A$, so that $c_{\rm exp} = R c_{\rm sim}$ $\mathrm{Jmol^{-1}K^{-1}}$.

For magnetic properties, the differences between quantum and classical spins must be accounted for. We can obtain a scaling between the magnetic moments of classical, μ_z^C, and quantum, μ_z^Q, spins by considering the magnetic moment of a single spin in an external field, $B = \mu_0 H$, applied in the (arbitrary) z direction [100, 104],

$$\begin{aligned} \mu_z^C &= g\mu_B S f_L(x), \\ \mu_z^Q &= g\mu_B S f_B(x), \end{aligned} \tag{3.7}$$

with the Langevin and Brillouin functions

$$\begin{aligned} f_L(x) &= \coth(x) - \frac{1}{x}, \\ f_B(x) &= \frac{2S+1}{2S}\coth\!\left(\frac{2S+1}{2S}x\right) - \frac{1}{2S}\coth\!\left(\frac{1}{2S}x\right), \end{aligned} \tag{3.8}$$

where $x = \frac{g\mu_B S}{k_B T} B$. Taking the small B limit,

$$\begin{aligned} \mu_z^C &= g^2\mu_B^2 S^2 B + O(B^3), \\ \mu_z^Q &= g^2\mu_B^2 S(S+1) B + O(B^3), \end{aligned} \tag{3.9}$$

so we take the quantum-classical ratio of magnetic moments in an external field as $\mu^Q/\mu^C = (S+1)/S$. We assume this holds at at all temperatures and fields. Therefore, to convert magnetization results from $S = 1$ simulations to experiment, we use the relation,

$$\mu_z^{\rm exp} = g(S+1) m_z \ \mu_B \text{ per Mn}, \tag{3.10}$$

where g can be determined by fitting the susceptibility to experiments, as done in the next section. m_z is the z-component of the magnetization, $\mathbf{m}$, measured in simulations. In a non-zero external field, $\mathbf{h}$, the z-axis is defined as the direction of this field.

The energy of a saturated magnetic moment in an external field is $U^{\rm exp} = \mu_0 H g \mu_B S$ J, whereas in our simulations $U^{\rm sim} = k_B J_1 h S^2$ J (after multiplying by $J_1 S^2$), so setting these energies equal, to convert between the external field in simulations, h, and that in experiments, $\mu_0 H$,

$$\mu_0 H = \frac{k_B J_1 S}{g\mu_B} h \text{ T}. \tag{3.11}$$

Finally, we consider the magnetic susceptibility. In experiments, the molar susceptibility,

$$\chi_{\text{exp}}(T_{\text{exp}}) = \frac{N_A}{N}\left(\frac{\partial \mu_z^t}{\partial H}\right)_{H\to 0, T_{\text{exp}}} \text{m}^3\text{mol}^{-1}, \tag{3.12}$$

is measured, where μ_z^t is the total magnetic moment in the z-direction, along which H is applied. On the other hand, in simulations we measure the susceptibility per site,

$$\chi_{\text{sim}}(T_{\text{sim}}) = N\left(\frac{\partial m_z}{\partial h}\right)_{h\to 0, T_{\text{sim}}} = \frac{N}{T_{\text{sim}}}\left(\langle m_z^2\rangle - \langle m_z\rangle^2\right)_{T_{\text{sim}}}. \tag{3.13}$$

Note, that this expression uses a single component of the magnetization, which is different to what is often measured in MC simulations,

$$\chi_{\text{abs}} = \frac{N}{T}\left(\langle m^2\rangle - \langle |m|\rangle^2\right), \tag{3.14}$$

typically used to avoid issues arising due to ergodicity breaking.

Using the expressions for μ_z^{exp} and H above, which take care of the scaling of the magnetic moment as well as of energies,

$$\chi_{\text{exp}}(T_{\text{exp}}) = \frac{N_A g^2 \mu_B^2 \mu_0 (S+1)}{k_B J_1 S}\chi_{\text{sim}}(J_1 S^2 T_{\text{sim}})\ \text{m}^3\text{mol}^{-1}. \tag{3.15}$$

We now proceed to compare simulation results to experimental measurements.

3.4 Comparison to Experiment

3.4.1 Fitting Exchange Coefficients

In order to compare our model to experiment, we fit the magnetic susceptibility using the exchange interactions J_1, J_2 and Landé g-factor as fitting parameters. The fitting procedure is as follows:

- With $D = 0$, fix J_1 and perform many simulations for different J_2, obtaining a $\chi T(T)$ curve for each.
- Find the best fit to interpolated experimental data of $\chi T(T)$, using J_1 to scale T and g to scale χ (see eq. (3.15)).
- For several of the J_2, check if the optimal J_1, g change when letting $D = D_{\text{exp}}$.

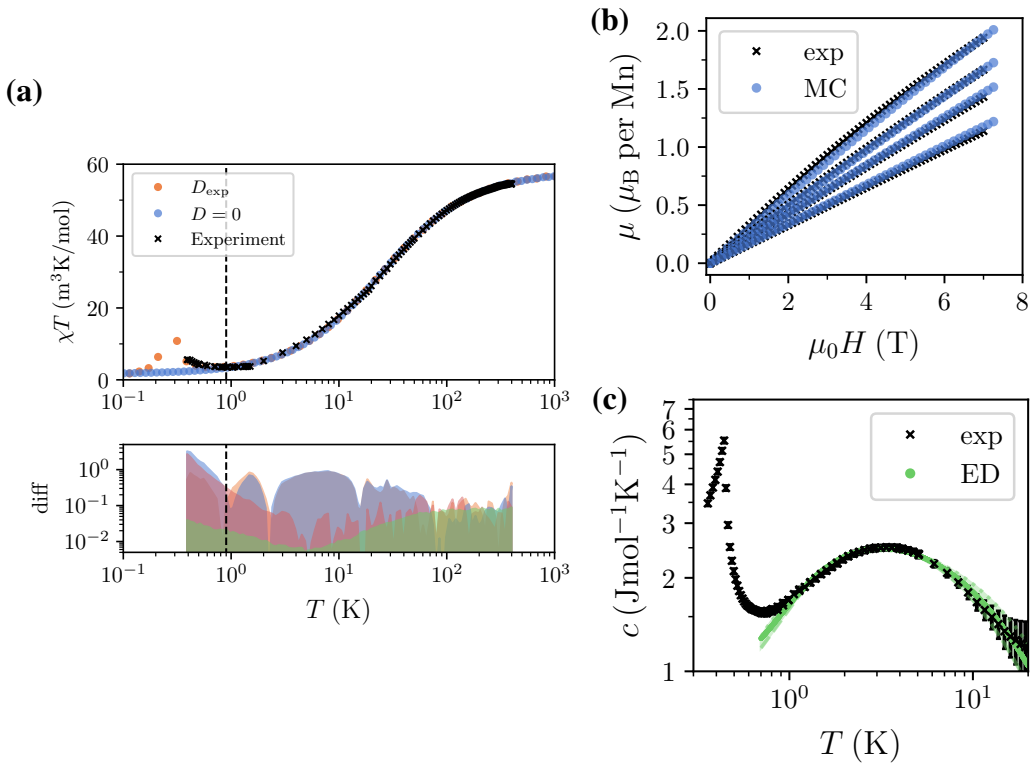

Figure 3.2: **(a)** Comparison of magnetic susceptibility from experiment and fitted simulations with (D_{exp}) and without ($D = 0$) dipolar interactions. The optimal fitting parameters $J_1 = 2\,\mathrm{K}, \eta = 0.6625$ and $g = 2.05$ are used. For $D = 0$, the fitted values for $\eta \pm 10\%$ shift the curve by no more than the point size. The bottom panel shows the differences between the simulations and experiments with (orange) and without (blue) dipolar interactions, as well as the difference between the two simulations (red). MC error for $D = 0$ simulations is plotted in green. The fitting procedure was performed using interpolated experimental data above $T = 0.9\,\mathrm{K}$, indicated by the dashed line. **(b)** Magnetization in an external field for temperatures $T = 5, 10, 15, 25\,\mathrm{K}$ (from top to bottom). The MC results are obtained using the optimal fitting parameters of the susceptibility and a field applied in the cubic z-direction. **(c)** Specific heat measured in experiment compared to exact diagonalization (ED) results for a single tetrahedron. The ED results were fitted using J_1 and an additional y-scaling of the specific heat. The optimal fit was found for $J_1 = 1.95\,\mathrm{K}$, $\eta = 0.57$ and $y = 0.8$.

We perform the fit for $T > 0.9\,\mathrm{K}$ to avoid the region where the material's ordering transition (not captured by the $D = 0$ model) significantly impacts the susceptibility. The ordering transition is discussed in more detail later in this section. We find the optimal fit for $J_1 = 2.0\,\mathrm{K}, \eta = 0.6625$ and $g = 2.05$. This is in good agreement with the exchange parameters computed from DFT, $J_1^{\mathrm{DFT}} = 2\text{–}4\,\mathrm{K}, \eta = 0.61\text{–}0.77$, and the g extracted from a Curie-Weiss fit of the experimentally measured susceptibility, $g^{\mathrm{exp}} = 2.05$. A comparison of susceptibility curves for these parameters to experiment is displayed in fig. 3.2(a). We find that the inclusion of dipolar interactions does not affect these optimal values.

In all results presented in this section we set the dipolar cut-off at $R/a = 0.55$ (up to 4$^{\mathrm{th}}$

nn) in MC simulations, where results are well-converged with respect to the inclusion of longer range interactions, as shown in section 3.6. The experimental data appears to flatten off at about $1\,\mathrm{K}$, which could be indicative of a low-temperature Curie law (section 1.4), a signature of a classical spin liquid. However, this could also be due to the nearby transition. The curve must flatten in order to increase again.

These parameters put [Mn(ta)$_2$] firmly in the classical spin liquid regime of the $D = 0$ model, where the effective description is an emergent charge fluid. However, in experiments, we see that the system orders at $T_c = 0.43\,\mathrm{K}$, so clearly the $D = 0$ model is missing an important piece of the puzzle. It turns out that setting $D = D_{\mathrm{exp}}$ induces an ordering transition at $T_d = 0.25\,\mathrm{K}$, the nature of which is discussed in more detail in section 3.6. Since the susceptibility measured in experiments and simulations with and without dipolar interactions are in good agreement for $T \gtrsim 1\,\mathrm{K}$, we expect that they do not significantly alter the state of the system at these temperatures, so can directly compare to experiments using results for the $D = 0$ model. We investigate the effect of dipolar interactions at these temperatures more closely in section 3.5. By the same token, experiments for $T < 1\,\mathrm{K}$ should be compared to simulations *with* dipolar interactions, as the effect of the nearby ordering transition will be significant.

3.4.2 Magnetization and Specific Heat

Armed with the optimal parameters matching the susceptibility in simulations and experiment, we now verify that other experimental features are reproduced by the model, in particular the magnetization in an external field and the specific heat.

First, we focus on the $D = 0$ model, where we expect to reproduce features for $T > 1\,\mathrm{K}$. We compare measurements of the magnetization in an external field to MC simulations with the optimal fitted parameters at $T = 5 - 25\,\mathrm{K}$, as shown in fig. 3.2(b), where simulations and experiment are in good agreement.

Our next point of comparison is the specific heat. However, the continuous nature of the classical spins in our model means that the specific heat behaves unphysically at low temperatures, approaching a constant, which in turn means that the entropy tends to infinity as $T \to 0$. Therefore, we turn to exact diagonalization (ED) of the Heisenberg Hamiltonian with $S = 5/2$ *quantum* spins. We compute the specific heat for a single tetrahedron of 5 spins with open boundary conditions and perform a similar fitting procedure to the susceptibility, using J_1, η and a scale factor, y, to find the optimal fit to the experimental data. We perform the fit for $T > 0.9\,\mathrm{K}$, finding optimal parameters of $J_1 = 1.95$, $\eta = 0.57$ and $y = 0.8$. A comparison of the ED and experimental results for the specific heat are presented in fig. 3.2(c).

Whilst computing the specific heat on a single tetrahedron is a crude approximation, it is able to capture the location and shape of the broad bump observed in experiment remarkably well. Since the model has $S = 5/2$, numerical simulations of the quantum model are

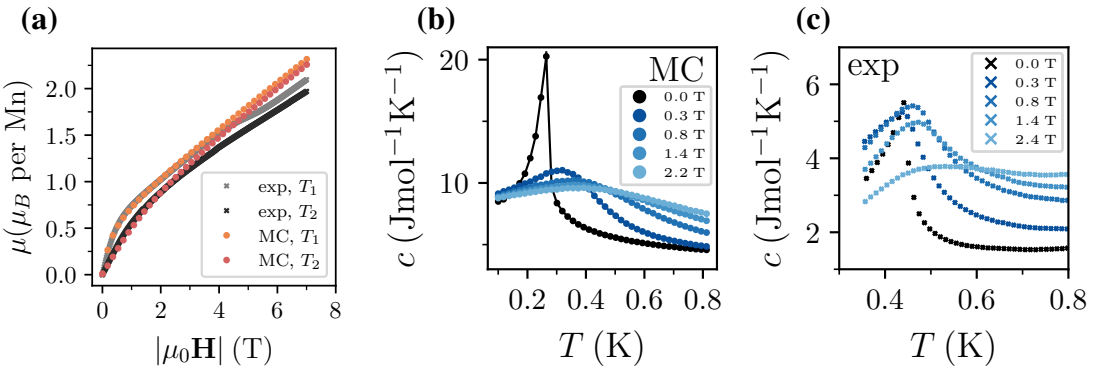

Figure 3.3: **(a)** Magnetization in an external field at temperatures $T_1 = 0.4\,\mathrm{K}$ and $T_2 = 1.0\,\mathrm{K}$. Simulation results are obtained for an $L = 12$ system with dipolar interactions ($R = 0.55$) and field direction (100). There is good agreement up to $|\mu_0\mathbf{H}| \approx 3\,\mathrm{T}$. **(b,c)** Specific heat at low temperatures in an external field, with MC results for the same parameters (including field direction) as **(a)**. Note the different x and y scales of the plots. In particular, the magnitude of the features observed in simulations are about a factor of 2 larger than in experiments. Nevertheless the qualitative behaviour, with the peak broadening and shifting to higher temperatures as external field is increased, is captured by the simulations. For both sets of simulations we verified that changing the field direction does not qualitatively affect the results.

highly challenging and the relatively short correlation lengths for these parameters in the model mean that a single tetrahedron may be able to capture many of the significant effects. The broad bump coincides with the spin liquid regime of the model, see section 3.5, and can be attributed to an increase in the specific heat upon entering the spin liquid regime from high temperature, followed by an entropy release as quantum fluctuations begin to modify the spin liquid manifold.

Now, let us compare experimental features in the $T < 1\mathrm{K}$ regime to the model with dipolar interactions. First, we compare the magnetization, measured at $T = 0.4\,\mathrm{K}$ and $1\,\mathrm{K}$, as shown in fig. 3.3(a). We find good agreement between simulations and experiments up to $|\mu_0\mathbf{H}| = 3\,\mathrm{T}$, however simulations fail to reproduce the kink observed in the $T = 0.4\,\mathrm{K}$ results between $4 - 5\,\mathrm{T}$. Experimental measurements are performed on powder samples so one should properly compare to simulation results averaged over all field directions, however we found little qualitative difference in the magnetization when performing the simulations for the field directions (100), (110), (111) and (211), so we would not expect these results to qualitatively change after averaging.

We also compare the specific heat in the temperature regime $0.4 \leq T \leq 1\,\mathrm{K}$ for fields up to $2.4\,\mathrm{T}$, see figs. 3.3(b,c). Whilst the scale of the features in specific heat do not match experiments, we find the same general features, with a broadening of the peak associated with the ordering transition and a shifting of the peak to higher temperatures, as well as the appearance of a high temperature tail, whose value increases with field strength. Here we verified that simulations do not qualitatively change for (100) and (110) fields.

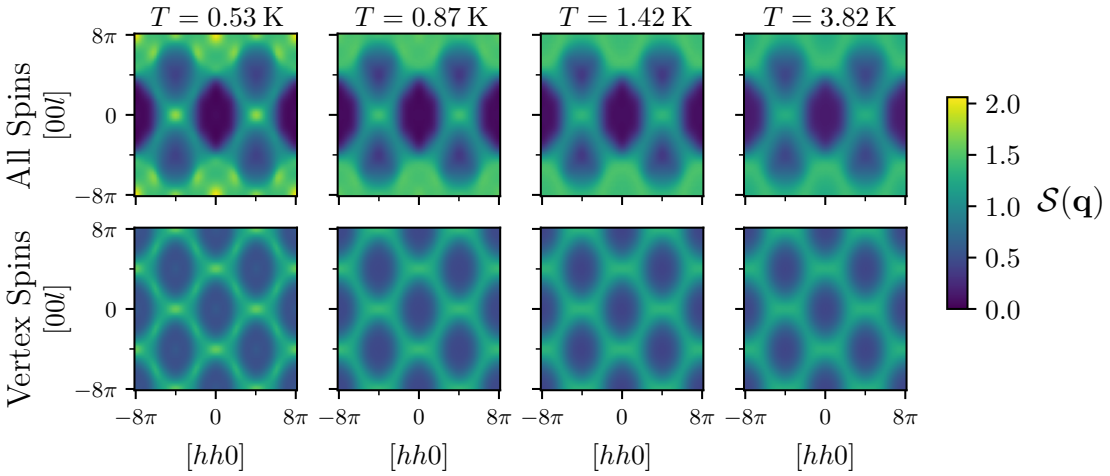

Figure 3.4: Spin structure factors computed for an $L = 8$ system with $R = 0.55$ and fitted exchange parameters, $J_1 = 2$ K and $\eta = 0.6625$. These can be compared to the structure factor without dipolar interactions in fig. 2.8 for $\gamma = 1.54$.

Overall, we see that in the regime near and just above the transition, the model with dipolar interactions is able to qualitatively reproduce features observed in experiment. The ordering temperature is underestimated, $T_d = 0.25$ K rather than 0.43 K, and the magnetization and specific heat show the same general features, but do not match quantitatively. This is a hint that the ordering observed in experiment could be similar to that induced by dipolar interactions (section 3.6), but our model lacks some features, whether that be quantum effects or additional terms in the Hamiltonian, such as single-ion or exchange anisotropy, to be able to provide a quantitative match to experiments in this temperature regime.

3.5 Finite Temperature Spin Liquid Regime

As we have seen, the model without dipolar interactions reproduces the magnetic properties measured in experiment for $T \gtrsim 1$ K, for exchange parameters consistent with the classical spin liquid. Introducing dipolar interactions has only a small effect on these magnetic properties, so it seems reasonable to expect that the spin liquid survives the inclusion of dipolar interactions at these temperatures. In this section, we verify this explicitly by comparing the spin structure factors at finite temperature, with and without dipolar interactions.

The spin structure factor with dipolar interactions is displayed in fig. 3.4. For $T \gtrsim 1$ K there is no qualitative difference between the structure factor with and without dipolar interactions. Going further, we compare the pinch points (bow ties) in the structure factor of vertex spins. For $T > 1$ K, we find only very small deviations, on the order of a few percent. We also observe that the width of the pinch points hardly changes with temperature in the range $1 \text{ K} \lesssim T \lesssim 6$ K. Therefore, we conclude that above $T \approx 1$ K, dipolar

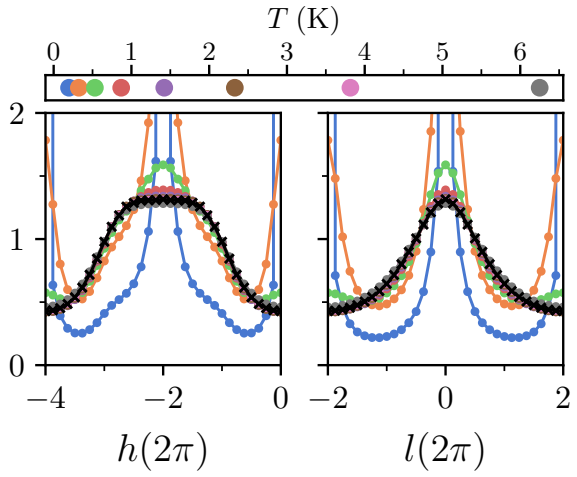

Figure 3.5: Cuts across the [hhl] plane of the vertex spin structure factor calculated for the model with dipolar interactions. The left panel is for $l = 0$ and right for $h = -4\pi$. The black crosses are from simulations without dipolar interactions at $T = 1.5$ K (which is representative of the $T \to 0$ limit) and the circles from simulations with dipolar interactions ($R = 0.55$) at the various temperatures indicated. All simulations are performed for an $L = 8$ system and the experimentally relevant parameters in fig. 3.4.

interactions do not have a significant effect and the system is in the classical spin liquid state, characterized by broad bow ties in the spin structure factor.

The fact that dipolar interactions are so easily washed out by temperature can be attributed to the large entropy of the classical spin liquid, as discussed in chapter 2. Since any additional terms which are not included in our model will have a lower energy scale than dipolar interactions, it is unlikely that these would destroy the classical spin liquid in this finite temperature regime. Therefore we propose that [Mn(ta)$_2$] realizes a classical spin liquid, whose effective description is an emergent charge fluid, at temperatures $1 \lesssim T \lesssim 6\,\mathrm{K}$.

3.6 Dipolar Ordered State

To investigate the ordered state induced by dipolar interactions, we perform MC simulations with $L = 4$, experimentally fitted exchange coefficients, $J_1 S^2 = 12.5K$, $\eta = 0.6625$, dipolar interaction strength D_{exp} and cut-off radii up to $R/a = 0.9$ (6^{th} nearest neighbour). We use $N_{\mathrm{MC}} = 10^5$ thermalization and measurement sweeps. The ordering we observe is captured by the magnetization of centre spins, $\mathbf{m}_{\mathrm{centres}}$, the local constraint (eq. (2.5)), averaged over all tetrahedra,

$$\bar{L}_t = \frac{1}{N_t} \sum_t L_t, \tag{3.16}$$

and the magnetization corresponding to the $T_{1,\mathrm{B}}$ irreducible representation, $\bar{\mathbf{m}}_{T_{1,\mathrm{B}}}$ (eq. (3.4)). Results are summarized in fig. 3.6. We verified that further increasing neither R nor L sig-

nificantly alters the results.

The vector components of $\mathbf{m}_{\text{centres}}$ and $\bar{\mathbf{m}}_{T_{1,B}}$ reveal a delicate transition region, with $\mathbf{m}_{\text{centres}}$ changing orientation from $\frac{1}{\sqrt{3}}(111) \rightarrow \frac{1}{\sqrt{2}}(110) \rightarrow (100)$ as T is lowered (up to permutations of the components). The orientation of $\bar{\mathbf{m}}_{T_{1,B}}$ also changes correspondingly. The low temperature ordered state can be understood in the following way. For $R = r_{\text{nn}}$, eq. (3.2) can be rewritten in the form $H = \sum_t H_t + \text{const}$, where

$$H_t = \frac{J_2}{2} L_t^2 + 2\sqrt{2} D_{\text{nn}} \mathbf{S}_{t,c} \cdot \mathbf{m}_{T_{1,B},t}. \tag{3.17}$$

The two terms on the right hand side cannot be simultaneously minimized since spin weight used to satisfy the local constraint reduces the weight available to maximize $\left|\mathbf{m}_{T_{1,B},t}\right|$. Since J_2 is large relative to D_{nn}, the dipolar interactions can be thought of as a perturbation to the Heisenberg part of the Hamiltonian. Therefore to construct a ground state we should ensure the local constraint, $L_t = 0$, is satisfied, which polarizes the vertex spins on a tetrahedron antiparallel to the centre spin. Since $\gamma < 4$, the vertex spins retain some finite weight after satisfying the local constraint which can be put into the $T_{1,B}$ channel to further minimize the energy.

To verify this picture we propose a pair of single tetrahedron ansätze, corresponding to (100) and (110) centre spin orientations,

$$\begin{gathered}
\mathbf{S}_c = (1,0,0), \\
\mathbf{S}_1 = (-a,b,b), \qquad \mathbf{S}_2 = (-a,-b,-b), \qquad \mathbf{S}_3 = (-a,-b,b), \qquad \mathbf{S}_4 = (-a,b,-b), \\
a = \frac{\gamma}{4}, \qquad b = \sqrt{\frac{1}{2}\left(1 - \frac{\gamma^2}{16}\right)},
\end{gathered} \tag{3.18}$$

and

$$\begin{gathered}
\mathbf{S}_c = \frac{1}{\sqrt{2}}(1,1,0), \\
\mathbf{S}_1 = (c,c,d), \qquad \mathbf{S}_2 = \frac{1}{\sqrt{2}}(-1,-1,0), \qquad \mathbf{S}_3 = \frac{1}{\sqrt{2}}(-1,-1,0), \qquad \mathbf{S}_4 = (c,c,-d), \\
c = \frac{2-\gamma}{2\sqrt{2}}, \qquad d = \sqrt{1 - \frac{(2-\gamma)^2}{4}}.
\end{gathered} \tag{3.19}$$

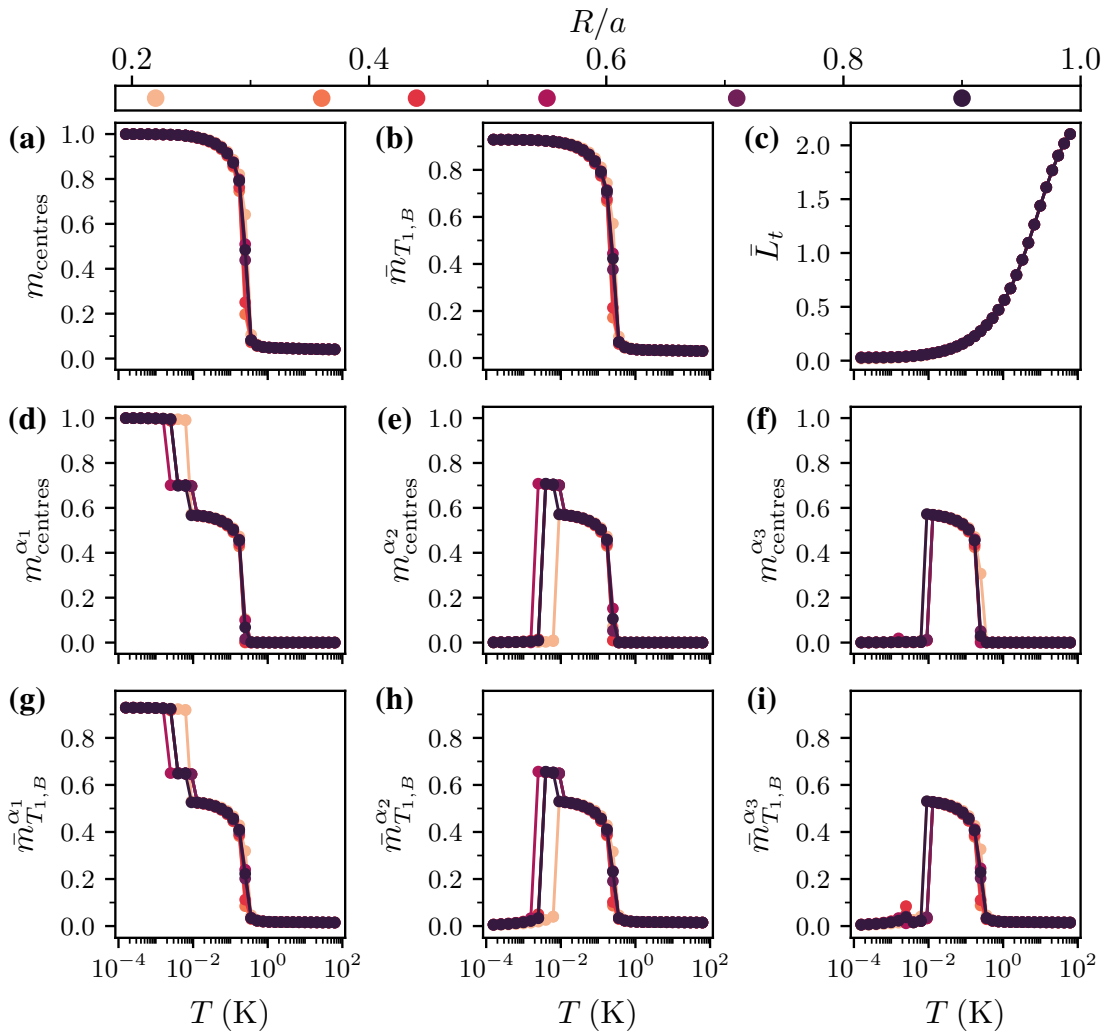

Figure 3.6: MC results for the quantities which describe the order induced by dipolar interactions. Results shown are for $L = 4$, experimentally relevant couplings, $J_1 S^2 = 12.5$ K, $\eta = 0.6625$, $\frac{DS^2}{r_{\text{nn}}^3} = 0.27$ K with R up to 6^{th} nearest neighbours.**(a-c)** are absolute values, **(d-i)** the vector components of the respective magnetizations. We verified that this ordering is robust to the inclusion of longer range interactions (up to $R/a = 4$) and increasing the system size (up to $L = 8$).

Repeating on every tetrahedron gives an ansatz for the entire lattice. Restoring longer range dipolar interactions may introduce small modifications, but our simulations indicate that these do not significantly alter the order. For example, these states very closely reproduce the energies and magnetizations obtained from numerical minimization of eq. (3.2) on a single tetrahedron and large-scale MC simulations at low temperature for $R = r_{\text{nnn}}$, as summarized in table 3.1. The (100) state is slightly lower in energy than the (110) state, but at finite temperature, entropic effects, such as softer fluctuations about the ordered state may be responsible for the observed cascade of ordering axes.

In conclusion, the $T \to 0$ ordered state identified in MC simulations is an unsaturated

State	E/N(K)	$\bar{L}_t$	$\bar{m}_{A_2}$	$\bar{m}_E$	$\bar{m}_{T_{1,A}}$	$\bar{m}_{T_{1,B}}$	$\bar{m}_{T_2}$
Numerical	-9.05606	0.02924	0	0	0.37005	0.92901	0
Ansatz (100)	-9.05481	0	0	0	0.37736	0.92607	0
Ansatz (110)	-9.05462	0	0	0	0.37736	0.92500	0.04445
MC (100)	-9.05625	0.02983	0.00025	0.00044	0.36999	0.92879	0.00103
MC (110)	-9.05231	0.04433	0.00165	0.00258	0.36804	0.92299	0.03747

Table 3.1: Comparison of energies and vertex spin magnetizations corresponding to the irreducible representations defined in [197] with $R = r_{\text{nnn}}$ and using the experimentally relevant values of J_1, J_2, D. Numerical minimization of the energy is performed for a single tetrahedron. The ansatz results are computed from the states defined in eqs. (3.18) and (3.19). MC results are averaged over all tetrahedra in the lattice, at $T = 1.6 \times 10^{-4}$ K for the (100) result and $T = 3.9 \times 10^{-3}$ K for the (110). Note $m_{T_{1,A}}$ is the total magnetization of vertex spins on a tetrahedron so captures the finite moment of corner spins in order to ensure $L_t \approx 0$. In the numerical minimization we always find $\mathbf{S}_c = (1, 0, 0)$ (up to permutation of spin components) which corresponds to $\mathbf{m}_{\text{centres}} = (1, 0, 0)$ on the full lattice.

ferrimagnet with finite magnetic moment along a cubic axis, where on each tetrahedron the vertex spins realize a planar antiferromagnet perpendicular to this axis with the remaining spin weight, as illustrated in fig. 3.7.

3.6.1 Mean-field Spectrum

In the $R \to \infty$ limit of dipolar spin ice the ground state remains disordered, a result of self-screening of the dipolar interactions [114]. It was shown within a numerical mean-field calculation [113] that finite range dipolar interactions render the flat band in the mean-field energy spectrum dispersive, breaking the ground state degeneracy. However, as R becomes large the band flattens again. Since our simulations use a finite R, we verify whether in the large R limit the ground state degeneracy is restored, by applying this mean-field calculation (introduced in [201]) to the centred pyrochlore. The method is essentially a generalization of the Luttinger-Tisza method [170, 171], applied in section 2.2.3 to the

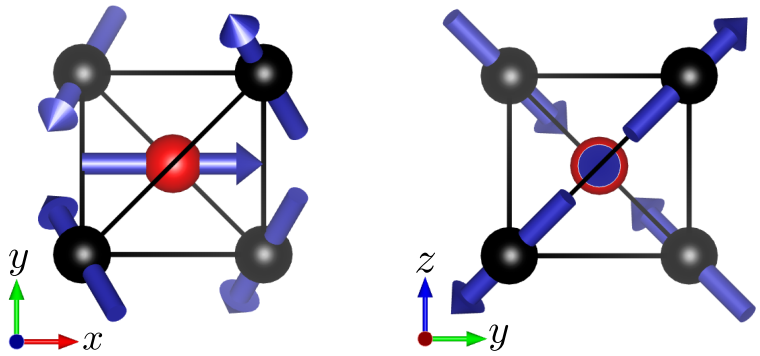

Figure 3.7: The $T \to 0$ ordered state identified in the Heisenberg + dipolar model. Shown is the (100) single-tetrahedron ansatz, eq. (3.18), for the fitted experimental parameter $\eta = 0.6625$.

Heisenberg model, to include dipolar interactions.

We want to express eq. (3.2) (with $\mathbf{h} = 0$) in terms of the Fourier modes

$$S^{\alpha}_{\mu}(\mathbf{q}) = \frac{1}{\sqrt{N_{\rm uc}}} \sum_{I} e^{-i\mathbf{q}\cdot(\mathbf{R}_I + \boldsymbol{\delta}_\mu)} S^{\alpha}(\mathbf{R} + \boldsymbol{\delta}_\mu), \tag{3.20}$$

with inverse

$$S^{\alpha}(\mathbf{R}_I + \boldsymbol{\delta}_\mu) = \frac{1}{\sqrt{N_{\rm uc}}} \sum_{I} e^{i\mathbf{q}\cdot(\mathbf{R}_I + \boldsymbol{\delta}_\mu)} S^{\alpha}_{\mu}(\mathbf{q}), \tag{3.21}$$

where $\alpha \in \{x, y, z\}$ labels spin components, I, the primitive unit cells, and $\mu \in \{a, b, 1 \ldots 4\}$, the sublattices. The Heisenberg part of the Hamiltonian is given by eq. (2.10), which in the current notation is

$$H_H = \sum_{\mathbf{q}} \sum_{\mu,\nu} \sum_{\alpha,\beta} \delta_{\alpha\beta} S^{\alpha}_{\mu}(\mathbf{q}) \mathrm{K}^{\mu\nu}(\mathbf{q}) S^{\beta}_{\nu}(-\mathbf{q}), \tag{3.22}$$

now with components

$$a_\mu = \frac{J_1}{2} e^{-i\mathbf{q}\cdot\boldsymbol{\delta}_\mu}, \qquad c_{\mu\nu} = J_2 \cos(\mathbf{q}\cdot(\boldsymbol{\delta}_\mu - \boldsymbol{\delta}_\nu)), \tag{3.23}$$

where $\mathrm{K}^{\mu\nu}$ is a matrix with the same structure as eq. (2.11).

The $\mathbf{S}_i \cdot \mathbf{S}_j / r_{ij}^3$ part of the dipolar contribution can be written as

$$A = \sum_{\alpha,\beta} \sum_{I,J} \sum_{\mu,\nu} \delta_{\alpha\beta} \frac{S^{\alpha}(\mathbf{R}_I + \boldsymbol{\delta}_\mu) S^{\beta}(\mathbf{R}_J + \boldsymbol{\delta}_\nu)}{|\mathbf{r}_i - \mathbf{r}_j|^3} (1 - \delta_{ij}). \tag{3.24}$$

Then taking the Fourier transform,

$$A = \frac{1}{N_{\rm u.c}} \sum_{\mathbf{q},\mathbf{q}'} \sum_{\alpha,\beta} \sum_{\mu,\nu} \delta_{\alpha,\beta} S^{\alpha}_{\mu}(\mathbf{q}) S^{\beta}_{\nu}(\mathbf{q}') e^{i(\mathbf{q}\cdot\delta_\mu + \mathbf{q}'\cdot\delta_\nu)} \sum_{I,J} \frac{e^{i\mathbf{q}\cdot(\mathbf{R}_I - \mathbf{R}_J)} e^{i\mathbf{R}_J\cdot(\mathbf{q}+\mathbf{q}')}}{|\mathbf{r}_i - \mathbf{r}_j|^3}, \tag{3.25}$$

where we have dropped the $(1 - \delta_{ij})$ term, which ensures $i \neq j$, for clarity. Due to translational invariance, $\mathbf{q} + \mathbf{q}' = 0$, and without loss of generality setting $\mathbf{R}_J = 0$, we obtain

$$\sum_{I,J} \frac{e^{i\mathbf{q}\cdot(\mathbf{R}_I - \mathbf{R}_J)} e^{i\mathbf{R}_J\cdot(\mathbf{q}+\mathbf{q}')}}{|\mathbf{r}_i - \mathbf{r}_j|^3} = N_{\rm u.c} \delta_{\mathbf{q}+\mathbf{q}'} \sum_{I} \frac{e^{i\mathbf{q}\cdot\mathbf{R}_I}}{|\mathbf{R}_I + \boldsymbol{\delta}_\mu - \boldsymbol{\delta}_\nu|^3}, \tag{3.26}$$

so

$$A = \sum_{\mathbf{q}} \sum_{\alpha,\beta} \sum_{\mu,\nu} \delta_{\alpha\beta} S^{\alpha}_{\mu}(\mathbf{q}) S^{\beta}_{\nu}(-\mathbf{q}) e^{i(\mathbf{q}\cdot\delta_\mu + \mathbf{q}'\cdot\delta_\nu)} \sum_{I} \frac{e^{i\mathbf{q}\cdot\mathbf{R}_I}}{|\mathbf{R}_i + \boldsymbol{\delta}_\mu - \boldsymbol{\delta}_\nu|^3}. \tag{3.27}$$

Similarly for the $-3(\mathbf{S}_i \cdot \mathbf{r}_{ij})(\mathbf{S}_j \cdot \mathbf{r}_{ij})/r_{ij}^5$ part of H_D,

$$B = \sum_{\mathbf{q}} \sum_{\alpha,\beta} \sum_{\mu,\nu} -3 S^{\alpha}_{\mu}(\mathbf{q}) S^{\beta}_{\nu}(-\mathbf{q}) e^{i(\mathbf{q}\cdot\delta_\mu + \mathbf{q}'\cdot\delta_\nu)} \sum_{I} \frac{e^{i\mathbf{q}\cdot\mathbf{R}_I} (\mathbf{R}_i + \boldsymbol{\delta}_\mu - \boldsymbol{\delta}_\nu)^{\alpha} (\mathbf{R}_i + \boldsymbol{\delta}_\mu - \boldsymbol{\delta}_\nu)^{\beta}}{|\mathbf{R}_i + \boldsymbol{\delta}_\mu - \boldsymbol{\delta}_\nu|^5}. \tag{3.28}$$

Introducing the notation $\mathbf{r}_{\mu\nu} = \mathbf{R}_i + \boldsymbol{\delta}_\mu - \boldsymbol{\delta}_\nu$, i.e it is the displacement from a site on sublattice ν to a site on sublattice μ (which may be in a different unit cell),

$$H_D = A + B = \sum_{\mathbf{q}} \sum_{\mu,\nu} \sum_{\alpha,\beta} S_\mu^\alpha(\mathbf{q}) \mathrm{D}_{\mu\nu}^{\alpha\beta} S_\nu^\beta(-\mathbf{q}), \tag{3.29}$$

with

$$\mathrm{D}_{\mu\nu}^{\alpha\beta} = \frac{D}{2} \sum_{r_{\mu\nu}<R} e^{i\mathbf{q}\cdot\mathbf{r}_{\mu\nu}} \left(\frac{\delta_{\alpha\beta}}{r_{\mu\nu}^3} - \frac{3(\mathbf{r}_{\mu\nu})^\alpha (\mathbf{r}_{\mu\nu})^\beta}{r_{\mu\nu}^5} \right), \tag{3.30}$$

and we have introduced the cut-off for the dipolar interactions.

The full Hamiltonian can then be written as,

$$H = \sum_{\mathbf{q}} \sum_{\mu,\nu} \sum_{\alpha,\beta} S_\mu^\alpha(\mathbf{q}) (\mathrm{K}_{\mu\nu}^{\alpha\beta} + \mathrm{D}_{\mu\nu}^{\alpha\beta}) S_\nu^\beta(-\mathbf{q}), \tag{3.31}$$

where $\mathrm{K}_{\mu\nu}^{\alpha\beta} = \delta_{\alpha\beta} \mathrm{K}^{\mu\nu}$. $\mathrm{K}_{\mu\nu}^{\alpha\beta}$ and $\mathrm{D}_{\mu\nu}^{\alpha\beta}$ are four-dimensional tensors, which can be rewritten as matrices, by introducing the superindex n, which runs over both α and μ. Therefore

$$H = \sum_{\mathbf{q}} \sum_{n,m=1}^{18} S_n(\mathbf{q}) \mathrm{M}_{nm}(\mathbf{q}) S_m(-\mathbf{q}), \tag{3.32}$$

and one obtains the mean-field spectrum for a given $\mathbf{q}$ by diagonalizing the 18×18 matrix

$$\mathrm{M}_{nm}(\mathbf{q}) = \begin{pmatrix} \mathrm{K}_{\mu\nu}(\mathbf{q}) + \mathrm{D}_{\mu\nu}^{xx}(\mathbf{q}) & \mathrm{D}_{\mu\nu}^{xy}(\mathbf{q}) & \mathrm{D}_{\mu\nu}^{xz}(\mathbf{q}) \\ \mathrm{D}_{\mu\nu}^{yx}(\mathbf{q}) & \mathrm{K}_{\mu\nu}(\mathbf{q}) + \mathrm{D}_{\mu\nu}^{yy}(\mathbf{q}) & \mathrm{D}_{\mu\nu}^{yz}(\mathbf{q}) \\ \mathrm{D}_{\mu\nu}^{zx}(\mathbf{q}) & \mathrm{D}_{\mu\nu}^{zy}(\mathbf{q}) & \mathrm{K}_{\mu\nu}(\mathbf{q}) + \mathrm{D}_{\mu\nu}^{zz}(\mathbf{q}) \end{pmatrix}, \tag{3.33}$$

presented here in terms of 6×6 blocks. In order to construct $\mathrm{D}_{\mu\nu}^{\alpha\beta}(\mathbf{q})$, for each μ, ν pair, all of the $\mathbf{r}_{\mu\nu}$ within the cut-off are generated numerically, then the elements are filled in according to eq. (3.30). Subsequently, $\mathrm{M}_{nm}(\mathbf{q})$ is diagonalized numerically at each $\mathbf{q}$ value of a momentum grid, in order to obtain the mean-field spectrum as a function of $\mathbf{q}$.

Since we are interested in the impact of dipolar interactions on the flat band, we use the exchange ratio $\eta = \frac{1}{\sqrt{2}} \approx 0.71$, for which the Heisenberg mean-field energy spectrum has a flat-band without reweighting the spins, as explained in section 2.2.3. This is within 10% of the fitted η obtained earlier in this chapter. We set $J_1 = 2\,\mathrm{K}$ and $D = 0.043 r_{\mathrm{nn}}^3\,\mathrm{K}$. Results are shown in fig. 3.8. We see that the energies of the lowest band converge for $R \geq 10$, with minima at momenta such as $\mathbf{q} \approx (3.875\pi, 0.125\pi, 0)$. Therefore dipolar interactions in the large R limit appear to select an ordered state. The momentum that minimizes the energy is incommensurate with the lattice, and the eigenvectors associated with this mode do not give physically normalized ($|\mathbf{S}_i| = 1$) spins, so we cannot reliably predict the ordered ground state from these calculations. Nevertheless, unlike dipolar spin ice, large R dipolar interactions do not restore the ground state degeneracy, so the finite values of R used in our MC simulations are likely sufficient to capture the correct low-temperature behaviour.

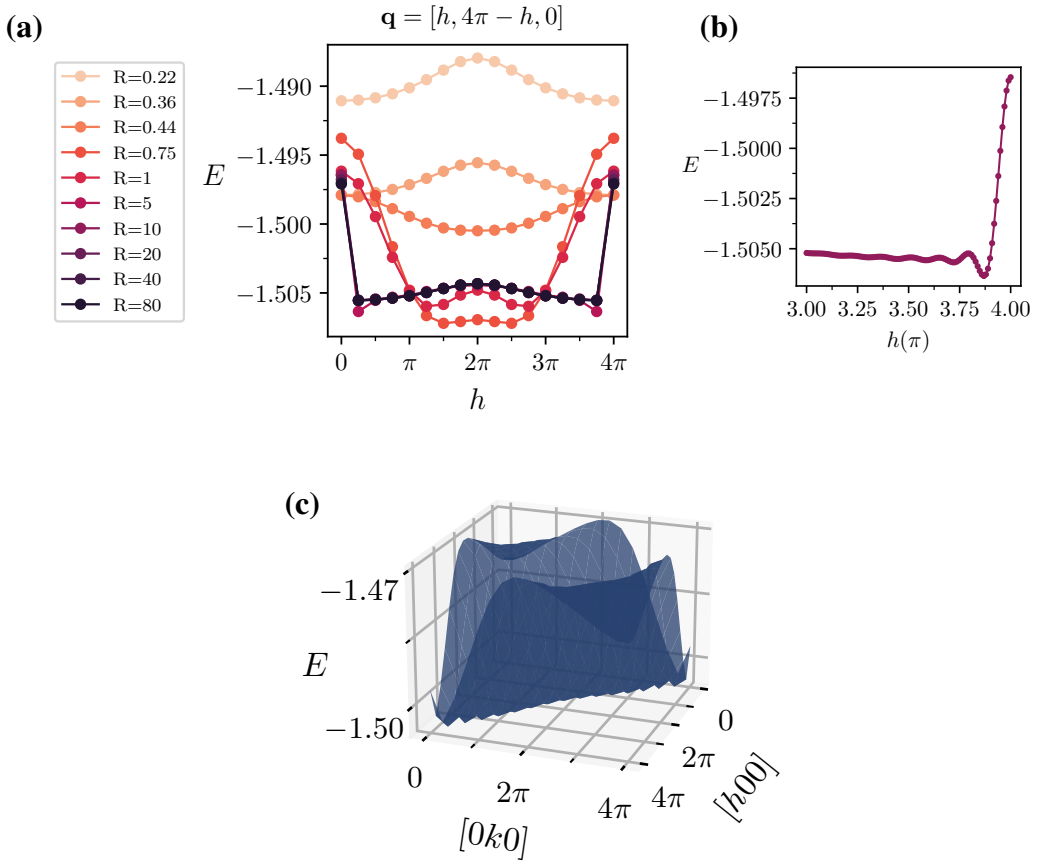

Figure 3.8: Lowest band of the mean-field energy spectrum with dipolar interactions for parameters $J_1 = 2\,\mathrm{K}$, $\eta = \frac{1}{\sqrt{2}}$, $D = 0.043 r_{\mathrm{nn}}^3$ and $S = 1$. **(a)** Convergence of the minimum energy along the $\mathbf{q} = (h, 4\pi - h, 0)$ line for various R. **(b)** Using a finer h grid for $R = 10$ the minimum is at about $h = 3.875\pi$. **(c)** In the $[hk0]$ plane for $R = 10$. The low-energy valley along $\mathbf{q} = (h, 4\pi - h, 0)$ is that plotted in **(a,b)**.

3.7 Summary and Outlook

In this chapter we introduced the Heisenberg + dipolar Hamiltonian as a model for the metal-organic framework $[\mathrm{Mn(ta)_2}]$, justified by ab initio DFT calculations and its electronic properties. Comparison of the model to experimental measurements of the magnetization, susceptibility and specific heat found that they are well approximated by the parameters $J_1 S^2 = 12.5 K$, $\eta = 0.6625$, $D S^2 r_{\mathrm{nn}}^3 = 0.27\mathrm{K}$. Our MC simulations showed that the dipolar interactions cause ordering into the (100) state, shown in fig. 3.7, at $T_d = 0.25\,\mathrm{K}$. We showed using a mean-field calculation that it is sufficient to consider dipolar interactions with a finite cut-off radius in this model, unlike in dipolar spin ice. Due its large entropy, the spin liquid, which is the ground state in the absence of dipolar interactions, survives at finite temperatures. Its characteristic $T \to 0$ signature, broadened bow ties in the static spin structure factor were observed in Monte Carlo simulations for temperatures $1\,\mathrm{K} \lesssim T \lesssim 6\,\mathrm{K}$. Therefore we propose that $[\mathrm{Mn(ta)_2}]$ realizes a classical spin liquid in this

temperature regime, where the effective description is that of an emergent charge fluid.

To further narrow down the effective Hamiltonian, and by extension, the states of matter realized in the material, requires experimental probes which are more sensitive to microscopic details, of which neutron scattering is the gold standard. However, extracting useful information from neutron scattering experiments on such a compound is challenging, due to the fact that it contains a high concentration of hydrogen atoms, which have a high incoherent scattering cross section [202], resulting in noisy data. Nevertheless, it is possible to extract useful inelastic spectra in similar metal-organic frameworks [203]. In addition, this effect can be mitigated by using deuterated ligands in the chemical synthesis, so that the hydrogen atoms in the compound are replaced by deuterium, which has a much lower incoherent scattering cross section. Furthermore, experiments are limited to powder samples, as it is currently not possible to grow large single crystals of [Mn(ta)$_2$].

Bearing these limitations in mind, the questions which could be addressed in near-term neutron scattering experiments include:

1. What is the ordered phase of [Mn(ta)$_2$]? The Bragg peaks from a neutron diffraction experiment could be compared to predictions from the Heisenberg + dipolar model to identify the nature of the ordered state in the material. Inelastic scattering measurements could also be compared to a spin wave analysis to give further insight. Any missing terms in the Hamiltonian required to reproduce the experimental behaviour could be found.

2. Does [Mn(ta)$_2$] realize the classical spin liquid for $1\ \mathrm{K} \lesssim T \lesssim 6\ \mathrm{K}$? Comparison of the powder-averaged static structure factor of the $J_1 - J_2$ model to neutron scattering results in the relevant temperature regime would give a strong indication of whether the material realizes the proposed classical spin liquid or not. Furthermore, the dynamical spin structure factor could be obtained using the molecular dynamics method [204], where the equilibrium spin configuration from a Monte Carlo simulation is time-evolved according to the classical equations of motion, to compare to experimental results.

The long-term goal would be to measure the $\mathbf{q}$-resolved static structure factor, to see if it agrees with the neutron scattering variant of the spin liquid structure factor in fig. 3.4, which would first require significant advancement in the growth of single crystals.

The centred pyrochlore spin liquid naturally hosts emergent charges in the ground state, in contrast to the charge-free vacuum of the pyrochlore spin liquid. This charge strength could be tuned via hydrostatic pressure to modify the ratio of exchange parameters η. Furthermore, the modularity of metal-organic frameworks offers further tunability. For example, it is possible to synthesize materials with different metal ions on centre and vertex sites, or modify the strength of exchange interactions by substituting ligands. Thus, metal-azolate frameworks provide an ideal system to explore exotic states of matter within the

framework of the emergent electrostatics and beyond. Furthermore, the frustrated centred pyrochlore geometry raises the possibility to explore related *quantum* effects in metal-azolate frameworks, by synthesizing materials with lower effective spin.

We end this chapter with a brief survey of the magnetic properties in other materials of the [M(II)(ta)$_2$] family. [Cu(ta)$_2$] has an effective $S = 1/2$ moment, but has a structural phase transition at lower temperatures, which distorts the centred pyrochlore lattice [189]. Magnetic susceptibility measurements indicate the formation of antiferromagnetic dimers amongst 2/3 of the Cu ions. It could be possible to suppress the structural phase transition by synthesizing the material with a different ligand, allowing one to study quantum magnetism on the centred pyrochlore. The mixed-valence framework [Fe(ta)$_2$(BF$_4$)$_x$] contains low-spin Fe^{3+} ions with effective $S = 1/2$ [191]. Magnetic susceptibility measurements indicate strong antiferromagnetic interactions, with no long-range magnetic ordering observed down to $T = 3\,\mathrm{K}$, corresponding to a frustration factor of at least $f = 27$. However, the conducting nature of these materials means that any model to study the low temperature magnetic properties will have to be quite different from the localized moments we assume here. Another mixed-valence framework [Cr(ta)$_2$(CF$_3$SO$_3$)$_0$.33] is found to have strong ferromagnetic exchange interactions with long-range magnetic order at $T_c = 225\,\mathrm{K}$ [127]. The diversity of these materials means there are surely many fascinating magnetic properties which remain unexplored.

Chapter 4

Quantum XXZ Model

We now move to investigating the possibility of realizing *quantum* spin liquids (QSLs) on the centred pyrochlore lattice. A good place to start is with the $S = 1/2$ XXZ model on the centred pyrochlore lattice. This is because, as in the pyrochlore case [90], one can introduce non-trivial quantum fluctuations perturbatively to the degenerate classical spin liquid manifold. The local constraint and associated degeneracy of the classical spin liquid is an important precursor for the gauge structure which can support a quantum spin liquid. Our focus is on the $1 < \gamma < 3$ region of the parameter space, where the Ising model ground state is a $\mathbb{Z}_2$ classical spin liquid with 3:1 configurations of vertex spins on every tetrahedron. For simplicity, we restrict ourselves to the $J_1^\perp, J_2^\perp$ ferromagnetic regime. We find using degenerate perturbation theory at $\gamma = 2$, up to fourth order, that the ground state is described by a $\mathrm{U}(1)$ lattice gauge theory coupled to fermionic matter, where the fermions carry an emergent electric charge. Restricting to third order, the effective Hamiltonian can be mapped to a family of Rokhsar-Kivelson type quantum dimer models [129], which have an exact quantum liquid ground state at a point in their parameter space. This provides us the framework for understanding the low-energy properties for small $J_1^\perp, J_2^\perp$. We then adapt the gauge mean-field method [149] to the centred pyrochlore lattice, finding that the only self-consistent solution within a zero-flux ansatz is a $\mathrm{U}(1)$ quantum spin liquid, which orders to an XY ferromagnet for large enough $J_2^\perp$. Finally, we perform exact diagonalization calculations on a 24-site cluster, obtaining the phase boundaries for the $(3{:}1)^\perp$ regime, the region between the Ising limit and the onset of long-range XY ferromagnetic order. We find that the ground state in this regime has high overlap with a QSL variational wavefunction inspired by the perturbation theory, demonstrating the perturbative framework remains valid away from the $\gamma = 2$ point and hinting at a quantum spin liquid ground state. The energy spectrum, fidelities and overlaps with the variational wavefunction suggest the possibility of multiple phases within the $(3{:}1)^\perp$ regime, despite severe finite size effects. Numerical simulations which can access larger system sizes are called for to further investigate the nature of the ground state.

4.1 Model

The model we study is the spin-1/2 XXZ model on the centred pyrochlore lattice

$$\begin{aligned} H = J_1^z \sum_{\langle ij \rangle} S_i^z S_j^z + J_1^\perp \sum_{\langle ij \rangle} \Big(S_i^+ S_j^- + \text{h.c} \Big) \\ + J_2^z \sum_{\langle\langle ij \rangle\rangle} S_i^z S_j^z + J_2^\perp \sum_{\langle\langle ij \rangle\rangle} \Big(S_i^+ S_j^- + \text{h.c} \Big). \end{aligned} \tag{4.1}$$

We choose to study this model inspired by the spin 1/2 XXZ model on the pyrochlore, where it is well-established that the ground state in the perturbative $J^\perp$ limit is a $\mathrm{U}(1)$ QSL [90, 145, 151]. The idea is that quantum fluctuations produce a superposition of the states in the ground state manifold of the Ising model. Similarly, on the centred pyrochlore lattice, we can use our knowledge of the classical spin liquid ground states of the Ising model (section 2.2.2) as a starting point to understand the XXZ model. Furthermore, at the Heisenberg point $J_1^\perp = J_1^z/2$, $J_2^\perp = J_2^z/2$, the model could be relevant for understanding the low temperature magnetic properties of $S = 1/2$ metal-azolate frameworks.

Let us first enumerate some of the symmetry properties of the Hamiltonian. It is useful to rewrite the Hamiltonian as a sum over tetrahedra, t,

$$\begin{aligned} H &= \sum_t H_t, \\ H_t &= J_1^z \sum_{v=1}^4 S_{t,c}^z S_{t,v}^z + J_1^\perp \sum_{v=1}^4 \Big(S_{t,c}^+ S_{t,v}^- + \text{h.c} \Big) \\ &\quad + \frac{J_2^z}{2} \sum_{w \neq v} S_{t,v}^z S_{t,w}^z + J_2^\perp \sum_{w \neq v} S_{t,v}^+ S_{t,w}^- \end{aligned} \tag{4.2}$$

where c labels centre sites and v, w vertex sites of a tetrahedron.

Since the J_1 terms are bipartite in the sense that they only connect centre to vertex spins, there are a pair of operators acting on centre spins which map between different regions of the parameter space. Consider a unitary operator,

$$U_c = \prod_t U_{t,c}, \tag{4.3}$$

which acts only on centre sites. The only part of the Hamiltonian which does not commute with U_c are the J_1 terms

$$H_{J_1} = J_1^z \sum_t S_{t,c}^z \sum_v S_{t,v}^z + J_1^\perp \Big(\sum_t S_{t,c}^+ \sum_v S_v^- + \sum_t S_{t,c}^- \sum_v S_v^+ \Big). \tag{4.4}$$

An appropriate choice of $U_{t,c}$ will transform the centre spins in such a way that $U_{t,c}^\dagger S_{t,c}^\alpha U_{t,c} = a S_{t,c}^\alpha$ and a can be interpreted as a transformation of the exchange interaction, $J_1^\alpha \to a J_1^\alpha$.

Since vertex spins are coupled both to centre spins and other vertex spins, an operator of the form eq. (4.3) but acting on all vertex spins will not transform the exchange interactions in this way.

First, choosing $U_{t,c} = S_i^x$, the spin inversion of the z-component of all centre spins,

$$X_c = \prod_{i \in \text{centres}} S_i^x, \tag{4.5}$$

gives the mapping $(X_c)^\dagger H(J_1^z, J_2^z, J_1^\perp, J_2^\perp)X_c = H(-J_1^z, J_2^z, J_1^\perp, J_2^\perp)$, that is, one can map from $J_1^z \to -J_1^z$ by inverting the z-component of all centre spins.

Second, taking $U_{t,c} = r_i^z(\pi)$ with the single-site π rotation operator in the local z basis,

$$r_i^z(\pi) = \begin{pmatrix} -i & 0 \\ 0 & i \end{pmatrix}, \tag{4.6}$$

so that the π rotation of all centre spins about the z-axis,

$$R_c^z(\pi) = \prod_{i \in \text{centres}} r_i^z(\pi), \tag{4.7}$$

yields the mapping $(R_c^z(\pi))^\dagger H(J_1^z, J_2^z, J_1^\perp, J_2^\perp)R_c^z(\pi) = H(J_1^z, J_2^z, -J_1^\perp, J_2^\perp)$, i.e rotation of all central spin components about the z-axis maps from $J_1^\perp \to -J_1^\perp$. Together, these two mappings are analogous to that in the classical Heisenberg model, where inverting all components of the central spins maps $J_1 \to -J_1$.

In this chapter, we largely present results for $J_1^z > 0$, $J_1^\perp < 0$, but they can be generalized to the opposite sign regions with a corresponding global inversion or rotation of the centre spins.

4.2 Degenerate Peturbation Theory

Here, we apply degenerate perturbation theory in the $J_1^\perp, J_2^\perp \ll J_1^z, J_2^z$ limit, to understand the effect of adding quantum fluctuations to the centred pyrochlore Ising model. Our starting point is the 3:1 regime of the Ising model, which is a distinct classical spin liquid to the pyrochlore ground state, in the hope that we will find phenomena beyond that already observed in quantum models on the pyrochlore. Note the perturbative analysis of a 3:1 manifold [205] and analytical [206] and numerical [131, 207] studies of the resulting effective model, find an ordered ground state proximate to a quantum spin liquid. However, in our model, the manifold is not e.g 3-up/1-down on *every* tetrahedron, as is the case in those studies, but may be either 3-up/1-down or 1-down/3-up. Furthermore, $J_1^\perp$ interactions with the central spin in principle allow fluctuations between the two.

4.2.1 Constructing H_{eff}

We use Schrieffer-Wolff degenerate perturbation theory [159, 160] (see also appendix B of [161] for a pedagogical explanation), following the approach of Hermele, Fisher and Balents (HFB) for the pyrochlore [90]. The analysis on the pyrochlore was described in section 1.6.3.

First, we split the Hamiltonian into an Ising part plus quantum fluctuations, as well as rewriting in terms of sums over tetrahedra,

$$\begin{aligned} H &= H^z + H^\perp, \\ H^z &= J_1^z \sum_{\langle ij \rangle} S_i^z S_j^z + J_2^z \sum_{\langle\langle ij \rangle\rangle} S_i^z S_j^z \\ &= \frac{J_2^z}{2} \sum_t G_t^2 - \frac{N_t}{4}\left(\frac{(J_1^z)^2}{2J_2^z} + 2J_2^z\right) = \sum_t H_t^z + \text{const} \\ H^\perp &= J_1^\perp \sum_{\langle ij \rangle} \left(S_i^+ S_j^- + \text{h.c}\right) + J_2^\perp \sum_{\langle\langle ij \rangle\rangle} \left(S_i^+ S_j^- + \text{h.c}\right) \\ &= J_1^\perp \sum_t \sum_{v=1}^4 \left(S_{t,c}^+ S_{t,v}^- + \text{h.c}\right) + J_2^\perp \sum_t \sum_{w \neq v} S_{t,v}^+ S_{t,w}^- \\ &= H_1^\perp + H_2^\perp, \end{aligned} \tag{4.8}$$

where

$$G_t = \sigma_t \left(\gamma S_{t,c}^z + \sum_{v=1}^4 S_{t,v}^z\right), \tag{4.9}$$

$\sigma_t = +(-1)$ when t is on the $a(b)$ sublattice and $\gamma = J_1^z/J_2^z$. The ground state of H^z (the Ising model) is determined by minimizing G_t, which gives the ground state phase diagram in fig. 2.2. G_t is the quantity previously referred to as L_t, which defines the ground state local constraint. We take $\gamma = 2$, such that dropping the constant term the ground state energy of H^z is $E_0 = 0$. Taking $\gamma = 2$ also simplifies the analysis as H_t^z eigenvalues of a 4:0 and 2:2 tetrahedron are equivalent, see table 4.1. We also assume that $J_1^\perp$, $J_2^\perp$ are of the same order.

Let us define the operator, P, which projects onto the ground state manifold of H^z, and

$$D = -\frac{1-P}{H^z - E_0}, \tag{4.10}$$

which projects onto the manifold of excited states with a prefactor determined by the energy of the excited state relative to the ground state. In the Schrieffer-Wolff formalism, our goal is to construct an effective Hamiltonian, H_{eff}, which describes the effect of $H^\perp$ acting within the degenerate ground state manifold, which we build up order by order.

At second order,

$$\begin{aligned} H_{\text{eff}}^{(2)} &= PH^\perp DH^\perp P \\ &= PH_1^\perp DH_1^\perp P + PH_2^\perp DH_2^\perp P. \end{aligned} \tag{4.11}$$

Abbreviation	State	$\lvert G_t\rvert$	$H_t^z(\gamma)$	$H_t^z(\gamma=2)$
4:0	$\lvert\Downarrow\uparrow\uparrow\uparrow\uparrow\rangle$	$\lvert-\frac{\gamma}{2}+2\rvert$	$\frac{J_2^z}{2}(-\frac{\gamma}{2}+2)^2$	$\frac{J_2^z}{2}$
3:1	$\lvert\Downarrow\uparrow\uparrow\uparrow\downarrow\rangle$	$\lvert-\frac{\gamma}{2}+1\rvert$	$\frac{J_2^z}{2}(-\frac{\gamma}{2}+1)^2$	0
2:2	$\lvert\Downarrow\uparrow\uparrow\downarrow\downarrow\rangle$	$\frac{\gamma}{2}$	$\frac{J_2^z\gamma^2}{8}$	$\frac{J_2^z}{2}$
3:1*	$\lvert\Downarrow\uparrow\downarrow\downarrow\downarrow\rangle$	$\frac{\gamma}{2}+1$	$\frac{J_2^z}{2}(\frac{\gamma}{2}+1)^2$	$2J_2^z$
4:0*	$\lvert\Downarrow\downarrow\downarrow\downarrow\downarrow\rangle$	$\frac{\gamma}{2}+2$	$\frac{J_2^z}{2}(\frac{\gamma}{2}+2)^2$	$\frac{9J_2^z}{2}$

Table 4.1: Modified single tetrahedron magnetization and corresponding energy eigenvalue of H_t^z for all single tetrahedron states. Centre spins are indicated by a double arrow, vertex spins by a single arrow. The asterisk in the abbreviation indicates the centre spin is parallel to the net moment of the vertices. States which are 3-up/1-down or 1-up/3-down are both referred to as 3:1 states, 4-up/0-down, 0-up/4-down as 4:0.

The two terms correspond to the two different virtual processes shown in fig. 4.1. For $\gamma = 2$, this gives a constant term since the perturbation acts on single tetrahedra in the 3:1 manifold and *all* states in the ground state manifold are 3:1 on *every* tetrahedron. Crucially, the energy of the intermediate (virtual) state is the same regardless of whether it is 2:2 or 4:0. Explicitly,

$$\begin{aligned} PH_1^\perp DH_1^\perp P &= -\frac{(J_1^\perp)^2}{J_2^z}\sum_t\sum_v\left(S_{t,c}^- S_{t,v}^+ S_{t,c}^+ S_{t,v}^- + \text{h.c}\right) \\ &= -\frac{3N_t(J_1^\perp)^2}{J_2^z} \end{aligned} \tag{4.12}$$

and

$$\begin{aligned} PH_2^\perp DH_2^\perp P &= -\frac{(J_2^\perp)^2}{J_2^z}\sum_t\sum_{v\neq w} S_{t,v}^- S_{t,w}^+ S_{t,v}^+ S_{t,w}^- \\ &= -\frac{3N_t(J_2^\perp)^2}{J_2^z}, \end{aligned} \tag{4.13}$$

where the factors of 3 come from the 3 ways to get a contribution on each tetrahedron. For a given 3:1 single-tetrahedron spin configuration, there are three vertex spins which can exchange with the centre, or with the single anti-parallel spin respectively, which must then be exchanged back. These terms are diagonal, mapping any ground state back to itself. Off-diagonal terms are not possible because if one maps between distinct 3:1 single-tetrahedron states, one would have to "repair" the defects on the adjacent tetrahedra as well to get back to a ground state. This is only possible for operations which form closed loops on the lattice, the shortest of which is the length-6 hexagonal loop which appears at third order.

When $\gamma \neq 2$ (but ground states are still in the 3:1 manifold), these terms are no longer constant. For $\gamma < 2$, 2:2 states are lower in energy than 4:0, so we expect the degeneracy of

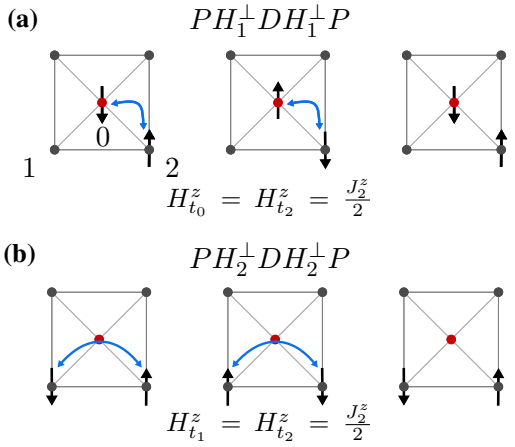

Figure 4.1: Processes contributing to second order terms in the perturbation theory for $\gamma = 2$, reading from left to right. They give a constant contribution to H_{eff}. The non-zero energies of virtual states for relevant tetrahedra are shown underneath. The squares represent tetrahedra of the centred pyrochlore lattice. The leftmost illustration of **(a)** shows the labels, i, of the displayed and adjacent (not-displayed) tetrahedra which corresponds to the t_i index for the energies.

the 3:1 manifold to be broken by the second order term, with states where the perturbation can create the highest number of virtual 2:2 tetrahedra becoming lower in energy. Similarly, for $\gamma > 2$, states where the perturbation can create the highest number of virtual 4:0 states will have lower energy. Whether this selects an ordered state or effectively reduces the dimension of the ground state manifold is not immediately clear.

At third order, there are three non-zero terms, the triangular hopping and ring-exchange term familiar from the pyrochlore, as well as a term analogous to $PH_2^\perp DH_2^\perp P$ where the centre spin mediates an effective $J_2^\perp$ interaction, so

$$H_{\text{eff}}^{(3)} = 2PH_1^\perp DH_1^\perp DH_2^\perp P + PH_2^\perp DH_2^\perp DH_2^\perp P, \tag{4.14}$$

where the factor of 2 comes from the fact that $PH_1^\perp DH_1^\perp DH_2^\perp P$ is equivalent to $PH_2^\perp DH_1^\perp DH_1^\perp P$ (but $PH_1^\perp DH_2^\perp DH_1^\perp P = 0$ as the $H_2^\perp$ term cannot flip spins which are already parallel) and

$$PH_2^\perp DH_2^\perp DH_2^\perp P = H_{\text{eff}}^{(3)}(\triangle) + H_{\text{eff}}^{(3)}(\hexagon). \tag{4.15}$$

For $\gamma = 2$, the only non-constant term is the ring-exchange, since

$$\begin{aligned} PH_1^\perp DH_1^\perp DH_2^\perp P &= \frac{(J_1^\perp)^2 J_2^\perp}{(J_2^z)^2} \sum_t \sum_{v<w} \left(S^+_{t,c} S^-_{t,v} S^-_{t,c} S^+_{t,w} S^-_{t,w} S^+_{t,v} + S^-_{t,c} S^+_{t,v} S^+_{t,c} S^-_{t,w} S^+_{t,w} S^-_{t,v} \right) \\ &= \frac{3N_t (J_1^\perp)^2 J_2^\perp}{(J_2^z)^2}, \end{aligned} \tag{4.16}$$

and

$$\begin{aligned} H^{(3)}_{\text{eff}}(\triangle) &= \frac{(J_2^\perp)^3}{(J_2^z)^2}\sum_t \sum_{u,v,w\in\triangle}\left(S^+_{t,w}S^-_{t,u}S^+_{t,u}S^-_{t,v}S^+_{t,v}S^-_{t,w} + \text{h.c}\right) \\ &= \frac{6N_t(J_2^\perp)^3}{(J_2^z)^2}, \end{aligned} \tag{4.17}$$

where the sum is over all $u \neq v \neq w$ which make up a triangle on a single tetrahedron, as shown in fig. 4.2(b), along with illusrations of all third-order processes. The prefactors again come from counting the number of processes which return to the original 3:1 state. For the ring-exchange term,

$$\begin{aligned} H^{(3)}_{\text{eff}}(\hexagon) &= K_1\sum_{\hexagon}\left(S^+_{v,0}S^-_{v,1}S^+_{v,2}S^-_{v,3}S^+_{v,4}S^-_{v,5} + \text{h.c}\right), \\ &= K_1\sum_{\hexagon}\left(A_{\hexagon} + A^\dagger_{\hexagon}\right) \end{aligned} \tag{4.18}$$

with $K_1 = 12(J_2^\perp)^3/(J_2^z)^2$. The vertex sites are labelled in a clockwise fashion around the hexagonal loop, as shown in fig. 4.2(c). The factor of 12 comes from the choice of one of six tetrahedra for the first $J_2^\perp$ term, followed by a choice of one of the two other compatible tetrahedra, which fixes the tetrahedron for the last.

As before, for $\gamma \neq 2$, these terms are more complicated, lowering the energy of states in the 3:1 manifold which pass through virtual 2:2 or 4:0 states, for $\gamma < 2$ and $\gamma > 2$ respectively.

At fourth order, disconnected processes also enter, as one can have a pair of second order processes on distinct tetrahedra. This means that terms of different form enter the series, such that

$$\begin{aligned} H^{(4)}_{\text{eff}} = PH^\perp DH^\perp DH^\perp DH^\perp P - \frac{1}{2}PH^\perp DH^\perp PH^\perp D^2H^\perp P \\ - \frac{1}{2}PH^\perp D^2H^\perp PH^\perp DH^\perp P, \end{aligned} \tag{4.19}$$

however, since the second order processes are constant (for $\gamma = 2$), they also give a constant contribution at fourth order.

Focussing on non-constant terms,

$$\begin{aligned} PH^\perp DH^\perp DH^\perp DH^\perp P &= PH_1^\perp DH_2^\perp DH_1^\perp DH_2^\perp P + \text{permutations} \\ &\quad + PH_2^\perp DH_2^\perp DH_2^\perp DH_2^\perp P + \ldots \\ &= H^{(4)}_{\text{eff}}(\hexagon) + H^{(4)}_{\text{eff}}(\bigcirc) + \ldots, \end{aligned} \tag{4.20}$$

where the six permutations of the $H_1^\perp$, $H_2^\perp$ operators (1122, 1212, 1221, 2112, 2121, 2211) contribute equally to $H^{(4)}_{\text{eff}}(\hexagon)$ and $H^{(4)}_{\text{eff}}(\bigcirc)$ is a length-8 ring-exchange, analogous

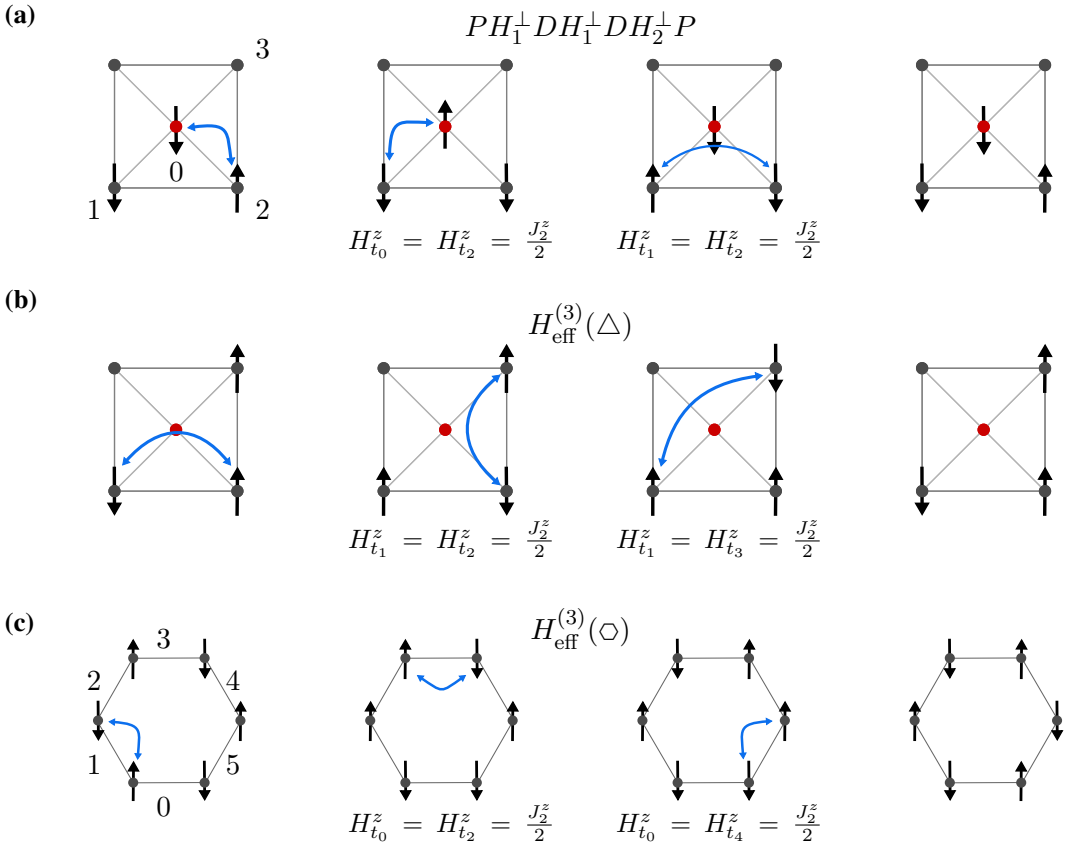

Figure 4.2: Processes contributing to third order terms in the perturbation theory for $\gamma = 2$, with the single-tetrahedron energies of the intermediate states shown below. **(a)** Shows the labels, i, of the displayed tetrahedron and its neighbours which corresponds to the t_i index for the energies. In **(b)** the sites involved in the process form a triangle. **(c)** Shows the labelling convention for tetrahedra making up a hexagonal loop, with v_i labelling the vertex spin clockwise from the centre of the i^{th} tetrahedron and c_i its centre spin. Only the edges of the tetrahedra making up the loop are shown.

to $H^{(3)}_{\text{eff}}(\hexagon)$. We find that,

$$
\begin{aligned}
H^{(4)}_{\text{eff}}(\hexagon) &= K_2 \sum_{\hexagon} \left(B_{\hexagon} + B^{\dagger}_{\hexagon} \right), \\
K_2 = -\frac{12(J_1^{\perp})^2(J_2^{\perp})^2}{(J_2^z)^3},\ B_{\hexagon} &= \sum_{i=0}^{5} \sum_{j=i+1}^{5} B^{ij}_{\hexagon}, \\
B^{ij}_{\hexagon} &= \begin{cases} S^+_{c_i} S^-_{c_j} S^-_{v_i} \dots S^+_{v_{j-1}} S^+_{v_j} \dots S^-_{v_{i+5}} \text{ for } j-i \text{ even} \\ S^+_{c_i} S^+_{c_j} S^-_{v_i} \dots S^-_{v_{j-1}} S^-_{v_j} \dots S^-_{v_{i+5}} \text{ for } j-i \text{ odd} \end{cases}.
\end{aligned}
\tag{4.21}
$$

This is similar to $H^{(3)}_{\text{eff}}(\hexagon)$, exchanging a string of spins around a hexagon, but includes a pair of centre-vertex spin exchanges, analogous to the loop move identified in the Ising model in section 2.2.2. The v indices in $B^{ij}_{\hexagon}$ are defined modulo 5 and the ellipsis corre-

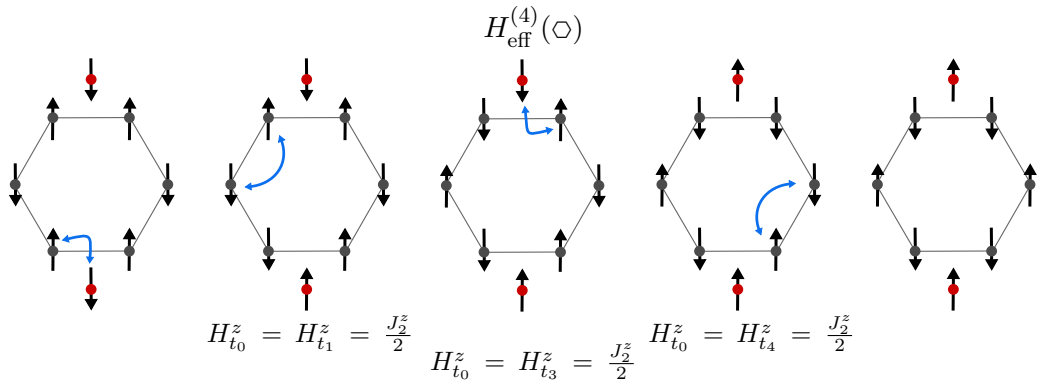

Figure 4.3: A process, $B^{03}_{\hexagon}$, contributing to the non-constant fourth order hexagonal loop term. The convention for labelling of the tetrahedra making up the loop is shown in fig. 4.2. Sites at the centre of tetrahedra are red, vertices grey.

sponds to a string of alternating S^+, S^- operators. Explicitly writing out some of these terms for different i, j,

$$\begin{aligned} B^{02}_{\hexagon} &= S^+_{c,0}S^-_{c,2}S^-_{v,0}S^+_{v,1}S^+_{v,2}S^-_{v,3}S^+_{v,4}S^-_{v,5}, \\ B^{03}_{\hexagon} &= S^+_{c,0}S^+_{c,3}S^-_{v,0}S^+_{v,1}S^-_{v,2}S^-_{v,3}S^+_{v,4}S^-_{v,5}. \end{aligned} \tag{4.22}$$

We left out $B^{ii}_{\hexagon}$ terms which have the same effect as a third order loop, with the centre spin on tetrahedron i mediating an effective $J_2^\perp$ term between its vertices, effectively rescaling $H^{(3)}_{\text{eff}}(\hexagon)$. The factor of 12 in K_2 comes from the six different permutations of $H_1^\perp, H_2^\perp$ and the fact that for given i, j, which fixes the $J_1^\perp$ contribution, there is a choice of two positions on the hexagon for the first $J_2^\perp$ contribution, which then fixes the position of the second. For example, in fig. 4.3, the $J_2^\perp$ flip of vertex spins can occur in either order.

For simplicity, we ignore $H^{(4)}_{\text{eff}}(\hexagon)$; we do not expect that this term will qualitatively change the properties of H_{eff}.

Therefore, our effective Hamiltonian up to fourth order is

$$H_{\text{eff}} = K_1 \sum_{\hexagon} \left(A_{\hexagon} + A^\dagger_{\hexagon} \right) - K_2 \sum_{\hexagon} \left(B_{\hexagon} + B^\dagger_{\hexagon} \right), \tag{4.23}$$

which acts within the 3:1 manifold.

4.2.2 Properties of H_{eff}

We now consider the qualitative properties of H_{eff}, extending the HFB mapping to a lattice gauge theory so that the centre spins are included, as well as relating H_{eff} to quantum dimer models.

First, the vertex spins can be expressed in terms of directed quantum rotor variables,

$$S^z_{v_i} \to \sigma_r e_{rr'}, \qquad S^\pm_{v_i} \to e^{\pm i\sigma_r a_{rr'}}, \tag{4.24}$$

where r, r' label diamond sites (i.e the centre sites) and rr' the link joining the two sites (i.e the link corresponds to a vertex site). The eigenvalues of $e_{rr'}$ are the set of all half-integers, whereas those of $a_{rr'} \in [0, 2\pi)$. This rewriting is exact provided the eigenvalue constraint $e_{rr'} \in \{-1/2, 1/2\}$ is enforced. These variables are conjugate, $[a_{rr'}, e_{rr'}] = i$ and can be interpreted as a vector potential and electric field respectively. Using this mapping, the effective Hamiltonian up to third order is

$$H^{(3)}_{\text{rotor}} = U_e \sum_{\langle rr' \rangle} e^2_{rr'} + 2K_1 \sum_{\hexagon} \cos(\text{curl}\, a)_{\hexagon}, \tag{4.25}$$

where

$$(\text{curl}\, a)_{\hexagon} = \sum_{i=0}^{5} a_{r_i r_{i+1}}. \tag{4.26}$$

We use the convention of labelling diamond sites making up a hexagonal loop in the same clockwise fashion as for the vertex sites. To enforce the constraint on the $e_{rr'}$, one should take the limit $(U_e/K_1) \to \infty$. In terms of the rotors

$$G_r = \cdots + \text{div}(e)_r, \qquad \text{div}(e)_r = \sum_{r' \to r} e_{rr'}, \tag{4.27}$$

where r' are the nearest neighbours (on the diamond lattice) of the site r. This is a U(1) lattice gauge theory, since $[H^{(3)}_{\text{rotor}}, G_r] = 0$ and G_r generates the local U(1) transformation

$$a_{rr'} \to a_{rr'} + \chi_{r'} - \chi_r. \tag{4.28}$$

Numerical simulations [145] showed that the corresponding (non-overlapping) quantum dimer model to $H^{(3)}_{\text{rotor}}$ is a quantum liquid, which means that $H^{(3)}_{\text{rotor}}$ is deconfined for all U_e/K_1 in the $\text{div}(e)_r = 0$ sector of the theory. In contrast to the pyrochlore, we have additional variables (the centre spins) which appear in the Ising ground state constraint $G_r = 0$. Therefore we are interested in the properties of the theory in a different gauge sector to the pyrochlore case, where it is a priori not known if it will be deconfined in the $(U_e/K_1) \to \infty$ limit.

We can rewrite the centre spins as static charges,

$$2S^z_r \to -\sigma_r q_r, \tag{4.29}$$

for $\gamma = 2$, and the constraint to the physical gauge sector becomes

$$\text{div}(e)_r = q_r, \tag{4.30}$$

where $q_r \in \{-1, 1\}$. Since the q_r do not appear explicitly in $H^{(3)}_{\text{rotor}}$, the static charge configuration is an external parameter we are free to choose. If the theory is deconfined in the $G_r = 0$ gauge sector, then static charges will interact via a Coulomb potential. In this case, the charge background with the lowest energy would be the Zincblende structure, with positive and negative charges occupying each sublattice of the diamond lattice respectively. In terms of spins, this corresponds to a ferromagnetic alignment of the central

spins. Since $H^{(3)}_{\text{eff}}$ does not couple sectors with different centre spin configurations this implies spontaneous breaking of spatial inversion symmetry by selection of one of the two degenerate ways to obtain a Zincblende structure. In terms of spins this is a spontaneous breaking of spin inversion symmetry, choosing one of $S^z_i = +(-)1/2$ for all centre spins. This implies the possibility of a symmetry-broken QSL phase, however the degeneracy associated with the symmetry-breaking would generically be lifted at higher orders of the perturbation theory.

A complementary view to the effective gauge theory is instead to think of $H^{(3)}_{\text{eff}}$ as a variant of a dimer model (see section 1.6.1). Mapping the vertex spins to dimers, such that $S^z_i = +(-)1/2$ corresponds to the presence(absence) of a dimer on the corresponding link of the diamond lattice. In order to respect the 3:1 constraint, if the centre spin on a diamond site is $+1/2$, then there must be only one dimer touching that site, whereas if the centre spin is $-1/2$, then the constraint is that three dimers touch that site. Therefore, in the dimer language,

$$H^{(3)}_{\text{eff}}(\hexagon) = K_1 \sum_{\hexagon} \Bigg(\left|\right\rangle\left\langle\right| + \left|\right\rangle\left\langle\right| \Bigg), \tag{4.31}$$

which acts on different Hilbert spaces depending on the central spin configuration, giving rise to what can be thought of as a family of separate dimer models. The Hilbert space can be further divided into sectors within which configurations are connected by $A^{(\dagger)}_h = \left|\right\rangle\left\langle\right| \left(\left|\right\rangle\left\langle\right| \right)$. The Hamiltonian can be brought to the Rokhsar-Kivelson (RK) form [129] by adding a "chemical potential",

$$H_{\text{RK}} = -|K_1| \sum_{\hexagon} \Bigg(\left|\right\rangle\left\langle\right| + \left|\right\rangle\left\langle\right| \Bigg) + \mu \sum_{\hexagon} \Bigg(\left|\right\rangle\left\langle\right| + \left|\right\rangle\left\langle\right| \Bigg). \tag{4.32}$$

At the RK point, $|K_1| = \mu$, in each disconnected sector, the ground state is the equal superposition of all valid 3:1 vertex spin configurations, a quantum dimer liquid. All of these ground states are degenerate at the RK point, but the degeneracy will be broken away from it. The question of whether the ground state of $H^{(3)}_{\text{rotor}}$ is deconfined is equivalent to asking whether the quantum dimer liquid at the RK point survives to $\mu = 0$, in the centre spin configuration sector which has the lowest energy ground state.

Note that, for centre spins all up (or down, mapping down vertex spins to the presence of a dimer instead), the Hilbert space of vertex spins, is the same as the Hilbert space of non-overlapping dimers on the diamond lattice which is the model studied in [131, 206, 207]. Ref. [131] showed numerically that the quantum liquid only survives down to $\mu_c = 0.75(2)/|K_1|$, where it transitions into an ordered state called the R state. This is adiabatically connected to the $\mu \to -\infty$ ground state of maximal number of flippable plaquettes. This suggests, though does not prove, that the ground state of $H^{(3)}_{\text{eff}}$ is ordered, since, if $H^{(3)}_{\text{rotor}}$ is deconfined in all sectors, the lowest energy charge configuration is that corresponding to ferromagnetic centres. In that sector a confined phase is actually lower in

energy. It is nevertheless possible that the component of the energy not coming from the static charge configuration makes the deconfined phase of another sector lower in energy. Furthermore, higher order terms in the perturbation theory introduce non-zero matrix elements between different centre spin configurations, which means this picture breaks down. Even if the ground state of $H^{(3)}_{\text{eff}}$ is ordered, higher order terms could ultimately melt the order.

Moving on to higher order, we map the centre spins to Abrikosov fermions [22], where the mapping depends on the sublattice of the spins, such that

$$\begin{gathered} S^z_r = -\frac{\sigma_r}{2}\Big(f^\dagger_{r+}f_{r+} - f^\dagger_{r-}f_{r-}\Big), \\ S^+_r = \begin{cases} f^\dagger_{r-}f_{r+}, & r \in a \\ f^\dagger_{r+}f_{r-}, & r \in b \end{cases}, \qquad S^-_r = \begin{cases} f^\dagger_{r+}f_{r-}, & r \in a \\ f^\dagger_{r-}f_{r+}, & r \in b \end{cases}. \end{gathered} \tag{4.33}$$

We label the fermion flavour by an electric charge $+, -$, since now

$$G_r = n_{r-} - n_{r+} + \operatorname{div}(e)_r, \tag{4.34}$$

so in the $G_r = 0$ sector

$$\operatorname{div}(e)_r = n_{r+} - n_{r-}, \tag{4.35}$$

where we have introduced the number operator $n_{r\pm} = f^\dagger_{r\pm}f_{r\pm}$. This is an exact mapping provided the constraint $n_{r+} + n_{r-} = 1$ is enforced, i.e there is one fermion per site. In terms of the fermion operators,

$$B^{ij}_{\hexagon} = \begin{cases} f^\dagger_{r_i-}f_{r_i+}f^\dagger_{r_j+}f_{r_j-}e^{i(\operatorname{curl}^* a)_{ij}}, \text{ for } j-i \text{ even}, \ r_i, r_j \in a \\ f^\dagger_{r_i+}f_{r_i-}f^\dagger_{r_j-}f_{r_j+}e^{-i(\operatorname{curl}^* a)_{ij}}, \text{ for } j-i \text{ even}, \ r_i, r_j \in b \\ f^\dagger_{r_i-}f_{r_i+}f^\dagger_{r_j+}f_{r_j-}e^{i(\operatorname{curl}^* a)_{ij}}, \text{ for } j-i \text{ odd}, \ r_i \in a, \ r_j \in b \\ f^\dagger_{r_i+}f_{r_i-}f^\dagger_{r_j-}f_{r_j+}e^{-i(\operatorname{curl}^* a)_{ij}}, \text{ for } j-i \text{ odd}, \ r_i \in b, \ r_j \in a \end{cases} \tag{4.36}$$

where we define a modified curl,

$$(\operatorname{curl}^* a)_{ij} = -\sum_{i'=i}^{j-1} a_{r_{i'}r_{i'+1}} + \sum_{i'=j}^{i-1} a_{r_{i'}r_{i'+1}}. \tag{4.37}$$

The fourth order part of the effective Hamiltonian can be written compactly as

$$\begin{gathered} H^{(4)}_{\text{eff}} = -K_2 \sum_{\hexagon} \sum_{i=0}^{5} \sum_{j=i+1}^{5} \Big(\tilde{B}^{ij}_{\hexagon} + \text{h.c}\Big), \\ \tilde{B}^{ij}_{\hexagon} = f^\dagger_{r_i-}f_{r_i+}f^\dagger_{r_j+}f_{r_j-}e^{i(\operatorname{curl}^* a)_{ij}}. \end{gathered} \tag{4.38}$$

A $\tilde{B}^{ij}_{\hexagon}$ operator hops a $+$ fermion from site i to j and a $-$ fermion from site j to i, flipping the electric field on the two paths between them, thereby leaving G_r invariant. This is shown schematically in fig. 4.4.

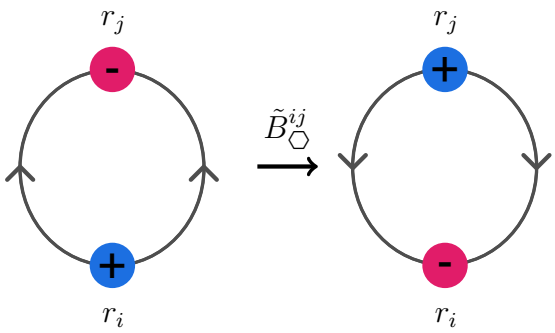

Figure 4.4: Schematic representation of the action of the $\tilde{B}^{ij}_{\hexagon}$ operator. The charges represent the fermionic spinons and the grey lines the electric field, $e_{rr'}$. The operators act on length-6 hexagonal loops.

Thus the effective Hamiltonian, eq. (4.23), in the fermion and rotor variables is

$$\begin{aligned} H^{(4)}_{\text{rotor}} &= U_e \sum_{\langle rr' \rangle} e^2_{rr'} + U_f \sum_r \left((n_{r+} - \frac{1}{2})(n_{r-} - \frac{1}{2}) \right) \\ +2K_1 \sum_{\hexagon} \cos(\text{curl}\, a)_{\hexagon} &- K_2 \sum_{\hexagon} \sum_{i=0,j=i+1}^{5} \left(f^\dagger_{r_i-} f_{r_i+} f^\dagger_{r_j+} f_{r_j-} e^{i(\text{curl}^* a)_{ij}} + \text{h.c} \right), \end{aligned} \tag{4.39}$$

which corresponds to the physical H_{eff} in the $U_e, U_f \to \infty$ limit and $G_r = 0$ gauge sector, which enforces the appropriate constraints on the rotors and fermions. By construction, $[H^{(4)}_{\text{rotor}}, G_r] = 0$, which is a U(1) local symmetry, due to the gauge transformation

$$\begin{aligned} a_{r_i r_j} &\to a_{r_i r_j} + \chi_{r_j} - \chi_{r_i}, \\ f_{r_i+} \to f_{r_i+} e^{-i\chi_{r_i}},\ & f_{r_i-} \to f_{r_i-} e^{i\chi_{r_i}}, \end{aligned} \tag{4.40}$$

for $\chi_r \in [0, 2\pi)$. Thus the effective theory is a frustrated U(1) lattice gauge theory with fermionic matter. Due to the coupling of different central spin sectors, one cannot simply write down a relevant RK-type quantum dimer model.

HFB discussed the topological properties of the U(1) QSL on the pyrochlore in terms of the electric flux

$$\Phi^E_k = \sum_{\langle rr' \rangle \in \text{plane}} e_{rr'}, \tag{4.41}$$

where the sum is over all links which pierce a plane oriented perpendicular to the cubic axis, $k \in \{x, y, z\}$, which is analogous to the winding number in classical spin-ice. This quantity is not conserved by $H^{(4)}_{\text{rotor}}$ since

$$[\Phi^E_k, \tilde{B}^{ij}_{\hexagon}] = -2\tilde{B}^{ij}_{\hexagon}, \qquad [\Phi^E_k, (\tilde{B}^{ij}_{\hexagon})^\dagger] = (2\tilde{B}^{ij}_{\hexagon})^\dagger, \tag{4.42}$$

where i, j are such that the hexagonal loop is intersected by the plane. This is the same algebra as raising and lowering operators, where $(\tilde{B}^{ij}_{\hexagon})^\dagger$ and $\tilde{B}^{ij}_{\hexagon}$ raise and lower the eigenvalue of Φ^E_k by 2 respectively. The $\tilde{B}^{ij(\dagger)}_{\hexagon}$ are analogous to the moves in the classical Ising

model which change the winding number by ± 2, illustrated in fig. 2.3. In the quantum effective model this property of Φ_k^E is a manifestation of the fact that sectors with even or odd numbers of $+1/2$ centre spins have internal non-zero matrix elements but are mutually disconnected. In the charge language this translates to the fact that the difference in population of the charge species, i.e the total charge,

$$N_q = N_+ - N_- = \sum_r \Big(n_{r+} - n_{r-} \Big), \tag{4.43}$$

is conserved.

The question going forwards is if the ground state of eq. (4.39) is deconfined in the physical limit and gauge sector. If so, this corresponds to a $\mathrm{U}(1)$ QSL, similar to the $\mathrm{U}(1)$ QSL on the pyrochlore. Another possibility is for single fermions (spinons) to be deconfined but for spinon pairs to condense, which would lead to a $\mathbb{Z}_2$ QSL via the Higgs mechanism [22]. Also pertinent, is whether the $\gamma = 2$ point, where eq. (4.39) was derived, is a special point in the parameter space or whether the low energy properties of the model in a broader region of the parameter space can be understood in the lattice gauge theory/quantum dimer model picture. In the following sections, we attempt to gain some insight using parton mean-field and exact diagonalization calculations.

4.3 Gauge mean-field theory

Applying the gauge mean-field theory (gMFT) method, originally introduced in [149], we investigate, at $\gamma = 2$ and assuming the ground state is deconfined, what the ground state phase boundaries are, and whether the deconfined phase is a $\mathrm{U}(1)$ or $\mathbb{Z}_2$ QSL. Ultimately, we construct a mean-field ground state phase diagram in $J_1^\perp$, $J_2^\perp$ space.

The convention for vectors pointing from a to b diamond sites we use is

$$\mathbf{e}_1 = \frac{1}{4}(1,1,1),\ \mathbf{e}_2 = \frac{1}{4}(1,-1,-1),\ \mathbf{e}_3 = \frac{1}{4}(-1,1,-1),\ \mathbf{e}_4 = \frac{1}{4}(-1,-1,1). \tag{4.44}$$

Our starting point is the XXZ Hamiltonian written as

$$H = \frac{J_2^z}{2} \sum_{\mathbf{r}} Q_{\mathbf{r}}^2 + J_1^\perp \sum_{\mathbf{r}} \left(S_{\mathbf{r}}^+ \sum_\mu S_{\mathbf{r},\mathbf{r}+\sigma_{\mathbf{r}}\mathbf{e}_\mu}^- + \mathrm{h.c} \right) + J_2^\perp \sum_{\mathbf{r}} \sum_{\mu \neq \nu} S_{\mathbf{r},\mathbf{r}+\sigma_{\mathbf{r}}\mathbf{e}_\mu}^+ S_{\mathbf{r},\mathbf{r}+\sigma_{\mathbf{r}}\mathbf{e}_\nu}^-, \tag{4.45}$$

where

$$Q_{\mathbf{r}} = \sigma_{\mathbf{r}} \left(\gamma S_{\mathbf{r}}^z + \sum_{\mathbf{r}' \to \mathbf{r}} S_{\mathbf{r}\mathbf{r}'}^z \right), \tag{4.46}$$

which is the quantity we called $G_{\mathbf{r}}$ in the previous section. We explicitly make the diamond lattice positions, $\mathbf{r}$, a vector and $\mu, \nu \in \{1 \ldots 4\}$. For general γ, the possible eigenvalues of $Q_{\mathbf{r}}$ are $\{-2 \pm \gamma/2, -1 \pm \gamma/2, \pm\gamma/2, 1 \pm \gamma/2, 2 \pm \gamma/2\}$. $Q_{\mathbf{r}}$ is treated as the angular

momentum of a quantum rotor, with the conjugate angular variable $\zeta_{\mathbf{r}}$, such that $[\zeta_{\mathbf{r}}, Q_{\mathbf{r}'}] = i\delta_{\mathbf{r}\mathbf{r}'}$. The raising/lowering operators of $Q_{\mathbf{r}}$ are

$$\Phi^\dagger_{\mathbf{r}} = e^{i\zeta_{\mathbf{r}}}, \qquad \Phi_{\mathbf{r}} = e^{-i\zeta_{\mathbf{r}}}, \tag{4.47}$$

such that

$$[Q_{\mathbf{r}}, \Phi^\dagger_{\mathbf{r}'}] = \Phi^\dagger_{\mathbf{r}'}\delta_{\mathbf{r}\mathbf{r}'}, \qquad [Q_{\mathbf{r}}, \Phi_{\mathbf{r}'}] = -\Phi_{\mathbf{r}'}\delta_{\mathbf{r}\mathbf{r}'}. \tag{4.48}$$

The $\Phi^{(\dagger)}_{\mathbf{r}}$ are the annihilation(creation) operators of charge-1 bosonic spinons which must satisfy the constraint $|\Phi_{\mathbf{r}}|^2 = 1$. Due to the J_1 terms, it is also useful to introduce charge γ spinons,

$$\Psi_{\mathbf{r}} = e^{-i\gamma\zeta_{\mathbf{r}}}, \qquad [Q_{\mathbf{r}}, \Psi_{\mathbf{r}'}] = -\gamma\Psi_{\mathbf{r}'}\delta_{\mathbf{r}\mathbf{r}'}, \tag{4.49}$$

with corresponding relations for the creation operators.

The approach can now be summarized as follows. We define an additional Hilbert space $\mathcal{H}_Q$ for the $Q_{\mathbf{r}}$, and consider the enlarged Hilbert space $\mathcal{H} = \mathcal{H}_Q \otimes \mathcal{H}_S$, where $\mathcal{H}_S$ is the Hilbert space of the spins. After constructing a parton Hamiltonian which acts in $\mathcal{H}$ such that it will reproduce all the matrix elements of eq. (4.45) in $\mathcal{H}_s$, we treat $Q_{\mathbf{r}}$ as independent of the spin operators, which would recover the physical theory provided we enforce eq. (4.46) as a constraint. It is an uncontrolled approximation of the method that this constraint is not enforced, with $Q_{\mathbf{r}}$ ultimately integrated over all values in the range $[-\infty, \infty]$ [153].

Now, to construct the appropriate parton representation of the spin operators, we should look at the effect of the $J_1^\perp$ and $J_2^\perp$ terms of eq. (4.45) on the eigenvalues of $Q_{\mathbf{r}}$. Consider a state in the S^z basis, then acting with $S^+_{\mathbf{r},\mathbf{r}+\sigma_{\mathbf{r}}\mathbf{e}_\mu} S^-_{\mathbf{r},\mathbf{r}+\sigma_{\mathbf{r}}\mathbf{e}_\nu}$ maps

$$Q_{\mathbf{r}} \to Q_{\mathbf{r}}, \qquad Q_{\mathbf{r}+\sigma_{\mathbf{r}}\mathbf{e}_\mu} \to Q_{\mathbf{r}+\sigma_{\mathbf{r}}\mathbf{e}_\mu} - \sigma_{\mathbf{r}}, \qquad Q_{\mathbf{r}+\sigma_{\mathbf{r}}\mathbf{e}_\nu} \to Q_{\mathbf{r}+\sigma_{\mathbf{r}}\mathbf{e}_\nu} + \sigma_{\mathbf{r}}, \tag{4.50}$$

whereas $S^+_{\mathbf{r}} S^-_{\mathbf{r},\mathbf{r}+\sigma_{\mathbf{r}}\mathbf{e}_\mu}$ maps

$$Q_{\mathbf{r}} \to Q_{\mathbf{r}} + \sigma_{\mathbf{r}}(\gamma - 1), \qquad Q_{\mathbf{r}+\sigma_{\mathbf{r}}\mathbf{e}_\mu} \to Q_{\mathbf{r}+\sigma_{\mathbf{r}}\mathbf{e}_\mu} + \sigma_{\mathbf{r}}, \tag{4.51}$$

and similarly for $S^-_{\mathbf{r}} S^+_{\mathbf{r},\mathbf{r}+\sigma_{\mathbf{r}}\mathbf{e}_\mu}$. This is illustrated in fig. 4.5. The physical spins are decomposed into spinons and pseudospins, $s^\alpha_{\mathbf{r}}$,

$$\begin{aligned}
&S^z_{\mathbf{r}} = s^z_{\mathbf{r}}, && S^z_{\mathbf{r},\mathbf{r}+\sigma_{\mathbf{r}}\mathbf{e}_\mu} = s^z_{\mathbf{r},\mathbf{r}+\sigma_{\mathbf{r}}\mathbf{e}_\mu}, && \\
&S^+_{\mathbf{r}} = \Psi^\dagger_{\mathbf{r}} s^+_{\mathbf{r}}, && S^+_{\mathbf{r},\mathbf{r}+\mathbf{e}_\mu} = \Phi^\dagger_{\mathbf{r}} s^+_{\mathbf{r},\mathbf{r}+\mathbf{e}_\mu} \Phi_{\mathbf{r}+\mathbf{e}_\mu}, && \mathbf{r} \in a, \\
&S^+_{\mathbf{r}} = \Psi_{\mathbf{r}} s^+_{\mathbf{r}}, && S^+_{\mathbf{r},\mathbf{r}-\mathbf{e}_\mu} = \Phi^\dagger_{\mathbf{r}-\mathbf{e}_\mu} s^+_{\mathbf{r},\mathbf{r}+\mathbf{e}_\mu} \Phi_{\mathbf{r}}, && \mathbf{r} \in b,
\end{aligned} \tag{4.52}$$

and corresponding Hermitian conjugates. The spinons account for the effect on $Q_{\mathbf{r}}$ and the pseudospins ensure the correct matrix elements. The pseudospins obey the normal spin $1/2$ algebra. Vertex pseudospins can be related to the electric field and vector potential of the perturbation theory,

$$s^z_{\mathbf{r},\mathbf{r}'} \to \sigma_{\mathbf{r}} e_{\mathbf{r}\mathbf{r}'}, \qquad s^\pm_{\mathbf{r},\mathbf{r}'} \to e^{\pm i\sigma_{\mathbf{r}} a_{\mathbf{r}\mathbf{r}'}}, \tag{4.53}$$

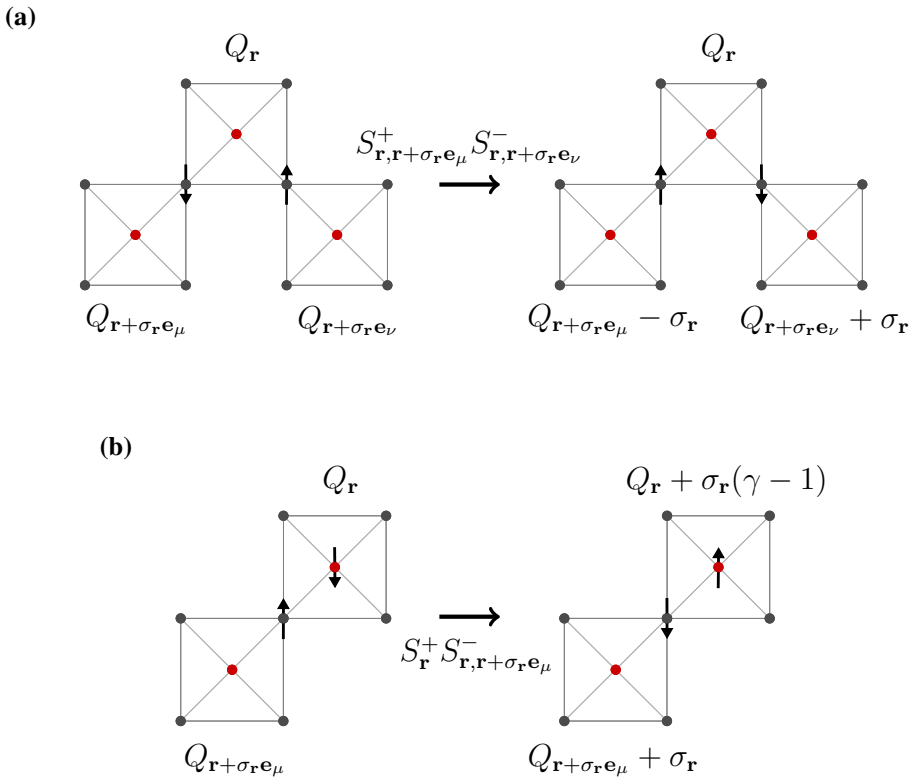

Figure 4.5: Illustration of the effect of the $J_2^\perp$ (**a**) and $J_1^\perp$ (**b**) terms on the eigenvalues of $Q_{\mathbf{r}}$. This can be incorporated into the parton decomposition of the spin operators by attaching the appropriate spinon creation/annihilation operators.

and the centres with the fermions, as in eq. (4.33).

With this rewriting, eq. (4.45) becomes

$$\begin{aligned} H_{\mathrm{gMFT}} = \frac{J_2^z}{2} \sum_{\mathbf{r}} Q_{\mathbf{r}}^2 \\ + J_1^\perp \sum_{\mu} \Bigg(\sum_{\mathbf{r}\in a} (\Psi_{\mathbf{r}}^\dagger \Phi_{\mathbf{r}+\mathbf{e}_\mu}^\dagger \Phi_{\mathbf{r}} s_{\mathbf{r}}^+ s_{\mathbf{r},\mathbf{r}+\mathbf{e}_\mu}^- + \Psi_{\mathbf{r}} \Phi_{\mathbf{r}}^\dagger \Phi_{\mathbf{r}+\mathbf{e}_\mu} s_{\mathbf{r}}^- s_{\mathbf{r},\mathbf{r}+\mathbf{e}_\mu}^+) \\ + \sum_{\mathbf{r}\in b} (\Psi_{\mathbf{r}} \Phi_{\mathbf{r}}^\dagger \Phi_{\mathbf{r}-\mathbf{e}_\mu} s_{\mathbf{r}}^+ s_{\mathbf{r},\mathbf{r}-\mathbf{e}_\mu}^- + \Psi_{\mathbf{r}}^\dagger \Phi_{\mathbf{r}-\mathbf{e}_\mu}^\dagger \Phi_{\mathbf{r}} s_{\mathbf{r}}^- s_{\mathbf{r},\mathbf{r}-\mathbf{e}_\mu}^+) \Bigg) \\ + J_2^\perp \sum_{\mu\neq\nu} \Bigg(\sum_{\mathbf{r}\in a} \Phi_{\mathbf{r}+\mathbf{e}_\mu}^\dagger \Phi_{\mathbf{r}+\mathbf{e}_\nu} s_{\mathbf{r},\mathbf{r}+\mathbf{e}_\mu}^- s_{\mathbf{r},\mathbf{r}+\mathbf{e}_\nu}^+ + \sum_{\mathbf{r}\in b} \Phi_{\mathbf{r}-\mathbf{e}_\mu}^\dagger \Phi_{\mathbf{r}-\mathbf{e}_\nu} s_{\mathbf{r},\mathbf{r}-\mathbf{e}_\mu}^+ s_{\mathbf{r},\mathbf{r}-\mathbf{e}_\nu}^- \Bigg). \end{aligned} \tag{4.54}$$

The two different species of spinons makes working with H_{gMFT} in this form difficult. However, for $\gamma = 2$, the theory can be simplified. The physical spectrum becomes $Q_{\mathbf{r}} \in \{-3, -2, -1, 0, 1, 2, 3\}$ and the effect of the $J_1^\perp$ term on $Q_{\mathbf{r}}$ can be accounted for by letting

$\Psi_{\mathbf{r}} = \Phi_{\mathbf{r}}^2$. Therefore, for $\gamma = 2$,

$$\begin{aligned} H_{\mathrm{gMFT}} = \frac{J_2^z}{2}\sum_{\mathbf{r}} Q_{\mathbf{r}}^2 \\ + J_1^{\perp}\sum_{\mu}\Bigg(\sum_{\mathbf{r}\in a}(\Phi_{\mathbf{r}}^{\dagger}\Phi_{\mathbf{r}+\mathbf{e}_\mu}^{\dagger}s_{\mathbf{r}}^{+}s_{\mathbf{r},\mathbf{r}+\mathbf{e}_\mu}^{-} + \Phi_{\mathbf{r}}\Phi_{\mathbf{r}+\mathbf{e}_\mu}s_{\mathbf{r}}^{-}s_{\mathbf{r},\mathbf{r}+\mathbf{e}_\mu}^{+}) \\ + \sum_{\mathbf{r}\in b}(\Phi_{\mathbf{r}}\Phi_{\mathbf{r}-\mathbf{e}_\mu}s_{\mathbf{r}}^{+}s_{\mathbf{r},\mathbf{r}-\mathbf{e}_\mu}^{-} + \Phi_{\mathbf{r}}^{\dagger}\Phi_{\mathbf{r}-\mathbf{e}_\mu}^{\dagger}s_{\mathbf{r}}^{-}s_{\mathbf{r},\mathbf{r}-\mathbf{e}_\mu}^{+})\Bigg) \\ + J_2^{\perp}\sum_{\mu\neq\nu}\Bigg(\sum_{\mathbf{r}\in a}\Phi_{\mathbf{r}+\mathbf{e}_\mu}^{\dagger}\Phi_{\mathbf{r}+\mathbf{e}_\nu}s_{\mathbf{r},\mathbf{r}+\mathbf{e}_\mu}^{-}s_{\mathbf{r},\mathbf{r}+\mathbf{e}_\nu}^{+} + \sum_{\mathbf{r}\in b}\Phi_{\mathbf{r}-\mathbf{e}_\mu}^{\dagger}\Phi_{\mathbf{r}-\mathbf{e}_\nu}s_{\mathbf{r},\mathbf{r}-\mathbf{e}_\mu}^{+}s_{\mathbf{r},\mathbf{r}-\mathbf{e}_\nu}^{-}\Bigg), \end{aligned} \tag{4.55}$$

By construction, recalling that $Q_{\mathbf{r}}$ and the pseudospins should be treated as independent variables, the quantity $G_{\mathbf{r}} = Q_{\mathbf{r}} - \sigma_{\mathbf{r}}\left(2s_{\mathbf{r}}^z + \sum_\mu s_{\mathbf{r},\mathbf{r}+\sigma_{\mathbf{r}}\mathbf{e}_\mu}^z\right)$ commutes with H_{gMFT}. The physical sector is where $G_{\mathbf{r}} = 0$, which also enforces the constraint on the angular momentum of the quantum rotors. This is a local U(1) symmetry, H_{gMFT} is invariant under the gauge transformation

$$\Phi_{\mathbf{r}} \to \Phi_{\mathbf{r}}e^{-i\chi_{\mathbf{r}}}, \qquad s_{\mathbf{r},\mathbf{r}'}^{\pm} \to s_{\mathbf{r},\mathbf{r}'}^{\pm}e^{\pm i\sigma_{\mathbf{r}}(\chi_{\mathbf{r}'}-\chi_{\mathbf{r}})}, \qquad s_{\mathbf{r}}^{\pm} \to s_{\mathbf{r}}^{\pm}e^{\mp 2i\sigma_{\mathbf{r}}\chi_{\mathbf{r}}} \tag{4.56}$$

with $\chi_{\mathbf{r}} \in [0, 2\pi)$, which is analogous to the gauge transformation identified in the perturbation theory.

4.3.1 Mean-field Decoupling

We construct a mean-field Hamiltonan, H_{MF} through the decoupling,

$$\begin{aligned} &\Phi_{\mathbf{r}}\Phi_{\mathbf{r}'} \to \langle\Phi_{\mathbf{r}}\Phi_{\mathbf{r}'}\rangle + \delta(\Phi_{\mathbf{r}}\Phi_{\mathbf{r}'}), \\ &s_{\mathbf{r}}^{\alpha} \to \langle s_{\mathbf{r}}^{\alpha}\rangle + \delta(s_{\mathbf{r}}^{\alpha}), \\ &s_{\mathbf{r},\mathbf{r}'}^{\alpha} \to \langle s_{\mathbf{r},\mathbf{r}'}^{\alpha}\rangle + \delta(s_{\mathbf{r},\mathbf{r}'}^{\alpha}), \end{aligned} \tag{4.57}$$

retaining terms up to first order in the fluctuations. The mean-field Hamiltonian can be separated into a central pseudospin, vertex pseudospin and rotor part,

$$H_{\mathrm{MF}} = \sum_{x=a,b} H_x + \sum_{\mu} H_\mu + H_{\mathrm{rotor}}. \tag{4.58}$$

We will attempt to find a self-consistent mean-field solution for the $J_{1,2}^{\perp} < 0$ region of the parameter space. Possible mean-field ground states and their associated expectation values are summarized in table 4.2.

State	$\langle s^z_\mu \rangle$	$\langle s^\pm_\mu \rangle$	$\langle s^z_{\mathbf{r}} \rangle$	$\langle s^\pm_{\mathbf{r}} \rangle$	$\langle \Phi_{\mathbf{r}} \Phi_{\mathbf{r}'} \rangle$	$\langle \Phi^\dagger_{\mathbf{r}} \Phi_{\mathbf{r}'} \rangle$	$\langle \Phi_{\mathbf{r}} \rangle$
$\mathrm{U}(1)$ QSL	0	$\neq 0$	0	$\neq 0$	0	$\neq 0$	0
$\mathbb{Z}_2$ QSL	0	$\neq 0$	0	$\neq 0$	$\neq 0$	$\neq 0$	0
XY Ferro	0	$\neq 0$	0	$\neq 0$	$\neq 0$	$\neq 0$	$\neq 0$

Table 4.2: Possible ground states of H_{MF} and their characteristic pseudospin and spinon expectation values. $\langle \Phi_{\mathbf{r}} \rangle$ does not enter the mean-field theory directly but a non-zero value implies long-range off-diagonal order [149].

4.3.2 Zero-flux Ansatz

As in [150] we make a zero-flux ansatz for the ground state, arguing that replacing the variables in eq. (4.39) with mean-field averages, the energy is minimized when $\bar{a}_{\mathbf{r}\mathbf{r}'} = 0$ and $\langle f^\dagger_{\mathbf{r}-} f_{\mathbf{r}+} \rangle = \langle f^\dagger_{\mathbf{r}+} f_{\mathbf{r}-} \rangle$ is real for all $\mathbf{r}$. Relating these quantities to the pseudospin expectation values,

$$\begin{aligned} \langle s^\pm_{\mathbf{r},\mathbf{r}'} \rangle &= \left| \langle s^\pm_{\mathbf{r},\mathbf{r}'} \rangle \right| e^{\pm i \sigma_{\mathbf{r}} \bar{a}_{\mathbf{r}\mathbf{r}'}}, \\ \langle s^+_{\mathbf{r}_a} \rangle = \langle f^\dagger_{\mathbf{r}_a -} f_{\mathbf{r}_a +} \rangle, &\qquad \langle s^-_{\mathbf{r}_a} \rangle = \langle f^\dagger_{\mathbf{r}_a +} f_{\mathbf{r}_a -} \rangle, \\ \langle s^+_{\mathbf{r}_b} \rangle = \langle f^\dagger_{\mathbf{r}_b +} f_{\mathbf{r}_b -} \rangle, &\qquad \langle s^-_{\mathbf{r}_b} \rangle = \langle f^\dagger_{\mathbf{r}_b -} f_{\mathbf{r}_b +} \rangle, \end{aligned} \tag{4.59}$$

where $\mathbf{r}_{a(b)}$ is a diamond site on the $a(b)$ sublattice. Therefore, we assume that the expectation values of all pseudospins are real, which corresponds to a zero-flux state. As discussed in [150], one should in general compare the energies of mean-field ansätze with all possible flux patterns, which correspond to different projective symmetry groups [44]. However, given the known zero-flux nature of the $\mathrm{U}(1)$ QSL in the pyrochlore XXZ model with ferromagnetic $J^\perp$, and based off the relation between the pyrochlore and centred pyrochlore effective Hamiltonians in perturbation theory, the assumption of a zero-flux state on the centred pyrochlore lattice for ferromagnetic $J_1^\perp, J_2^\perp$ seems reasonable. We also assume that the other mean-field parameters respect the translational symmetry of the lattice.

Therefore the ansatz is

$$\begin{aligned} \langle s^+_{\mathbf{r},\mathbf{r}+\sigma_{\mathbf{r}}\mathbf{e}_\mu} \rangle = \langle s^-_{\mathbf{r},\mathbf{r}+\sigma_{\mathbf{r}}\mathbf{e}_\mu} \rangle = \langle s^\pm_\mu \rangle = \Delta, \\ \langle s^-_{\mathbf{r}_a} \rangle = \langle s^+_{\mathbf{r}_a} \rangle = s_a, \qquad \langle s^-_{\mathbf{r}_b} \rangle = \langle s^+_{\mathbf{r}_b} \rangle = s_b, \\ \langle \Phi^a_{\mathbf{r}} \Phi^b_{\mathbf{r}+\mathbf{e}_\mu} \rangle = \langle \Phi^b_{\mathbf{r}} \Phi^a_{\mathbf{r}-\mathbf{e}_\mu} \rangle = \alpha_\mu, \qquad \langle \Phi^{a\dagger}_{\mathbf{r}} \Phi^{b\dagger}_{\mathbf{r}+\mathbf{e}_\mu} \rangle = \langle \Phi^{b\dagger}_{\mathbf{r}} \Phi^{a\dagger}_{\mathbf{r}-\mathbf{e}_\mu} \rangle = \alpha^*_\mu, \\ \langle \Phi^{a\dagger}_{\mathbf{r}+\mathbf{e}_\mu-\mathbf{e}_\nu} \Phi^a_{\mathbf{r}} \rangle = \chi^a_{\mu\nu}, \qquad \langle \Phi^{a\dagger}_{\mathbf{r}} \Phi^a_{\mathbf{r}+\mathbf{e}_\mu-\mathbf{e}_\nu} \rangle = \chi^{a*}_{\mu\nu}, \\ \langle \Phi^{b\dagger}_{\mathbf{r}+\mathbf{e}_\mu} \Phi^b_{\mathbf{r}+\mathbf{e}_\nu} \rangle = \chi^b_{\mu\nu}, \qquad \langle \Phi^{b\dagger}_{\mathbf{r}+\mathbf{e}_\nu} \Phi^b_{\mathbf{r}+\mathbf{e}_\mu} \rangle = \chi^{b*}_{\mu\nu}, \end{aligned} \tag{4.60}$$

where $\mathbf{r}_{a(b)}$ is a diamond site on the $a(b)$ sublattice and $\Phi^{a(b)}$ indicates which sublattice the spinon operator is acting on. Note that the perturbation theory argument for s_a and s_b to be real implies that $s_a = s_b$, although we will not enforce this a priori.

The mean-field Hamiltonians for centre spins are

$$\begin{aligned} H_a &= J_1^\perp \sum_\mu \sum_{\mathbf{r}\in a} \left(\langle \Phi_{\mathbf{r}}^{a\dagger} \Phi_{\mathbf{r}+\mathbf{e}_\mu}^{b\dagger} \rangle \langle s_\mu^- \rangle s_{\mathbf{r}}^+ + \langle \Phi_{\mathbf{r}}^{a} \Phi_{\mathbf{r}+\mathbf{e}_\mu}^{b} \rangle \langle s_\mu^+ \rangle s_{\mathbf{r}}^- \right), \\ H_b &= J_1^\perp \sum_\mu \sum_{\mathbf{r}\in b} \left(\langle \Phi_{\mathbf{r}}^{b} \Phi_{\mathbf{r}-\mathbf{e}_\mu}^{a} \rangle \langle s_\mu^- \rangle s_{\mathbf{r}}^+ + \langle \Phi_{\mathbf{r}}^{b\dagger} \Phi_{\mathbf{r}-\mathbf{e}_\mu}^{a\dagger} \rangle \langle s_\mu^+ \rangle s_{\mathbf{r}}^- \right). \end{aligned} \tag{4.61}$$

Notice that $J_1^\perp$ is coupled to mean-field expectation values of the form $\langle \Phi_{\mathbf{r}} \Phi_{\mathbf{r}'} \rangle$, which, when finite, imply spinon pair condensation and therefore a $\mathbb{Z}_2$ QSL ground state. On the mean-field level, the $J_1^\perp$ term causes spinon pair condensation. Defining the dot product $a \cdot b = a^z b^z + a^+ b^+ + a^- b^-$ the mean-field Hamiltonians can be written as

$$H_x = \vec{h}_x \cdot \sum_{\mathbf{r}\in x} \vec{s}_{\mathbf{r}}, \tag{4.62}$$

where

$$\vec{h}_a = (\vec{h}_b)^* = (h^z, h^+, h^-) = J_1^\perp \Delta (0, \sum_\mu \alpha_\mu^*, \sum_\mu \alpha_\mu). \tag{4.63}$$

For a generic single-spin Hamiltonian $\vec{h} \cdot \vec{s}$, where $\vec{h} = (0, a, a^*)$, the eigenvalues and eigenvectors are

$$\lambda_\pm = \pm |a|, \qquad |x_\pm\rangle = \frac{1}{\sqrt{2}} \begin{pmatrix} \pm \frac{a}{|a|} \\ 1 \end{pmatrix}, \tag{4.64}$$

and therefore the ground state expectation values

$$\langle s^+ \rangle = -\frac{a^*}{2|a|}, \qquad \langle s^- \rangle = -\frac{a}{2|a|}. \tag{4.65}$$

Evaluating these for the centre spins

$$s_a = s_b = s = -\frac{J_1^\perp \Delta \sum_\mu \alpha_\mu}{2\left| J_1^\perp \Delta \sum_\mu \alpha_\mu \right|} = -\frac{J_1^\perp \Delta \sum_\mu \alpha_\mu^*}{2\left| J_1^\perp \Delta \sum_\mu \alpha_\mu^* \right|}, \tag{4.66}$$

which tells us that $\sum_\mu \alpha_\mu$ is real. Furthermore, assuming that $\sum_\mu \alpha_\mu$, along with Δ, are positive, we obtain $s = 1/2$, since $J_1^\perp$ is negative.

For the vertex spins, the mean-field Hamiltonian is

$$\begin{aligned} H_\mu = J_1^\perp \sum_{\mathbf{r}\in a} \Bigg[& \left(\langle \Phi_{\mathbf{r}}^{a\dagger} \Phi_{\mathbf{r}+\mathbf{e}_\mu}^{b\dagger} \rangle \langle s_{\mathbf{r}_b}^- \rangle + \langle \Phi_{\mathbf{r}}^{a} \Phi_{\mathbf{r}+\mathbf{e}_\mu}^{b} \rangle \langle s_{\mathbf{r}_a}^- \rangle \right) s_\mu^+ \\ & + \left(\langle \Phi_{\mathbf{r}}^{a\dagger} \Phi_{\mathbf{r}+\mathbf{e}_\mu}^{b\dagger} \rangle \langle s_{\mathbf{r}_a}^+ \rangle + \langle \Phi_{\mathbf{r}}^{a} \Phi_{\mathbf{r}+\mathbf{e}_\mu}^{b} \rangle \langle s_{\mathbf{r}_b}^+ \rangle \right) s_\mu^- \Bigg] \\ + J_2^\perp \sum_{\mathbf{r}\in a} \sum_{\nu\neq\mu} \Bigg[& \left(\langle \Phi_{\mathbf{r}+\mathbf{e}_\nu}^{b\dagger} \Phi_{\mathbf{r}+\mathbf{e}_\mu}^{b} \rangle \langle s_\nu^- \rangle + \langle \Phi_{\mathbf{r}}^{a\dagger} \Phi_{\mathbf{r}+\mathbf{e}_\mu-e_\nu}^{a} \rangle \langle s_\nu^- \rangle \right) s_{\mathbf{r},\mathbf{r}+\mathbf{e}_\mu}^+ + \\ & \left(\langle \Phi_{\mathbf{r}+\mathbf{e}_\mu}^{b\dagger} \Phi_{\mathbf{r}+\mathbf{e}_\nu}^{b} \rangle \langle s_\nu^+ \rangle + \langle \Phi_{\mathbf{r}+\mathbf{e}_\mu-\mathbf{e}_\nu}^{a\dagger} \Phi_{\mathbf{r}}^{a} \rangle \langle s_\nu^+ \rangle \right) s_{\mathbf{r},\mathbf{r}+\mathbf{e}_\mu}^- \Bigg], \end{aligned} \tag{4.67}$$

where replacing the expectation values with the ansatz parameters,

$$H_\mu = \vec{h}_\mu \cdot \sum_{\mathbf{r}\in a} \vec{s}_{\mathbf{r},\mathbf{r}+\mathbf{e}_\mu}, \tag{4.68}$$

with

$$\vec{h}_\mu = \Big(0,\ 2J_1^\perp s\alpha_\mu + J_2^\perp \Delta\chi_\mu^*,\ 2J_1^\perp s\alpha_\mu + J_2^\perp \Delta\chi_\mu\Big), \qquad \chi_\mu = \sum_{\nu\neq\mu}(\chi^a_{\mu\nu} + \chi^b_{\mu\nu}), \tag{4.69}$$

and

$$\begin{aligned}\langle s^+_{\mathbf{r},\mathbf{r}+\mathbf{e}_\mu}\rangle = \langle s^-_{\mathbf{r},\mathbf{r}+\mathbf{e}_\mu}\rangle = \Delta &= -\frac{2J_1^\perp s\alpha_\mu + J_2^\perp\Delta\chi_\mu^*}{2\big|2J_1^\perp s\alpha_\mu + J_2^\perp\Delta\chi_\mu^*\big|} \\ &= -\frac{2J_1^\perp s\alpha_\mu + J_2^\perp\Delta\chi_\mu}{2\big|2J_1^\perp s\alpha_\mu + J_2^\perp\Delta\chi_\mu\big|},\end{aligned} \tag{4.70}$$

which implies χ_μ is real and assuming α_μ, χ_μ are positive, we obtain $\Delta = 1/2$.

Moving on to the rotor part of the mean-field Hamiltonian,

$$\begin{aligned}H_{\text{rotor}} &= \frac{J_2^z}{2}\sum_{\mathbf{r}} Q_{\mathbf{r}}^2 + H_\Phi, \\ H_\Phi &= J_1^\perp \Delta s \sum_\mu \left[\sum_{\mathbf{r}\in a}\left(\Phi^\dagger_{\mathbf{r}}\Phi^\dagger_{\mathbf{r}+\mathbf{e}_\mu} + \text{h.c}\right) + \sum_{\mathbf{r}\in b}\left(\Phi_{\mathbf{r}}\Phi_{\mathbf{r}-\mathbf{e}_\mu} + \text{h.c}\right)\right] \\ &\qquad + J_2^\perp\Delta^2 \sum_{\mu,\nu\neq\mu}\left[\sum_{\mathbf{r}\in a}\Phi^\dagger_{\mathbf{r}+\mathbf{e}_\mu}\Phi_{\mathbf{r}+\mathbf{e}_\nu} + \sum_{\mathbf{r}\in b}\Phi^\dagger_{\mathbf{r}-\mathbf{e}_\mu}\Phi_{\mathbf{r}-\mathbf{e}_\nu}\right]\end{aligned} \tag{4.71}$$

To solve this, we turn to a path-integral formulation in imaginary time, which allows us to integrate out the $Q_{\mathbf{r}}$ term. Our goal is to obtain expressions for the real-space correlators, $\alpha_\mu^{(*)}$ and $\chi_{\mu\nu}^{(*)}$ to verify the ansatz is self-consistent. The corresponding action is (see appendix A.1)

$$S = \int_{-\infty}^{\infty} d\tau \frac{1}{2J_2^z}\sum_{\mathbf{r}} \partial_\tau\Phi_{\mathbf{r},\tau}\partial_\tau\Phi^*_{\mathbf{r},\tau} + H_\Phi + \lambda\sum_{\mathbf{r}}(|\Phi_{\mathbf{r},\tau}|^2 - 1), \tag{4.72}$$

where we have introduced the Lagrange multiplier λ to enforce the $|\Phi_{\mathbf{r}}|^2 = 1$ constraint. One could enforce the constraint on the gauge sector, $G_{\mathbf{r}} = 0$, through an additional Lagrange multiplier [153, 208], but for the sake of being able to solve for the Green's functions, this is not done.

We define the Fourier transform (FT)

$$\Phi^x_{\mathbf{r},\tau} = \frac{1}{\sqrt{N_{\text{u.c}}}}\int_{-\infty}^{\infty}\frac{d\omega}{2\pi}\sum_{\mathbf{k}}\Phi^x_{\mathbf{k},\omega}e^{-i(\omega\tau - \mathbf{k}\cdot\mathbf{r})}, \tag{4.73}$$

where $N_{\mathrm{u.c}}$ is the number of primitive unit cells and $x \in \{a, b\}$ labels the sublattice. Taking the FT of eq. (4.72) results in

$$\begin{aligned} S &= \int_{-\infty}^{\infty} \frac{d\omega}{2\pi} \sum_{\mathbf{k}} \vec{\Phi}^{\dagger}_{\mathbf{k},\omega} \mathrm{M}_{\mathbf{k},\omega} \vec{\Phi}_{\mathbf{k},\omega}, \\ \mathrm{M}_{\mathbf{k},\omega} &= \begin{pmatrix} x_{\mathbf{k},\omega} & 0 & 0 & y^{*}_{\mathbf{k}} \\ 0 & x_{\mathbf{k},\omega} & y^{*}_{\mathbf{k}} & 0 \\ 0 & y_{\mathbf{k}} & x_{\mathbf{k},\omega} & 0 \\ y_{\mathbf{k}} & 0 & 0 & x_{\mathbf{k},\omega} \end{pmatrix}, \ \vec{\Phi}_{\mathbf{k},\omega} = \begin{pmatrix} \Phi^{a}_{\mathbf{k},\omega} \\ \Phi^{a*}_{-\mathbf{k},-\omega} \\ \Phi^{b}_{\mathbf{k},\omega} \\ \Phi^{b*}_{-\mathbf{k},-\omega} \end{pmatrix} \end{aligned} \tag{4.74}$$

where

$$\begin{aligned} x_{\mathbf{k},\omega} &= \frac{1}{2}\left(\frac{\omega^2}{2J_2^z} + \lambda + 2J_2^{\perp}\Delta^2 c_{\mathbf{k}} \right), \qquad y_{\mathbf{k}} = J_1^{\perp}\Delta s d_{\mathbf{k}}, \\ c_{\mathbf{k}} &= \sum_{\mu,\nu<\mu} \cos\left(\mathbf{k}\cdot(e_{\mu} - e_{\nu})\right), \qquad d_{\mathbf{k}} = \sum_{\mu} e^{-i\mathbf{k}\cdot e_{\mu}}. \end{aligned} \tag{4.75}$$

$\mathrm{M}_{\mathbf{k},\omega}$ is diagonalized by

$$\mathrm{U}_{\mathbf{k}} = \frac{1}{\sqrt{2}} \begin{pmatrix} 0 & -\tilde{y}^{*}_{\mathbf{k}} & 0 & \tilde{y}^{*}_{\mathbf{k}} \\ -\tilde{y}^{*}_{\mathbf{k}} & 0 & \tilde{y}^{*}_{\mathbf{k}} & 0 \\ 1 & 0 & 1 & 0 \\ 0 & 1 & 0 & 1 \end{pmatrix}, \tag{4.76}$$

where $\tilde{y}_{\mathbf{k}} = \frac{y_{\mathbf{k}}}{|y_{\mathbf{k}}|}$, with eigenvalues

$$l^{1,2}_{\mathbf{k},\omega} = l^{-}_{\mathbf{k},\omega} = x_{\mathbf{k},\omega} - |y_{\mathbf{k}}|, \qquad l^{3,4}_{\mathbf{k},\omega} = l^{+}_{\mathbf{k},\omega} = x_{\mathbf{k},\omega} + |y_{\mathbf{k}}|. \tag{4.77}$$

The Green's function, $\mathrm{G}(\mathbf{k},\omega) = \mathrm{M}^{-1}_{\mathbf{k},\omega}$, component-wise is

$$G_{\alpha\beta}(\mathbf{k},\omega) = \sum_{m=1}^{4} \frac{u^{\alpha,m}_{\mathbf{k}} u^{\beta,m}_{\mathbf{k}}}{l^{m}_{\mathbf{k},\omega}}, \tag{4.78}$$

where the $u^{\alpha,m}_{\mathbf{k}}$ are the elements of the matrix $\mathrm{U}_{\mathbf{k}}$. We want the equal time Green's function $G_{\alpha\beta}(\mathbf{k}, \tau = 0) = \int_{-\infty}^{\infty} \frac{d\omega}{2\pi} G_{\alpha\beta}(\mathbf{k},\omega)$, so integrating over ω using the residue theorem, then summing over m,

$$G_{\alpha\beta}(\mathbf{k}) = \begin{pmatrix} a_{\mathbf{k}} & 0 & 0 & b^{*}_{\mathbf{k}} \\ 0 & a_{\mathbf{k}} & b^{*}_{\mathbf{k}} & 0 \\ 0 & b_{\mathbf{k}} & a_{\mathbf{k}} & 0 \\ b_{\mathbf{k}} & 0 & 0 & a_{\mathbf{k}} \end{pmatrix}, \tag{4.79}$$

where

$$\begin{aligned} a_{\mathbf{k}} &= \frac{1}{2}\left(\frac{1}{\omega^{-}_{\mathbf{k}}} + \frac{1}{\omega^{+}_{\mathbf{k}}} \right), \qquad b_{\mathbf{k}} = \frac{\tilde{y}_{\mathbf{k}}}{2}\left(\frac{1}{\omega^{+}_{\mathbf{k}}} - \frac{1}{\omega^{-}_{\mathbf{k}}} \right), \\ \frac{1}{\omega^{\pm}_{\mathbf{k}}} &= \sqrt{\frac{2J_2^z}{\lambda + \epsilon^{\pm}_{\mathbf{k}}}}, \qquad \epsilon^{\pm}_{\mathbf{k}} = 2\left(J_2^{\perp}\Delta^2 c_{\mathbf{k}} \pm \left| J_1^{\perp}\Delta s d_{\mathbf{k}} \right| \right). \end{aligned} \tag{4.80}$$

The equal-time momentum-space correlators can be read off from eq. (4.79),

$$\begin{aligned}
\langle \Phi^{x*}_{\mathbf{k}} \Phi^{x}_{\mathbf{k}} \rangle &= \langle \Phi^{x*}_{-\mathbf{k}} \Phi^{x}_{-\mathbf{k}} \rangle = G_{\alpha\alpha}(\mathbf{k}) = \frac{1}{2}\left(\frac{1}{\omega^{-}_{\mathbf{k}}} + \frac{1}{\omega^{+}_{\mathbf{k}}} \right), \\
\langle \Phi^{a*}_{\mathbf{k}} \Phi^{b*}_{-\mathbf{k}} \rangle &= G_{14}(\mathbf{k}) = \langle \Phi^{a}_{-\mathbf{k}} \Phi^{b}_{\mathbf{k}} \rangle = G_{23}(\mathbf{k}) = \frac{\tilde{y}^{*}_{\mathbf{k}}}{2}\left(\frac{1}{\omega^{+}_{\mathbf{k}}} - \frac{1}{\omega^{-}_{\mathbf{k}}} \right), \\
\langle \Phi^{a}_{\mathbf{k}} \Phi^{b}_{-\mathbf{k}} \rangle &= G_{41}(\mathbf{k}) = \langle \Phi^{a*}_{-\mathbf{k}} \Phi^{b*}_{\mathbf{k}} \rangle = G_{32}(\mathbf{k}) = \frac{\tilde{y}_{\mathbf{k}}}{2}\left(\frac{1}{\omega^{+}_{\mathbf{k}}} - \frac{1}{\omega^{-}_{\mathbf{k}}} \right).
\end{aligned} \tag{4.81}$$

We can now express the real-space correlators $\alpha^{(*)}_{\mu}$ and $\chi^{(*)}_{\mu\nu}$ in terms of the expressions in eq. (4.81). Using

$$\Phi^{x}_{\mathbf{r}} = \frac{1}{\sqrt{N_{\mathrm{u.c}}}} \sum_{\mathbf{k}} \Phi^{x}_{\mathbf{k}} e^{i\mathbf{k}\cdot\mathbf{r}}, \tag{4.82}$$

we obtain the relations between real and momentum-space correlators,

$$\langle \Phi^{x*}_{\mathbf{r}} \Phi^{x'}_{\mathbf{r}'} \rangle = \frac{1}{N_{\mathrm{u.c}}} \sum_{\mathbf{k}} \langle \Phi^{x*}_{\mathbf{k}} \Phi^{x'}_{\mathbf{k}} \rangle e^{i\mathbf{k}\cdot(\mathbf{r}'-\mathbf{r})}, \qquad \langle \Phi^{x}_{\mathbf{r}} \Phi^{x'}_{\mathbf{r}'} \rangle = \frac{1}{N_{\mathrm{u.c}}} \sum_{\mathbf{k}} \langle \Phi^{x}_{\mathbf{k}} \Phi^{x'}_{-\mathbf{k}} \rangle e^{-i\mathbf{k}\cdot(\mathbf{r}'-\mathbf{r})}. \tag{4.83}$$

Therefore, the explicit expressions for the mean-field parameters are

$$\begin{aligned}
\chi^{a}_{\mu\nu} &= \langle \Phi^{a*}_{\mathbf{r}+\mathbf{e}_\mu-\mathbf{e}_\nu} \Phi_{\mathbf{r}} \rangle = \frac{1}{2N_{\mathrm{u.c}}} \sum_{\mathbf{k}} \left(\frac{1}{\omega^{-}_{\mathbf{k}}} + \frac{1}{\omega^{+}_{\mathbf{k}}} \right) e^{i\mathbf{k}\cdot(\mathbf{e}_\nu-\mathbf{e}_\mu)} = \frac{1}{2N_{\mathrm{u.c}}} \sum_{\mathbf{k}} I_{\mu\nu}(\mathbf{k}), \\
\alpha_{\mu} &= \langle \Phi^{a}_{\mathbf{r}} \Phi^{b}_{\mathbf{r}+\mathbf{e}_\mu} \rangle = \frac{1}{2N_{\mathrm{u.c}}} \sum_{\mathbf{k}} \left(\frac{1}{\omega^{+}_{\mathbf{k}}} - \frac{1}{\omega^{-}_{\mathbf{k}}} \right) \frac{J^{\perp}_{1} \sum_{\nu=1}^{4} e^{-i\mathbf{k}\cdot(\mathbf{e}_\mu+\mathbf{e}_\nu)}}{\left| J^{\perp}_{1} d_{\mathbf{k}} \right|} = \frac{1}{2N_{\mathrm{u.c}}} \sum_{\mathbf{k}} J_{\mu}(\mathbf{k}).
\end{aligned} \tag{4.84}$$

In order to evaluate these expressions, one first needs to find the value for the Lagrange multiplier, λ, which is done by enforcing the constraint $|\Phi_r|^2 = 1$ on average,

$$\langle \Phi^{a*}_{\mathbf{r}} \Phi^{a}_{\mathbf{r}} \rangle = \langle \Phi^{b*}_{\mathbf{r}} \Phi^{b}_{\mathbf{r}} \rangle = \frac{1}{2N_{\mathrm{u.c}}} \sum_{\mathbf{k}} \left(\frac{1}{\omega^{-}_{\mathbf{k}}} + \frac{1}{\omega^{+}_{\mathbf{k}}} \right) = 1. \tag{4.85}$$

One can evaluate this expression numerically for specific $J^{\perp}_{1}, J^{\perp}_{2}$ and using systematic "guesses" for λ, for example using the bisection method [209], to find $\lambda(J^{\perp}_{1}, J^{\perp}_{2})$ which satisfies eq. (4.85) up to a desired accuracy.

To evaluate sums of the form $\sum_{\mathbf{k}} f(\mathbf{k})$, it is easier to work in units of the reciprocal lattice vectors [149]. The reciprocal lattice vectors of the face-centred cubic lattice (with lattice vectors defined in eq. (1.2)) are

$$\mathbf{b}_1 = 2\pi(1,1,-1), \qquad \mathbf{b}_2 = 2\pi(-1,1,1), \qquad \mathbf{b}_3 = 2\pi(-1,1,1) \tag{4.86}$$

and we define the variable $\mathbf{q} = (q_1, q_2, q_3)$ through

$$\mathbf{k} = \sum_{i=1}^{3} q_i \mathbf{b}_i. \tag{4.87}$$

For a periodic 1D system with L unit cells, $\sum_k f(k) = \sum_q f(q)$, where $q \in \{-1/2, -1/2+1/L, \ldots, 1/2-1/L\}$, so that $\sum_k$ is over the first Brillouin zone. Using the Riemann sum,

$$\int_a^b f(x)dx = \lim_{\Delta x_i \to 0} \sum_{i=1}^{n} f(x_i)\Delta x_i, \qquad \Delta x_i = x_i - x_{i-1},\ x_0 = a,\ x_n = b, \tag{4.88}$$

in the $L \to \infty$ limit,

$$\frac{1}{L}\sum_k f(k) \to \int_{-\frac{1}{2}}^{\frac{1}{2}} f(q)dq \tag{4.89}$$

and therefore generalizing to 3D,

$$\frac{1}{N_{\text{u.c}}}\sum_{k\in \text{BZ}_1} \to \int_{-\frac{1}{2}}^{\frac{1}{2}} f(\mathbf{q})d^3q. \tag{4.90}$$

where the integral is over a cube in $\mathbf{q}$ space corresponding to the first Brillouin zone.

However, before proceeding to evaluate the momentum integrals one should verify the periodicity of the summands. The sums in eq. (4.84) are in principle over all momenta and it is only through the periodicity of the summand that one can restrict the sum to a smaller region of momentum space. Since $\mathbf{e}_\mu - \mathbf{e}_\nu = \sum_{i=1}^3 n_i \mathbf{a}_i$ with n_i integer and $\mathbf{a}_i$ the fcc lattice vectors, $c_{\mathbf{k}+\mathbf{b}_i} = c_{\mathbf{k}}$. Furthermore, since $d_{\mathbf{k}} = \sqrt{4+2c_{\mathbf{k}}}$, we find $d_{\mathbf{k}+\mathbf{b}_i} = d_{\mathbf{k}}$. Therefore, $I_{\mu\nu}(\mathbf{k})$ has the periodicity of a reciprocal lattice vector and to evaluate $\chi^x_{\mu\nu}$ one only needs to integrate over the first Brillouin zone.

On the other hand, $f(\mathbf{k}) = e^{-i\mathbf{k}\cdot(\mathbf{e}_\mu+\mathbf{e}_\nu)}$ is antiperiodic when translating by a reciprocal lattice vector, $f(\mathbf{k}+\mathbf{b}_i) = -f(\mathbf{k})$, and is therefore periodic after translating to the next nearest reciprocal lattice site, $f(\mathbf{k}+\mathbf{b}_i+\mathbf{b}_j) = f(\mathbf{k})$. In this case one should sum momenta up to the second Brillouin zone,

$$\sum_{\mathbf{k}\in \text{BZ}_2} J_\mu(\mathbf{k}) = \sum_{\mathbf{k}\in \text{BZ}_1} \Big(J_\mu(\mathbf{k}) + J_\mu(\mathbf{k}+\mathbf{b}_i) \Big) = 0, \tag{4.91}$$

and therefore $\alpha_\mu^{(*)} = 0$ for all $J_1^\perp, J_2^\perp$. $J_\mu(\mathbf{q})$ is plotted in fig. 4.6(b) to show these properties. This means that within our ansatz there is no self-consistent $\mathbb{Z}_2$ QSL solution, which originates from the fact that the spinon creation/annihilation operators in α_μ act on adjacent diamond sites, leading to this cancellation in momentum space.

Therefore the only self-consistent zero-flux QSL solution we find is the $\text{U}(1)$ QSL where $\langle s^\pm_{r_a}\rangle = \langle s^\pm_{r_b}\rangle = \langle \Phi_r^{a(*)}\Phi^{b(*)}_{r+e_\mu}\rangle = 0$, which is valid for $J_2^\perp$ small enough that the spinons do not condense. The condensation of spinons implies ordering to the XY ferromagnet. For this solution, H_{MF} is the same as for the XXZ model on the pyrochlore, thus gMFT predicts the U(1) QSL is the ground state in the region $0 \le |J_2^\perp| \le 0.19 J_2^z$ [149] or equivalently $0 \le |J_2^\perp| \le 0.095 J_1^z$. The spinons condense when a singularity appears in the momentum space Green's function, causing the momentum integrals to diverge [149].

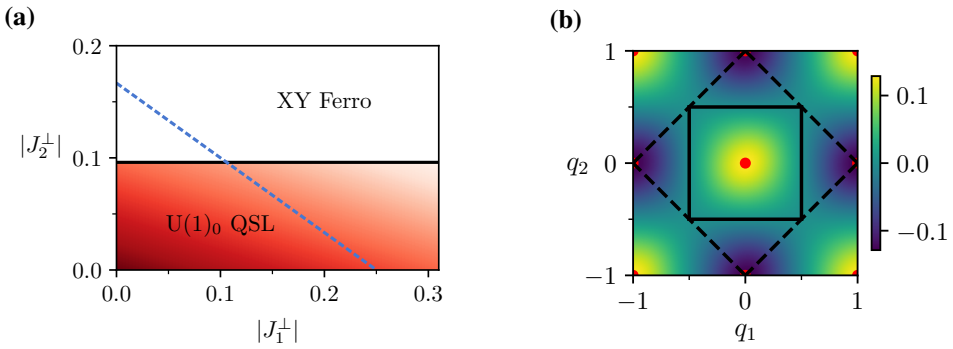

Figure 4.6: **(a)** Sketch of phase diagram obtained from gMFT for $J_1^z = 1, J_2^z = 0.5$ and $J_1^\perp, J_2^\perp < 0$. The solid line is the transition from the U(1) QSL to XY ferromagnet found from gMFT, which occurs at the same value, $J_2^\perp = 0.19 J_2^z$ as when applying gMFT to the XXZ model on the pyrochlore. Note that $J_1^\perp$ has no effect on the location of this transition in gMFT. The blue dotted line is an estimate of the transition from comparing the energies of the XY ferromagnetic and 3:1 states in the classical model. **(b)** Plot of $J_\mu(\mathbf{q})$ in $\mathbf{q} = (q1, q2, 0)$ momentum space for $\mu = 0$, $J_1^\perp = J_2^\perp = -0.05, \lambda = 1, J_1^z = 1, J_2^z = 0.5$. In $\mathbf{q}$-space the reciprocal lattice vectors (red dots) form a cubic lattice. The first Brillouin zone is indicated by a solid line, the second by a dashed line. One can see that $J_\mu(\mathbf{q})$ is not periodic after the first Brillouin zone, but is after the second. Contributions exactly cancel when integrating over the first two Brillouin zones which leads to $\alpha_\mu^{(*)} = 0$ in the mean-field ansatz.

The location of the phase boundary is obtained as follows. For $\alpha_\mu = s = 0$,

$$\langle \Phi_{\mathbf{k}}^{x*} \Phi_{\mathbf{k}}^{x} \rangle = \sqrt{\frac{2J_2^z}{\lambda - 2\left|J_2^\perp\right| \Delta^2 c_{\mathbf{k}}}}, \tag{4.92}$$

which first diverges when $\lambda = \lambda_c = 12\left|J_2^\perp\right|\Delta^2$, since $c_{\mathbf{k}} = 6$ at its maximum for $\mathbf{k} = 0$. This can be interpreted as the point where the chemical potential of the spinons falls below the lowest energy of the spinon dispersion. The transition can be located as a function of $J_2^\perp$ by putting λ_c into the $\langle \Phi_{\mathbf{r}}^* \Phi_{\mathbf{r}} \rangle = 1$ constraint,

$$\langle \Phi_{\mathbf{r}}^{a*} \Phi_{\mathbf{r}}^{a} \rangle = \frac{1}{N_{\text{u.c}}} \sum_{\mathbf{q} \neq 0} \sqrt{\frac{2J_2^z}{\lambda_c - 2\left|J_2^\perp\right| \Delta^2 c_{\mathbf{q}}}}, \tag{4.93}$$

telling us the largest value of $\left|J_2^\perp\right|$ at which the spinons have not condensed. Re-arranging, this boundary is at

$$\left(\frac{\left|J_2^\perp\right|}{J_2^z}\right)_c = \frac{1}{2N_{\text{u.c}}} \left(\sum_{\mathbf{q} \neq 0} \sqrt{\frac{1}{3 - \frac{1}{2} c_{\mathbf{q}}}} \right)^2 \tag{4.94}$$

which can be evaluated numerically and extrapolated to the $N_{\text{u.c}} \to \infty$ limit, which gives the result stated above for the extent of the U(1) QSL phase.

In our zero-flux gMFT results, the QSL to XY ferromagnet transition does not depend on the value of $J_1^\perp$, our gMFT ansatz fails to properly account for the fact that $J_1^\perp$ can induce

long-range ferromagnetic XY correlations, as well as any effects on the U(1) QSL. This is because within the mean-field theory $J_1^\perp$ is coupled to terms of the form $\langle \Phi_r \Phi_{r'} \rangle$, so only has an effect in the $\mathbb{Z}_2$ QSL, for which we don't find self-consistent solutions anywhere in the phase diagram. Furthermore, since the $G_{\mathbf{r}} = 0$ constraint is not enforced on the rotors, the mean-field spinon action we use is the same as for the pyrochlore except for the $J_1^\perp$ term; the fact that a quantum spin liquid in this regime is based off a 3:1 rather than 2:2 manifold is not accounted for.

An estimate for the transition to the XY ferromagnet which accounts for the role of $J_1^\perp$ can be obtained by comparing the energies of a 3:1 state and XY ferromagnet in the *classical* model. The classical XXZ model can be written as a sum over tetrahedra, $H = \sum_t H_t$, with

$$\begin{aligned} H_t = J_1^z S_{t,c}^z \sum_v S_{t,v}^z + 2J_1^\perp \sum_v \left(S_{t,c}^x S_{t,v}^x + S_{t,c}^y S_{t,v}^y \right) \\ + J_2^z \sum_{w<v} S_{t,v}^z S_{t,w}^z + 2J_2^\perp \sum_{w<v} \left(S_{t,v}^x S_{t,w}^x + S_{t,v}^y S_{t,w}^y \right), \end{aligned} \tag{4.95}$$

so that the energies of a 3:1 state (along z) and ferromagnetic state (along x) are

$$E_{3:1} = -\frac{J_1^z}{2}, \qquad E_{\mathrm{XY}} = 2J_1^\perp + 3J_2^\perp. \tag{4.96}$$

Setting these energies equal gives the boundary plotted in fig. 4.6(a).

Summarizing, within gMFT for $\gamma = 2$, if there is a deconfined phase, it will be a U(1) QSL for all $J_1^\perp$, $J_2^\perp$ small enough not to induce long-range XY ferromagnetic order.

4.4 Exact Diagonalization

We now study the ground state of the XXZ Hamiltonian with ferromagnetic $J_{1,2}^\perp$ using the Lanczos method (see appendix B). Although there are significant finite size effects, this allows us to go beyond perturbation theory and gMFT, accessing the ground state for $\gamma \neq 2$.

These calculations were performed on an $N = 24$ site cluster (one conventional unit cell) with periodic boundary conditions, which is shown in fig. 4.7. Due to the small size of the cluster, the lattice contains closed loops of length 4, in addition to the usual length-6 loops on the infinite centred pyrochlore lattice. Furthermore, loops which wind around the periodic boundaries can be as small as length 4, which means topological features of the model will not be evident.

This modifies the $\gamma = 2$ perturbation theory of section 4.2 by introducing non-constant lower order loop processes, which are illustrated in fig. 4.8. At second order, the non-

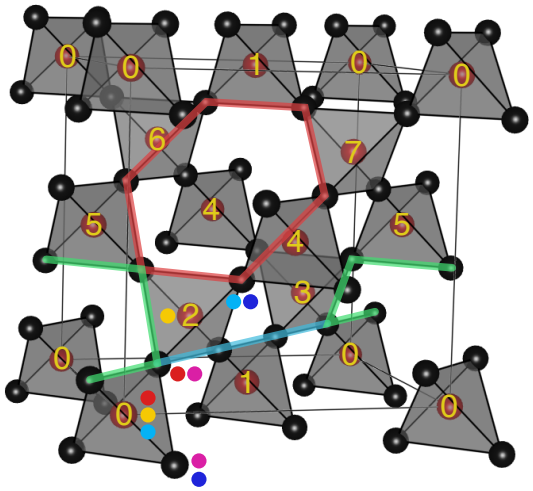

Neighbours	Colour
1st	●
2nd	●
3rd	●
4th	●
5th	●

Figure 4.7: The 24 site cluster used in exact diagonalization. The tetrahedra are numbered to show the periodic boundaries. The green and cyan highlighted paths are non-winding and winding loops of length-4 respectively, whereas the red path is the length-6 hexagonal loop. The five (i, j) neighbour pairs with distinct distances between the sites are shown with matching dots, with the sorted list in order of distances shown in the table.

constant contribution to $PH_2^\perp DH_2^\perp P$ is

$$H_{\text{eff}}^{(2)}(\square) = K_1^\square \sum_\square \left(S_{v,0}^+ S_{v,1}^- S_{v,2}^+ S_{v,3}^- + \text{h.c} \right) = K_1^\square \sum_\square \left(A_\square + A_\square^\dagger \right), \tag{4.97}$$

where $K_1^\square \propto -(J_2^\perp)^2/J_2^z$, which is the analogue of the third order hexagonal ring-exchange in eq. (4.18). In the dimer language,

$$H_{\text{eff}}^{(2)}(\square) = K_1^\square \sum_\square \left(\left| \, \vert \; \vert \, \right\rangle \left\langle \, = \, \right| + \left| \, = \, \right\rangle \left\langle \, \vert \; \vert \, \right| \right). \tag{4.98}$$

At third order, one obtains the analogue of the ring exchange involving centre spins, eq. (4.21),

$$\begin{aligned} H_{\text{eff}}^{(3)}(\square) &= K_2^\square \sum_\square \left(B_\square + B_\square^\dagger \right), \qquad B_\square = \sum_{i=0}^{3} \sum_{j=i+1}^{3} B_\square^{ij}, \\ B_\square^{ij} &= \begin{cases} S_{c_i}^+ S_{c_j}^- S_{v_i}^- \dots S_{v_{j-1}}^+ S_{v_j}^+ \dots S_{v_{i+3}}^- & \text{for } j-i \text{ even} \\ S_{c_i}^+ S_{c_j}^+ S_{v_i}^- \dots S_{v_{j-1}}^- S_{v_j}^- \dots S_{v_{i+3}}^- & \text{for } j-i \text{ odd} \end{cases}, \end{aligned} \tag{4.99}$$

where $K_2^\square \propto J_2^\perp (J_1^\perp)^2/(J_2^z)^2$. In fig. 4.8, we also show the fourth order non-constant $PH_1^\perp DH_1^\perp DH_1^\perp DH_1^\perp P$, which has the same effect as eq. (4.97), with a pair of $J_1^\perp$ terms acting as a $J_2^\perp$ term. Therefore, even with $J_2^\perp = 0$, one still has a non-zero ring-exchange type term in the effective Hamiltonian. On the infinite centred pyrochlore lattice, this $J_1^\perp$ only ring-exchange first appears at sixth order.

Including $H^{(2)}_{\text{eff}}(\square)$ and $H^{(3)}_{\text{eff}}(\square)$ in the effective Hamiltonian does not change its symmetry properties, one still obtains a U(1) lattice gauge theory after mapping to rotors and fermions. Therefore, although the low-energy physics will differ in the details, calculations on small clusters still give useful insight into the model.

In our calculations we use the fact that the Hamiltonian commutes with $m_z = \sum_i S^z_i$, diagonalizing the Hamiltonian in each m_z sector separately. In the ground state, we measure the correlators

$$\mathcal{S}^z_{ij} = \langle S^z_i S^z_j \rangle, \qquad \mathcal{S}^{\pm}_{ij} = \langle S^+_i S^-_j + \text{h.c} \rangle. \tag{4.100}$$

The $N = 24$ cluster contains up to 5th nearest neighbours, as shown in fig. 4.7.

To locate ground state phase boundaries, we use the second derivative of the ground state energy, which, for example, was used in [210] to locate the boundaries of a gapless quantum spin liquid on small clusters. At $T = 0$ the free energy reduces to the ground state energy, which is a function of the parameters of the Hamiltonian, $E_0 = E_0(\mathbf{J})$. Therefore non-analyticities in the ground state energy with respect to the parameters, which are detected via discontinuities in its derivatives, indicate a quantum phase transition [211]. As such, we measure the second derivative $\partial^2 E_0(\mathbf{J}))/(\partial J^\alpha_i)^2$, at various points and along various directions of the parameter space $\mathbf{J} = (J^z_1, J^\perp_1, J^z_2, J^\perp_2)$. In particular, since the ground state energy is obtained on a discrete grid, we compute the finite central difference

$$c^\alpha_i(\mathbf{J}) = \frac{\partial^2 E_0(\mathbf{J})}{(\partial J^\alpha_i)^2} \approx \frac{E_0(\mathbf{J} + \delta \hat{\mathbf{J}}^\alpha_i) - 2E_0(\mathbf{J}) + E_0(\mathbf{J} - \delta \hat{\mathbf{J}}^\alpha_i)}{\delta^2}, \tag{4.101}$$

to approximate the second derivative.

A quantum phase transition also implies a discontinuous change in the ground state wavefunction, which can be detected by computing fidelities,

$$F(\mathbf{J}) = |\langle \Psi_0(\mathbf{J}) | \Psi_0(\mathbf{J} + \boldsymbol{\delta}) \rangle|, \tag{4.102}$$

between adjacent points in the parameter space. In both cases, on small clusters, the features associated with the phase transition will not be very sharp, so it can be challenging to decipher whether a feature corresponds to a true phase transition in the thermodynamic limit. In general, one should verify what happens to these features as system size is increased, however, since our model is 3D, we are extremely limited in which system sizes can be accessed in exact diagonalization.

(a)

$$PH_2^{\perp}DH_2^{\perp}P$$

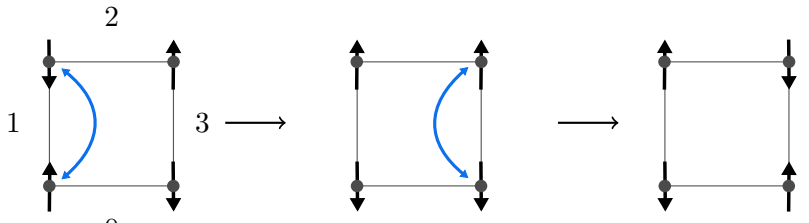

$$H^z_{t_0} = H^z_{t_2} = \frac{J^z_2}{2}$$

(b)

$$PH_1^{\perp}DH_1^{\perp}DH_2^{\perp}P$$

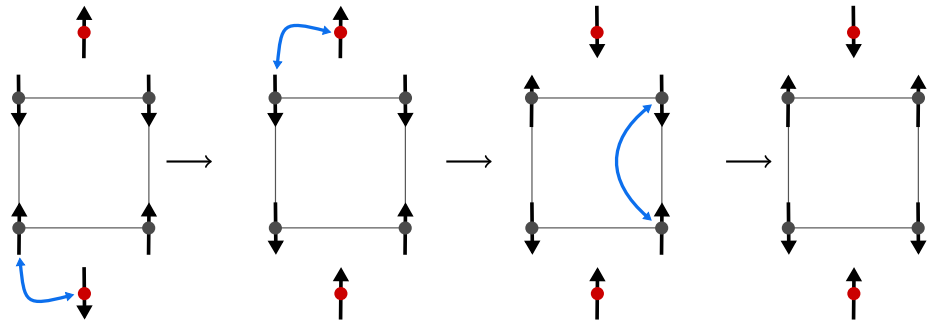

$$H^z_{t_0} = H^z_{t_1} = \frac{J^z_2}{2} \qquad H^z_{t_0} = H^z_{t_2} = \frac{J^z_2}{2}$$

(c)

$$PH_1^{\perp}DH_1^{\perp}DH_1^{\perp}DH_1^{\perp}P$$

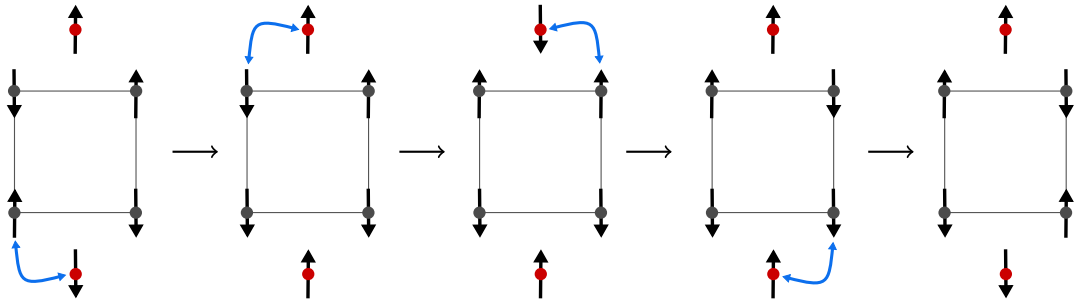

$$H^z_{t_0} = H^z_{t_1} = \frac{J^z_2}{2} \qquad H^z_{t_0} = H^z_{t_2} = \frac{J^z_2}{2} \qquad H^z_{t_0} = H^z_{t_3} = \frac{J^z_2}{2}$$

Figure 4.8: Loop processes in perturbation theory which arise in clusters containing length-4 closed loops. Note that the square shown is not a tetrahedron, the spins making up the loop belong to four tetrahedra around the outside of the loop (not explicitly shown). The labels, i, used to label the tetrahedra, t_i, are indicated in **(a)**.

Ground state phase diagram

In the following we set $J_1^z = 1$ and tune the ratio γ through J_2^z as well as parametrizing $J_1^\perp = -J^\perp \cos\theta, J_2^\perp = -J^\perp \sin\theta$. First, we set $\theta = \pi/4$, and diagonalize the Hamiltonian on a $J_2^z, J^\perp$ grid, measuring the second derivative of the energy as well as correlators. This is summarized in fig. 4.9.

For $J_2^z \geq 0.36$ we find that the ground state is in the $m_z = 0$ sector. For J_2^z smaller than this, the ground state has finite magnetization as a result of the proximity to the Ising ferrimagnet at $J_2^z \leq 1/3$. At larger $J^\perp$ the ground state is the XY ferromagnet, but as one would expect from the viewpoint of adding quantum fluctuations to the Ising model, there are two phases for small $J^\perp$, based off of the 3:1 and 2:2 manifolds for $J_2^z < 1$ and $J_2^z > 1$ which we call the $(3{:}1)^\perp$ and $(2{:}2)^\perp$ states respectively. They do not show any obvious signs of long-range order in the correlation functions. There is no direct phase transition at finite $J^\perp$ between the $(3{:}1)^\perp$ and $(2{:}2)^\perp$ states, instead always passing through the XY ferromagnet. Our focus is on the $(3{:}1)^\perp$ regime, which, as discussed in the previous sections, could host a $\mathrm{U}(1)$ QSL ground state. Although, this state is fragile, surviving at its greatest extent up to about $J_c^\perp/J_1^z \approx 0.03$, this is comparable to the extent of the $\mathrm{U}(1)$ QSL on the pyrochlore, which exists up to $-J_{2,c}^\perp/J_2^z \approx 0.05$ [151].

At $J_2^z = 0.5$, we also investigate the effect of different $J_1^\perp, J_2^\perp$ on the ground state energy and correlations, shown in fig. 4.10. We find the anticipated XY ferromagnet ground state for ferromagnetic $J_1^\perp$, which becomes a ferrimagnet for antiferromagnetic $J_1^\perp$, a result of the transformation properties of the Hamiltonian discussed at the beginning of this chapter. The $(3{:}1)^\perp$ state is slightly more stable to $J_1^\perp$ than $J_2^\perp$ terms, likely a result of the larger coordination number (6 vs 4) of the $J_2^\perp$ term.

Next, we take a closer look at the $(3{:}1)^\perp$ state as J_2^z is varied. The spectrum, second derivative and ground state fidelity are shown in fig. 4.11. There are subtle changes in the energy spectrum as well as small features in the second derivative and ground state fidelity across $J_2^z \approx 0.5$, which could be indicative of a qualitative change in the ground state properties. However, the magnitude of these features is small compared to those which appear at the phase transition to the XY ferromagnet, so could also be due to finite size effects. We return to the question of whether $J_2^z = 0.5$ is a critical point, or the $(3{:}1)^\perp$ state a continuous phase across the whole region, when we compare the $(3{:}1)^\perp$ ground state to a trial wavefunction later in this section.

To investigate the effect of varying $J_1^\perp/J_2^\perp$ on the $(3{:}1)^\perp$ state, we take a cut along $J^\perp = 0.02$, varying θ between 0 and $\pi/2$. For θ small, $J_2^\perp \approx 0$, so the highest order non-constant terms in the perturbation theory are those where there is ring-exchange entirely mediated by $J_1^\perp$. These terms are of twice the order of their $J_2^\perp$ counterparts, so energy gaps produced by this term will be small, as we see in the energy spectrum for low θ. On the other hand, for $\theta \gtrsim 3\pi/8$ we observe that the energy gap also becomes very small. At $\theta = \pi/2$ (where $J_1^\perp = 0$), the gap is of similar magnitude to numerical precision. This is consis-

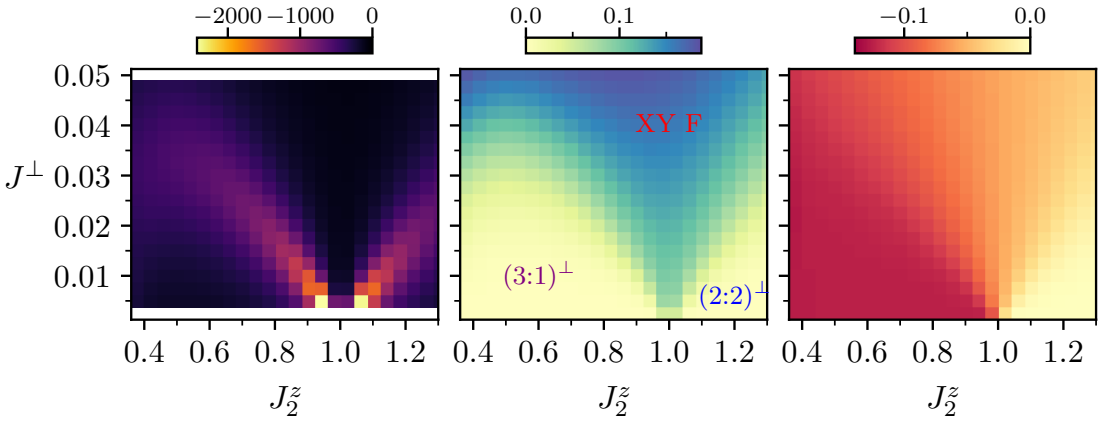

Figure 4.9: Ground state properties for $J_1^z = 1, J_1^\perp = J_2^\perp = -J^\perp/\sqrt{2}$ in the $m_z = 0$ sector. (Left) $c^\perp$ computed using finite differences, which is large in magnitude along two paths in the parameter space which meet at $J_2^z = 1$. (Middle) The $\mathcal{S}_{ij}^{\pm}$ correlator measured between 5th nearest neighbours (the furthest distance possible on the $N = 24$ cluster). For $J^\perp$ sufficiently large these correlations are large and positive, indicating the transition to a long-range XY ferromagnet. (Right) The $\mathcal{S}_{ij}^{z}$ correlator between nearest neighbours. Below the transition to the XY ferromagnet, for $J_2^z < 1$, $\mathcal{S}_{ij}^{z} \approx -0.125$, indicating that the ground state is made up of a superposition of states in the 3:1 manifold, whilst for $J_2^z > 1$, $\mathcal{S}_{ij}^{z} \approx 0$, consistent with a superposition of states from the 2:2 manifold.

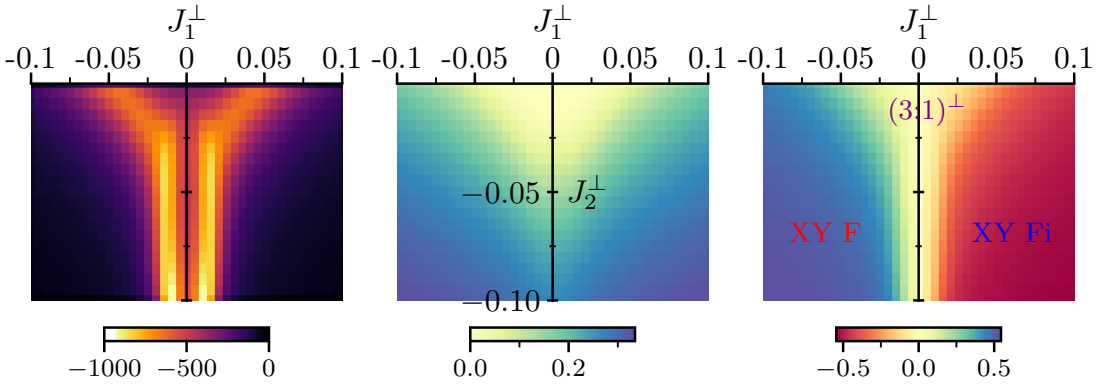

Figure 4.10: Constructing a ground state phase diagram for $J_1^z = 1, J_2^z = 0.5$. (Left) The sum of the second derivatives, $c_1^\perp + c_2^\perp$ computed using finite differences. (Centre) $\mathcal{S}_{ij}^{\pm}$ for 5th nearest neighbours, showing the onset of long-range ferromagnetic XY correlations between vertex spins for larger $J^\perp$. (Right) $\mathcal{S}_{ij}^{\pm}$ for nearest neighbours. This shows how for antiferromagnetic $J_1^\perp$ the ordered state at larger $J^\perp$ is an XY ferrimagnet, with centres and vertices anticorrelated. This must be the case given the transformation properties of the Hamiltonian discussed at the beginning of this chapter. For small $J_1^\perp$ there is an intermediate region where centres and vertices are uncorrelated.

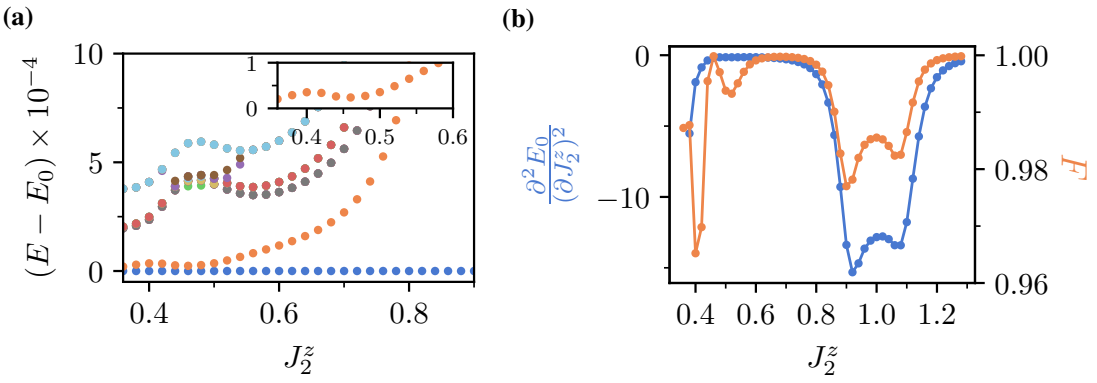

Figure 4.11: Low energy properties for $J^{\perp} = 0.01$ as a function of J_2^z. **(a)** The 20 lowest energy eigenvalues relative to the ground state energy, with the gap to the first excited state shown in the inset. The gap has a local minimum at $J_2^z = 0.45$, where there is a cusp in the energies of the excited states. **(b)** The second derivative of the ground state energy and fidelity $F = |\langle \Psi_0(J_2^z) | \Psi_0(J_2^z + \delta) \rangle|$. The fidelity shows a small dip around $J_2^z = 0.5$, with a corresponding small dip in the second derivative which is not visible on this scale. However, these features are small relative to the double peaks which result from transitions to and from the XY ferromagnet. At low J_2^z the second derivative decreases due to the nearby transition to the Ising ferrimagnet, with the fidelity also indicating the proximity of this transition.

tent with the fact that, up to the lowest order non-constant term in perturbation theory, the ground states in the different spin-inversion sectors will be degenerate. Furthermore the onset of this quasi-degeneracy coincides with a small dip in the fidelity and second derivative of the energy before a discontinuity in the fidelity at $\theta = \pi/2$. The onset of this quasi-degeneracy could correspond to a phase transition where spin-inversion symmetry is spontaneously broken in the thermodynamic limit.

Comparison to QSL variational wavefunction

To get more insight into the nature of the ground state in the $(3{:}1)^{\perp}$ region, we define a trial QSL wavefunction which corresponds to the deconfined phase of the lattice gauge theory derived in perturbation theory. We start at third order in perturbation theory, where we discussed how in the deconfined phase, the lowest energy static centre spin configuration would be ferromagnetic. Although, at third order, we know that the liquid state will not be the ground state [131], we assume that higher order terms in the perturbation theory and/or the effect of the finite system size, for example the effect of $H_{\text{eff}}^{(2)}(\square)$, ultimately melt this ordered ground state.

Therefore, our starting point is the equal weight superposition of all 3:1 configurations compatible with centre spins all up, $|RK(\uparrow)\rangle$. Note that the third order length-6 ring-exchange term on the infinite lattice is *not* ergodic within this sector, however the second-order length-4 ring-exchange term which exists on the finite size cluster is. Now, we also want to include the effect of the $J_1^{\perp}$ term which enters at third-order on length-4 loops

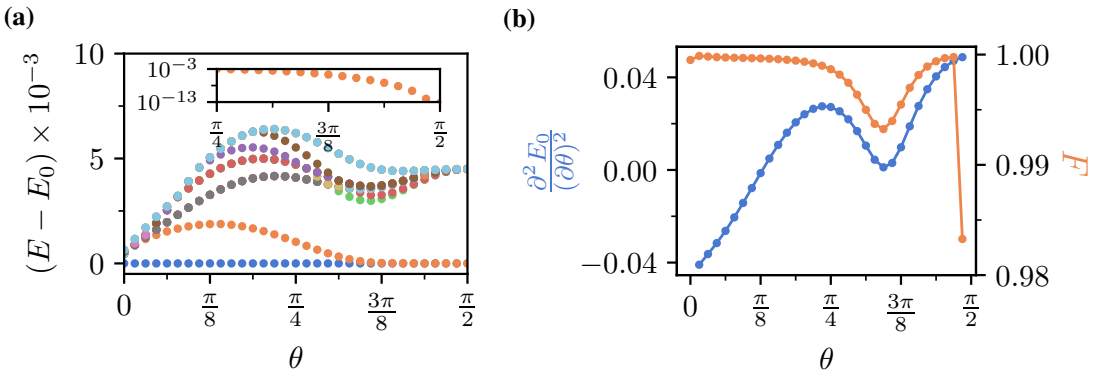

Figure 4.12: Low energy properties for $J_2^z = 0.5$, $J^\perp = 0.02$, whilst varying θ. **(a)** The 20 lowest energy eigenvalues relative to the ground state energy, with the gap to the first excited state shown in the inset on a log scale. The gap becomes small (of order 10^{-5}) at $\theta \approx 3\pi/8$ where there is also a local minimum in the energies of the excited states. **(b)** The second derivative of the ground state energy and fidelity $F = |\langle\Psi_0(\theta)|\Psi_0(\theta+\delta)\rangle|$. The fidelity and second derivative show a small dip at the same value of θ.

and fourth-order on length-6 loops. We observe that $\sum_{\hexagon}(B_{\hexagon} + B_{\hexagon}^\dagger)\,|RK(\uparrow)\rangle$, where $\hexagon$ represents all length-6 loops, both winding and non-winding, introduces all of the configurations included by $(B_\square + B_\square^\dagger)$ plus some additional ones. Furthermore, since the full Hamiltonian commutes with the spin inversion operator, X, we ensure the wavefunction is spin-inversion symmetric ($X = +1$) or antisymmetric ($X = -1$). Therefore, our variational wavefunction is

$$\Psi_v(X,\phi) \propto \left(\cos\phi + \sin\phi \sum_{\hexagon}\left(B_{\hexagon} + B_{\hexagon}^\dagger\right)\right)(|RK(\uparrow)\rangle \pm |RK(\downarrow)\rangle), \tag{4.103}$$

where ϕ is parameter which may be optimized to maximize overlap with the ground state. This wavefunction can be though of as the truncated and parameterized form of

$$e^{\sum_{\hexagon}(B_{\hexagon}+B_{\hexagon}^\dagger)}(|RK(\uparrow)\rangle \pm |RK(\downarrow)\rangle). \tag{4.104}$$

Since with $J_1^\perp, J_2^\perp < 0$, the Hamiltonian is stoquastic, the ground state cannot have $X = -1$, but we introduce this as we find the $X = -1$ state has high overlap with the first excited state. For $X = +1, \phi = 0$ the wavefunction is the spin inversion symmetrized RK wavefunction corresponding to the ground state of the Hamiltonian

$$H_{\mathrm{RK}}(\square) = -\left|K_1^\square\right| \sum_{\square}\left(|\,\vdots\,\vdots\,\rangle\langle\,\vdots\,\vdots\,| + |\,\vdots\,\vdots\,\rangle\langle\,\vdots\,\vdots\,|\right) + \mu_\square \sum_{\square}\left(|\,\vdots\,\vdots\,\rangle\langle\,\vdots\,\vdots\,| + |\,\vdots\,\vdots\,\rangle\langle\,\vdots\,\vdots\,|\right) \tag{4.105}$$

at $K_1^\square = \mu_\square$ in a 3:1 Hilbert space with ferromagnetic centres.

First, we compute the overlaps of the ground and first excited states for $J_2^z = 0.5, J^\perp = 0.02$, allowing θ to vary. This is the same cut in parameter space as fig. 4.12. For $J_2^z = 0.5$, the perturbation theory is directly applicable.

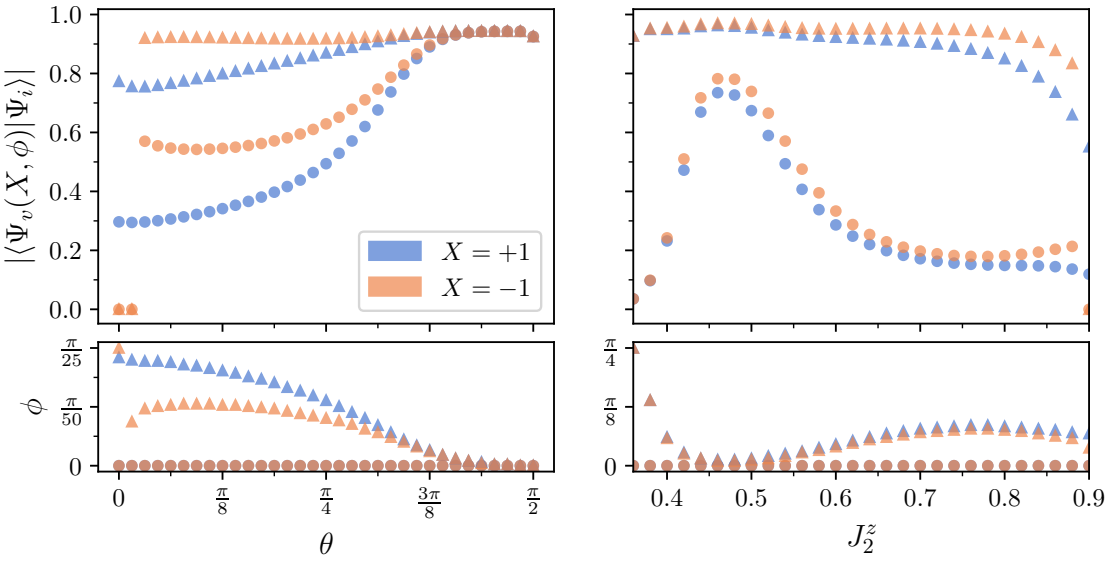

Figure 4.13: (Upper panels) Overlap of the QSL variational wavefunction with the ground state (for $X = +1$) and first excited state (for $X = -1$). For the data represented by triangles ϕ is optimized to maximize the overlap, whereas for circles $\phi = 0$, i.e it is the pure RK-like wavefunction. The optimal ϕ is shown in the lower panels. The left panels are for parameters $J_2^z = 0.5, J^\perp = 0.02$, right for $\theta = \pi/4, J^\perp = 0.01$.

We find that for $\theta \gtrsim 3\pi/8$ the overlap of the $\phi = 0$ wavefunctions is high (at around 90%), which is consistent with perturbation theory since $J_1^\perp$ is small so correlations induced by terms higher-order than the $J_2^\perp$ ring-exchange are minimal. The closing of the energy gap, and high overlap with the RK wavefunction, point towards a ground state well-described by the deconfined phase of the $J_2^\perp$ only perturbation theory. However, as discussed in section 4.2, the ground state in the relevant effective dimer model on the infinite lattice is actually ordered, so the fact we appear to find a liquid phase is likely a finite size effect, in particular, the presence of length-4 loops on the lattice means that the lowest order effective dimer model is eq. (4.105) rather than eq. (4.32).

As θ is decreased, i.e turning on $J_1^\perp$, the optimal ϕ increases, as the role of the $B_{\square,\hexagon}$ become more significant. The point where the optimal ϕ increases significantly almost coincides with the opening of the energy gap and anomalies in the second derivative of the energy and fidelity, so these features may be associated with a change in the ground state wavefunction to include $B_\hexagon$-induced correlations. The overlap with ground state drops to below 80% at small θ, which may be the result of only including $(B_\hexagon + B_\hexagon^\dagger)$ at first order in the variational wavefunction.

Next, fixing $\theta = \pi/4$ and $J^\perp = 0.01$, we compute the overlaps as a function of J_2^z, this time the same path in parameter space as fig. 4.11. The ground state fidelity is over 90% for a substantial portion of the parameter space around $J_2^z = 0.5$, decreasing as J_2^z approaches the phase transition to the XY ferromagnet. The optimal ϕ is minimum around

$J_2^z = 0.47$, which coincides with the local minimum in the energy gap and nearby to the anomalous feature in the fidelity. In both paths through parameter space we see that a closing of the energy gap and features in the fidelity coincide with larger overlap with the RK wavefunction. For our finite size system, it is however not possible to say whether this corresponds to a critical point, and at least for this cluster, the ground state wavefunction is liquid-like either side of these points.

Using exact diagonalization, we have located the region in parameter space where the ground state consists of a 3:1 manifold plus quantum fluctuations. The high overlap of a QSL variational wavefunction we motivated from perturbation theory with the ground state in this regime, even away from $J_2^z = 0.5$, suggests that the effective lattice gauge theory and quantum dimer models derived in perturbation theory offer the appropriate perspective from which to understand the low-energy properties. Due to the small system size, we are not able to establish whether this regime is a single phase or hosts several different phases. However, we identify points at $J_2^z \approx 0.5$ and $\theta \approx 3\pi/8$ which are candidates for critical points. Numerical simulations on larger system sizes are needed to resolve the nature of these points, as well as to determine whether a liquid state survives to larger system sizes.

4.5 Summary and Outlook

In this chapter we studied the ground state properties of the quantum spin 1/2 XXZ model on the centred pyrochlore lattice. In perturbation theory, for $\gamma = 2$, we derived an effective frustrated $\mathrm{U}(1)$ lattice gauge theory coupled to fermionic matter. The deconfined phase of this theory, without condensation of spinon pairs, is a $\mathrm{U}(1)$ QSL, closely related to that on the pyrochlore lattice. Turning to gauge mean-field for $\gamma = 2$, we found the only self-consistent solution in our zero-flux ansatz is the $\mathrm{U}(1)$ QSL, identical to the mean-field form of the $\mathrm{U}(1)$ QSL on the pyrochlore lattice. This suggests that, if the ground state is deconfined, it will be a $\mathrm{U}(1)$, not $\mathbb{Z}_2$, QSL. This calculation, however, does not account for the role of the 3:1 manifold. Turning to exact diagonalization on an $N = 24$ cluster, we found a region in the parameter space, for small $J^{\perp}$, where the ground state is a superposition of 3:1 states, a prerequisite for realizing the QSL. We saw that the ground state in this regime has high overlap with a QSL variational wavefunction inspired by perturbation theory, even away from the $\gamma = 2$ point where it was derived. This indicates that the perturbation theory and, therefore, the effective gauge theory and associated dimer models, provide the right framework for understanding the low-energy properties. However, these simulations suffer from severe finite size effects, so simulations on larger system sizes are called for to settle the precise nature of the phase(s) in the $(3{:}1)^{\perp}$ region.

Looking ahead, exact diagonalization calculations are probably not possible for lattice sizes large enough that, with periodic boundaries, the smallest closed loops are length-6 hexagons, which would allow us to rule out effects from lower order perturbative processes. However, if one works instead in the reduced Hilbert space of the effective perturbative

Hamiltonian, similar to [155] these lattice sizes are within reach. Furthermore, such an approach could also be used to simulate the perturbative regime for $J^{\perp}$ antiferromagnetic, where, on the pyrochlore, the ground state is a π-flux $\mathrm{U}(1)$ QSL. This, however comes at the cost of only being valid for $\gamma = 2$, and not for the broader parameter space. On the other hand, one could also use quantum Monte Carlo, which does not suffer from the sign problem for ferromagnetic $J^{\perp}$, to study the full XXZ Hamiltonian, similar to the calculations performed in [151]. To identify the QSL, one could, for example, compare correlation functions to those of the RK wavefunction for an appropriate configuration of centre spins. One possible ordered state which would need to be ruled out, is the R state [131, 205, 206] found at smaller μ in the effective third order dimer model for ferromagnetic centres. This is expected to be the ground state for parameters $J_2^z = 0.5, J_1^{\perp} = 0, \left|J_2^{\perp}\right| \ll 1$, and could occupy a finite extent in the parameter space.

If a QSL ground state is identified in the $(3{:}1)^{\perp}$ regime, it would then be interesting to characterize the properties of the state by interpreting the effective lattice gauge theory as an emergent quantum electrodynamics. One could, for example, extract the fine structure constant or speed of light for different values of the parameters in the spirit of [155].

On the experimental side, a material whose low temperature properties are described by the XXZ model with ferromagnetic $J^{\perp}$ on the centred pyrochlore lattice is probably unrealistic, however, more promising, is the prospect of realizing a spin $1/2$ material with entirely antiferromagnetic interactions. This could be possible, for example, in a Cu(II)-based metal-organic framework. More speculatively, perhaps it could be possible to find effective $S = 1/2$ degrees of freedom in a variant with strong spin-orbit coupling, as in the dipolar-octupolar pyrochlores [156]. In the perturbation theory, one can change the sign of $J_2^{\perp}$ terms by an appropriate unitary transformation [90], as well as changing the sign of $J_1^{\perp}$ through a global π-rotation of all centre spins about the z-axis. Therefore, the effective perturbative Hamiltonian can be mapped from the ferromagnetic to antiferromagnetic case. A QSL ground state in the perturbative regime would likely be closely related to the π-flux $\mathrm{U}(1)$ QSL on the pyrochlore. Whether such a QSL exists and its extent in the parameter space if it does, would be interesting questions to investigate.

This work is the first step towards understanding possible QSLs on the centred pyrochlore lattice and their effective gauge theory descriptions. Nevertheless, we already glimpse the potential for realizing exotic $\mathrm{U}(1)$ lattice gauge theories with matter, which could lead to the observation of phenomena beyond that allowed by the “standard" quantum electrodynamics which governs our universe.

Conclusion

In this thesis, we have presented the first studies of classical and quantum spin models on the centred pyrochlore lattice. We found that this geometry supplements the emergent gauge fields of ground states on the pyrochlore with charge degrees of freedom. This provides a new approach for engineering exotic states of matter, by modifying the Hamiltonian to manipulate these charges, one can tune from ordered to disordered ground states and the states in between. The applicability of such an approach is not restricted to the centred pyrochlore, but could be applied to other lattice geometries based on centred (frustrated) clusters.

Let us summarize the main results and highlight possibilities for future study. First, the minimal Ising model on the centred pyrochlore lattice hosts a rich phase diagram, including both $\mathbb{Z}_2$ and $\mathrm{U}(1)$ classical spin liquid ground states. Many of these features carry over to the Heisenberg model which supports a low-temperature classical spin liquid in a large region of the parameter space. For $\eta \gtrsim 0.5$, this spin liquid is characterized by broad bow ties in the spin structure factor, which can be rationalized as the result of exponential screening of spin correlations, due to the emergence of effective electric charges in the ground state. A complementary view is to see this as the thin-film realization of a higher-dimensional Coulomb spin liquid. The analogous model defined on the 2D centred kagome lattice displays these same features. Furthermore, adding a J_3 term to the centred pyrochlore Hamiltonian can order the charges in the ground state, leading to the recovery of the divergence-free Coulomb spin liquid in three dimensions.

An interesting path forward is to study the effect of terms beyond the minimal Ising or Heisenberg Hamiltonians, whose effects could lead to the observation of further exotic states of matter. In particular, the centred pyrochlore geometry lends itself to studying the interplay between order and low-temperature fluctuations.

Our motivation for studying the centred pyrochlore lattice came from its experimental realization in the metal-organic framework $[\mathrm{Mn(ta)_2}]$. Comparing the properties of the classical Heisenberg + dipolar model to the magnetization, susceptibility and specific heat measured in experiments, we concluded that $[\mathrm{Mn(ta)_2}]$ is well-approximated for parameters where our model hosts a finite temperature spin liquid regime. We also obtained a prediction for the low-temperature ordered state, induced by dipolar interactions. These

predictions are readily verifiable in, for example, neutron scattering experiments, where the predicted order can be compared to Bragg peaks from neutron diffraction and the powder-averaged static structure factor of the spin liquid compared to diffuse neutron scattering results.

Finally, we investigated the spin-$1/2$ quantum XXZ model with ferromagnetic $J^{\perp}$, as a case study for the possibility of realizing quantum spin liquids on the centred pyrochlore lattice. In perturbation theory, we identified that the low-energy effective theory in the 3:1 regime is a $\mathrm{U}(1)$ lattice gauge theory with fermionic matter. Gauge mean-field calculations suggest that in the deconfined phase, spinon pairs will not condense, so corresponds to a $\mathrm{U}(1)$ quantum spin liquid. Exact diagonalization calculations on a small cluster showed that the ground state properties can be understood within the framework of the perturbative effective theory, even away from the $\gamma = 2$ point where it was derived. These results call for large-scale numerical simulations to ascertain whether the ground state in this regime is indeed the conjectured $\mathrm{U}(1)$ QSL. Future work could investigate how this fits into the emergent quantum electrodynamics picture of the pyrochlore lattice, since the centred pyrochlore hosts charges in its “vacuum".

This thesis provides the framework for understanding the properties of spin models on the centred pyrochlore lattice, hopefully there are many fascinating phenomena waiting to be discovered.

Appendix A

Quantum Rotors

In both perturbation theory and gauge mean-field theory for the spin $1/2$ XXZ model we map spins to $O(2)$ quantum rotors. An $O(2)$ quantum rotor is equivalent to a particle on a circle, see fig. A.1, which has the degrees of freedom x_1, x_2, p_1, p_2 subject to the constraint $x_1^2 + x_2^2 = 1$. These satisfy the canonical commutation relations, $[x_i, p_j] = i\delta_{ij}$. The rotor has angular momentum $L = x_1 p_2 - x_2 p_1$ and we can reduce x_1, x_2 to a single degree of freedom by setting

$$x_1 = \cos\theta = \frac{1}{2}(e^{i\theta} + e^{-i\theta}), \qquad x_2 = \sin\theta = \frac{1}{2i}(e^{i\theta} - e^{-i\theta}), \tag{A.1}$$

which defines the angular variable θ. Note that

$$[L, x_1] = -x_2[p_1, x_1] = ix_2, \qquad [L, x_2] = x_1[p_2, x_2] = -ix_1, \tag{A.2}$$

where these commutation relations are reproduced if

$$[L, \theta] = -i. \tag{A.3}$$

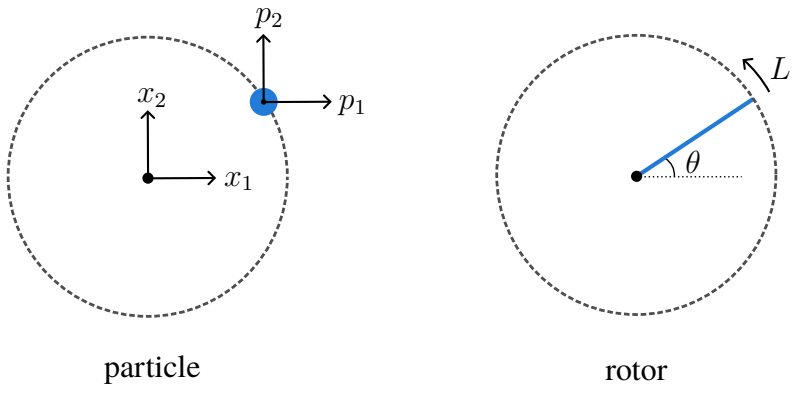

Figure A.1: An $O(2)$ rotor (right) is equivalent to a particle constrained to move on a circle (left). The variables describing the two systems are shown.

The properties of the eigenstates of L and θ can be found by working in the angular representation where $L \to -i\frac{\partial}{\partial\theta}$. Let the eigenstates of θ and L be $|\theta\rangle$ and $|L\rangle$ respectively, where a suitable angular representation of $|L\rangle$ is

$$\langle\theta|L\rangle = e^{iL\theta}. \tag{A.4}$$

Furthermore the eigenstates of θ are also the eigenstates of $\Phi = e^{-i\theta}$. In the many-body context we define a rotor, L_r, θ_r, on each lattice site such that

$$\langle\theta_{r'}|L_r\rangle = \delta_{rr'}e^{iL_r\theta_r}, \tag{A.5}$$

with the eigenstates which form a complete basis,

$$1 = \frac{1}{\mathcal{N}}\prod_r \int_0^{2\pi} d\theta_r \, |\theta_r\rangle \langle\theta_r| \,, \tag{A.6}$$

$$1 = \frac{1}{\mathcal{N}'}\prod_r \int_{-\infty}^{\infty} dL_r \, |L_r\rangle \langle L_r| \,, \tag{A.7}$$

where $\mathcal{N}, \mathcal{N}'$ are normalization factors.

A.1 Path Integral Formulation

In gauge mean-field theory (section 4.3), to solve the spinon part of the mean-field Hamiltonian we reformulate the problem as a path integral. We want to compute ground state expectation values

$$\langle O\rangle = \frac{\langle\Psi_0| O |\Psi_0\rangle}{\langle\Psi_0|\Psi_0\rangle} = \lim_{\beta\to\infty} \frac{\langle\Psi| e^{-\beta H} O e^{-\beta H} |\Psi\rangle}{\langle\Psi| e^{-\beta H} e^{-\beta H} |\Psi\rangle}, \tag{A.8}$$

where $|\Psi\rangle$ is an arbitrary state. In particular, we are interested in the form of the (effective) partition function

$$Z = \lim_{\beta\to\infty} \langle\Psi| e^{-\beta H} e^{-\beta H} |\Psi\rangle \,. \tag{A.9}$$

The Hamiltonian, $H = H_{\text{rotor}} = \frac{J_z^2}{2}\sum_r Q_r^2 + H_\Phi(\zeta_r)$ depends on the variables Q_r and ζ_r, which are respectively the angular momentum, L_r and angular variable, θ_r, of the rotors.

In anticipation of time-slicing, let the initial and final state $|\Psi\rangle = \prod_{r(0)=1}^N \left|\zeta_{r(0)}\right\rangle = \prod_{r(2n)=1}^N \left|\zeta_{r(2n)}\right\rangle$, where the index in brackets labels the time-slice and $\prod_{r(i)=1}^N \left|\zeta_{r(i)}\right\rangle = |\zeta'\rangle \otimes |\zeta'\rangle \otimes \cdots \otimes |\zeta'\rangle$, where N is the number of lattice sites. This is the product state with $\zeta_r = \zeta'$ on all sites. Time-slicing, $e^{-\beta H} = (e^{-\Delta\tau H})^n$ and inserting resolutions of the identity, eq. (A.6),

$$\begin{aligned} Z \propto \lim_{\beta\to\infty} \prod_{r(0)\ldots r(2n)} \int_0^{2\pi} d\zeta_{r(2n-1)} \int_0^{2\pi} d\zeta_{r(2n-2)} \cdots \int_0^{2\pi} d\zeta_{r(1)} \cdot \\ \left\langle\zeta_{r(2n)}\right| e^{-\Delta\tau H} \left|\zeta_{r(2n-1)}\right\rangle \cdots \left\langle\zeta_{r(j+1)}\right| e^{-\Delta\tau H} \left|\zeta_{r(j)}\right\rangle \cdots \left\langle\zeta_{r(1)}\right| e^{-\Delta\tau H} \left|\zeta_{r(0)}\right\rangle , \end{aligned} \tag{A.10}$$

with $\Delta\tau = \frac{\beta}{n}$. The key quantity to evaluate is $x = \left\langle \zeta_{r(j+1)} \right| e^{-\Delta\tau H} \left| \zeta_{r(j)} \right\rangle$. Inserting the resolution of the identity, eq. (A.7),

$$x = \prod_{r'(j)} \int_{-\infty}^{\infty} dQ_{r'(j)} \left\langle \zeta_{r(j+1)} \middle| Q_{r'(j)} \right\rangle \left\langle Q_{r'(j)} \right| e^{-\Delta\tau H} \left| \zeta_{r(j)} \right\rangle . \tag{A.11}$$

From eq. (A.5),

$$\left\langle \zeta_{r(j+1)} \middle| Q_{r'(j)} \right\rangle = \delta_{r,r'} e^{iQ_{r(j)}\zeta_{r(j+1)}}. \tag{A.12}$$

Then for $\left\langle Q_{r'(j)} \right| e^{-\Delta\tau H} \left| \zeta_{r(j)} \right\rangle$, first write $H = H_Q + H_\Phi$. Using $e^{\hat{X}} e^{\hat{Y}} = e^{\hat{X}+\hat{Y}+\cdots}$, and dropping terms of greater than first order in $\Delta\tau$, anticipating the $\Delta\tau \to 0$ limit we will take later, we can write $e^{-\Delta\tau H} = e^{-\Delta\tau H_Q} e^{-\Delta\tau H_\Phi}$. Replacing the operators with their eigenvalues,

$$\left\langle Q_{r'(j)} \right| e^{-\Delta\tau H} \left| \zeta_{r(j)} \right\rangle = \delta_{r',r} e^{-\Delta\tau H_{r(j)}} e^{-iQ_{r(j)}\zeta_{r(j)}}, \tag{A.13}$$

where H_r is the terms of the Hamiltonian acting on the site r. Bringing this together

$$x = \int_{-\infty}^{\infty} dQ_{r(j)} e^{-\Delta\tau \tilde{J} Q_{r(j)}^2 + iQ_{r(j)}(\zeta_{r(j+1)} - \zeta_{r(j)})} e^{-\Delta\tau H_{\Phi r(j)}}, \tag{A.14}$$

where $\tilde{J} = \frac{J_2^z}{2}$. Completing the square for $Q_{r(j)}$ and then integrating it out leaves

$$x \propto e^{-\Delta\tau L_j}, \qquad L_j = \frac{(\zeta_{r_j}^{j+1} - \zeta_{r_j}^{j})^2}{2J_2^z \Delta\tau^2} + H_{\Phi_r(j)}. \tag{A.15}$$

Taking the continuum limit, $n \to \infty$, and explicitly writing out the sum over lattice sites in the exponent (which is implied by the products over lattice sites),

$$Z \propto \int D\zeta \, e^{S[\zeta]}, \qquad S[\zeta] = \int_{-\infty}^{\infty} d\tau \mathcal{L}(\zeta_r, \partial_\tau \zeta_r) = \int_{-\infty}^{\infty} d\tau \frac{1}{2J_2^z} \sum_r (\partial_\tau \zeta_r)^2 + H_\Phi. \tag{A.16}$$

Since $\Phi_r = e^{-i\zeta_r}$, H_Φ is interacting at all orders so to proceed we recast the functional integral in terms of Φ, Φ^* rather than ζ. Subject to the constraint $|\Phi_r|^2 = 1$, $(\partial_\tau \zeta_r)^2 = \partial_\tau \Phi_r \partial_\tau \Phi_r^*$ so the Lagrangian can be written in terms of the Φ_r. In the integrals we replace $\int_0^{2\pi} d\zeta_r \to \int_{-\infty}^{\infty} d\Phi_r d\Phi_r^*$, which breaks the $|\Phi_r|^2 = 1$ constraint. To remedy this we introduce a Lagrange multiplier, λ, which implements the constraint on average. Then the partition function becomes

$$Z \propto \int D(\Phi, \Phi^*) \, e^{S[\Phi,\Phi^*]}, \tag{A.17}$$

$$S[\Phi, \Phi^*] = \int_{-\infty}^{\infty} d\tau \mathcal{L}(\Phi_r, \Phi_r^*, \partial_\tau \Phi_r, \partial_\tau \Phi_r^*) = \int_{-\infty}^{\infty} d\tau \frac{1}{2J_2^z} \sum_r \partial_\tau \Phi_r \partial_\tau \Phi_r^* + H_\Phi + \lambda \sum_r (|\Phi_r|^2 - 1). \tag{A.18}$$

This is the starting point for solving the spinon part of the mean-field Hamiltonian.

Appendix B

Exact Diagonalization

To obtain unbiased numerical results for quantum spin models on the centred pyrochlore lattice, we diagonalize the many-body Hamiltonian [212, 213] to obtain exact energy eigenvalues and corresponding eigenstates. For simplicity, we will describe the application of the method to a general spin-S XXZ Hamiltonians with nearest neighbour interactions,

$$H = J^z \sum_{\langle ij \rangle} S_i^z S_j^z + J^\perp \sum_{\langle ij \rangle} \left(S_i^+ S_j^- + S_i^- S_j^+ \right), \tag{B.1}$$

which can be readily generalized to the $J_1 - J_2$ case we study in this thesis. The lattice and boundary conditions will be arbitrary for the purposes of this discussion, but we specify a total of N lattice sites.

To represent the Hamiltonian in matrix form, we must first choose an appropriate set of basis states. We choose to work in the S^z basis,

$$|n\rangle = \left| S_0^z, S_2^z, \ldots, S_{N-1}^z \right\rangle, \tag{B.2}$$

such that each orthonormal state is specified by a unique configuration of S_i^z values. The local dimension of the Hilbert space is $d = 2S + 1$, so that the total Hilbert space dimension, $D = d^N$. A generic state is written as

$$|\Psi\rangle = \sum_{n=1}^{D} c_n |n\rangle, \tag{B.3}$$

which can be encoded using the length D vector

$$\mathbf{x} = (c_1, c_2, \ldots, c_D)^T, \tag{B.4}$$

where the c_n can be chosen to be real coefficients, since the matrix form of this Hamiltonian is real symmetric. We assign each state in the Hilbert space an integer index n. The matrix form of the Hamiltonian, H, is obtained by computing its matrix elements

$$H_{n'n} = \langle n' | H | n \rangle \tag{B.5}$$

for all n, n'.

The J^z and $J^\perp$ terms correspond to diagonal and off-diagonal parts of the Hamiltonian respectively, so it is useful to write

$$H = H^z + H^\perp. \tag{B.6}$$

To evaluate the $H^\perp$ parts, we use the relations [214]

$$S_i^+ \left|S_i^z\right\rangle = \alpha_i \left|S_i^z + 1\right\rangle, \qquad S_i^- \left|S_i^z\right\rangle = \beta_i \left|S_i^z - 1\right\rangle, \tag{B.7}$$

where

$$\alpha_i = \sqrt{S(S+1) - S_i^z(S_i^z+1)}, \qquad \beta_i = \sqrt{S(S+1) - S_i^z(S_i^z-1)}. \tag{B.8}$$

The matrix elements are given by

$$H_{nn'} = \begin{cases} E^z, & n' = n, \\ E_{ij}^\pm, & n' \neq n, \end{cases} \tag{B.9}$$

where

$$\begin{aligned} E^z &= J^z \sum_{\langle ij \rangle} S_i^z S_j^z, \\ E_{ij}^\pm &= \begin{cases} J^\perp \alpha_i \beta_j, & \text{if } \left|n\right\rangle \xrightarrow{S_i^+ S_j^-} a \left|n'\right\rangle, \\ J^\perp \beta_i \alpha_j, & \text{if } \left|n\right\rangle \xrightarrow{S_i^- S_j^+} a \left|n'\right\rangle, \\ 0, & \text{otherwise.} \end{cases} \end{aligned} \tag{B.10}$$

The notation $\left|n\right\rangle \xrightarrow{O} a \left|n'\right\rangle$ means that the operator O maps the state $\left|n\right\rangle$ to $a \left|n'\right\rangle$, where a is a non-zero prefactor. Note that for $S = 1/2$, α_i and β_i can only take the values 0 or 1.

Encoding Many-Body Basis States

In order to construct the Hamiltonian numerically, we first represent the basis states in an appropriate fashion to be stored and manipulated on a computer. We map the set of S_i^z values on each site to non-negative integers, $n_i \in \{0, \ldots, d-1\}$ (equivalent to mapping the spins to bosons), through the relation

$$n_i = S_i^z + S, \tag{B.11}$$

such that, for $S = 1/2$, $S_i^z = -(+)\frac{1}{2} \rightarrow n_i = 0(1)$. We can then interpret the configuration corresponding to each basis state as an integer represented in base-d

$$\left|n\right\rangle = \left|n_0, \ldots, n_{N-1}\right\rangle \rightarrow n_{N-1} n_{N-2} \ldots n_0 \xrightarrow{f_{10}} s_n, \tag{B.12}$$

$\|n\rangle$ (Spins)	$\|n\rangle$ (Bosons)	s_n^d (base-d int)	s_n (int)	n (index)
$\|\uparrow,\uparrow,\downarrow,\downarrow\rangle$	$\|1,1,0,0\rangle$	0011	3	0
$\|\uparrow,\downarrow,\uparrow,\downarrow\rangle$	$\|1,0,1,0\rangle$	0101	5	1
$\|\downarrow,\uparrow,\uparrow,\downarrow\rangle$	$\|0,1,1,0\rangle$	0110	6	2
$\|\uparrow,\downarrow,\downarrow,\uparrow\rangle$	$\|1,0,0,1\rangle$	1001	9	3
$\|\downarrow,\uparrow,\downarrow,\uparrow\rangle$	$\|0,1,0,1\rangle$	1010	10	4
$\|\uparrow,\downarrow,\downarrow,\uparrow\rangle$	$\|1,0,0,1\rangle$	1100	12	5

Table B.1: Different representations of the basis states for $N = 4$, $S = 1/2$ in the $m^z = 0$ sector. The s_n values are stored in the vector $\mathbf{s}$ at position n. The n^{th} coefficient of the vector $\mathbf{x} = (c_1, c_2, \ldots, D)$ is the coefficient of that basis state in $|\Psi\rangle$.

where the final arrow represents the mapping from a base-d integer to a (unique) base-10 integer, s_n. We generate each configuration in the Hilbert space, then map this to an integer, creating a sorted vector of integers,

$$\mathbf{s} = (s_1, s_2, \ldots, s_D), \tag{B.13}$$

i.e the n^{th} element of this sorted vector is the integer representation of the basis state with index n. All of these mappings between representations can be reversed.

Note that the need for the length-D vector $\mathbf{S}$ can be eliminated by using a hashing algorithm which maps directly from the bosonic configuration to the state index [215, 216]. This also means that one does not need to search through $\mathbf{S}$ when computing off-diagonal matrix elements. However, the hashing algorithms can make the implementation of symmetries more challenging.

Full Diagonalization

If we require all eigenvalues of the Hamiltonian, for example, to compute quantities at finite temperature, we construct the full $D \times D$ matrix H then diagonalize it numerically. H can be constructed using the following algorithm.

For every state index $n \in \{1, \ldots, D\}$:

1. Obtain the integer representation, s_n, of the state $|n\rangle$ by accessing the n^{th} element of $\mathbf{s}$.
2. Convert s_n to a configuration in the S_i^z representation
3. Compute the diagonal contribution $E^z(n)$, using the expression in eq. B.10 and set $H_{nn} = E^z(n)$.
4. Compute the off-diagonal contribution. For each (i, j) nearest neighbour pair:
   (a) Verify if there is a non-zero matrix element, according to eq. B.10.
   (b) If so compute $E_{ij}^{\perp}(n)$, else advance to the next (i, j) pair and continue from (a).

(c) Convert the $|n'\rangle$ configuration to the integer $s_{n'}$.

(d) Search for the index, n', of $s_{n'}$ in $\mathbf{s}$.

(e) Set $H_{n'n} = E_{ij}^{\pm}(n)$.

The typical time complexity of diagonalization of H is $O(D^3)$ [209], with a memory cost of $O(D^2)$ if constructing the full matrix. Given D scales exponentially with the number of lattice sites, this approach is limited to very small system sizes, for an $N = 20$, $S = 1/2$ system it would require about 1TB to store the full matrix H. Therefore, in this thesis, we only used full diagonalization to compute finite temperature quantities of the $S = 5/2$ Heisenberg model on small clusters of 5 or 6 sites, see section 3.4.

Lanczos Method

Rather than constructing the full matrix, we can use the Lanczos method [217], as long as we are only interested in the lowest few eigenvalues. In the variant we employ, we construct H “on the fly" rather than saving it in memory. This has some cost in time complexity, but requires less memory, which is often the limiting factor for implementing these sorts of calculations. In the Lanczos method [213], an orthonormal basis is constructed in the Krylov space of the Hamiltonian, a subspace of the full Hilbert space obtained by repeated application of the Hamiltonian according to the relation

$$|\Psi_{m+1}\rangle \propto H\,|\Psi_m\rangle - a_m\,|\Psi_m\rangle - b_{m-1}\,|\Psi_{m-1}\rangle\,, \tag{B.14}$$

starting from an initial random state, $|\Psi_0\rangle$. Here, the a_m and b_m are coefficients chosen to ensure the orthogonality of the states. By construction, the matrix form of the Hamiltonian is a $k \times k$ tridiagonal matrix in this subspace, with k typically on the order of a few tens or hundreds. The exact dimension depends on the number of Krylov states, k, required for the eigenvalues to reach a certain convergence criterion. The limiting factor of Lanczos calculations is the memory required to store the length-D Krylov space vectors, $|\Psi_m\rangle$, each of which would require about 1TB of memory to store for an $N = 40$, $S = 1/2$ system, approximately doubling the number of lattice sites achievable with full diagonalization.

In our implementation we use the implicitly restarted Lanczos method (IRLM) contained in ARPACK [218], where the crux of the implementation is computing the action of the Hamiltonian on an arbitrary state,

$$|\Psi'\rangle = H\,|\Psi\rangle\,, \tag{B.15}$$

which can be deduced from the matrix-vector multiplication,

$$\mathbf{x}' = \mathrm{H}\mathbf{x}. \tag{B.16}$$

The procedure for the matrix-vector multiplication is as follows.

1. Initialize a vector $\mathbf{x}'$ with all zeroes.

2. For every state index $n \in \{1, \ldots, D\}$:
   (a) Obtain the integer representation, s_n, of the state $|n\rangle$ by accessing the n^{th} element of $\mathbf{s}$.
   (b) Convert s_n to a configuration in the S_i^z representation.
   (c) Compute the diagonal contribution $E^z(n)$, using the expression in eq. B.10 and increment the n^{th} element of $\mathbf{x}'$ by $c_n E^z(n)$.
   (d) Compute the off-diagonal contribution. For each (i, j) nearest neighbour pair:
      i. Verify if there is a non-zero matrix element, according to eq. B.10.
      ii. If so compute $E_{ij}^{\perp}(n)$, else advance to the next (i, j) pair and continue from (i).
      iii. Convert the $|n'\rangle$ configuration to the integer $s_{n'}$.
      iv. Search for the index, n', of $s_{n'}$ in $\mathbf{s}$.
      v. Increment the n'^{th} element of $\mathbf{x}'$ by $c_n E_{ij}^{\perp}(n)$.

In our implementation we use OpenMP [219] to parallelize the outer `for` loop, effectively breaking $\mathbf{x}$ into smaller blocks, whose contribution to $\mathbf{x}'$ is computed on separate threads. Note that the ARPACK implementation of the implicitly restarted Lanczos method (IRLM) is able to find degenerate eigenstates, unlike the vanilla Lanczos method, as it uses a so-called block method [218]. Furthermore, the implicit restarting [220] maintains a low-dimensional Krylov space by performing a QR decomposition [209] to remove unnecessary components.

Symmetries

To access the largest system sizes possible, exact diagonalization should be implemented making use of discrete symmetries [221], which allows one to diagonalize smaller blocks of H, corresponding to different symmetry sectors, separately. In our implementation, we use the fact that $m_z = \sum_i S_i^z$ commutes with the Hamiltonian to reduce the effective dimension of the Hilbert space. This is a simple symmetry to implement, when generating the basis, $\{|n\rangle\}$, one ensures only to keep those with the target m_z eigenvalue. To access larger system sizes, one could make use of the S^z spin inversion symmetry in the $m_z = 0$ sector, as well as translational symmetries. However, translational symmetries are challenging to implement in an efficient way on 3D lattices.

Bibliography

[1] R. P. Nutakki, L. D. C. Jaubert, and L. Pollet, "The classical Heisenberg model on the centred pyrochlore lattice", *SciPost Phys.* **15**, 040 (2023).

[2] R. P. Nutakki et al., "Frustration on a centered pyrochlore lattice in metal-organic frameworks", *Phys. Rev. Research* **5**, L022018 (2023).

[3] L. Landau, "On the Theory of Phase Transitions", *Zh. Eksp. Teor. Fiz.* **7**, 19–32 (1937).

[4] V. L. Ginzburg and L. D. Landau, "On the theory of superconductivity", *Zh. Eksp. Teor. Fiz.* **20**, 1064–1082 (1950).

[5] K. Mehran, *Statistical Physics of Fields* (Cambridge University Press, Cambridge, 2007).

[6] S. G. Brush, "History of the Lenz-Ising Model", *Rev. Mod. Phys.* **39**, 883–893 (1967).

[7] E. V. Thuneberg, "Superfluidity", in *Encyclopedia of Condensed Matter Physics*, Vol. 1, edited by F. Bassani, G. L. Liedl, and P. Wyder (Elsevier Academic Press, 2005), pp. 128–133.

[8] J. F. Greitemann, "Investigation of Hidden Multipolar Spin Order in Frustrated Magnets Using Interpretable Machine Learning Techniqes", PhD thesis (LMU Munich, Munich, 2019).

[9] G. H. Wannier, "Antiferromagnetism. The Triangular Ising Net", *Phys. Rev.* **79**, 357–364 (1950).

[10] K. Kano and S. Naya, "Antiferromagnetism. The Kagome Ising Net", *Progress of Theoretical Physics* **10**, 158–172 (1953).

[11] P. W. Anderson, "Ordering and Antiferromagnetism in Ferrites", *Physical Review* **102**, 1008–1013 (1956).

[12] L. Balents, "Spin liquids in frustrated magnets", *Nature* **464**, 199–208 (2010).

[13] J. T. Chalker, "Geometrically Frustrated Antiferromagnets: Statistical Mechanics and Dynamics", in *Introduction to Frustrated Magnetism*, Vol. 164, Springer Series in Solid-State Sciences (Springer Berlin Heidelberg, Heidelberg, 2011), pp. 3–22.

[14] P. W. Anderson, "Resonating Valence Bonds: A New Kind of Insulator", *Mat. Res. Bull.* **8**, 153–160 (1973).

[15] S. J. Miyake, "Spin-Wave Results for the Staggered Magnetization of Triangular Heisenberg Antiferromagnet", *Journal of the Physical Society of Japan* **61**, 983–988 (1992).

[16] B. Bernu et al., "Exact spectra, spin susceptibilities, and order parameter of the quantum Heisenberg antiferromagnet on the triangular lattice", *Phys. Rev. B* **50**, 10048–10062 (1994).

[17] A. V. Chubukov, S. Sachdev, and T. Senthil, "Large-S expansion for quantum antiferromagnets on a triangular lattice", *J. Phys.: Condens. Matter* **6**, 8891–8902 (1994).

[18] L. Capriotti, A. E. Trumper, and S. Sorella, "Long-Range Néel Order in the Triangular Heisenberg Model", *Phys. Rev. Lett.* **82**, 3899–3902 (1999).

[19] W. Zheng et al., "Excitation spectra of the spin-1/2 triangular-lattice Heisenberg antiferromagnet", *Phys. Rev. B* **74**, 224420 (2006).

[20] S. R. White and A. L. Chernyshev, "Neél Order in Square and Triangular Lattice Heisenberg Models", *Phys. Rev. Lett.* **99**, 127004 (2007).

[21] C. Lhuillier and G. Misguich, "Introduction to Quantum Spin Liquids", in *Introduction to Frustrated Magnetism*, Vol. 164, edited by C. Lacroix, P. Mendels, and F. Mila, Springer Series in Solid-State Sciences (Springer Berlin Heidelberg, Heidelberg, 2011), pp. 23–44.

[22] L. Savary and L. Balents, "Quantum Spin Liquids", *Rep. Prog. Phys.* **80**, 016502 (2017).

[23] Y. Zhou, K. Kanoda, and T.-K. Ng, "Quantum spin liquid states", *Rev. Mod. Phys.* **89**, 025003 (2017).

[24] J. Knolle and R. Moessner, "A Field Guide to Spin Liquids", *Annu. Rev. Condens. Matter Phys.* **10**, 451–472 (2019).

[25] D. C. Tsui, H. L. Stormer, and A. C. Gossard, "Two-Dimensional Magnetotransport in the Extreme Quantum Limit", *Phys. Rev. Lett.* **48**, 1559–1562 (1982).

[26] R. E. Prange et al., eds., *The Quantum Hall Effect*, Graduate Texts in Contemporary Physics (Springer New York, New York, NY, 1990).

[27] H. L. Stormer, "Nobel Lecture: The fractional quantum Hall effect", *Rev. Mod. Phys.* **71**, 875–889 (1999).

[28] X. G. Wen, *Quantum Field Theory of Many-Body Systems* (Oxford University Press, Oxford, 2004).

[29] E. Fradkin, *Field Theories of Condensed Matter Physics*, 2nd ed. (Cambridge University Press, Cambridge, 2013).

[30] D. Tong, "The Quantum Hall Effect", 2016.

[31] X.-G. Wen, "Topological Order: From Long-Range Entangled Quantum Matter to a Unified Origin of Light and Electrons", *ISRN Condensed Matter Physics* **2013**, 1–20 (2013).

[32] X.-G. Wen, "*Colloquium* : Zoo of quantum-topological phases of matter", *Rev. Mod. Phys.* **89**, 041004 (2017).

[33] X. G. Wen and Q. Niu, "Ground-state degeneracy of the fractional quantum Hall states in the presence of a random potential and on high-genus Riemann surfaces", *Phys. Rev. B* **41**, 9377–9396 (1990).

[34] X. G. Wen, "Topological Orders in Rigid States", *International Journal of Modern Physics B* **04**, 239–271 (1990).

[35] X.-G. Wen, "Topological orders and edge excitations in fractional quantum Hall states", *Advances in Physics* **44**, 405–473 (1995).

[36] X.-G. Wen, "Quantum order: a quantum entanglement of many particles", *Physics Letters A* **300**, 175–181 (2002).

[37] J. M. Leinaas and J. Myrheim, "On the theory of identical particles", *Il Nuovo Cimento B Series 11* **37**, 1–23 (1977).

[38] F. Wilczek, "Quantum Mechanics of Fractional-Spin Particles", *Phys. Rev. Lett.* **49**, 957–959 (1982).

[39] V. Lahtinen and J. Pachos, "A Short Introduction to Topological Quantum Computation", *SciPost Phys.* **3**, 021 (2017).

[40] V. Kalmeyer and R. B. Laughlin, "Equivalence of the resonating-valence-bond and fractional quantum Hall states", *Phys. Rev. Lett.* **59**, 2095–2098 (1987).

[41] S. A. Kivelson, D. S. Rokhsar, and J. P. Sethna, "Topology of the resonating valence-bond state: Solitons and high-Tc superconductivity", *Phys. Rev. B* **35**, 8865–8868 (1987).

[42] J. G. Bednorz and K. A. Mueller, "Possible High T_c Superconductivity in the Ba-La-Cu-O System", *Zeitschrift fuer Physik B Condensed Matter* **64**, 189–193 (1986).

[43] B. Keimer et al., "From quantum matter to high-temperature superconductivity in copper oxides", *Nature* **518**, 179–186 (2015).

[44] X.-G. Wen, "Quantum orders and symmetric spin liquids", *Phys. Rev. B* **65**, 165113 (2002).

[45] M. J. Harris et al., "Geometrical Frustration in the Ferromagnetic Pyrochlore $Ho_2Ti_2O_7$", *Phys. Rev. Lett.* **79**, 2554–2557 (1997).

[46] S. T. Bramwell and M. J. Harris, "Frustration in Ising-type spin models on the pyrochlore lattice", *J. Phys.: Condens. Matter* **10**, L215–L220 (1998).

[47] S. T. Bramwell and M. J. Harris, "The history of spin ice", *J. Phys.: Condens. Matter* **32**, 374010 (2020).

[48] C. Castelnovo, R. Moessner, and S. Sondhi, "Spin Ice, Fractionalization, and Topological Order", *Annu. Rev. Condens. Matter Phys.* **3**, 35–55 (2012).

[49] C. Castelnovo, R. Moessner, and S. L. Sondhi, "Magnetic monopoles in spin ice", *Nature* **451**, 42–45 (2008).

[50] S. V. Isakov et al., "Dipolar Spin Correlations in Classical Pyrochlore Magnets", *Phys. Rev. Lett.* **93**, 167204 (2004).

[51] C. Castelnovo and C. Chamon, "Topological order and topological entropy in classical systems", *Phys. Rev. B* **76**, 174416 (2007).

[52] L. D. C. Jaubert et al., "Topological-Sector Fluctuations and Curie-Law Crossover in Spin Ice", *Physical Review X* **3**, 10.1103/PhysRevX.3.011014 (2013).
[53] C. Nayak et al., "Non-Abelian Anyons and Topological Quantum Computation", *Rev. Mod. Phys.* **80**, 1083–1159 (2008).
[54] A. Kitaev, "Fault-tolerant quantum computation by anyons", *Annals of Physics* **303**, 2–30 (2003).
[55] A. Kitaev, "Anyons in an exactly solved model and beyond", *Annals of Physics* **321**, 2–111 (2006).
[56] G. Jackeli and G. Khaliullin, "Mott Insulators in the Strong Spin-Orbit Coupling Limit: From Heisenberg to a Quantum Compass and Kitaev Models", *Phys. Rev. Lett.* **102**, 017205 (2009).
[57] S. Trebst and C. Hickey, "Kitaev materials", *Physics Reports* **950**, 1–37 (2022).
[58] Y. Kasahara et al., "Majorana quantization and half-integer thermal quantum Hall effect in a Kitaev spin liquid", *Nature* **559**, 227–231 (2018).
[59] M. R. Norman, "Colloquium: Herbertsmithite and the search for the quantum spin liquid", *Rev. Mod. Phys.* **88**, 14 (2016).
[60] T.-H. Han et al., "Fractionalized excitations in the spin-liquid state of a kagome-lattice antiferromagnet", *Nature* **492**, 406–410 (2012).
[61] V. Porée et al., "Fractional matter coupled to the emergent gauge field in a quantum spin ice", *arXiv:2304.05452* (2023).
[62] H. Bartolomei et al., "Fractional statistics in anyon collisions", *Science* **368**, 173–177 (2020).
[63] J. Nakamura et al., "Direct observation of anyonic braiding statistics", *Nat. Phys.* **16**, 931–936 (2020).
[64] J. Cai et al., "Signatures of fractional quantum anomalous Hall states in twisted $MoTe_2$", *Nature* **622**, 63–68 (2023).
[65] Y. Zeng et al., "Thermodynamic evidence of fractional Chern insulator in moiré $MoTe_2$", *Nature* **622**, 69–73 (2023).
[66] E. Altman et al, "Quantum Simulators: Architectures and Opportunities", *Physical Review X* **2**, 017003 (2021).
[67] G. Semeghini et al., "Probing topological spin liquids on a programmable quantum simulator", *Science* **374**, 1242–1247 (2021).
[68] G. Giudici, M. D. Lukin, and H. Pichler, "Dynamical Preparation of Quantum Spin Liquids in Rydberg Atom Arrays", *Phys. Rev. Lett.* **129**, 090401 (2022).
[69] J. Léonard et al., "Realization of a fractional quantum Hall state with ultracold atoms", *Nature* **619**, 495–499 (2023).
[70] Y. P. Zhong et al., "Emulating Anyonic Fractional Statistical Behavior in a Superconducting Quantum Circuit", *Phys. Rev. Lett.* **117**, 110501 (2016).
[71] C. Song et al., "Demonstration of Topological Robustness of Anyonic Braiding Statistics with a Superconducting Quantum Circuit", *Phys. Rev. Lett.* **121**, 030502 (2018).

[72] K. J. Satzinger et al., "Realizing topologically ordered states on a quantum processor", *Science* **374**, 1237–1241 (2021).
[73] M. Iqbal et al., "Creation of Non-Abelian Topological Order and Anyons on a Trapped-Ion Processor", *arXiv:2305.03766* (2023).
[74] S. Xu et al., "Digital Simulation of Projective Non-Abelian Anyons with 68 Superconducting Qubits", *Chinese Phys. Lett.* **40**, 060301 (2023).
[75] Google Quantum AI and Collaborators et al., "Non-Abelian braiding of graph vertices in a superconducting processor", *Nature* **618**, 264–269 (2023).
[76] C. L. Henley, "The "Coulomb Phase" in Frustrated Systems", *Annu. Rev. Condens. Matter Phys.* **1**, 179–210 (2010).
[77] J. Villain, "Insulating spin glasses", *Z Physik B* **33**, 31–42 (1979).
[78] J. Villain et al., "Order as an effect of disorder", *Journal de Physique* **41**, 1263–1272 (1980).
[79] M. Udagawa and L. Jaubert, eds., *Spin Ice*, Vol. 197, Springer Series in Solid-State Sciences (Springer International Publishing, Cham, 2021).
[80] E. H. Lieb and F. Y. Wu, "Two-dimensional Ferroelectric Models", in *Phase Transitions and Critical Phenomena* (Academic Press, London, 1972).
[81] D. A. Lavis and G. M. Bell, "The Eight-Vertex Model", in *Statistical Mechanics of Lattice Systems of 2: Exact, Series and Renormalization Group Methods*, Texts and Monographs in Physics (Springer Berlin Heidelberg, New York, 1999), pp. 167–202.
[82] L. Pauling, "The Structure and Entropy of Ice and of Other Crystals with Some Randomness of Atomic Arrangement", *J. Am. Chem. Soc.* **57**, 2680–2684 (1935).
[83] J. N. Reimers, "Absence of long-range order in a three-dimensional geometrically frustrated antiferromagnet", *Phys. Rev. B* **45**, 7287–7294 (1992).
[84] R. Moessner and J. T. Chalker, "Properties of a Classical Spin Liquid: The Heisenberg Pyrochlore Antiferromagnet", *Phys. Rev. Lett.* **80**, 2929–2932 (1998).
[85] R. Moessner and J. T. Chalker, "Low-temperature properties of classical geometrically frustrated antiferromagnets", *Phys. Rev. B* **58**, 12049–12062 (1998).
[86] D. Tong, "Statistical Field Theory", Lecture Notes, 2017.
[87] C. L. Henley, "Power-law spin correlations in pyrochlore antiferromagnets", *Physical Review B* **71**, 014424 (2005).
[88] J. D. Jackson, *Classical Electrodynamics* (John Wiley & Sons, New York, 1962).
[89] R. K. Pathria, *Statistical Mechanics*, Second (Butterworth-Heinemann, Oxford, 1996).
[90] M. Hermele, M. P. A. Fisher, and L. Balents, "Pyrochlore photons: The U (1) spin liquid in a S = 1/2 three-dimensional frustrated magnet", *Phys. Rev. B* **69**, 064404 (2004).
[91] R. Moessner and K. Raman, "Quantum Dimer Models", in *Introduction to Frustrated Magnetism*, Vol. 164, Springer Series in Solid-State Sciences (Springer Berlin Heidelberg, Heidelberg, 2011), pp. 437–480.

[92] D. A. McQuarrie, *Statistical mechanics*, Harper's Chemistry Series (Harper & Row, New York, 1976).
[93] D. C. Brydges and P. A. Martin, "Coulomb systems at low density", *Journal of Statistical Physics* **96**, 1163–1330 (1999).
[94] C. Castelnovo, R. Moessner, and S. L. Sondhi, "Debye-Hückel theory for spin ice at low temperature", *Phys. Rev. B* **84**, 144435 (2011).
[95] P. W. Debye and E. Hueckel, "Zur Theorie der Elektrolyte", *Physikalische Zeitschrift* **9**, 185–206 (1923).
[96] Y. Levin, "Electrostatic correlations: from plasma to biology", *Rep. Prog. Phys.* **65**, 1577–1632 (2002).
[97] A. P. Ramirez, "Strongly Geometrically Frustrated Magnets", *Annual Review of Materials Science* **24**, 453–480 (1994).
[98] G.-W. Chern, "Artificial Spin Ice: Beyond Pyrochlores and Magnetism", in *Spin Ice*, Vol. 197, Springer Series in Solid-State Sciences (Springer International Publishing, 2021), pp. 419–454.
[99] D. Jiles, *Introduction to Magnetism and Magnetic Materials* (Springer US, Boston, MA, 1991).
[100] S. Blundell, *Magnetism in Condensed Matter*, Oxford Master Series in Condensed Matter Physics (Oxford University Press, Oxford, 2001).
[101] R. Pohle and L. D. C. Jaubert, "Curie-law crossover in spin liquids", *Phys. Rev. B* **108**, 024411 (2023).
[102] A. P. Ramirez et al., "Zero-point entropy in 'spin ice"', *Nature* **399**, 333–335 (1999).
[103] S. T. Bramwell et al., "Spin Correlations in $Ho_2Ti_2O_7$: A Dipolar Spin Ice System", *Phys. Rev. Lett.* **87**, 047205 (2001).
[104] C. Kittel, *Introduction to solid state physics*, 8th ed (Wiley, Hoboken, NJ, 2005).
[105] S. M. Girvin and K. Yang, *Modern Condensed Matter Physics* (Cambridge University Press, Cambridge, 2019).
[106] S. T. Bramwell, "Neutron Scattering and Highly Frustrated Magnetism", in *Introduction to Frustrated Magnetism*, Vol. 164, Springer Series in Solid-State Sciences (Springer Berlin Heidelberg, Heidelberg, 2011), pp. 45–78.
[107] R. M. Moon, T. Riste, and W. C. Koehler, "Polarization Analysis of Thermal-Neutron Scattering", *Phys. Rev.* **181**, 920–931 (1969).
[108] T. Fennell et al., "Magnetic Coulomb Phase in the Spin Ice $Ho_2Ti_2O_7$", *Science* **326**, 415–417 (2009).
[109] G. Dhanaraj et al., eds., *Springer Handbook of Crystal Growth* (Springer Berlin Heidelberg, Berlin, Heidelberg, 2010).
[110] B. T. M. Willis and C. J. Carlile, *Experimental Neutron Scattering* (Oxford University Press, Oxford, 2013).
[111] J. E. Greedan, "Geometrically frustrated magnetic materials", *J. Mater. Chem.* **11**, 37–53 (2001).

[112] J. G. Rau and M. J. Gingras, "Frustrated Quantum Rare-Earth Pyrochlores", *Annu. Rev. Condens. Matter Phys.* **10**, 357–386 (2019).

[113] M. J. P. Gingras and B. C. den Hertog, "Origin of Spin Ice Behavior in Ising Pyrochlore Magnets with Long Range Dipole Interactions: an Insight from Mean-Field Theory", *Canadian Journal of Physics* **79**, 1339–1351 (2000).

[114] S. V. Isakov, R. Moessner, and S. L. Sondhi, "Why Spin Ice Obeys the Ice Rules", *Phys. Rev. Lett.* **95**, 217201 (2005).

[115] J. S. Gardner et al., "Glassy Statics and Dynamics in the Chemically Ordered Pyrochlore Antiferromagnet Y2Mo2O7", *Phys. Rev. Lett.* **83**, 211–214 (1999).

[116] H. J. Silverstein et al., "Liquidlike correlations in single-crystalline $Y_2Mo_2O_7$: An unconventional spin glass", *Phys. Rev. B* **89**, 054433 (2014).

[117] S.-H. Lee et al., "Emergent excitations in a geometrically frustrated magnet", *Nature* **418**, 856–858 (2002).

[118] P. H. Conlon and J. T. Chalker, "Absent pinch points and emergent clusters: Further neighbor interactions in the pyrochlore Heisenberg antiferromagnet", *Phys. Rev. B* **81**, 224413 (2010).

[119] K. W. Plumb et al., "Continuum of quantum fluctuations in a three-dimensional S = 1 Heisenberg magnet", *Nature Phys* **15**, 54–59 (2019).

[120] H. Furukawa et al., "The Chemistry and Applications of Metal-Organic Frameworks", *Science* **341**, 1230444 (2013).

[121] J.-R. Li, R. J. Kuppler, and H.-C. Zhou, "Selective gas adsorption and separation in metalorganic frameworks", *Chem. Soc. Rev.* **38**, 1477 (2009).

[122] K. Sumida et al., "Carbon Dioxide Capture in MetalOrganic Frameworks", *Chem. Rev.* **112**, 724–781 (2012).

[123] J. Lee et al., "Metalorganic framework materials as catalysts", *Chem. Soc. Rev.* **38**, 1450 (2009).

[124] P. Horcajada et al., "MetalOrganic Frameworks in Biomedicine", *Chem. Rev.* **112**, 1232–1268 (2012).

[125] M. Kurmoo, "Magnetic metalorganic frameworks", *Chem. Soc. Rev.* **38**, 1353 (2009).

[126] J. M. Bulled et al., "Geometric Frustration on the Trillium Lattice in a Magnetic Metal-Organic Framework", *Phys. Rev. Lett.* **128**, 177201 (2022).

[127] J. G. Park, "Magnetic ordering through itinerant ferromagnetism in a metalorganic framework", *Nature Chemistry* **13**, 11 (2021).

[128] P. Fendley, "Quantum loop models and the non-abelian toric code", *arXiv:0711.0014* (2007).

[129] D. S. Rokhsar and S. A. Kivelson, "Superconductivity and the Quantum Hard-Core Dimer Gas", *Phys. Rev. Lett.* **61**, 2376–2379 (1988).

[130] S. Bravyi et al., "The complexity of stoquastic local Hamiltonian problems", *QIC* **8**, 361–385 (2008).

[131] O. Sikora et al., "Extended quantum U (1) -liquid phase in a three-dimensional quantum dimer model", *Phys. Rev. B* **84**, 115129 (2011).

[132] C. Castelnovo, *Disorder-free localisation phenomena in quantum spin liquids*, Lecture, Trieste, 2022.

[133] A. Zee, *Group theory in a nutshell for physicists*, In a Nutshell (Princeton University Press, Princeton, 2016).

[134] M. Levin and X.-G. Wen, "Detecting Topological Order in a Ground State Wave Function", *Phys. Rev. Lett.* **96**, 110405 (2006).

[135] A. Kitaev and J. Preskill, "Topological Entanglement Entropy", *Phys. Rev. Lett.* **96**, 110404 (2006).

[136] M. A. Nielsen and I. L. Chuang, *Quantum computation and quantum information*, 10th anniversary ed (Cambridge University Press, Cambridge ; New York, 2010).

[137] A. Hamma, R. Ionicioiu, and P. Zanardi, "Bipartite entanglement and entropic boundary law in lattice spin systems", *Phys. Rev. A* **71**, 022315 (2005).

[138] S. Furukawa and G. Misguich, "Topological entanglement entropy in the quantum dimer model on the triangular lattice", *Phys. Rev. B* **75**, 214407 (2007).

[139] A. M. Läuchli, E. J. Bergholtz, and M. Haque, "Entanglement scaling of fractional quantum Hall states through geometric deformations", *New J. Phys.* **12**, 075004 (2010).

[140] Y. Zhang, T. Grover, and A. Vishwanath, "Topological entanglement entropy of Z_2 spin liquids and lattice Laughlin states", *Phys. Rev. B* **84**, 075128 (2011).

[141] H.-C. Jiang, H. Yao, and L. Balents, "Spin liquid ground state of the spin-1/2 square J1 - J2 Heisenberg model", *Phys. Rev. B* **86**, 024424 (2012).

[142] M. F. A. de Resende, "A pedagogical overview on 2D and 3D Toric Codes and the origin of their topological orders", *Rev. Math. Phys.* **32**, 2030002 (2020).

[143] C. Castelnovo and C. Chamon, "Topological order in a three-dimensional toric code at finite temperature", *Phys. Rev. B* **78**, 155120 (2008).

[144] T. Grover, A. M. Turner, and A. Vishwanath, "Entanglement entropy of gapped phases and topological order in three dimensions", *Phys. Rev. B* **84**, 195120 (2011).

[145] N. Shannon et al., "Quantum Ice: A Quantum Monte Carlo Study", *Phys. Rev. Lett.* **108**, 067204 (2012).

[146] M. J. P. Gingras and P. A. McClarty, "Quantum spin ice: a search for gapless quantum spin liquids in pyrochlore magnets", *Rep. Prog. Phys.* **77**, 056501 (2014).

[147] A. Banerjee et al., "Unusual Liquid State of Hard-Core Bosons on the Pyrochlore Lattice", *Phys. Rev. Lett.* **100**, 047208 (2008).

[148] O. Benton, O. Sikora, and N. Shannon, "Seeing the light: Experimental signatures of emergent electromagnetism in a quantum spin ice", *Phys. Rev. B* **86**, 075154 (2012).

[149] L. Savary and L. Balents, "Coulombic Quantum Liquids in Spin-1/2 Pyrochlores", *Phys. Rev. Lett.* **108**, 037202 (2012).

[150] S. Lee, S. Onoda, and L. Balents, "Generic quantum spin ice", *Phys. Rev. B* **86**, 104412 (2012).

[151] C.-J. Huang et al., "Dynamics of Topological Excitations in a Model Quantum Spin Ice", *Phys. Rev. Lett.* **120**, 167202 (2018).

[152] O. Benton et al., "Quantum Spin Ice with Frustrated Transverse Exchange: From a π-Flux Phase to a Nematic Quantum Spin Liquid", *Phys. Rev. Lett.* **121**, 067201 (2018).

[153] F. Desrochers, L. E. Chern, and Y. B. Kim, "Symmetry fractionalization in the gauge mean-field theory of quantum spin ice", *Phys. Rev. B* **107**, 064404 (2023).

[154] S. C. Morampudi, F. Wilczek, and C. R. Laumann, "Spectroscopy of Spinons in Coulomb Quantum Spin Liquids", *Phys. Rev. Lett.* **124**, 097204 (2020).

[155] S. D. Pace et al., "Emergent Fine Structure Constant of Quantum Spin Ice Is Large", *Phys. Rev. Lett.* **127**, 117205 (2021).

[156] Y.-P. Huang, G. Chen, and M. Hermele, "Quantum Spin Ices and Topological Phases from Dipolar-Octupolar Doublets on the Pyrochlore Lattice", *Phys. Rev. Lett.* **112**, 167203 (2014).

[157] E. M. Smith et al., "Case for a $U(1)_\pi$ Quantum Spin Liquid Ground State in the Dipole-Octupole Pyrochlore $Ce_2Zr_2O_7$", *Phys. Rev. X* **12**, 021015 (2022).

[158] R. Sibille et al., "Experimental signatures of emergent quantum electrodynamics in $Pr_2Hf_2O_7$", *Nature Phys* **14**, 711–715 (2018).

[159] J. R. Schrieffer and P. A. Wolff, "Relation between the Anderson and Kondo Hamiltonians", *Phys. Rev.* **149**, 491–492 (1966).

[160] S. Bravyi, D. P. DiVincenzo, and D. Loss, "SchriefferWolff transformation for quantum many-body systems", *Annals of Physics* **326**, 2793–2826 (2011).

[161] K. Slagle and Y. B. Kim, "Fracton topological order from nearest-neighbor two-spin interactions and dualities", *Phys. Rev. B* **96**, 165106 (2017).

[162] J. B. Kogut, "An introduction to lattice gauge theory and spin systems", *Rev. Mod. Phys.* **51**, 659–713 (1979).

[163] R. Moessner and S. L. Sondhi, "Three-dimensional resonating-valence-bond liquids and their excitations", *Phys. Rev. B* **68**, 184512 (2003).

[164] L. D. C. Jaubert et al., "Spin ice Thin Film: Surface Ordering, Emergent Square ice, and Strain Effects", *Phys. Rev. Lett.* **118**, 207206 (2017).

[165] É. Lantagne-Hurtubise, J. G. Rau, and M. J. P. Gingras, "Spin-Ice Thin Films: Large- N Theory and Monte Carlo Simulations", *Phys. Rev. X* **8**, 021053 (2018).

[166] S. Nelakanti, "Monte Carlo Simulations of the Ising Model on the Centred Pyrochlore Lattice", MA thesis (LMU Munich, Munich, 2023).

[167] L. D. C. Jaubert, *Private correspondence*, 2023.

[168] D. A. Garanin and B. Canals, "Classical spin liquid: Exact solution for the infinite-component antiferromagnetic model on the kagomé lattice", *Phys. Rev. B* **59**, 443–456 (1999).

[169] J. N. Reimers, A. J. Berlinsky, and A.-C. Shi, "Mean-field approach to magnetic ordering in highly frustrated pyrochlores", *Phys. Rev. B* **43**, 865–878 (1991).

[170] J. M. Luttinger, "A Note on the Ground State in Antiferromagnetics", *Phys. Rev.* **81**, 1015–1018 (1951).

[171] D. H. Lyons and T. A. Kaplan, "Method for Determining Ground-State Spin Configurations", *Phys. Rev.* **120**, 1580–1585 (1960).

[172] H. Katsura et al., "Ferromagnetism in the Hubbard model with topological/non-topological flat bands", *EPL* **91**, 57007 (2010).

[173] K. Essafi, L. D. C. Jaubert, and M. Udagawa, "Flat bands and Dirac cones in breathing lattices", *J. Phys.: Condens. Matter* **29**, 315802 (2017).

[174] A. M. Mathai and H. J. Haubold, *Linear Algebra: A Course for Physicists and Engineers*, De Gruyter Textbook (Walter de Gruyter, Berlin/Boston, 2017).

[175] Y. Katznelson and Y. R. Katznelson, *A (Terse) Introduction to Linear Algebra*, Vol. 44, The Student Mathematical Library (American Mathematical Society, Providence, Rhode Island, 2007).

[176] J. Greitemann, *TK-SVM: Probing Hidden Spin Order with Interpretable Machine Learning*, 2019.

[177] F. R. Brown and T. J. Woch, "Overrelaxed heat-bath and Metropolis algorithms for accelerating pure gauge Monte Carlo calculations", *Phys. Rev. Lett.* **58**, 2394–2396 (1987).

[178] M. Creutz, "Overrelaxation and Monte Carlo simulation", *Physical Review D* **36**, 515–519 (1987).

[179] D. P. Landau and K. Binder, *A Guide to Monte Carlo Simulations in Statistical Physics*, Third (Cambridge University Press, Cambridge, 2009).

[180] M. Creutz, "Monte Carlo study of quantized SU(2) gauge theory", *Phys. Rev. D* **21**, 2308–2315 (1980).

[181] W. Janke, "Monte Carlo Methods in Classical Statistical Physics", *Lect. Notes Phys.* Lecture Notes in Physics **739**, 79–140 (2008).

[182] N. Shannon, K. Penc, and Y. Motome, "Nematic, vector-multipole, and plateau-liquid states in the classical O (3) pyrochlore antiferromagnet with biquadratic interactions in applied magnetic field", *Phys. Rev. B* **81**, 184409 (2010).

[183] E. Lhotel, L. D. C. Jaubert, and P. C. W. Holdsworth, "Fragmentation in Frustrated Magnets: A Review", *J Low Temp Phys* **201**, 710–737 (2020).

[184] O. Benton and R. Moessner, "Topological Route to New and Unusual Coulomb Spin Liquids", *Phys. Rev. Lett.* **127**, 107202 (2021).

[185] R. A. Borzi, D. Slobinsky, and S. A. Grigera, "Charge Ordering in a Pure Spin Model: Dipolar Spin Ice", *Phys. Rev. Lett.* **111**, 147204 (2013).

[186] D. Slobinsky, G. Baglietto, and R. A. Borzi, "Charge and spin correlations in the monopole liquid", *Phys. Rev. B* **97**, 174422 (2018).

[187] J. Rehn, A. Sen, and R. Moessner, "Fractionalized Z_2 Classical Heisenberg Spin Liquids", *Phys. Rev. Lett.* **118**, 047201 (2017).

[188] F. Gándara et al., "Porous, Conductive Metal-Triazolates and Their Structural Elucidation by the Charge-Flipping Method", *Chem. Eur. J.* **18**, 10595–10601 (2012).

[189] M. Grzywa et al., "CuN_6 JahnTeller centers in coordination frameworks comprising fully condensed Kuratowski-type secondary building units: phase transitions and magneto-structural correlations", *Dalton Trans.* **41**, 4239 (2012).

[190] X.-H. Zhou et al., "Hydrothermal syntheses and structures of three novel coordination polymers assembled from 1,2,3-triazolate ligands", *CrystEngComm* **11**, 1964 (2009).

[191] J. G. Park et al., "Charge Delocalization and Bulk Electronic Conductivity in the Mixed-Valence MetalOrganic Framework Fe(1,2,3-triazolate)$_2$(BF_4)$_x$", *J. Am. Chem. Soc.* **140**, 8526–8534 (2018).

[192] M. Grzywa et al., "Cooperative Large-Hysteresis Spin-Crossover Transition in the Iron(II) Triazolate [Fe(ta)$_2$] MetalOrganic Framework", *Inorg. Chem.* **59**, 10501–10511 (2020).

[193] L. Sun et al., "Is iron unique in promoting electrical conductivity in MOFs?", *Chem. Sci.* **8**, 4450–4457 (2017).

[194] K. Millard and H. S. Leff, "Infinite-Spin Limit of the Quantum Heisenberg Model", *Journal of Mathematical Physics* **12**, 1000–1005 (1971).

[195] E. H. Lieb, "The classical limit of quantum spin systems", *Communications in Mathematical Physics* **31**, 327–340 (1973).

[196] B. Javanparast et al., "Fluctuation-Driven Selection at Criticality in a Frustrated Magnetic System: The Case of Multiple- k Partial Order on the Pyrochlore Lattice", *Phys. Rev. Lett.* **114**, 130601 (2015).

[197] H. Yan et al., "Theory of multiple-phase competition in pyrochlore magnets with anisotropic exchange with application to $Yb_2Ti_2O_7$, $Er_2Ti_2O_7$, and $Er_2Sn_2O_7$", *Phys. Rev. B* **95**, 094422 (2017).

[198] S. Zhang et al., "Dynamical Structure Factor of the Three-Dimensional Quantum Spin Liquid Candidate $NaCaNi_2F_7$", *Phys. Rev. Lett.* **122**, 167203 (2019).

[199] A. M. Samarakoon et al., "Machine-learning-assisted insight into spin ice $Dy_2Ti_2O_7$", *Nat Commun* **11**, 892 (2020).

[200] D. R. Yahne et al., "Understanding Reentrance in Frustrated Magnets: The Case of the $Er_2Sn_2O_7$ Pyrochlore", *Phys. Rev. Lett.* **127**, 277206 (2021).

[201] N. P. Raju et al., "Transition to long-range magnetic order in the highly frustrated insulating pyrochlore antiferromagnet $Gd_2Ti_2O_7$", *Phys. Rev. B* **59**, 14489–14498 (1999).

[202] V. F. Sears, "Neutron scattering lengths and cross sections", *Neutron News* **3**, 26–37 (1992).

[203] J. Pitcairn et al., "Low-Dimensional MetalOrganic Magnets as a Route toward the S = 2 Haldane Phase", *J. Am. Chem. Soc.* **145**, 1783–1792 (2023).

[204] P. H. Conlon and J. T. Chalker, "Spin Dynamics in Pyrochlore Heisenberg Antiferromagnets", *Phys. Rev. Lett.* **102**, 237206 (2009).

[205] D. L. Bergman et al., "Quantum Effects in a Half-Polarized Pyrochlore Antiferromagnet", *Phys. Rev. Lett.* **96**, 097207 (2006).

[206] D. L. Bergman, G. A. Fiete, and L. Balents, "Ordering in a frustrated pyrochlore antiferromagnet proximate to a spin liquid", *Phys. Rev. B* **73**, 134402 (2006).

[207] O. Sikora et al., "Quantum Liquid with Deconfined Fractional Excitations in Three Dimensions", *Phys. Rev. Lett.* **103**, 247001 (2009).

[208] J. Shah et al., "Quantum spin ice in three-dimensional Rydberg atom arrays", *arXiv:2301.04657* (2023).

[209] W. H. Press et al., *Numerical Recipes - The Art of Scientific Computing*, Third (Cambridge University Press, Cambridge, 2007).

[210] C. Hickey et al., "Field-driven gapless spin liquid in the spin-1 Kitaev honeycomb model", *Phys. Rev. Research* **2**, 023361 (2020).

[211] S. Sachdev, *Quantum Phase Transitions*, 2nd ed. (Cambridge University Press, Cambridge, 2011).

[212] A. WeiSSe and H. Fehske, "Exact Diagonalization Techniques", *Lect. Notes Phys.* **739**, 529–544 (2008).

[213] A. W. Sandvik, A. Avella, and F. Mancini, "Computational Studies of Quantum Spin Systems", in AIP Conf. Proc. Vol. 1297 (2010), pp. 135–338.

[214] J. J. Sakurai and J. Napolitano, *Modern quantum mechanics*, 2nd ed (Addison-Wesley, Boston, 2011).

[215] S. Liang, "A perfect hashing function for exact diagonalization of many-body systems of identical particles", *Computer Physics Communications* **92**, 11–15 (1995).

[216] C. Jia et al., "Paradeisos: A perfect hashing algorithm for many-body eigenvalue problems", *Computer Physics Communications* **224**, 81–89 (2018).

[217] C. Lanczos, "Solution of systems of linear equations by minimized iterations", *J. RES. NATL. BUR. STAN.* **49**, 33 (1952).

[218] R. B. Lehoucq, D. C. Sorensen, and C. Yang, "ARPACK User's Guide: Solution of Large Scale Eigenvalue Problems with Implicitly Restarted Arnoldi Methods", 1997.

[219] L. Dagum and R. Menon, "OpenMP: an industry standard API for shared-memory programming", *IEEE Computational Science and Engineering* **5**, 46–55 (1998).

[220] D. C. Sorensen, "Implicit Application of Polynomial Filters in a k-step Arnoldi Method", *SIAM Journal on Matrix Analysis and Applications* **13**, 357–385 (1992).

[221] A. Wietek and A. M. Läuchli, "Sublattice coding algorithm and distributed memory parallelization for large-scale exact diagonalizations of quantum many-body systems", *Phys. Rev. E* **98**, 033309 (2018).

Acknowledgements

I have thoroughly enjoyed my time in Munich working towards my PhD (although there have been some ups and downs), which is almost entirely thanks to the people I have worked with and met along the way. I only got to this point thanks to all of you.

First, I would like to thank Lode for his support and guidance over the last four years. You gave me the freedom to develop, letting me try out my own ideas, without putting me under any pressure. I have really learnt a lot.
Thanks to Ludo for helping me learn the ropes with pyrochlore physics, many great ideas for our work together, hosting me during my stay in Bordeaux and many zoom meetings. This thesis would not be possible without you.
I am grateful to my experimental collaborators: Richard, Dirk, Alexander, Anton, Hans-Albrecht and Phillip, for getting this project started and invaluable expertise on what can be done from a synthesis or measurement point of view.

To the chair (past and present), thanks to everyone who made it such a fun place to be since we got back to the office, I'll miss you guys. Special shout out to everyone who proofread and helped with parts of this thesis: Giovanni, Henning, Matjaz, Mattia, Felix and Nico.
Cordula, thanks for all your help and patience over the years.
Thanks to Sonya for all your support and encouragement in getting the most out of IMPRS.

The beginning of my time in Munich wasn't the easiest, so I would like to thank Max and Janine for keeping me company with many bike rides and concerts. I couldn't have gotten through the pandemic years without my housemates Nina, Louay and Yanis, Lukas, king of the double bogey Jai Nutakki, the RPG gang (Stanley and Barnaby), and the settlers of NXG.
Everyone else I have had the pleasure of hanging out with in Munich, it's been wonderful.
Last but not least, to all my friends and family from back home, I've missed you a lot but I have really treasured the moments we got to meet up.